FEATURED IMAGE

Bilateral Pelvic Kidney Masquerading as Horseshoe Kidney in Fanconi Anemia. Tanigassalam Sindhu et al. See page 379.

JNMT Journal of NUCLEAR MEDICINE TECHNOLOGY

The Official Publication of **SNMMI-TS**

MISSION: SNMMI-TS is dedicated to the advancement of molecular and nuclear medicine technologists by providing education, advocating for the profession, and supporting research to achieve clinical excellence and optimal patient outcomes. **VISION:** To be recognized as the leader in molecular imaging and therapy. To be dedicated to the advancement of the profession through adoption of emerging technologies.

JNMT

Volume 50, Number 4 • December 2022

A novel investigational PSMA-targeting technology for prostate cancer imaging

In recent years, radiopharmaceutical innovations have greatly improved our ability to detect and localize prostate cancer. Until recently, conventional imaging, including bone scan, computed tomography (CT), and magnetic resonance imaging (MRI), has been the standard of care in prostate cancer imaging. These conventional imaging modalities have limitations, including diagnostic performance at low prostate-specific antigen (PSA) levels.[1,2] Technological advances have led to the research and development of more sensitive imaging agents and modalities.[1,3] Specifically, positron emission tomography (PET) radiopharmaceuticals are increasingly being used to target prostate-specific membrane antigen (PSMA), and a growing body of scientific evidence supports their favorable imaging performance.[1] *Blue Earth Diagnostics is exploring a new investigational PSMA targeting technology with unique potential.[4-6]*

PSMA as a target

PSMA is an obvious target for PET imaging in prostate cancer. It is a well characterized type II transmembrane protein with folate hydrolase activity. Present in normal prostatic tissue, PSMA is upregulated in the majority of primary and metastatic prostate cancer lesions.[7-9]

Several characteristics make PSMA an ideal target for molecular imaging, including:

• High expression on prostate cancer cells[10]

• Limited expression on benign prostate tissue and extraprostatic tissue[10]

• Well-characterized binding site that can be targeted by small-molecule ligands[10]

• Internalization of bound agents, allowing for concentration within tumor cells[10]

• PSMA expression can be correlated with Gleason grade and has been shown to be enhanced in metastatic and castrate-resistant prostate cancer[9,10]

PSMA imaging agents are designed to bind to the extracellular domain of PSMA to then be internalized by prostate cancer cells via endocytosis. When labeled with a ß+ emitting radioisotope, these agents can detect extracellular expression of PSMA with PET imaging.[9-11] PSMA-targeting radiopharmaceuticals are characterized by rapid clearance from the blood and nontarget tissue, which can result in low background activity.[9]

Radioisotope selection and labeling

Currently available PSMA agents are either labeled with gallium-68 (^{68}Ga) or fluorine-18 (^{18}F), 2 ß+ emitting radioisotopes. In recent years, ^{18}F has been recognized to have certain advantages over ^{68}Ga.[9]

While ^{68}Ga can be produced with either a cyclotron or generator, production capacity via generator is limited to 2 to 4 patient doses daily. ^{68}Ga also has a relatively short half-life of 68 minutes, limiting its transportation to centers.[9] ^{18}F has an 110-minute half-life and may be produced in large batches via a cyclotron, which allows for centralized production and subsequent broad distribution to imaging facilities (see Table 1).[12,13]

Blue Earth Diagnostics is at the forefront in the investigation of prostate cancer imaging, with worldwide exclusive licenses to radiohybrid PSMA (rhPSMA) technology.

Figure 1. Example of a radiohybrid structure

^{nat}Lu — PSMA-inhibitor — ^{18}F **A**

^{18}F-^{nat}Lu-rhPSMA

^{177}Lu — PSMA-inhibitor — ^{19}F **B**

^{19}F-^{177}Lu-rhPSMA
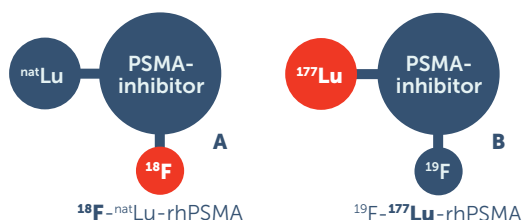
Adapted from Wurzer A et al. *J Nucl Med.* 2020.[6]

The rhPSMA design features 2 radionuclide acceptor sites that can be labeled with α or ß emitting radionuclides (Figure 1). Figure 1A depicts the rhPSMA molecule for potential diagnostic use, where one acceptor site is labeled with a radioactive imaging isotope, and the other site with a nonradioactive isotope. Figure 1B depicts the molecule for potential therapeutic use, where one acceptor site is labeled with a radioactive therapeutic isotope and the other site with a nonradioactive isotope.[6]

Review the phase 3 clinical studies for rhPSMA technology[4,5]:

- Learn more about the LIGHTHOUSE study in men with newly diagnosed prostate cancer at clinicaltrials.gov/ct2/show/NCT04186819
- Learn more about the SPOTLIGHT study in men with suspected prostate cancer recurrence at clinicaltrials.gov/ct2/show/NCT04186845

Blue Earth Diagnostics is committed to breaking new ground

Blue Earth Diagnostics is an established leader in the development of novel PET imaging agents to inform clinical management decisions with the goal of positively impacting overall outcomes for patients with prostate cancer.

Our goals are to:

- Develop cutting-edge technology
- Build innovative solutions
- Enhance access to radiopharmaceuticals and provide customer and practice support

Sponsored by Blue Earth Diagnostics, Inc.

Radiohybrid PSMA technology is investigational and not approved by the US Food and Drug Administration (FDA).

References: 1. Jadvar H, Calais J, Fanti S, et al. *J Nucl Med.* 2022;63(1):59-68. doi:10.2967/jnumed.121.263262 **2.** Expert Panel on Urologic Imaging; Froemming AT, Verma S, Eberhardt SC, et al. *J Am Coll Radiol.* 2018;15(5S):S132-S149. doi:10.1016/j.jacr.2018.03.019 **3.** Crawford ED, Koo PJ, Shore N, et al. *J Urol.* 2019;201(4):682-692. doi:10.1016/j.juro.2018.05.164 **4.** Blue Earth Diagnostics. March 17, 2022. Accessed July 27, 2022. https://clinicaltrials.gov/ct2/show/NCT04186819 **5.** Blue Earth Diagnostics. March 17, 2022. Accessed July 27, 2022. https://clinicaltrials.gov/ct2/show/NCT04186845 **6.** Wurzer A, Di Carlo D, Schmidt A, et al. *J Nucl Med.* 2020;61(5):735-742. doi:10.2967/jnumed.119.234922 **7.** Sarkar S, Das S. *Biomed Eng Comput Biol.* 2016;7(suppl 1):1-15. doi:10.4137/BECB.S34255 **8.** Hofman MS, Hicks RJ, Maurer T, Eiber M. *Radiographics.* 2018;38(1):200-217. doi:10.1148/rg.2018170108 **9.** Piron S, Verhoeven J, Vanhove C, De Vos F. *Nucl Med Biol.* 2022;106-107:29-51. doi:10.1016/j.nucmedbio.2021.12.005 **10.** Donin NM, Reiter RE. *J Nucl Med.* 2018;59(2):177-182. doi:10.2967/jnumed.117.191874 **11.** Tolvanen T, Kalliokoski K, Malaspina S, et al. *J Nucl Med.* 2021;62(5):679-684. doi:10.2967/jnumed.120.252114 **12.** Jacobson O, Kiesewetter DO, Chen X. *Bioconjug Chem.* 2015;26(1):1-18. doi:10.1021/bc500475e **13.** Gorin MA, Pomper MG, Rowe SP. *BJU Int.* 2016;117(5):715-716. doi:10.1111/bju.13435 **14.** Conti M, Eriksson L. *EJNMMI Phys.* 2016;3(1):8. doi:10.1186/s40658-016-0144-5

BLUE EARTH DIAGNOSTICS — A Bracco Company | Prostate Cancer

©2022 Blue Earth Diagnostics, Inc. All rights reserved. MLR22-P003A 08/22

In addition, ^{18}F has an energy profile that may contribute to a more favorable spatial resolution, which may enable ^{18}F to better detect lesions that are small and near each other compared with ^{68}Ga (see Table 1).[9,12-14]

Table 1. Radioisotope features[9,12-14]

	^{18}F	^{68}Ga
Half-life	110 minutes	68 minutes
Positron decay ratio	97%	89%
Maximum positron energy	0.635 MeV	1.899 MeV
Mean positron range	0.6 mm	3.5 mm
Production method	Cyclotron	Generator or cyclotron

SNMMI-TS Is Working for YOU!

Krystle W. Glasgow, MIS, CNMT, NMTCB(CT), NMAA, FSMMMI-TS

Many exciting things are on the horizon for the world of nuclear medicine and molecular imaging. The SNMMI-TS has its finger on the pulse of the latest and greatest aspects of diagnostics and therapeutics. There are many initiatives and projects being worked on and developed by our talented committee members, and there are also new challenges that we are diligently working to overcome. I would like to take the time to discuss some of these.

Barriers to Access and Workforce Pipeline Challenges

This is a main focus of the Biden Administration. In January of this year, the U.S. Department of Health and Human Services (HHS) secretary hosted a virtual roundtable to discuss challenges related to the health care workforce pipeline, which have been further exacerbated by the COVID-19 pandemic. Nuclear medicine technologists (NMTs) are not alone in this issue. Employment in health care occupations is projected to grow 16 percent from 2020 to 2030—much faster than the average for all occupations—adding about 2.6 million new jobs.

In addition, almost 50 percent of technologists working in the field are 50+ years of age, so there may be a large number of retirements in the next 10–15 years. Also, fewer students entered the NMT programs in 2021, and this, coupled with a lower graduation rate due to COVID-19 in 2020, begs the question, "Who is going to fill our future workforce needs?" Moreover, we are seeing exponential growth in radiopharmaceutical therapies. There will need to be additional education and specialization needed for NMTs specific to therapies.

What Is the SNMMI-TS Doing to Address These Challenges with the NMT Workforce Pipeline?

The SNMMI-TS has initiated the creation of a Workforce Pipeline Task Force to better understand the current challenges of entry into the field and understand the way students are exposed to nuclear medicine as a career pathway during high school and undergraduate education. In addition, through outreach, education, and the exchange of knowledge, the SNMMI-TS hopes to create communication bridges for NMT programs to work collaboratively with institutions around the country who need to hire qualified NMTs.

The purpose of this task force is:

- To gather data regarding the current number of NMT positions available versus the number of practicing NMTs
- To identify challenges and opportunities for entry and retention within the field of nuclear medicine technology
- To create comprehensive pathway options for students into the field

The SNMMI wants to ensure that there is a sufficient number of professionals who are qualified to practice in all aspects of nuclear medicine and molecular imaging both now and in the future. In order to accomplish this goal, we have partnered with IMV to complete a comprehensive Nuclear Medicine Workforce Study. IMV is a recognized leader in market research and online publishing for the medical imaging and clinical diagnostic instruments markets. The company is looking specifically at factors affecting the future outlook for nuclear medicine departments.

Krystle W. Glasgow, MIS, CNMT, NMTCB(CT), NMAA, FSNMMI-TS

The SNMMI also wants to increase awareness of nuclear medicine and molecular imaging as an appealing and rewarding field for students interested in STEM (science, technology, engineering, and mathematics) careers. For the technologist pipeline, we are focused on 3 main areas:

- Chapter Collaboration—Creating a panel on workforce challenges
  - There will be discussion on how to solve challenges with a *regional* focus—we realize that different geographic areas have different challenges at times.
  - This will be a place to share best practices in order to disseminate the information to all regions.
- Career Pathways—Showcase different career options for technologists
  - "How did you get to where you are today, and what was needed to get there?"
  - SNMMI-TS has created a 4- to 5-minute video and social media uploads that are available this fall.
- Program Directors—Survey program directors (both current and ones from recently closed programs)
  - We want to determine why programs are closing.
  - We also want to identify possible institutions that can collaborate to train across the country.
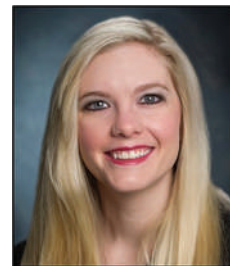
Advancement through Advocacy

With nuclear medicine and molecular imaging rapidly expanding, it is *critical* that professionals within the field have a dedicated society working for them on behalf of their best interests. I am proud to say that the SNMMI truly is

working for YOU! By working together, we can bring greater value to the fields of imaging and medicine, advancing scientific discovery, and further improving patient outcomes.

The SNMMI monitors state-level issues impacting the field, with our Technologist Advocacy Group (TAG) members representing all 50 states. Our focus is seeking licensure and appropriate regulation for nuclear medicine technologists at the state level as well as appropriate reimbursement at the physician level. The SNMMI also advocates for members on national and local levels by monitoring news, laws/regulations, and policy changes that affect SNMMI's technologists.

Current advocacy efforts include 3 states:

- Pennsylvania: We are continuing to work on a bill that would make changes to the Medical Practices Act and require licensing of imaging professionals.
- Michigan: Administrative rules are being debated concerning which jurisdiction nuclear medicine falls into related to state legislation and agencies. SNMMI provided policymakers with a list of Nuclear Regulatory Commission state licensure statutes and regulations and continues to work to pass our bill.
- Georgia: We are currently working on a certification requirement to perform medical imaging or radiation therapy. We are collaborating and negotiating on language beneficial to nuclear medicine technologists.

Molecular Therapy Task Force

Because radiopharmaceutical therapy is rapidly growing, SNMMI-TS leadership recognized that we needed to put special focus and emphasis on this area. I am very excited to see what this group does this year. There are 4 major goals for this task force:

1. Create a comprehensive radiopharmaceutical therapy educational program for technologists.
2. Develop radiopharmaceutical therapy clinical tools and resources for technologists.
3. Serve as the leader in identifying and managing professional practice issues for technologists within radiopharmaceutical therapy.
4. Create a comprehensive outreach strategy to disseminate education and resources to technologists.

Technologist Quality Committee

This committee has been going strong for several years now. The SNMMI-TS is committed to quality, and I wanted to take the time to highlight what this group is currently working on. The 4 main charges for this committee this year are:

1. Develop a quality survey to identify metrics (KPIs) used routinely in nuclear medicine to assess quality.
2. Create education for gap areas (these were identified in the 2022 Quality Survey) and develop working documents for reference and publication.
3. Develop educational materials and presentations/webinars related to improving quality in nuclear medicine and molecular imaging.
4. Meet with stakeholders to ensure buy-in collaboration to move initiatives forward.

The committee is currently developing a white paper with an analytical comparison of the 2015 and 2022 quality surveys. The group is also developing educational resources regarding dose calibrator calibration, quality control, and appropriate usage. Be on the lookout for these in the near future!

Nuclear Medicine ARRT Clinical Refreshers

The SNMMI partnered with the American Registry of Radiologic Technologists (ARRT) to develop nuclear medicine–specific Continuing Qualification Requirements (CQRs). This project began in 2018 and was completed in late 2021. Under the guidance of the SNMMI-TS CE Committee, the Clinical Refreshers were born. These refreshers are designed to meet the new CQRs of the ARRT and were developed by 32 subject matter experts, 7 SNMMI staff and consultants, and 3 ARRT reviewers. The Clinical Refreshers provide quick (15 minutes or less) basic information, in video format, on how to do nuclear medicine procedures. The videos follow the clinical competency outline and provide information on 44 specific topic areas. The clinical refreshers are available on the ARRT website.

Wellness Initiative

Finally, I want to leave you with a discussion on one of the newest initiatives of the SNMMI. The purpose of the Wellness Initiative is to help members identify and reflect on internal and external factors impacting personal well-being in a supportive environment of professional peers. We want to provide an avenue to combat burnout impacting the emotional, mental, and physical well-being of health care professionals around the world. The focus areas are burnout, emotional and mental exhaustion, guilt and anxiety, depression, and loneliness. This initiative is sponsored by the SNMMI In-Training Committee and Early Career Professionals Committee.

Remember, the SNMMI-TS is working for YOU … but also know that your membership matters and YOU matter. I look forward to the rest of this year and to helping to facilitate the exciting things that are coming!

Five Years in Review

Kathy S. Thomas, MHA, CNMT, PET, FSNMMI-TS

Editor, *JNMT*

This December 2022 issue marks my fifth year as *JNMT* editor. In my first December editorial, I took readers on a walk down memory lane to highlight the successes achieved in my first year. We launched new sections in *JNMT,* including the Educators' Forum, Practical Protocol Tips, Brief Communications, increased CE offerings, and the *JNMT* Twitter Club. Although the *JNMT* Twitter Club met with limited success, the other new sections remain strong today. Thanks to the fantastic work of Mary Beth Farrell, CE Associate Editor, and the expertise shared by my associate and consulting editors as mentors and authors, *JNMT* has published at least 12 continuing education (CE) articles in each of the past 5 years. In that same period, many new authors took advantage of our "Help is available" offer and successfully published educational or scientific manuscripts in *JNMT*. Additionally, the Educators' Forum continues to support the vital work of our educators; the Practical Protocol Tips provide clinical technologists with concise imaging or therapeutic protocols that can be easily incorporated into a department's procedure manual; and *JNMT* content continues to explore and identify new opportunities to support the rapid and ever-changing world of nuclear medicine technology today. It's important to note, however, that these successes were possible only through the continuous help and support of my associate and consulting editors, as well as the patience and continued guidance of Susan Alexander, Paulette McGee, Mark Sumimoto, and Susan Nath, SNMMI's journals team, and Caroline Krystek and Jane Kamm in the Education Department.

As we look forward to 2023 and beyond, it's time to re-measure *JNMT*'s content with the needs of the professional community. Does *JNMT* meet your professional needs? In the coming months, a new survey will be developed; and yes, I know, no one likes surveys! However, without your input, the growth and development of *JNMT* content is a "best guess" that it is meeting your needs. So please, when you receive your survey, take a few moments to answer the questions and, most importantly, be honest and frank. What works? What is no longer relevant? What could be added to (or deleted from) *JNMT* to meet your professional needs? With your help and input, *JNMT* content will continue to grow with the rapidly changing technology in nuclear medicine and molecular imaging.

This issue offers a wide diversity of CE articles. The Clinical Trials Network returns with an informative discussion on the use of imaging agents in developing and approving therapeutic drugs (*1*). The adage "to err is human" extends to every medical setting where the complexity of providing medical care can result in unexpected and sometimes catastrophic events that require a careful review and assessment to avoid similar occurrences in the future. The discussion on root cause analysis provides one example of a systematic approach to pinpoint the cause of a sentinel or near-miss safety event (*2*). The final CE offering explores the role of diuretic renal scintigraphy to differentiate obstructive and nonobstructive hydronephrosis (*3*). A diuretic renography Practical Protocol Tip follows the CE, which can be used to update or can be incorporated into the department's procedure manual (*4*).

Kathy S. Thomas, MHA, CNMT, PET, FSNMMI-TS

Three discussions on brain imaging are offered in this issue. Sugiura et al. provide statistical data on the influence of minimum count in brain perfusion SPECT in phantom and clinical studies (*5*); Kong et al. review ^{68}Ga-DOTATATE PET/CT in the diagnosis of recurrent meningioma (*6*); and Djekidel presents the use of a subtraction technique using ^{18}F-FDG PET in medically refractory epilepsy (*7*).

The Educators' Forum returns with two practical discussions. Currie and Currie introduce the concept of emotional intelligence as it relates to better patient care and improved well-being of healthcare professionals (*8*), and Patchoros and Tursi-Wenzler explore the use of Joint Review Committee on Educational Programs in Nuclear Medicine Technology (JRCNMT) compliance forms in building program efficiencies (*9*).

Additional scientific manuscripts and teaching case studies offer a diverse variety of topics to provide helpful information and techniques that can be useful in the clinical setting.

And I would be remiss if I didn't step up on my soapbox once again to solicit new authors and reviewers for *JNMT*. So many potential authors are reluctant to share their expertise because they don't know how—but how many times have you heard me say, "Help is available!"? If you would like to share scientific information or develop an educational offering but don't know where to start, please get in touch with me! And the quality of *JNMT* relies on the volunteer efforts of its reviewers. If you would like to share your expertise by becoming a reviewer, please contact me at ksthomas0412@msn.com!

Finally, I would like to wish you all a wonderful holiday season and a very happy and healthy New Year!

REFERENCES

1. Jeffers CD, Lawhn-Heath C, Butterfield RI, Hoffman JM, Scott PJH. SNMMI Clinical Trials Network research series for technologists: clinical research primer—use of imaging agents in therapeutic drug development and approval. *J Nucl Med Technol.* 2022;50:292–300.
2. Dhingra J, Farrell MB, Halkar RK. Root cause analysis in nuclear medicine for sentinel events. *J Nucl Med Technol.* 2022;50:301–308.
3. Banks KP, Farrell MB, Peacock JG. Diuretic renal scintigraphy protocol considerations. *J Nucl Med Technol.* 2022;50:309–318.
4. Farrell MB. Diuretic renal scintigraphy. *J Nucl Med Technol.* 2022;50:319–321.
5. Sugiura A, Onoguchi M, Shibutani T, Kouno Y. Influence of minimum count in brain perfusion SPECT: phantom and clinical studies. *J Nucl Med Technol.* 2022; 50:342–347.
6. Kong MJ, Yang AF, Vora SA, Ross JS, Yang M. The complementary role of ^{68}Ga-DOTATATE PET/CT in diagnosis of recurrent meningioma. *J Nucl Med Technol.* 2022;50:348–352.
7. Djekidel M. Making the case for brain ^{18}F-FDG PET subtraction in medically refractory epilepsy: a novel, useful tool—practical points? *J Nucl Med Technol.* 2022;50:353–356.
8. Currie J, Currie GM. Emotional intelligence and productive relationships with patients and colleagues. *J Nucl Med Technol.* 2022;50:357–365.
9. Patchoros G, Wenzler G. Building program efficiencies using JRCNMT compliance forms. *J Nucl Med Technol.* 2022;50:366–371.

SNMMI Clinical Trials Network Research Series for Technologists: Clinical Research Primer—Use of Imaging Agents in Therapeutic Drug Development and Approval

Charlotte Denise Jeffers[1], Courtney Lawhn-Heath[2], Regan I. Butterfield[3], John M. Hoffman[3,4], and Peter J.H. Scott[5]

[1]Department of Radiology, University of Alabama at Birmingham, Birmingham, Alabama; [2]Department of Radiology and Biomedical Imaging, University of California San Francisco, San Francisco, California; [3]Center for Quantitative Cancer Imaging, Huntsman Cancer Institute, University of Utah, Salt Lake City, Utah; [4]Department of Radiology and Imaging Sciences, University of Utah School of Medicine, Salt Lake City, Utah; and [5]Department of Radiology, University of Michigan, Ann Arbor, Michigan

The process of bringing a new drug to market is complex and has recently necessitated a new drug-discovery paradigm for the pharmaceutical industry that is both more efficient and more economical. Key to this task has been the increasing use of nuclear medicine and molecular imaging to support drug discovery efforts by answering critical questions on the pathway to development and approval of a new therapeutic drug. Some of these questions include whether the new drug reaches its intended target in the body at sufficient levels to effectively treat or diagnose disease without unacceptable toxicity; how the drug is absorbed, metabolized, and excreted; and what the effective dose is in humans. To conduct the appropriate imaging studies to answer such questions, pharmaceutical companies are increasingly partnering with molecular imaging departments. Nuclear medicine technologists are critical to this process, as they perform scans to collect the qualitative and quantitative imaging data used to measure study endpoints. This article describes preclinical and clinical research trials and provides an overview of the different ways that radiopharmaceuticals are used to answer critical questions during therapeutic drug development.

Key Words: clinical research; nuclear medicine; PET and SPECT; drug development; clinical trials

For pharmaceutical companies, the process of discovering a new diagnostic or therapeutic drug and developing it for market is enormously complex (Fig. 1) and includes preclinical testing, investigational-new-drug (IND) applications, clinical trials, new-drug applications (NDAs), marketing approval from the U.S. Food and Drug Administration (FDA), and postmarketing studies. The goal is to bring safe and effective drugs to market as quickly as possible, but it can take up to 10 y to complete this drug development process, and the lifetime of a U.S. patent (during which pharmaceutical companies need to complete drug discovery, translation, and approval; establish the drug's market share; recoup the research investment; and turn a profit) is only 20 y. Recent studies estimate the average cost of therapeutic drug development at $1.3 billion per drug, but it can be as high as $5.5 billion (*1,2*). This challenge is further exacerbated when promising drug candidates fail to meet prespecified endpoints in later-stage clinical trials after many years of expensive investment. Reimbursement from the Centers for Medicare and Medicaid Services and other insurance carriers also goes through a review process.

These challenges have necessitated a new drug-development paradigm for the pharmaceutical industry that is both more efficient and more economical, and as a result, new technologies are being used to reduce both the costs and the risks associated with drug development. Molecular imaging and nuclear medicine are tools that play a key role in modern drug development because of their ability to address important questions at each step of the drug discovery process (*2,3*). For example, imaging studies costing a few tens to hundreds of thousands of dollars enable companies to reduce risk and more confidently make key go/no-go decisions about advancing drugs to clinical studies costing millions to billions of dollars (depending on size and scope). Such imaging studies require access to different radiopharmaceuticals (e.g., established radiotracers, new radiotracers, and radiolabeled drug candidates) and can be both preclinical and clinical. For example, early drug discovery efforts involve preclinical studies (e.g., in vitro autoradiography, in vivo animal imaging, and ex vivo biodistribution), whereas later drug development trials pivot to clinical studies on human volunteers (phase I, II, and III clinical trials
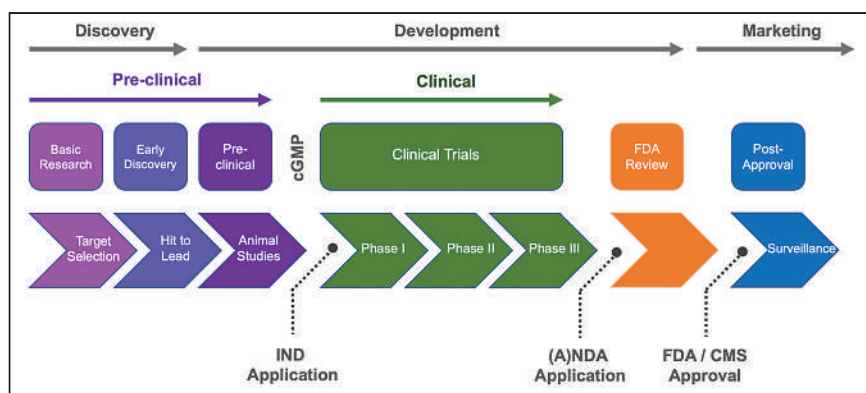
FIGURE 1. Drug development process. A(NDA) = abbreviated NDA; cGMP = current good manufacturing practice; CMS = Centers for Medicare and Medicaid Services.

conducted under approved IND applications). On completion of phase III studies, an NDA can be filed and, once approved, give the sponsor marketing authorization for the drug. Post-marketing phase IV trials may be required by the FDA for long-term surveillance of drug safety and efficacy.

In this primer, we describe regulatory and logistical considerations for nuclear medicine departments to participate in preclinical and clinical research, as well as an overview of the different ways that radiopharmaceuticals can be used to answer critical questions pertaining to therapeutic drug development (2,3). This paper is a companion to other articles in this series published to date (4).

TYPES OF IMAGING STUDIES CONDUCTED DURING DRUG DEVELOPMENT PROCESS

Nuclear medicine imaging (with PET and SPECT) enables industry and academic teams to answer questions central to new-drug development. PET and SPECT are increasingly used to answer questions during both preclinical in vitro (cells) and in vivo (animal models) studies and during clinical trials (human research subjects), including the following: Does a drug reach the tissue of interest in pharmacologically active concentrations? Does the drug go anywhere else in the body that could cause unwanted side effects? Does the molecule engage with the target (e.g., receptor or protein) of interest? What is the quantitative relationship between the extent of the drug's interaction with the target and the dose administered to a patient (e.g., receptor occupancy)? Can the pharmacologic effects of a therapeutic dose be determined using an imaging biomarker (e.g., tumor shrinkage or ^{18}F-FDG metabolism and uptake (3)), and how long do these effects persist? The answers to these questions are critical to translating a drug to initial clinical trials, as well as to advancing the drug through clinical trials (phases I–III), and imaging offers a powerful means for drug discovery teams to address such questions.

The questions concerning the distribution and target engagement of a drug can often be answered by labeling a drug molecule itself. For example, radiolabeling of a drug with a PET radionuclide, such as ^{11}C, can be accomplished

without altering the properties of the drug. Since it is estimated that about 20% of prescribed drugs and about 30% of leading blockbuster drugs contain a fluorine atom (5), in such cases the same can also be accomplished with ^{18}F (6). The labeled drug can then be used in preclinical and clinical biodistribution studies.

PET imaging can also be used to quantify the pharmacologic effects of a therapeutic dose. Such imaging capitalizes on the concept of biologic markers (i.e., biomarkers). A biomarker is an objective measurement that is an indicator of a biologic process in a patient and can serve as an indicator of health. Classic biomarkers are based on laboratory tests (e.g., blood, urine, and tissue biopsy), whereas an imaging biomarker is a measurement of a biologic process, such as quantification of amyloid burden using amyloid PET. Frequently, these types of studies might use companion PET radiotracers rather than a radiolabeled drug. Before commencing such studies, it is necessary to confirm that a radiotracer is appropriate for that purpose. When validating a PET tracer, a test–retest experiment is usually conducted to measure the repeatability of the measurements and determine within-subject variability (7). The test–retest is particularly important if a PET radiotracer is to be used in studies involving multiple measurements on the same subject (e.g., receptor occupancy or before and after a therapeutic intervention).

If an imaging biomarker exists for a given condition, it can be used to diagnose disease and both predict and monitor patient response to experimental new therapeutics in clinical trials. Extending the latter concept further, imaging biomarkers can also be used as a surrogate endpoint in a clinical trial. A surrogate endpoint is defined by the FDA as "a clinical trial endpoint used as a substitute for a direct measure of how a patient feels, functions, or survives" (8). Imaging biomarkers and surrogate endpoints are recognized by the agency and have been widely used in the drug approval and licensure process (8,9). The main difference between an imaging biomarker and a surrogate endpoint is the level of validation. For an imaging biomarker to function as a surrogate endpoint, there must be clinical trials demonstrating the relationship between the imaging biomarker and the true clinical endpoint. Imaging biomarkers have been reviewed (10), and in the case of cancer trials, an imaging biomarker road map has been established (11). Examples of imaging biomarkers used as surrogate endpoints include amyloid imaging (12), assessment of tumor response (13–15), and ^{11}C-raclopride PET for antipsychotic efficacy (16,17).

REGULATORY CONSIDERATIONS

Use of nuclear medicine imaging techniques to support drug development involves both preclinical and clinical

studies. Such work must be conducted in compliance with applicable institutional, state, and federal regulations governing the use of radioactive material, as well as the rules and regulations describing responsible and ethical conduct in animal and human research. These various regulatory requirements are summarized briefly here and are covered in detail in other articles in this series (4).

Radioactive materials need to be handled under the auspices of approved radioactive materials licenses granted by the Nuclear Regulatory Commission or the local state government for agreement states. Such work must also be performed according to the as-low-as-reasonably-achievable principles, which involve making every reasonable effort to ensure that worker exposures to ionizing radiation are as low as practical.

In the United States, PET radiopharmaceuticals are prepared according to the principles of current good manufacturing practices outlined in the *U.S. Pharmacopeia* chapter <1823> (18) or chapter <825> (19) and in part 212 of title 21 of *Code of Federal Regulations* (CFR) (20). Other radiopharmaceuticals (e.g., radiotherapeutics) are often prepared according to requirements outlined in 21 CFR parts 210 (21) and 211 (22). The regulations on current good manufacturing practices cover types of facilities, cleanliness and maintenance of the facilities, laboratory controls, equipment, personnel, training, quality assurance, documentation about materials and processes, drug product controls, packaging and labeling requirements, complaint handling, and record keeping.

Preclinical (animal) studies need to be conducted under the purview of an Institutional Animal Care and Use Committee, and it is typical for pharmaceutical companies to also require collaborating sites to hold Association for Assessment and Accreditation of Laboratory Animal Care International certification. The use of animals to advance medicine and science when there are no nonanimal alternatives remains a critical part of drug development, and preclinical work should be conducted in accord with the highest scientific, humane, and ethical principles as laid out in the *Guide for the Care and Use of Laboratory Animals* (23).

Clinical studies can be conducted only after receiving both FDA approval (e.g., Radioactive Drug Research Committee [RDRC] or IND application) and institutional approval (e.g., Institutional Review Board). Regulations for using radiopharmaceuticals under RDRC approval are described in 21 CFR part 361, whereas the requirements for conducting research under an IND are laid out in 21 CFR part 312. For a detailed description, refer to a companion article in this series (4).

TYPES OF RESEARCH STUDIES

Preclinical Studies

Although nuclear medicine technologists work predominantly in clinical PET imaging, some may find themselves working in academic PET centers or pharmaceutical companies. In the latter instances, they will likely be involved in preclinical studies. Preclinical studies are intended to get earlier answers to many of the same questions that will ultimately be investigated clinically and often to make go/no-go decisions about costly clinical translation. There are 4 main types of preclinical protocols: cell studies, autoradiography experiments with postmortem tissue samples (in vitro or ex vivo), in vivo PET (or SPECT) imaging studies on living animals, and ex vivo biodistribution studies in which animals are euthanized after injection of the tracer, dissected, and their organs counted in a γ-counter to establish the biodistribution and dosimetry of the tracer.

Cell Studies. Cell uptake studies evaluate uptake of a new radiotracer in a cell expressing the drug target of interest. These studies are an economic starting point as they cost considerably less than animal studies. Cell uptake studies offer a preliminary indication of target engagement for a new radiotracer and also help researchers decide promising ones to advance to animal studies.

Binding Affinity Experiments. Binding studies quantify the binding characteristics of a new radiopharmaceutical, such as affinity for its target, which is expressed as the dissociation constant (K_D). Lower K_D values correspond to higher-affinity molecules. Such studies can be conducted using tissue pellets or autoradiography.

Autoradiography Experiments. Autoradiography is a technique in which tissues are incubated with a radiotracer (24) and then exposed to photographic film or phosphor imaging plates to visualize the location of the radiolabeled molecules. In vitro autoradiography studies use postmortem animal or human tissue samples (e.g., a histologic slice of brain or tumor) that have been previously harvested. The radiolabeled molecule is incubated with postmortem tissue samples, giving the molecule time to bind to its target (e.g., receptor or protein). The samples are then washed and exposed to film or plates. In vitro autoradiography does not account for the in vivo environment (e.g., metabolism). If such information is needed, ex vivo autoradiography studies can be undertaken. The radiotracer is first administered intravenously, and after some time point, the animals are euthanized (with or without in vivo PET imaging first) and organs and tissues of interest are harvested for autoradiography. The postmortem tissue samples are washed and exposed to film or plates analogously to in vitro autoradiography.

Autoradiography has been used to quantify and localize drugs in organs, tissues, and cells for decades. The data can be used to determine K_D for a radiotracer, and target engagement of a therapeutic drug can be confirmed by observing a reduction in the signal of the specific radiotracer in the presence of a therapeutic dose (either dosed to the animal [ex vivo autoradiography] or added to the incubation solution [in vitro autoradiography]). Alternatively, the technique can be combined with immunohistochemistry on an adjacent slice of tissue, and colocalization of the autoradiography signal with the fluorescence of target-specific antibodies can be observed. Such datasets are critical in validating a new radiotracer and deciding whether to advance to preclinical and eventual clinical in vivo imaging studies.

In Vivo PET (or SPECT) Imaging Studies. In vivo imaging study logistics closely resemble human studies in that doses, imaging protocols, timing, intravenous catheter placement, interventions, attenuation correction, reconstruction, and radiation safety all have to be accounted for and planned in the same way. An additional consideration with animal work is that, unlike human subjects, animals need to be anesthetized for the duration of the study. Depending on the mechanism of action of a drug, the choice of anesthesia can affect the PET data and may need to be accounted for in study design (25). For preclinical PET imaging, small mice typically receive no more than 9.25 MBq of radiotracer, whereas larger animals receive higher doses depending on weight (e.g., rodents receive ≤37 MBq and primates receive ≤185 MBq). PET scans can be dynamic, and typical scan lengths are 60 min for a ^{11}C-labeled tracer or up to 120 min for an ^{18}F-labeled tracer. Static scans, which could be 5–20 min, can also be acquired at one or more time points after administration of the radiotracer. Baseline scans will give pharmacokinetic and distribution information on a given tracer or labeled drug candidate, whereas intervention studies (e.g., with a dose of therapeutic) can be used to answer questions about specific binding, target engagement, and receptor occupancy at a given dose, among others. In some studies, the animal may be euthanized immediately after the imaging study and organs harvested for further evaluation using autoradiography. Figure 2 shows a baseline nonhuman-primate PET scan obtained with ^{18}F-AH114726, a new radiotracer targeting the γ-aminobutyric acid type A receptor (26). The scan reveals high uptake in the cortical region, which is known to have high expression of γ-aminobutyric acid type A receptors. To confirm selectivity of the new compound for the target, the scan was repeated in the presence of a 1 mg/kg dose of flumazenil, a known selective γ-aminobutyric acid type A receptor antagonist. The repeated scan confirmed target engagement and selectivity of AH114726,

as complete displacement of the radiotracer was apparent on dosing with flumazenil.

Biodistribution Studies. Ex vivo biodistribution studies are operationally more complex than in vivo imaging, as they involve euthanizing animals at a predetermined time point after dosing the radiotracer, dissecting them, and counting the individual organs in a γ-counter. Such studies provide comprehensive biodistribution data (percentage injected dose per gram of tissue) that can be input into software programs such as OLINDA (27) to generate the human dosimetry estimates that need to be included in any IND filings supporting translation of PET radiotracers into clinical studies.

Clinical Studies

Clinical studies, using PET, most frequently apply established radiotracers that are either FDA-approved or investigational. Investigational radiotracers can be used under the approval of an institutional RDRC committee or an FDA-approved IND, depending on the intended application (4,28). Approved radiotracers are used under the auspices of either an NDA or, in the case of generic drugs, an abbreviated NDA. The different phases of clinical trials are summarized in Table 1 and described in detail in a previous article in this series (4).

HOW RADIOPHARMACEUTICALS CAN BE DEPLOYED IN RESEARCH

Several types of radiopharmaceuticals are used in imaging collaborations with pharmaceutical companies (Table 2). They include use of FDA-approved products as tracers or biomarkers to study aspects of disease, investigational agents to interrogate biologic systems and functions, investigational imaging or therapeutic radiopharmaceuticals being developed for FDA approval, and radiolabeled drug compounds to study biodistribution and receptor occupancy. The selection of an appropriate imaging agent depends on the study in question and on local availability. For example, different imaging agents might be used at various sites in the same clinical trial, depending on availability from nearby commercial nuclear pharmacies.

FDA-Approved Imaging Radiopharmaceuticals for Diagnosis, Staging, and Monitoring of Therapy

Approved radiopharmaceuticals can be used for diagnosis of disease, staging, and monitoring of response to therapy (experimental or approved). Importantly, if patients respond to therapy they continue receiving the same treatment, whereas if they do not respond they can be switched to alternate therapies rapidly, saving both time and money and
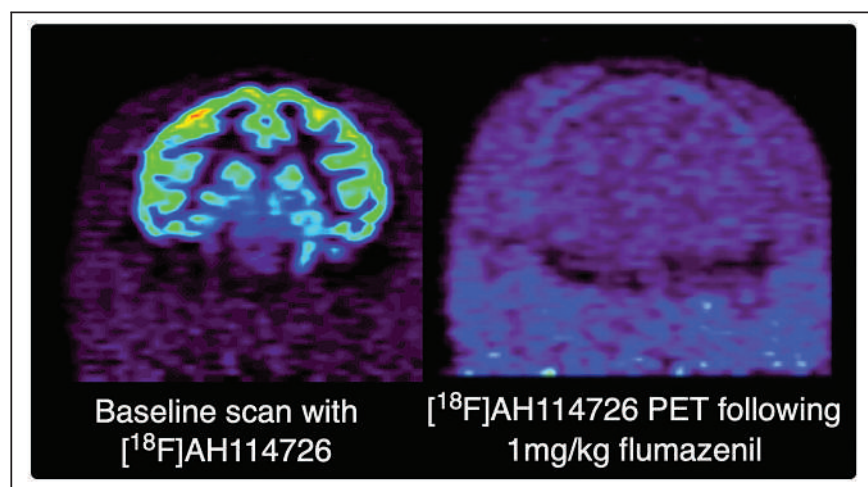
FIGURE 2. Representative coronal small-animal PET images of control animal imaged with ^{18}F-AH114726 at baseline and after displacement with 1 mg/kg dose of flumazenil. (Reprinted with permission of (26).)

TABLE 1
Overview of Clinical Trial Process

Phase	No. of subjects	Scope
0/I	Few dozen (therapeutic); 10–30 (diagnostic)	New drug is first given to small number of people; studies might be exploratory, involving several candidate molecules to select lead for development (46), and are intended to demonstrate safety of new agent and dose-limiting toxicity
II	Few hundred (therapeutic); 20–40 (diagnostic)	Study is undertaken to demonstrate proof of efficacy and to reveal less common side effects; if enough patients benefit from new drug, and side effects are acceptable, then phase III trials can be initiated; additional safety data are obtained
III	Several hundred (therapeutic); 50–100 (diagnostic)	Trials are intended to compare safety and efficacy of new diagnostic or therapeutic agent against standard of care and typically are large and multicenter; research subjects are picked at random to receive standard of care or new treatment; when neither doctor nor subject knows which treatment subject is getting, trial is considered double-masked; additional safety data are obtained, and if new drug is found to be as effective as or more effective than existing drugs, or is safer, NDA can be submitted to FDA
IV	Thousands	Postapproval studies are intended to monitor FDA-approved drugs over long period (e.g., several years)

reducing the duration of unnecessary side effects. Pioneering work was conducted by the team of Van den Abbeele at the Dana-Farber Cancer Institute to diagnose and treat gastrointestinal stromal tumors (GISTs) (28). ^{18}F-FDG PET can be used to diagnose, localize, and stage GISTs and to monitor response to imatinib (Gleevec; Novartis) therapy (Fig. 3). The functional information on tumor metabolism of glucose from serial ^{18}F-FDG scans can be used to detect both short-term

TABLE 2
Radiopharmaceuticals Used in Clinical Trials

Type	Examples
FDA-approved imaging radiopharmaceuticals*	^{18}F-FDG
	^{18}F-florbetapir (Amyvid)
	^{18}F-florbetaben (Neuraceq)
	^{18}F-flutemetamol (Vizamyl)
	^{18}F-flortaucipir (Tauvid)
	^{68}Ga-DOTATATE (NETSPOT; Advanced Accelerator Applications)
	^{64}Cu-DOTATATE (Detectnet; Curium US LLC)
	^{68}Ga-PSMA-11 (University of California San Francisco and UCLA)
	^{18}F-DCFPyL (Pylarify; Progenics Pharmaceuticals, Inc.)
	^{123}I-ioflupane (DaTscan; GE Healthcare)
	^{18}F-fluciclovine (Axumin; Blue Earth Diagnostics)
	[8]F-fluroestradiol (Cerianna; Zionexa US Corp.)
	^{99m}Tc-sestamibi
	^{18}F-fluorodopa (Feinstein Institutes for Medical Research)
	^{68}Ga-PSMA-gozetotide (Locametz; Novartis)
FDA-approved therapeutic radiopharmaceuticals	^{177}Lu-DOTATATE (Lutathera; Advanced Accelerator Applications)
	^{177}Lu-PSMA-617 (Pluvicto; Novartis)
Investigational agents for research under RDRC or IND	^{11}C-Pittsburgh compound B
	^{18}F-fluorothymidine
	^{18}F-FEOBV
Investigational imaging and therapeutic agents for commercialization	^{18}F-flupiridaz (imaging)
	[225]Ac-PSMA-617 (therapy)
Investigational radiotracers to support therapeutic trials (e.g., receptor occupancy)	^{18}F-SPARQ
Radiolabeled drugs or drug candidates	^{11}C-ibrutinib
	^{11}C-docetaxel
	^{18}F-lansoprazole

*For diagnosis, staging, and monitoring of therapy or as biomarker or surrogate endpoint.
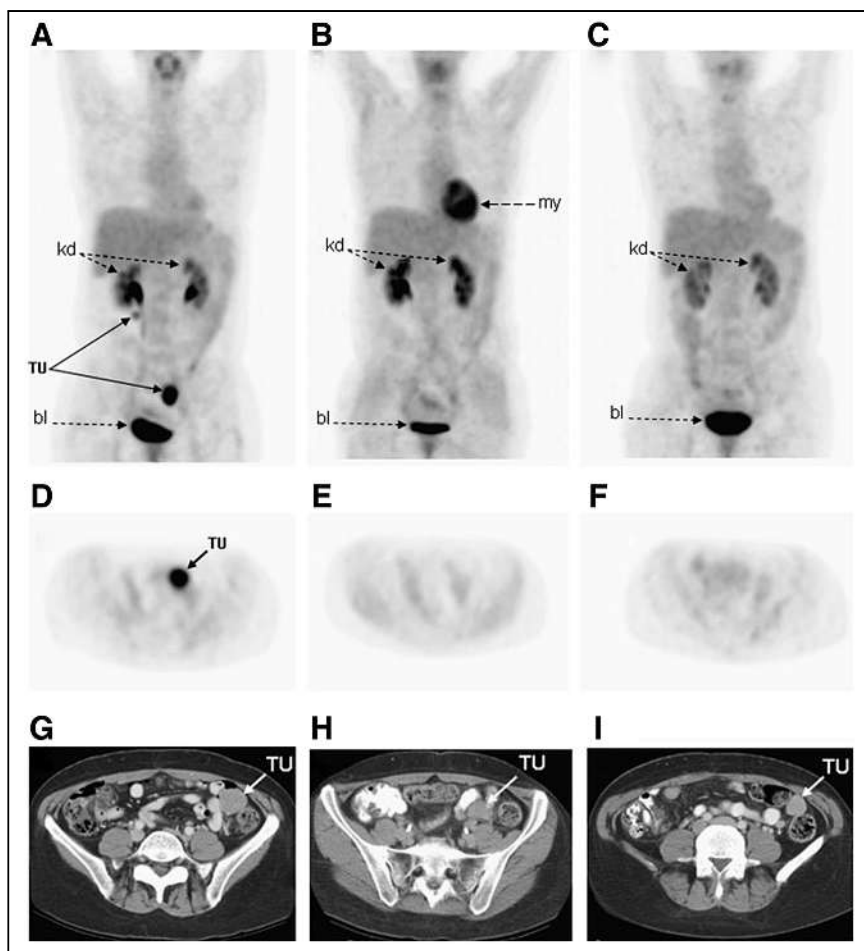
FIGURE 3. ^{18}F-FDG PET maximum-intensity projections (A–C), axial PET images (D–F), and axial CT images (G–I) through pelvis in patient with metastatic GIST. Normal physiologic ^{18}F-FDG uptake is seen in urinary collecting system in both kidneys (kd), in myocardium (my), and in bladder (bl). (A) Intense ^{18}F-FDG uptake is seen in left lower pelvis and contiguous to right proximal ureter (TU) at baseline before imatinib therapy, consistent with metastatic GIST. (B) Resolution of abnormal ^{18}F-FDG uptake is noted in both tumor masses as early as 1 wk after treatment. (C) Continuous metabolic response to imatinib is seen in this patient 2 mo after initiation of therapy despite presence of residual mass on CT. (Reprinted with permission of (29).)

and long-term tumor responses that may not be obvious with CT. The team noted that ^{18}F-FDG PET responses were apparent even 24 h after the first dose of imatinib. Significant changes in ^{18}F-FDG uptake (>25% decrease in SUV_{max} relative to baseline) were apparent within 1 mo of starting imatinib therapy in all GIST patients who responded. Any lack of response was quickly apparent on the PET scans, such that treatment could be changed to sunitinib (Sutent; Pfizer), which is a second drug approved for treatment of GIST and to which non–imatinib-responding patients may be more sensitive.

Use of FDA-Approved Imaging Agents as Biomarkers or Surrogate Endpoints in Clinical Trials

A recent example of using PET radiotracers to support therapeutic trials applied amyloid imaging (^{18}F-florbetapir [Amyvid; Eli Lilly], ^{18}F-flutemetamol [Vizamyl; GE Healthcare], and ^{18}F-florbetaben [Neuraceq; Life Molecular Imaging]) and tau PET (^{18}F-flortaucipir [Tauvid; Eli Lilly] and MK6240) to support development of Alzheimer disease therapeutics such as aducanumab. Such therapeutic agents are recombinant human monoclonal antibodies that bind aggregated types of β-amyloid that form the hallmark amyloid plaques in Alzheimer disease. PET imaging played a crucial role in confirming the initial eligibility of a given patient to participate in a clinical trial and in monitoring the subsequent response to therapy. In clinical trials of aducanumab, amyloid PET revealed decreases in β-amyloid neuritic plaque accumulation on treatment (Fig. 4) (29).

Investigational Agents for Research Use Under RDRC or IND

Imaging agents can be used for research applications under the approval of an institutional RDRC (30) or under an approved IND (31). To use a radiotracer according to the RDRC mechanism, the following provisions must be met: the research must be considered basic science research and be done for the purpose of advancing scientific knowledge; the research study must be authorized by an FDA-approved RDRC; the pharmacologic dose of the radioactive drug must be known not to cause any clinically detectable pharmacologic effect on humans; and the radiation dose to be administered must be justified by the quality of the study and the information it seeks to obtain. If these provisions cannot be met, an approved IND application is required for the agent before any human research can be conducted (32,33). Academic medical centers frequently have many established radiotracers available for use in RDRC protocols and likely also hold IND approvals for several additional radiotracers. Additional research protocols can be added to INDs by submission of amendments to the FDA. After a radiotracer has been used in humans under an IND, it can be advanced to additional clinical trials with a goal of commercialization. Alternatively, if the pharmacologic dose did not cause any clinically detectable pharmacologic effects, it can subsequently be transitioned to RDRC studies for additional research, assuming the other criteria are met.

The transition from RDRC to IND can be illustrated by ^{18}F-(−)5-fluoroethoxybenzovesamicol (^{18}F-FEOBV), a PET radiotracer that was developed at the University of Michigan and is
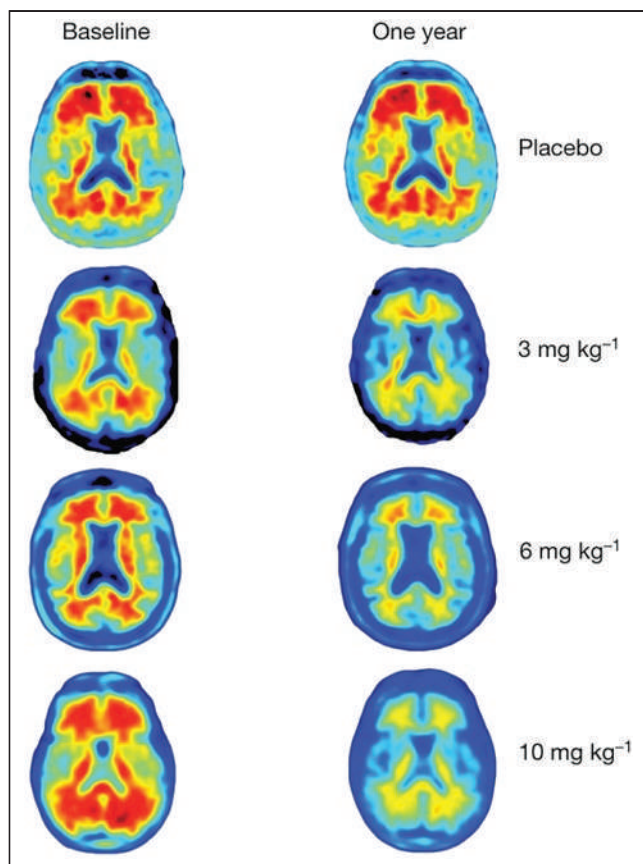
FIGURE 4. ^{18}F-florbetapir (Amyvid) amyloid PET images at baseline and 1 y after aducanumab treatment, showing amyloid plaque reduction after different doses of aducanumab but not placebo. (Reprinted with permission of (30).)

based on a vesamicol analog used to image the vesicular acetylcholine transporter (34). After preclinical development along the lines described in this article, the team wrote an IND and received approval from the FDA to proceed with first-in-humans studies. Whole-body ^{18}F-FEOBV scans were initially conducted on 3 healthy volunteers. Seven additional subjects underwent dynamic brain imaging (Fig. 5), and kinetic modeling revealed agreement between reference tissue modeling and late single-scan imaging. This study allowed quantification of human dosimetry, indicating that more than 400 MBq could be administered without exceeding radiation dose limits. No pharmacologic or physiologic changes were observed after intravenous administration of no more than 1.3 μg of ^{18}F-FEOBV. This information subsequently enabled use of ^{18}F-FEOBV under RDRC approval (and related mechanisms in other countries) by other research teams in the United States and elsewhere (35–37). For example, Kanel et al. recently used ^{18}F-FEOBV to investigate age-related declines in regional cholinergic neuron terminal density (Fig. 5) (38).

Investigational Imaging and Therapeutic Agents Being Developed for Commercialization

Development of new radiopharmaceuticals for commercialization follows the process illustrated in Figure 1. Since companies do not have access to research subjects, clinical trials are usually conducted in collaboration with academic medical centers. After preclinical work, an IND is obtained to enable clinical trials with new agents to prove safety and efficacy. High-profile examples are the theranostic agents targeting prostate-specific membrane antigen (PSMA) for
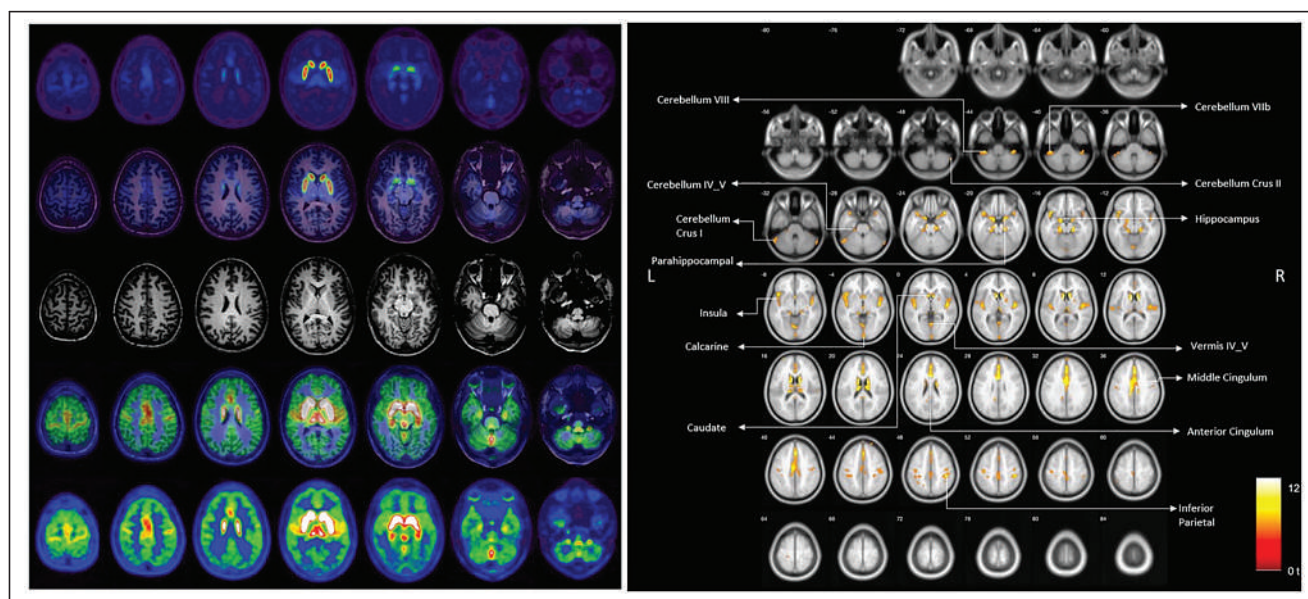
FIGURE 5. (Left) ^{18}F-FEOBV PET, MR, and overlay images from healthy control subject. (Reprinted from (35).) (Right) Age-related reduced Vesicular acetylcholine transporter binding reductions (Reprinted from (39).)
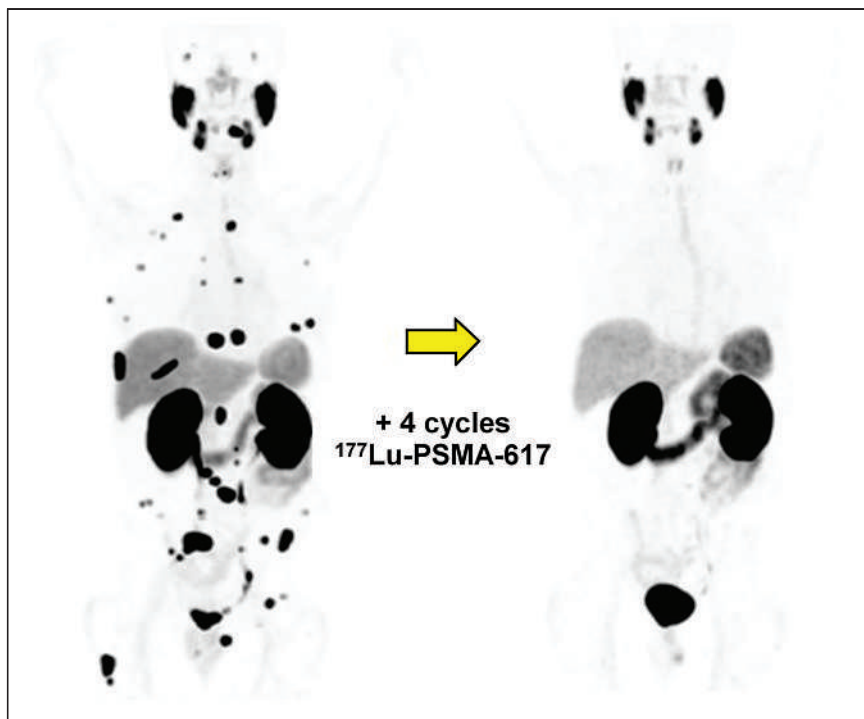
FIGURE 6. ^{68}Ga-PSMA-11 PET before and after treatment with ^{177}Lu-PSMA-617. (Reprinted from (*42*).)

imaging and treatment of prostate cancer. In the case of ^{68}Ga-PSMA-11, after pioneering work from Heidelberg, an NDA for ^{68}Ga-PSMA-11 was obtained by UCLA and the University of California San Francisco through an academic partnership (*39*). They conducted a phase III trial, and separate NDAs for each institution were approved by the FDA. Subsequent approvals for kits to produce ^{68}Ga-PSMA-11 have been obtained by Telix and Novartis, and the agent has been used to image thousands of patients (*40*).

Concurrently with these efforts, ^{177}Lu-PSMA-617 was developed for radiotherapy of prostate cancer. PSMA PET is used to confirm patient eligibility and to monitor response to

therapy. Phase 2 studies showed promising results (Fig. 6) (*41*), and the rights for development were acquired by Endocyte (later purchased by Novartis). In the large, international, multicenter phase 3 VISION trial, 831 patients underwent randomization. VISION provided evidence for significantly improved progression-free and overall survival in late-stage prostate cancer patients who were treated with ^{177}Lu-PSMA-617 (compared with the standard of care) (*42,43*). FDA approval for ^{177}Lu-PSMA-617 was granted earlier this year.

New Radiotracers Developed to Support Therapeutic Trials

If radiotracers do not exist for a given therapeutic target, it is necessary to develop the appropriate companion diagnostic when PET studies are needed. One seminal report on the use of PET imaging to guide therapeutic development was Merck's work with Emend (aprepitant), a neurokinin 1 receptor antagonist being developed both for treatment of chemotherapy-induced nausea and as an antidepressant (*44*). Instead of labeling the drug itself, Merck developed a companion tracer, ^{18}F-SPARQ (Substance P Antagonist Receptor Quantifier), and used it to determine the receptor occupancy achieved by different doses of Emend in healthy humans. Importantly, greater than 95% receptor occupancy was found at the proposed dose (Fig. 7), indicating the correct dose selection. Merck knew that this dose was effective for managing nausea caused by chemotherapy, moved forward with the antinausea indication, and gained marketing approval from the FDA. In contrast, Merck also knew that the study dose of Emend had no antidepressant effects, and the PET study revealed that a larger dose would not increase receptor occupancy. As such, the results of this study (likely costing tens of thousands of dollars) allowed Merck to cancel development of Emend for depression and save millions of dollars on what would have been a futile phase III trial (*44*).

Radiolabeled Drugs or Drug Candidates

Important questions concerning a drug can be answered by labeling the drug molecule itself. Clinical imaging studies using labeled drugs allow drug developers to obtain information about biodistribution and target engagement.
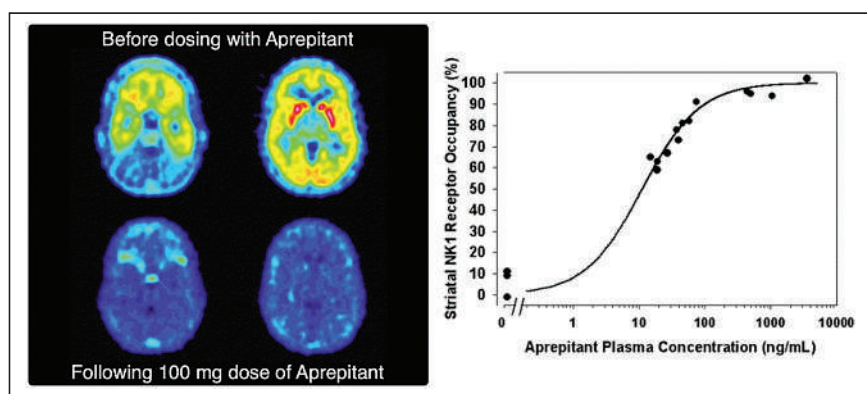
FIGURE 7. (Left) ^{18}F-SPARQ PET images of subject who received 100 mg of aprepitant: predosing (top row) and postdosing (bottom row) are shown, with estimated receptor occupancy of 94%. (Right) Relationship between plasma concentration of aprepitant and receptor occupancy. NK1 = neurokinin-1. (Reprinted with permission of (*45*).)

This information can be used to confirm patient eligibility for a given treatment, as well as to predict response. This approach holds particular promise for anticancer drugs. In a given malignancy, certain chemotherapeutics will be used on the basis of demonstrated clinical efficacy (e.g., tumor response or improved survival). A one-size-fits-all approach has been used in which patients are started on a standard regimen for their cancer. However, failure of a given chemotherapeutic occurs in certain patients because many cancers do not respond consistently. Therefore, nonresponders are often subjected to the psychologic burden of chemotherapy along with frequent associated toxicities without gaining any benefit. In this age of personalized medicine, a new era of chemotherapy that abandons this one-size-fits-all approach is needed. Molecular imaging has an important role to play in this paradigm shift.

Proof of concept for docetaxel has been demonstrated by van der Veldt et al. at VU University Medical Center in Amsterdam. This cytotoxic drug is a taxane that was initially approved for treatment of anthracycline-refractory metastatic breast cancer and has subsequently been approved for treatment of several other cancers (e.g., metastatic prostate cancer, head and neck cancer, and non–small cell lung cancer). However, cancers often do not respond consistently to chemotherapeutics. Docetaxel failure in some patients means that they experience associated toxicities without any benefit. To explore a more personalized approach to deciding which patients would benefit from docetaxel therapy, the team prepared ^{11}C-docetaxel (45). Using PET imaging in conjunction with microdoses of ^{11}C-docetaxel (to eliminate toxicity concerns), the team was able to quantify tumor uptake of the labeled drug across patients. This work showed that ^{11}C-docetaxel PET can be used to predict tumor uptake of the drug during subsequent docetaxel therapy, and the team also demonstrated that high tumor uptake of ^{11}C-docetaxel was related to improved tumor response after treatment.

Going forward, PET with radiolabeled drugs will enable straightforward confirmation of target engagement in humans and, in turn, predict treatment outcome in advance. The work with ^{11}C-docetaxel also suggests that radiolabeled drugs can help to reveal underlying mechanisms of treatment failure in subpopulations of patients (e.g., poor accumulation in a tumor or poor target engagement).

CONCLUSION

The power of nuclear medicine and molecular imaging to provide key information about new therapeutic candidates has become an integral part of the modern drug development paradigm. Preclinical studies can allow early go/no-go decisions about whether to advance a new drug to clinical trials. After clinical translation, imaging can be used to enrich clinical trials, predict response to therapy, monitor response, and obtain valuable information about target engagement and dosing. In this way, it is expected that nuclear medicine and molecular imaging using radiotracers or radiolabeled drugs will continue to provide insights during drug development. When combined with other emerging technologies, this approach will usher in a new era of personalized medicine in which rational treatment choices tailored to individual patients to improve outcomes will replace a one-size-fits-all approach to disease management.

REFERENCES

1. Herper M. The cost of creating a new drug now $5 billion, pushing big pharma to change. Forbes website. https://www.forbes.com/sites/matthewherper/2013/08/11/how-the-staggering-cost-of-inventing-new-drugs-is-shaping-the-future-of-medicine/?sh=1ec8793613c3. Published August 11, 2013. Accessed September 20, 2022.
2. Donnelly DJ. PET imaging in drug discovery and development. In: Kilbourn MR, Scott PJH, eds. *Handbook of Radiopharmaceuticals: Methodology and Applications*. 2nd ed. John Wiley and Sons Ltd.; 2021:703–725.
3. Kelloff GJ, Hoffman JM, Johnson B, et al. Progress and promise of FDG-PET imaging for cancer patient management and oncologic drug development. *Clin Cancer Res*. 2005;11:2785–2808.
4. Jeffers CD, Frye SA, Hoffman JM. SNMMI Clinical trials network research series for technologists: clinical research primer—regulatory process, part I: how and when radiopharmaceuticals can be used. *J Nucl Med Technol*. 2022;50:2–9.
5. O'Hagan D. Fluorine in health care: organofluorine containing blockbuster drugs. *J Fluor Chem*. 2010;131:1071–1081.
6. Gillis EP, Eastman KJ, Hill MD, et al. Applications of fluorine in medicinal chemistry. *J Med Chem*. 2015;58:8315–8359.
7. Baumgartner R, Joshi A, Feng D, et al. Statistical evaluation of test-retest studies in PET brain imaging. *EJNMMI Res*. 2018;8:13.
8. Table of surrogate endpoints that were the basis of drug approval or licensure. FDA website. https://www.fda.gov/drugs/development-resources/table-surrogate-endpoints-were-basis-drug-approval-or-licensure. Updated February 28, 2022. Accessed September 20, 2022.
9. Lal R. FDA facilitates the use of surrogate endpoints in drug development. FDA website. https://www.fda.gov/drugs/fda-facilitates-use-surrogate-endpoints-drug-development-november-5-2018-issue. Updated November 5, 2018. Accessed September 20, 2022.
10. Richter WS. Imaging biomarkers as surrogate endpoints for drug development. *Eur J Nucl Med Mol Imaging*. 2006;33:6–10.
11. O'Connor JP, Aboagye E, Adams J, et al. Imaging biomarker roadmap for cancer studies. *Nat Rev Clin Oncol*. 2017;14:169–186.
12. Scheinin NM, Scheinin M, Rinne JO. Amyloid imaging as a surrogate marker in clinical trials in Alzheimer's disease. *Q J Nucl Med Mol Imaging*. 2011;55:265–279.
13. Harry VN, Semple SI, Parkin DE, Gilbert FJ. Use of new imaging techniques to predict tumour response to therapy. *Lancet Oncol*. 2010;11:92–102.
14. Ko CC, Yeh LR, Kuo YT, et al. Imaging biomarkers for evaluating tumor response: RECIST and beyond. *Biomark Res*. 2021;9:52.
15. Mankoff DA, Pryma DA, Clark AS. Molecular imaging biomarkers for oncology clinical trials. *J Nucl Med*. 2014;55:525–528.
16. Nord M, Farde L. Antipsychotic occupancy of dopamine receptors in schizophrenia. *CNS Neurosci Ther*. 2011;17:97–103.
17. Roberts C, Waterton J, Maynard J, Hockings P. How imaging biomarkers are transforming drug development. Drug Target Review website. https://www.drugtargetreview.com/article/32843/how-imaging-biomarkers-are-transforming-drug-development/. Published 2017. Accessed September 20, 2022.
18. United States Pharmacopeia (USP). *General chapter <1823>: positron emission tomography drugs–information*. USP-NF. Rockville, MD: United States Pharmacopeia;

2022. USP website. https://www.uspnf.com/sites/default/files/usp_pdf/EN/USPNF/key-issues/general-chapter-1823-proposed-revision.pdf. Accessed November 1, 2022.

19. United States Pharmacopeia (USP). *General chapter <825>: radiopharmaceuticals – preparation, compounding, dispensing, and repackaging*. USP-NF. Rockville, MD: United States Pharmacopeia. USP website. https://www.usp.org/sites/default/files/usp/document/our-work/chemical-medicines/proposed-gc-825.pdf. Accessed November 2, 2022.

20. Current good manufacturing practice for positron emission tomography drugs. FDA website. https://www.accessdata.fda.gov/scripts/cdrh/cfdocs/cfcfr/CFRSearch.cfm?CFRPart=212. Updated March 29, 2022. Accessed September 20, 2022.

21. Current good manufacturing practice in manufacturing, processing, packing, or holding of drugs; general. FDA website. https://www.accessdata.fda.gov/scripts/cdrh/cfdocs/cfcfr/CFRSearch.cfm?CFRPart=210. Updated March 29, 2022. Accessed September 20, 2022.

22. Current good manufacturing practice for finished pharmaceuticals. FDA website. https://www.accessdata.fda.gov/scripts/cdrh/cfdocs/cfcfr/CFRSearch.cfm?CFRPart=211. Updated March 29, 2022. Accessed September 20, 2022.

23. *Guide for the Care and Use of Laboratory Animals*. 8th ed. National Academy Press; 2011.

24. Solon EG. Autoradiography techniques and quantification of drug distribution. *Cell Tissue Res*. 2015;360:87–107.

25. Alstrup AK, Smith DF. Anaesthesia for positron emission tomography scanning of animal brains. *Lab Anim*. 2013;47:12–18.

26. Rodnick ME, Hockley BG, Sherman P, et al. Novel fluorine-18 PET radiotracers based on flumazenil for GABA$_A$ imaging in the brain. *Nucl Med Biol*. 2013;40:901–905.

27. Stabin MG, Sparks RB, Crowe E. OLINDA/EXM: the second-generation personal computer software for internal dose assessment in nuclear medicine. *J Nucl Med*. 2005;46:1023–1027.

28. Ertuk M, Van den Abbeele AD. Infrequent tumors of the gastrointestinal tract including gastrointestinal stromal tumor (GIST). *PET Clin*. 2008;3:207–215.

29. Sevigny J, Chiao P, Bussière T, et al. The antibody aducanumab reduces Aβ plaques in Alzheimer's disease. *Nature*. 2016;537:50–56.

30. Radioactive drug research committee (RDRC) program. FDA website. https://www.fda.gov/drugs/science-and-research-drugs/radioactive-drug-research-committee-rdrc-program. Updated June 9, 2021. Accessed September 20, 2022.

31. Investigational new drug (IND) application. FDA website. https://www.fda.gov/drugs/types-applications/investigational-new-drug-ind-application. Updated July 20, 2022. Accessed September 20, 2022.

32. Jackson IM, Lee SJ, Sowa AR, et al. Use of 55 PET radiotracers under approval of a radioactive drug research committee (RDRC). *EJNMMI Radiopharm Chem*. 2020;5:24.

33. Mosessian S, Duarte-Vogel SM, Stout DB, et al. INDs for PET molecular imaging probes: approach by an academic institution. *Mol Imaging Biol*. 2014;16:441–448.

34. Petrou M, Frey KA, Kilbourn MR, et al. In vivo imaging of human cholinergic nerve terminals with (−)-5-^{18}F-fluoroethoxybenzovesamicol: biodistribution, dosimetry, and tracer kinetic analyses. *J Nucl Med*. 2014;55:396–404.

35. Saint-Georges Z, Zayed VK, Dinelle K, et al. First-in-human imaging and kinetic analysis of vesicular acetylcholine transporter density in the heart using [18F]FEOBV PET. *J Nucl Cardiol*. 2021;28:50–54.

36. Xia Y, Eeles E, Fripp J, et al. Reduced cortical cholinergic innervation measured using [18F]-FEOBV PET imaging correlates with cognitive decline in mild cognitive impairment. *Neuroimage Clin*. 2022;34:102992.

37. Aghourian M, Legault-Denis C, Soucy JP, et al. Quantification of brain cholinergic denervation in Alzheimer's disease using PET imaging with [18F]-FEOBV. *Mol Psychiatry*. 2017;22:1531–1538.

38. Kanel P, van der Zee S, Sanchez-Catasus CA. Cerebral topography of vesicular cholinergic transporter changes in neurologically intact adults: a [18F]FEOBV PET study. *Aging Brain*. 2022;2:100039.

39. Carlucci G, Ippisch R, Slavik R. ^{68}Ga-PSMA-11 NDA approval: a novel and successful academic partnership. *J Nucl Med*. 2021;62:149–155.

40. Abghari-Gerst M, Armstrong WR, Nguyen K, et al. A comprehensive assessment of ^{68}Ga-PSMA-11 PET in biochemically recurrent prostate cancer: results from a prospective multicenter study on 2,005 patients. *J Nucl Med*. 2022;63:567–572.

41. Calais J, Gafita A, Eiber M, et al. Prospective phase 2 trial of PSMA-targeted molecular RadiothErapy with ^{177}Lu-PSMA-617 for metastatic castration-reSISTant Prostate Cancer (RESIST-PC): efficacy results of the UCLA cohort. *J Nucl Med*. 2021;62:1440–1446.

42. Sartor O, de Bono J, Chi KN, et al. Lutetium-177-PSMA-617 for metastatic castration-resistant prostate cancer. *N Engl J Med*. 2021;385:1091–1103.

43. Czernin J, Calais J. ^{177}Lu-PSMA617 and the VISION trial: one of the greatest success stories in the history of nuclear medicine. *J Nucl Med*. 2021;62:1025–1026.

44. Bergström M, Hargreaves RJ, Burns HD, et al. Human positron emission tomography studies of brain neurokinin 1 receptor occupancy by aprepitant. *Biol Psychiatry*. 2004;55:1007–1012.

45. van der Veldt AA, Smit EF, Lammertsma AA. Positron emission tomography as a method for measuring drug delivery to tumors in vivo: the example of [11C]docetaxel. *Front Oncol*. 2013;3:208.

46. Carpenter AP Jr, Pontecorvo MJ, Hefti FF, Skovronsky DM. The use of the exploratory IND in the evaluation and development of ^{18}F-PET radiopharmaceuticals for amyloid imaging in the brain: a review of one company's experience. *Q J Nucl Med Mol Imaging*. 2009;53:387–393.

Root Cause Analysis in Nuclear Medicine for Sentinel Events

Jitesh Dhingra[1], Mary Beth Farrell[2], and Raghuveer Halkar[1]

[1]Allegheny General Hospital, Pittsburgh, Pennsylvania; and [2]Intersocietal Accreditation Commission, Ellicott City, Maryland

A sentinel event is any unexpected event that results in death or serious physical or psychologic injury to a patient unrelated to a patient's illness. Establishing and determining cause-and-effect relationships are key to preventing future sentinel or near-miss events. However, it can be challenging to establish a cause-and-effect relationship when a process involves multiple steps or people. Root cause analysis (RCA) is a technique that can pinpoint the causes of sentinel events for medical procedures involving numerous steps and people. This article provides a rationale for RCA and the basic steps in a nonmedical RCA investigation. The article then describes a more detailed, 9-step, RCA approach for investigating sentinel events and illustrates the technique with a nuclear medicine example.

Key Words: root cause analysis; sentinel event; quality

J Nucl Med Technol 2022; 50:301–308
DOI: 10.2967/jnmt.122.264851

A sentinel event is any unexpected event that results in death or serious physical or psychologic injury to a patient unrelated to a patient's illness (*1*). In contrast, near-miss events are errors occurring during medical care that are detected and corrected before a patient is harmed. Health-care providers must be aware of and scrutinize both event types critically to improve the safety and quality of care.

When investigating sentinel events and near misses, one must first identify the cause—or why something happened—and the effect of what happened. Establishing and determining cause-and-effect relationships are key to preventing future sentinel or near-miss events.

Determining the cause and the effect is usually straightforward for simple processes involving only one step or person. However, it is difficult to establish a cause-and-effect relationship when a process involves multiple steps or people. Root cause analysis (RCA) is a technique that can pinpoint

the causes of sentinel or near-miss events for processes involving multiple steps and people.

FACTORS GIVING RISE TO THE NEED FOR RCA IN HEALTH CARE

The United States' current, multifaceted health-care system has led to increased attention on sentinel and near-miss events and the need for providers to be familiar with how to perform a systematic RCA. When the causes of events are identified, problems can be addressed and health-care quality improved.

Need for Efficiency

First, the demand for scarce health-care financial resources in the United States is at critical levels (*2*). One reason is that life expectancy has increased from 70.1 y in 1960 to 76 in 2021 (*3,4*). Meanwhile, the percentage of gross domestic product spent on health care has increased from $247 billion (9.4% of the U.S. gross domestic product) in 1980 to around $4 trillion (18% of the U.S. gross domestic product) in 2020 (*5*). Thus, health-care spending has increased considerably, with only a modest increase in life expectancy. This finding points to the need for increased efficiency.

Medical Error Prevention

One strategy to increase efficiency is to decrease cost and waste. Medical errors are one of the leading causes of not only waste and increased cost but also morbidity and mortality. Original estimates in 2000 published in the Institute of Medicine's landmark report, *To Err Is Human: Building a Safer Health System,* pegged annual deaths related to medical errors at 98,000 (*6*). Today that number is estimated to be over 200,000 (*7*). In response to the unacceptable number of medical errors, the Joint Commission adopted the time-out, or call-to-order, concept in 2003 to curb the rising number of medical errors.

A time-out is an immediate pause by every surgical team member before any medical intervention or procedure to verify the correctness of the patient, procedure, and site (*8*). The initial time-out process evolved and expanded to become a review of detailed checklists—a concept borrowed from the airline industry, the industry with the best safety

record. The checklist model was further popularized in health care by Atul Gawande (*9*).

Time-outs and checklists have become standard practice. However, the number of sentinel events did not significantly change between 2005 and 2016 (*1,10*). In 2021, the Joint Commission registered 1,197 sentinel events (*11*). Although time-outs and checklists play a significant role in preventing medical errors, their weakness is that they cannot address a sentinel event or medical error after it happens.

Teamwork Care Delivery Model

Another factor supporting the need for RCA is the substantial change in how health care is delivered. In the past, solo or small groups were the typical practice model. However, solo practices decreased from 41% to 17% between 1983 and 2014 (*12*). Large medical groups and hospital conglomerations are now the norm. As a result, health care has become more team-based.

To become more efficient, health care unwittingly adopted the team-based assembly line approach of the auto industry popularized by Henry Ford in the early 1900s (*13*). The assembly line approach subdivides processes into multiple sequential tasks involving numerous people. Many steps are simple. However, a few steps are always more complex.

For example, in the nuclear medicine scenario, tasks are divided into scheduling, patient preparation, scan performance, interpretation, transcription, and coding and billing. With various personnel completing each task, the physician's time is spent interpreting images and making diagnoses (more complex tasks), whereas the other steps are distributed among schedulers, nurse navigators, technologists, transcriptionists, or coders (less complex tasks).

Another feature of the assembly line approach is that it matches task complexity to the skills and pay of the staff on the team (*13*). The more complex the task, the higher the wage. With only a fraction of the tasks paid at the higher rate and most tasks paid at the lower rate, overall payroll costs are reduced. However, the distribution of work into multiple steps performed by various people increases the risk of errors.

ORIGIN OF RCA AND THE 5 WHYS

Sakichi Toyoda, a Japanese inventor and industrialist, recognized the trade-off between the distribution of labor in the assembly line approach and mistakes. He developed the "5-whys analysis" to determine and eliminate the root causes of problems in the Toyota Motors manufacturing process (*14*).

The 5 whys is a simple problem-solving method for quickly getting to the root of a problem (*15*). The technique starts by identifying a problem and then asking "why?" 5 times sequentially to drill down and determine what caused a problem. Each time a why is questioned, the answer becomes the premise for the next why question. The technique forces the investigator to dig more deeply to find a problem's true cause.

To demonstrate, consider an example of administration of a bone scan dose to the wrong patient:

1. Why did the patient receive the wrong radiopharmaceutical? Because the technologist escorted the wrong patient from the waiting room.
2. Why was it the wrong patient? Because 2 patients with the same last name but scheduled for different tests were in the waiting room.
3. Why did the wrong patient come forward? Because the technologist only called out "Mr. Smith" in the waiting room.
4. Why did the technologist not realize it was the wrong Mr. Smith? Because the technologist did not use 2 patient-specific forms of identification.
5. Why did the technologist not use 2 forms of patient identification to identify the correct patient? Because use of 2 patient-specific identifiers was not standard practice at the clinic.

When asking and answering the 5 whys, one must obtain clear and concise answers, avoiding answers that are too simple or that overlook important details. The answers to the questions should be logical and backed by proof. One should look for patterns and not just at the isolated event, look for causes for which practical recommendations can be recommended, and ask why—multiple times—to identify the cause and not just the symptoms of a problem. Problems will usually resurface if only the symptoms are treated and the root cause is not identified and corrected.

For example, suppose a patient with chest pain were to go to the doctor to get a prescription to make the chest pain go away. If the doctor merely gives the patient nitroglycerin to make the chest pain go away, the chest pain would probably return and worsen. However, suppose the doctor were to ask why the patient has chest pain and investigate further. In that case, the doctor could diagnose a coronary artery blockage and fix the root of the problem with a stent or bypass.

BASIC RCA STEPS

RCA is a useful technique for pinpointing the cause of safety events. The term *event* is used here to refer to sentinel or near-miss events. To prevent similar recurrences, RCA discovers why, what, and how something happened (*16*).

There are 4 primary steps in the RCA process (Fig. 1). The first is to collect data. Data collection is critical for obtaining complete information, understanding the event, and identifying causal factors. Diagraming, the second step, helps to organize and analyze information and to identify knowledge gaps. After the causal factors have been identified, the third step is pinpointing the root cause. Finally, the fourth step is generating and implementing a solution. The solution should be achievable and aimed at preventing the event's recurrence.

APPLYING RCA TO SENTINEL EVENTS

Use of RCA to examine sentinel events, in which a patient could be harmed or die needlessly, must be systematic and
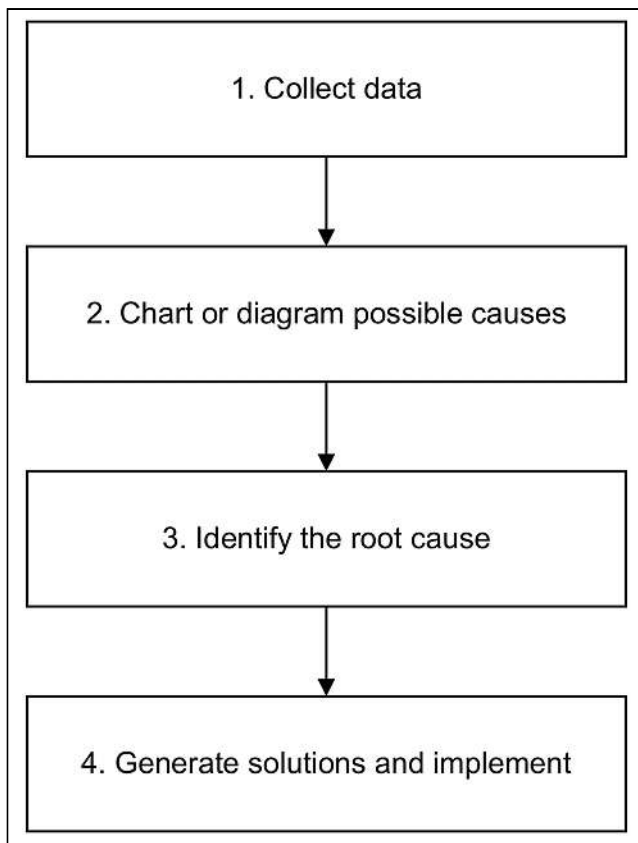
FIGURE 1. At its simplest, basic RCA involves 4 steps.

FIGURE 2. Because sentinel events happen in health-care settings involving multiple people and steps, RCA process is more involved than basic RCA.

comprehensive. The analysis should focus on systems and processes and not just the human element of error. Nine steps are recommended (Fig. 2) (*17*).

Step 1: Identifying an Event

The Joint Commission clearly defines and provides a long list of what is and is not considered a sentinel event (*18*). Common examples of sentinel events include falls, unintended retention of foreign objects, suicide, wrong surgery, and treatment delay. All staff should be trained to recognize sentinel events or close-call incidents and report them within the system. Usually, a risk-based triage system or committee is used to evaluate the incident and determine the need for RCA.

A fundamental principle of RCA is honest reporting without fear of reprisal. Regrettably, fear of retaliation can be a significant barrier that inhibits staff reporting of incidents. Besides the candid reporting of events, reporting must be prompt (without delay) to ensure that details are thoroughly and accurately documented (*17*).

Step 2: Assembling a Team

Once the need for RCA is established, a small team is assembled to analyze the incident. First, the team collects preliminary data to understand what the event was, where it happened, when it happened, who was involved, and how it happened.

Teams are usually made up of 4–6 individuals experienced in the field and conversant with the nuances of the process leading to the sentinel or near-miss event. Typically, teams include physicians, supervisors, staff, and quality improvement experts. The team members who perform an RCA investigation should not have been directly involved in the event, as bias can be an undesirable source of problems and inaccurate analysis.

Step 3: Creating an Initial Flowchart

Flowcharts are one of the best tools to describe a process or event graphically, in a manner that usually can be better understood than an essay description. Using the preliminary data, the team creates a flowchart to display the processes leading to the event and organize the facts (Fig. 3).

Step 4: Establishing the Event Story

The flowchart should trigger questions to guide the investigation into contributing factors. The 5-whys technique is
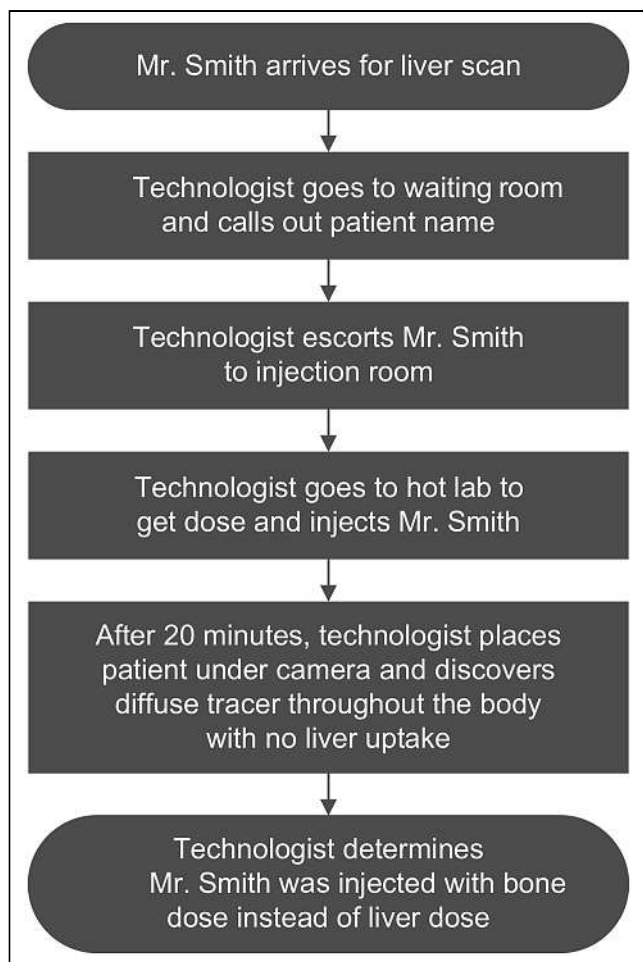
FIGURE 3. Initial flowchart for misadministration demonstrates facts surrounding situation in which technologist administered bone scan dose instead of liver scan dose.

used at this point. The goal is not only to assess the sentinel event but also to thoroughly evaluate the processes leading to the event. Therefore, fine granularity is essential in pinpointing the root cause or causes. The information gathered from the investigation adds detail to the initial flowchart for development of the event story map.

Step 5: Creating a Cause-and-Effect Diagram

Once the event story map is generated, the next step is to produce a cause-and-effect diagram. A cause-and-effect diagram is another visual tool to logically organize potential causes of a problem (effect). The diagram's purpose is to help the investigating team identify causal links and contributing factors to the root cause.

The components of a cause-and-effect diagram include a problem statement, potential causes (categories), and potential reasons for the causes. Using the same example of administering the wrong radiopharmaceutical to the patient (effect), there could be multiple causes related to scheduling, patient identification, pharmacy error, or patient factors (Fig. 4).

It is helpful to place the flowchart and event story map side by side when identifying causes. Potential causes are then repeatedly identified until knowledge of the event is exhausted. If few causes are identified, additional investigation is required.

Step 6: Identifying the Root Cause

The cause-and-effect diagram will show multiple causes for, steps to, or reasons that led to the event. It is crucial to single out the one cause of the cascade of failed steps that led to the event. Each cause is examined and discussed along with the contributing factors until a root cause is identified.

Step 7: Developing and Implementing Corrective Actions

The identified root cause is then examined again to develop corrective actions. The team should identify barriers and risk reduction strategies to ensure that the root cause does not recur. Multiple corrective steps may be required for each cause. Planning of the corrective action should include policy changes, training, and other steps to ensure and sustain compliance. In addition, the planning must eliminate implementation barriers and identify outcome measures. The corrective actions are then implemented.

Step 8: Identifying Outcome Measures

The success of any intervention or change implementation can be measured only by outcome analysis. The outcome metrics should be specific, quantifiable, and able to be measured over time. The time required for accurate outcome analysis depends on how frequently the procedure or process in question is done. The more frequently a procedure is performed, the shorter the period of outcome analysis.

Step 9: Communicating Results

The last step is communication of the results. The event, RCA, corrective actions, and outcome results should be reported to all staff involved and, more broadly, throughout the institution. If deemed important and not institution-specific, reporting an RCA in a peer-reviewed publication can have a more significant positive impact.

SPECIAL CIRCUMSTANCES FOR RCA IN NUCLEAR MEDICINE

The nuclear medicine and molecular imaging field is diverse, comprising nearly 100 diagnostic examinations and a rapidly increasing number of theranostic procedures (19). Numerous procedures require several staff members or the assistance of personnel from outside the department, such as personnel from cardiology, endocrinology, or oncology. In theranostic procedures, opportunities for variability are multiplied, with the added burden of risk of harm. This diverse number of procedures with multiple steps and various personnel presents many different opportunities for error (Tables 1 and 2).
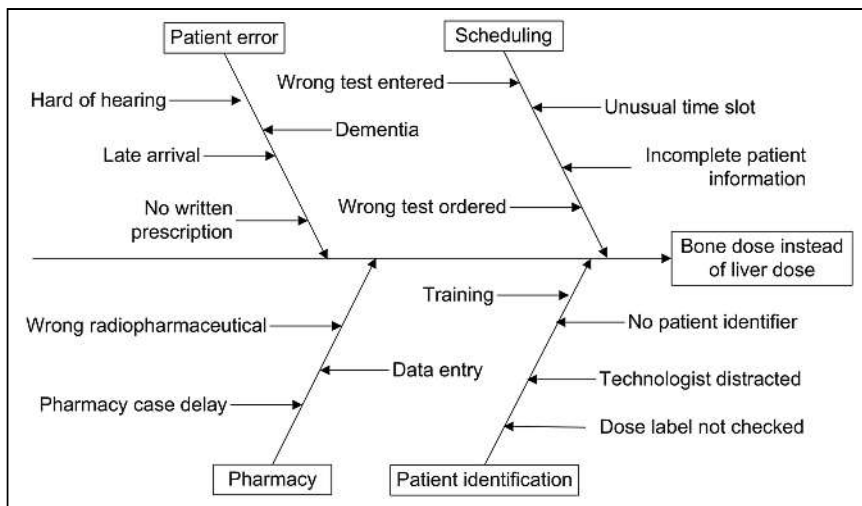
FIGURE 4. Effect and potential causes of misadministration of bone dose instead of liver dose are demonstrated in this fishbone diagram. Each probable cause has multiple reasons or contributing factors.

NUCLEAR MEDICINE RCA EXAMPLE

Let us apply the RCA process to a potential nuclear medicine sentinel event (a patient falls off the scan table) to make the RCA steps more understandable and meaningful. Was the technologist just careless?

Step 1: Identifying an Event

On August 26, 2022, an elderly patient, Mrs. Darling, underwent whole-body bone scanning and fell off the table while unattended. The incident happened at approximately 12:30 PM. Technologist Ray Gamma started the acquisition and left the room. About 15 min later, he found Mrs. Darling on the floor, moaning and complaining of hip pain.

Technologist Gamma immediately reported the event to his nuclear medicine supervisor, who completed the incident form and notified the risk management department. Subsequent radiography and examination found that Mrs. Darling had a broken right hip. The risk management director, Dr. Guardian, determined that the harm was not related to the patient's illness or the procedure. The harm was thus classified as a sentinel event.

Step 2: Assembling a Team

Dr. Guardian appointed an RCA team to investigate the event. The team included Dr. Roentgen, a staff nuclear medicine physician vacationing in Florida on the day of the event; the radiology department nurse, Nurse Ivy Line; the nuclear medicine scheduler, Ms. Ida Arrangér; a nuclear medicine technologist who works at a satellite office, Mr. Pho Ton; and one of the risk managers who is an expert in RCA, Nurse Al Waysmad.

Step 3: Creating an Initial Flowchart

The team created a simple flowchart to organize the preliminary facts and began the investigation (Fig. 5)

Step 4: Establishing the Event Story

Using the 5 whys, the team asked questions and interviewed other staff, such as the receptionist, lead technologist, and other technologists. The team asked questions such as why did Technologist Gamma leave the patient unattended? Why did not another staff member inject the patient

TABLE 1
Opportunities for Error in Diagnostic Nuclear Medicine

Procedure stage	Opportunities for error	Staff involved
Scheduling	Single vs. multiple-day procedures; procedures with delay between injection and imaging	Scheduler/referring physician
Screening	Scan appropriateness, medication interference, pregnancy/breastfeeding	Nuclear medicine physician
Patient preparation	Medications (prescribed and over counter), NPO status, hydration, caffeine avoidance, oral contrast agent (barium), intravenous contrast agent (iodinated)	Scheduler/technologist
Radiopharmaceutical administration	Correct radiopharmaceutical, amount, route, and timing	Technologist
Special techniques	Stress testing, injections in other departments (e.g., surgery)	Technologist/stress test personnel/other physician
Image acquisition	Collimator; energy window; matrix size; acquisition type (e.g., static vs. dynamic); planar vs. SPECT, SPECT/CT, or PET/CT; positioning; technical quality	Technologist
Image processing and display	Region-of-interest placement, image summation, filtering, reference database comparison, archiving	Technologist
Interpretation and reporting	Misdiagnoses, missed pathology, incomplete reporting, delayed reporting	Nuclear medicine physician

NPO = nothing by mouth.

TABLE 2
Opportunities for Error in Therapeutic Nuclear Medicine

Procedure stage	Opportunities for error	Staff involved
Scheduling	Single vs. multiple-day therapies; radioisotope availability	Scheduler/referring physician/ nuclear medicine physician
Screening	Therapy appropriateness, medication interference, pregnancy/breastfeeding	Referring physician/nuclear medicine physician/physicist
Consult	Pretreatment history, laboratory and other diagnostic testing results, patient factors (e.g., breastfeeding, incontinence, inability to swallow), and home environment	Patient/family/nuclear medicine physician
Patient preparation	Preparation length (e.g., few days to weeks), medications (prescribed and over counter), NPO status, hydration, oral contrast agent (barium), intravenous contrast agent (iodinate)	Scheduler/technologist/nurse/ nuclear medicine physician
Time-out/radioisotope administration	Correct patient, therapy, radioisotope, amount, route, and timing; complete dose administration	Technologist/authorized user/ nuclear medicine physician
Posttherapy	Imaging and timing, medical and radiation safety instructions	Technologist/nuclear medicine physician

NPO = nothing by mouth.

who was to undergo rest myocardial perfusion imaging (See Fig. 5)? Could Technologist Gamma maintain visual surveillance of the patient? What was the patient's mental acuity? Did Technologist Gamma tell Mrs. Darling he was leaving the room? Why did Mrs. Darling fall off the table?
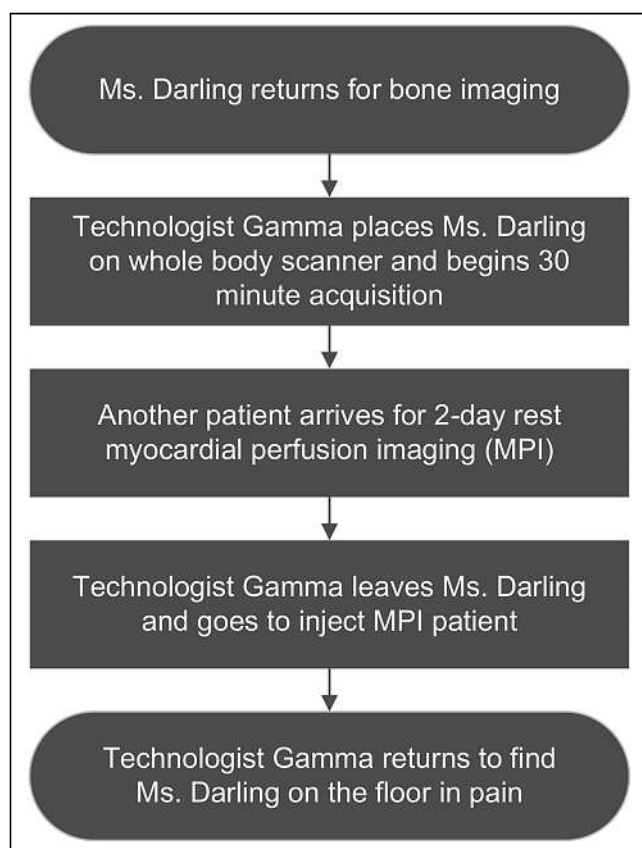
FIGURE 5. Initial flowchart for patient's falling off scanner table describes facts related to this sentinel event. These facts are used to stimulate questions for investigation and to create event story.

During the investigation, the team discovered several contributing factors. First, between the bone scan injection and the image acquisition, Mrs. Darling was told to drink 1.9 L (64 oz) of water. Second, Mrs. Darling did not empty her bladder right before the scan began because the restroom, located outside the department, was occupied. Third, Mrs. Darling had mild dementia and was hard of hearing. Fourth, half the technologists were at lunch when the myocardial perfusion patient was scheduled for injection; there were no other technologists available to inject the patient. Fifth, the hook-and-loop straps on the table were worn and would not fasten well. Finally, Mrs. Darling was uncomfortable and had to use the restroom. These factors and several others contributed to the patient's fall (Fig. 6).

Step 5: Creating a Cause-and-Effect Diagram

The team organized all the discovered factors to create the cause-and-effect diagram (Fig. 7). The problem (effect) was that the patient fell off the scan table. The major causal factors were related to the patient, department operation, equipment, and technologist. There were also multiple underlying reasons for each of the major causal factors.

Step 6: Identifying the Root Cause

The team evaluated the fishbone diagram related to Mrs. Darling's fall and identified the root cause. The department was short-staffed during lunch, but patients were routinely scheduled during that time, resulting in technologists caring for multiple patients simultaneously. Technologist Gamma believed he had no choice but to leave Mrs. Darling and inject the myocardial perfusion patient because no other technologists were available and the department was running behind schedule. Contributing factors were the nature of bone scan hydration requirements, lack of an available restroom near the nuclear medicine department,
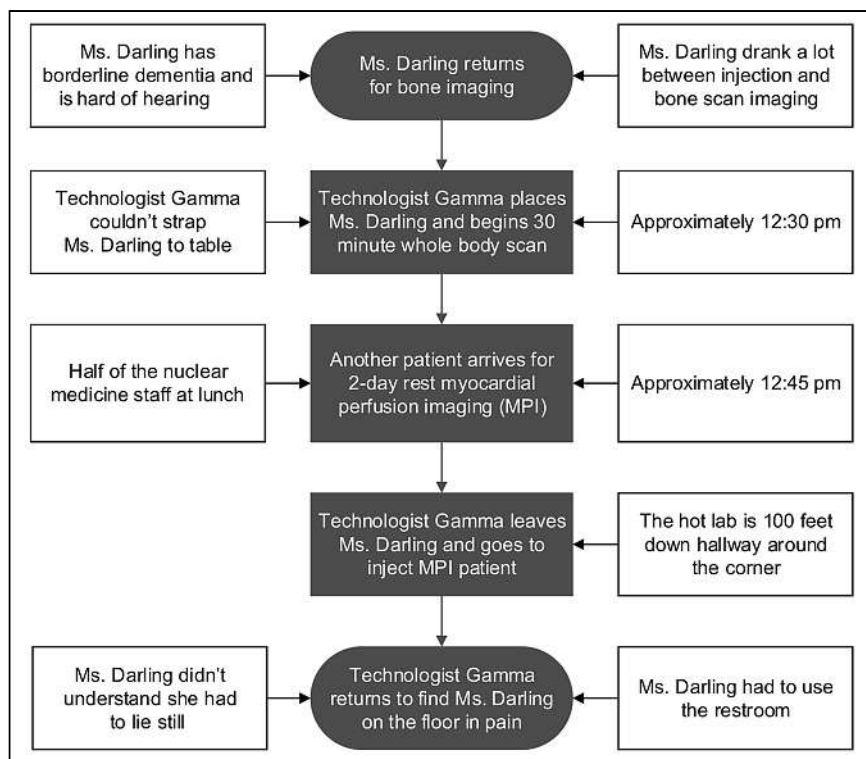
FIGURE 6. Event story flowchart adds factors contributing to patient-fall sentinel event, as determined during RCA.

malfunctioning table straps, and the patient's need for continuous monitoring. Although Technologist Gamma could have made other choices, there was more to the story than that he was simply careless.

Step 7: Developing and Implementing Corrective Actions

The team, the nuclear medicine supervisor, and other staff reviewed the cause-and-effect diagram and discussed the root cause. They implemented several changes. First, lunches were staggered over a more extended period so that fewer

FIGURE 7. Effect and potential causes of, and contributing factors to, patient's falling off scanner table are demonstrated in this fishbone diagram.

technologists were simultaneously absent from the department. Second, the schedule was adjusted so that technologists would not be responsible for more than one patient at a time. For example, a technologist would not have to inject one patient while scanning another. Finally, the table straps were replaced as a minor corrective action.

Step 8: Identifying Outcome Measures

To assess the effectiveness of the intervention, the team and nuclear medicine department monitored the number of times technologists had to care for more than one patient at a time. Because numerous procedures were performed daily, the team collected data for 1 mo and then evaluated and made changes as necessary.

Step 9: Communicating Results

To ensure that the corrective actions were implemented and sustained, the nuclear medicine supervisor created a new scheduling grid and shared instructions with the scheduling department. The supervisor also made a lunch schedule, which she posted on the lounge wall and shared during a staff meeting. Finally, the entire nuclear medicine department attended training on caring for patients with varying needs.

LIMITATIONS OF RCA

The limitations of applying the RCA methods of the automobile manufacturing industry to medicine have been well documented (*20*). Although RCA may be well suited to automobile manufacturing, in which the parts and final product are standardized in the form of model, year, and make of the vehicle, medicine deals with humans without the same model, year, and make. The diverse composition of the patient population and the unique needs of individual patients, including emotional and psychologic, create a situation far more complex than in an automobile assembly line. Consequently, RCA in health care must be more detailed and more involved, as described in the 9 steps for RCA in sentinel event investigation.

Another limitation of RCA is that it must be supported by the top administration and then by all administrative levels downward to improve safety and induce cultural changes (*21*).
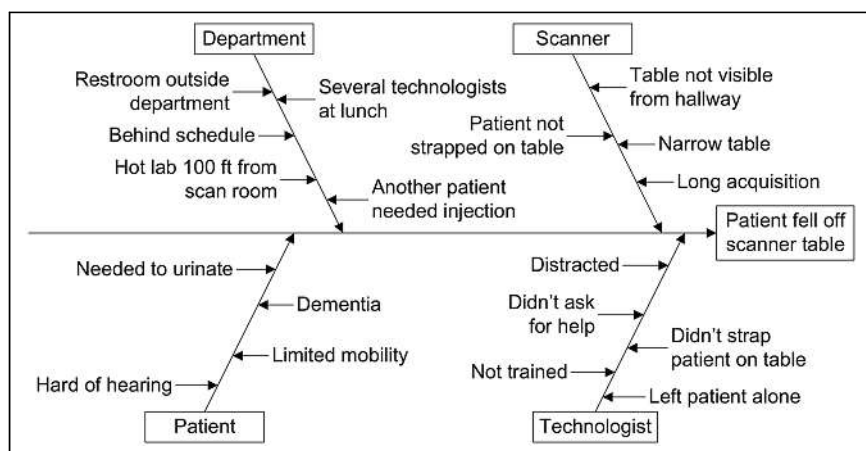
There must be a blame-free environment so that individuals feel safe and can be persuaded to talk openly about events. Effective sentinel event communication is key to institutional learning and preventing future events (*20*).

Finally, RCA can be time-consuming and requires adequately trained personnel. RCA is a complex, multistep process that is operator-dependent. The fact that it is often not properly performed affects the tool's utility. As a result, there is limited published research demonstrating the effectiveness of RCA in reducing sentinel events and near misses. Thus, to be effective, nuclear medicine personnel, including technologists, must be knowledgeable and skilled in the technique.

CONCLUSION

The reliability and accuracy of nuclear medicine procedures are highly dependent on the competency of the nuclear medicine technologist. Despite a technologist's training and skill, the complexity of nuclear medicine procedures increases the likelihood of sentinel events and near misses. Therefore, technologists play a pivotal role in RCA performance and the subsequent prevention of future events.

Team members need to know not only their assigned job but also the jobs of those who work in earlier and later steps of the multistep procedure. This knowledge can help to identify and correct errors before a small error snowballs into a catastrophic avalanche.

The technologist team player should not only understand and follow protocols but also understand the principle behind a protocol. Because of the diversity of procedures and of human anatomy and physiology, along with the need for patient-centered care, nuclear medicine technologists must be able to modify protocols without affecting the outcome. The use of RCA in nuclear medicine is an invaluable tool to address the many challenges encountered in the field.

DISCLOSURE

No potential conflict of interest relevant to this article was reported.

REFERENCES

1. Patra KP, De Jesus O. Sentinel event. National Center for Biotechnology Information website. https://www.ncbi.nlm.nih.gov/books/NBK564388/. Updated 2021 October 7, 2021. Accessed September 21, 2022.
2. Bindman A. Avoiding a health care financial meltdown. *JAMA*. 2020;324:17–18.
3. Medina L, Sabo S, Vespa J. Living longer: historical and projected life expectancy in the United States, 1960 to 2060. U.S. Census Bureau website. https://www.census.gov/library/publications/2020/demo/p25-1145.html. Published February 2020. Accessed September 21, 2022.
4. Arias E, Tejada-Vera B, Kochanek KD, Ahmad FB. Provisional life expectancy estimates for 2021. Centers for Disease Control and Prevention website. https://www.cdc.gov/nchs/data/vsrr/vsrr023.pdf. Published August 2022. Accessed September 21, 2022
5. Kurani N, Ortaliza J, Wager E, Fox L, Amin K. How has US spending on healthcare changed over time? Health System Tracker website. https://www.healthsystemtracker.org/chart-collection/u-s-spending-healthcare-changed-time/. Published February 25, 2022. Accessed September 21, 2022.
6. Kohn LT, Corrigan JM, Donaldson MS, eds. *To Err Is Human: Building a Safer Health System*. National Academies Press; 2000:1.
7. Makary MA, Daniel M. Medical error: the third leading cause of death in the US. *BMJ*. 2016;353:i2139.
8. Pellegrini CA. Time-outs and their role in improving safety and quality in surgery. Bulletin of the American College of Surgeons website. https://bulletin.facs.org/2017/06/time-outs-and-their-role-in-improving-safety-and-quality-in-surgery/. Published June 1, 2017. Accessed September 21, 2022.
9. Gawande A. *The Checklist Manifesto*. Profile Books; 2011:32–47.
10. Kellogg KM, Hettinger Z, Shah M, et al. Our current approach to root cause analysis: is it contributing to our failure to improve patient safety? *BMJ Qual Saf*. 2017; 26:381–387.
11. Summary data of sentinel events reviewed by The Joint Commission. The Joint Commission website. https://www.jointcommission.org/-/media/tjc/documents/resources/patient-safety-topics/sentinel-event/annual-se-report-2021.pdf/. Published December 31, 2021. Accessed September 21, 2022.
12. Squires D, Blumenthal D. Do small physician practices have a future? The Commonwealth Fund website. https://www.commonwealthfund.org/blog/2016/do-small-physician-practices-have-future. Published May 26, 2016. Accessed September 21, 2022.
13. Gale AH. The hospital as a factory and the physician as an assembly line worker. *Mo Med*. 2016;113:7–9.
14. Aboagye R, Cherala S, Senesac P, Johnston J. Quality improvement (QI) in evaluation: ask why again and again and again. Umass Chan Medical School website. https://repository.escholarship.umassmed.edu/handle/20.500.14038/34692. Published August 3, 2016 Accessed September 21, 2022.
15. Five whys tool for root cause analysis. www.cms.gov/medicare/provider-enrollment-and-certification/qapi/downloads/fivewhys.pdf/. Centers for Medicare and Medicaid Services website. Accessed September 21, 2022.
16. Rooney J, Vanden Heuvel L. Root cause analysis for beginners. *Qual Prog*. 2004; 37:45–53.
17. Charles R, Hood B, Derosier JM, et al. How to perform a root cause analysis for workup and future prevention of medical errors: a review. *Patient Saf Surg*. 2016; 10:20.
18. Sentinel event policy and procedures. The Joint Commission website, https://www.jointcommission.org/resources/patient-safety-topics/sentinel-event/sentinel-event-policy-and-procedures/. Accessed September 21, 2022.
19. Farrell M, Basso D, Kerr B, et al. *Quick-Reference Protocol Manual for Nuclear Medicine Technologists*. Society of Nuclear Medicine and Molecular Imaging; 2014.
20. Peerally MF, Carr S, Waring J, Dixon-Woods M. The problem with root cause analysis. *BMJ Qual Saf*. 2017;26:417–422.
21. Martin-Delgado J, Martínez-García A, Aranaz JM, Valencia-Martín JL, Mira JJ. How much of root cause analysis translates into improved patient safety: a systematic review. *Med Princ Pract*. 2020;29:524–531.

Diuretic Renal Scintigraphy Protocol Considerations

Kevin P. Banks[1,2], Mary Beth Farrell[3], and Justin G. Peacock[1,2]

[1]Brooke Army Medical Center, San Antonio, Texas; [2]Uniformed Services University of Health Sciences, Bethesda, Maryland; and [3]Intersocietal Accreditation Commission, Ellicott City, Maryland

Diuretic renal scintigraphy plays a critical diagnostic role by providing a physiologic means for differentiating between obstructive and nonobstructive hydronephrosis and by assessing the function of the affected kidney. The examination accuracy is highly dependent on and benefits from close attention to the protocol. This article reviews kidney anatomy and physiology, patient preparation, available radiopharmaceuticals, diuretic administration, acquisition, processing, quantification, and interpretation criteria in the United States.

Key Words: diuretic; renal; protocol; acquisition; processing; Lasix

T he role of the kidneys is to cleanse the blood of waste and turn the waste into urine while also maintaining the balance of fluid and electrolytes, particularly sodium. The paired organs are located along the posterior abdominal wall, on each side of the spine, between the levels of T12 and L3. Measuring about 10–13 cm in length, the kidneys are bean-shaped, with their long axis lying almost parallel to the body. The indentation of the bean, called the renal hilum, is oriented toward the spine. It is where arterial blood containing waste enters the kidney, cleansed venous blood exits, and urine containing waste exits. The renal parenchyma consists of an outer cortex and an inner medulla, encompassing the urine-collecting system (CS) comprising calyces and the renal pelvis (Fig. 1A). Each kidney has approximately a million small filters called nephrons within the parenchyma. Each nephron is a long, fine convoluted tubule 3–6 cm long, originating in the cortex at its glomerulus and ending in the medulla at the collecting duct (Fig. 1B). At the end of the collecting ducts, urine containing waste passes into the calyces and is then collected in the funnel-shaped renal pelvis. The pelvis drains via the ureter to the bladder.

The normal drainage of urine can be blocked because of a wide range of congenital and acquired disorders. Obstruction to urinary outflow may, in turn, lead to increased pressure in the renal CS and its subsequent dilatation and swelling of the kidney (Fig. 2). This condition, termed hydronephrosis, can lead to injury of the parenchyma and loss of function. Concern about obstruction is usually raised by detection of an elevated serum creatinine level versus imaging findings of a dilated renal pelvis or calyces. Occasionally, it may also be suspected in a patient undergoing follow-up after attempted correction of a previous obstruction (*1*). Unfortunately, neither a decline in renal function nor CS dilation on imaging is specific for obstruction; these findings may be due to a wide variety of nonobstructive disorders such as infection, vesicoureteral reflux, congenital anomalies, or residual changes after the resolution of a previous obstruction. Hence, in this scenario, diuretic renal scintigraphy (DRS) plays a critical diagnostic role by providing a noninvasive physiologic means for differentiating between obstructive and nonobstructive hydronephrosis as well as assessing the function of the affected kidney (*2*). The examination is based on the principle that under physiologic conditions, urine may be retained in a hydronephrotic renal pelvis for 1 of 2 reasons: either an anatomic obstruction preventing outflow or the reservoir effect, in which urine pools in the dilated renal pelvis until enough accumulates to spill over into the ureter. The reservoir effect is a pseudoobstruction that can mimic a mechanical obstruction, leading to unnecessary urologic interventions. DRS takes advantage of the fact that the reservoir effect can be overcome under high-flow conditions created with diuretic administration. By evaluating the washout of radiopharmaceutical from the CS and analyzing the parenchymal function, the presence of an obstruction and risk of renal damage can often be correctly assessed.

BACKGROUND

Before the advent of DRS, obstructive hydronephrosis was distinguished from nonobstructive by an invasive means: a
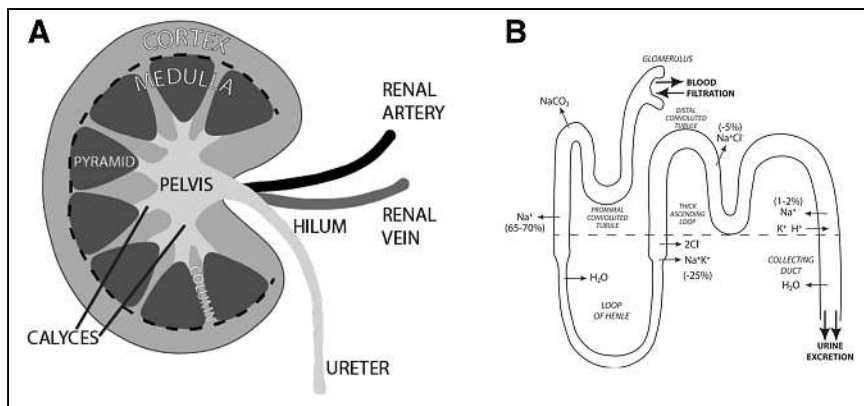
FIGURE 1. Kidney anatomy and glomerulus function. (A) Kidney is bean-shaped paired organ. Indentation is called hilum and is where renal artery enters, whereas renal vein and ureter exit. Parenchyma comprises outer cortex and inner medulla, with medulla further subdivided into pyramids and columns. This all surrounds CS, which is made up of multiple calyces feeding into pelvis. (B) Blood enters glomerulus containing waste and then leaves filtered. Nephron travels into and out of cortex (separated by dashed line), whereas electrolytes are exchanged and urine concentrated before being excreted into calyces.

pressure perfusion study, commonly known as the Whitaker test. The Whitaker test involved percutaneous kidney access via a posterior approach. A catheter was introduced into the dilated renal pelvis, and fluid was instilled at a flow rate of 5–10 mL/min while the pressure was monitored in the renal pelvis and bladder (*3*). An unobstructed renal pelvis and ureter tolerated this high flow readily, with no or only a small rise in pressure from baseline. However, if the pressure between the renal pelvis and bladder rose significantly, often greater than 15–20 cm of water, then the system was deemed obstructed (*4*). Fortunately, in 1979, DRS was introduced using ^{131}I-hippuran (orthoiodohippurate) and furosemide, offering a simpler, noninvasive means for evaluating equivocal pelviureteral obstruction (*5,6*). Soon thereafter, in 1980 (*7*) and 1986 (*8*), ^{99m}Tc-diethylenetriaminepentaacetate (^{99m}Tc-DTPA) and ^{99m}Tc-mercaptoacetyltriglycine (^{99m}Tc-MAG3),

FIGURE 2. (A) Normal kidney demonstrates small calyces and decompressed renal pelvis. (B) With obstruction (and other disorders), calyces and pelvis become dilated.

respectively, were introduced, both of which are still in widespread use today.

The examination accuracy is highly dependent on and benefits from close attention to patient preparation, timing of diuretic, method of acquisition, processing, quantification, and interpretation criteria (Tables 1 and 2).

PREPARATION

The ability of the kidneys to significantly increase urine production in response to diuretic administration is central to the diagnostic accuracy of DRS. An increase in urine production is determined by both renal function and hydration.

To best ensure appropriate hydration, the patient should be instructed to increase fluid intake the day before and the morning of the examination while avoiding natural diuretics (typically coffee, tea, and other caffeinated beverages). An additional 12 ounces of fluid with each of the 3 meals (totaling approximately 1 L) before the examination is a reasonable goal. This step is contraindicated in individuals on a fluid-restricted diet, which is most commonly a treatment for congestive heart failure and for rare disorders such as adrenal insufficiency and hyponatremia. Additionally, unlike many other nuclear medicine examinations, fasting beforehand should be discouraged since this could impair efforts to prehydrate.

Once the patient arrives at the clinic, additional oral hydration is recommended during the 30–60 min immediately preceding the examination. The preferred amount of oral hydration is 5–10 mL/kg based on an international scientific committee's consensus report (*9*), which was subsequently endorsed by the Society of Nuclear Medicine and Molecular Imaging (SNMMI) and the European Association of Nuclear Medicine (EANM) (*10*).

Patients prescribed diuretics as part of their routine medical care should be instructed to refrain from taking these medications the morning of the examination. Diuretics are most commonly prescribed for hypertension and to treat edema from heart, kidney, or liver failure. Having the patient withhold diuretics helps ensure adequate prehydration while avoiding the possibility of commencing the examination during an ongoing prescribed diuresis, which can last for 6–8 h after oral administration of furosemide (*11*).

Additionally, though not explicitly recommended in the applicable guidelines and parameters, kidney function assessment before the examination can help ensure the likelihood of a diagnostic examination. As renal function decreases, urine production and responsiveness to diuretics decrease. Hence, patients with impaired renal function may not have an adequate escalation in urine flow from the standard 40-mg intravenous

TABLE 1
Approach to Best Practices for Adult DRS: Patient Preparation and Acquisition

Parameter	Best practice
Patient preparation	
Increase in fluid intake day before and morning of examination	It may be optimal also to have patient avoid natural diuretics, though some experts believe effect is less than fluid consumed
Withdrawal of prescribed diuretics on morning of examination	Thiazides: hydrochlorothiazide, indapamide, metolazone, chlorthalidone
	Loop diuretics: furosemide, bumetanide, torsemide, ethacrynic acid
	Potassium sparing: amiloride, spironolactone, triamterene, eplerenone
	Carbonic anhydrase inhibitors: acetazolamide
Oral hydration 30–60 min beforehand	Patient drinks 5–10 mL/kg
	450–900 mL (15–30 oz, or 2–4 cups) for adults weighing 90.7 kg (200 lb)
	385–770 mL (13–26 oz, or 1.5–3 cups) for adults weighing 77.1 kg (170 lb)
Prevoiding	Patient voids immediately before beginning of examination
Acquisition	
^{99m}Tc-MAG3, 37–185 MBq (1–5 mCi) intravenously	^{99m}Tc-MAG3 is preferred over ^{99m}Tc-DTPA despite cost; lower doses are adequate given that flow/arterial phase can be omitted
Furosemide, 40 mg intravenously	If patient is on higher dose of furosemide at home, increase to match; consider 80–120 mg if known renal insufficiency
	Serum creatinine level > 1.2 ng/dL (women) or > 1.4 ng/dL (men)
	Estimated GFR < 90 mL/min/1.73 m^2 (either sex)
Acquisition and timing of diuretic (most common source of variability; remains actively debated topic with no clear best practice for all situations)	F=0 single acquisition or F+20 2-part acquisition; F+10, F+15, and F+30 are also used by many practices, and F+10sp is also considered suitable technique
Postvoid image (maximizes pressure differential between kidneys and bladder, facilitating physiologic drainage)	Patient stands or walks for 5 min, voids, and then is imaged in same position as examined

Many quantitative values are dependent on protocol and cannot be universally applied.

TABLE 2
Approach to Best Practices for Adult DRS: Processing and Quantification

Parameter	Best practice
Processing	
WK ROI	Is essential for relative function measurement; generally adequate if kidney function is normal
Cortical ROI	Includes only parenchyma, not CS and calyces; optimal for assessing functional parameters such as 20-min/max (renal retention) and Tpeak
CS ROI	Excludes parenchyma and has been shown to better represent CS drainage when calculating T-1/2
Background ROI	Is C-shaped or reniform, 2 pixels wide, and 1 pixel away from cortex
Relative (split) function	Must be derived from WK ROIs; may be measured using 2- to 3-min intervals, but intervals of 1–2 or 1–2.5 min are recommended if F=0 protocol is used
Quantification	
Relative (split function)	Normal is 45%–55%; abnormal if <40%
Tpeak	Normal is <5 min
T-1/2 emptying	Normal is <10–15 min; abnormal does not equate to obstruction
20-min/max	Normal is <0.35 as measured 20 min after Tpeak
Tissue transit time	Activity should be seen in CS by 5 min; >8 min is delayed
Postvoid kidney to maximum	Postvoid image is acquired 30 min after start, and activity is compared with Tpeak
Output efficiency	Helps overcome confounding effect of poor renal function on CS drainage assessment; requires special processing software
Normalized residual activity	Normal is <1.0 for 20- to 21-min interval and <0.10 when using 1-min interval acquired after voiding at 60 min from examination start

Many quantitative values are dependent on protocol and cannot be universally applied.

dose of furosemide. Therefore, the dose may need to be increased to achieve significant enough diuresis for diagnostic DRS results (12). Fortunately, in many cases, renal function testing is obtained as part of clinical care, and the resulting serum creatinine or estimated glomerular filtration rate (GFR) may be used to determine an optimal diuretic dose. It is generally agreed on that an abnormal serum creatinine level (>1.2 ng/dL in women and >1.4 in men) usually indicates a 50% loss of renal function (i.e., GFR) and the need to increase the dose administered for DRS (10).

Unfortunately, only case reports are available comparing the effectiveness of higher doses of furosemide with the standard 40-mg dose in patients with compromised renal function, and thus no evidence-based recommendations can be made (13). Given this, the SNMMI–EANM recommends a simple approach of doubling the dose of furosemide to 80 mg for patients with an elevated serum creatinine level or a depressed estimated GFR (<90 mL/min/1.73 m^2).

Some practices have further increased the dose to 120 mg or more in individuals with severe renal impairment (estimated GFR < 30 mL/min/1.73 m^2), given that prior research has shown that up to 171 mg may be necessary to achieve maximal diuresis when the estimated GFR reaches 15 mL/min/1.73 m^2 (14). One caveat to this approach is that individuals on chronic diuretic therapy are usually given at least the intravenous equivalent of their prescribed outpatient oral dose, with 1:2 being an acceptable intravenous-to-oral conversion for furosemide. The conversion for bumetanide and torsemide is 1:1 (15).

The final recommended preparation step is to start an intravenous line and have the patient void the bladder immediately before the examination begins. Voiding can reduce the possibility of patient motion from discomfort or needing to terminate the study prematurely for the patient to urinate. It also minimizes the backpressure effect that a distended bladder may have on slowing the draining of the upper tracts (16–19).

RADIOPHARMACEUTICAL

Two radiopharmaceuticals are currently in use for DRS: ^{99m}Tc-DTPA and ^{99m}Tc-MAG3. ^{99m}Tc-DTPA is entirely filtered by the glomerulus, allowing it to be used to measure GFR and assess the differential or relative function of each kidney and potential outflow obstruction (20). However, the kinetics of ^{99m}Tc-DTPA are poor in the setting of reduced renal perfusion and function, potentially leading to spurious results (21). In contrast, ^{99m}Tc-MAG3 undergoes extraction predominately by the tubular cells and is then secreted into the renal CS. Because its extraction fraction is more than twice that of ^{99m}Tc-DTPA, ^{99m}Tc-MAG3 kinetics are much less affected by impaired renal perfusion and function, providing superior image quality and making it the preferred agent 3:1 by institutions despite increased cost (22–24). For this reason, ^{99m}Tc-MAG3 is recommended for DRS by the SNMMI, EANM, and Society of Fetal Urology (16,25,26).

The appropriate administered activities of ^{99m}Tc-MAG3 and ^{99m}Tc-DTPA are not clearly established. Documentation of the American College of Radiology and Society of Pediatric Radiology states that up to 370 MBq (10 mCi) of ^{99m}Tc-MAG3 and up to 555 MBq (15 mCi) of ^{99m}Tc-DTPA may be used (20). The SNMMI–EANM procedure standard says that up to 370 MBq (10 mCi) is acceptable for either radiopharmaceutical, but 37–185 MBq (1–5 mCi) is preferred since a higher administered activity is significantly helpful only when higher counts are necessary for evaluating the arterial flow of a transplanted kidney (10,27).

The recommendation for using a lower administered activity was supported, in part, by a masked comparison of DRS examinations with and without the aid of the initial 1-min flow images. The results showed no significant difference in the ability to determine whether a kidney was obstructed (28). Furthermore, this same paper demonstrated the diagnostic equivalence of a lower (62.9 MBq [1.7 mCi]) and a higher administered activity (303 MBq [8.2 mCi]) of ^{99m}Tc-MAG3 for determining relative or split renal function. That said, no head-to-head studies of a higher (222 MBq [6–10 mCi]) versus a lower (37–185 [1–5 mCi]) administered activity have been performed to confirm the SNMMI–EANM recommendation for using a lower administered activity when evaluating for urine outflow obstruction. Interestingly, a recent survey of 110 U.S. nuclear medicine labs seeking Intersocietal Accreditation Commission (IAC) accreditation showed that a median administered activity of 370 MBq (10 mCi) for ^{99m}Tc-MAG3 and 447.7 MBq (12.1 mCi) for ^{99m}Tc-DTPA is used for DRS. The study also revealed that 10% of sites successfully use an administered activity averaging 185 MBq (5 mCi) (29).

DIURETIC

By far the most commonly used diuretic for DRS is furosemide, being universally used by 107 of 110 sites in the study of IAC-accredited nuclear medicine labs (24). Furosemide is a loop diuretic, meaning it decreases sodium and chloride absorption in the kidney at the ascending loop of Henle, which in turn increases water excretion (30). The adult dose of intravenous furosemide recommended by SNMMI–EANM is 0.5 mg/kg, versus 0.5–1.0 mg/kg recommended by the American College of Radiology–Society of Pediatric Radiology, with agreement on a maximum dose of 40 mg in healthy adults. A 40-mg intravenous dose of furosemide has been shown to achieve maximal diuresis in adults with normal renal function (10).

When administered intravenously, furosemide has an onset of action of approximately 5 min and reaches peak effect starting at 15 min, achieving 200–300 mL of urine production within 20–30 min after injection (31). In young, healthy adults, however, 20–30 mg may produce a diuresis sufficient for DRS and is preferred by some, given that it may avoid premature study termination in these patients because of the need to urinate (10).

Given the average weight of U.S. adults, the 40-mg dose is suitable for most patients without a history of renal insufficiency. However, those with decreased kidney function may benefit from an increased dose of 80 mg or higher in the setting of severe renal failure, whereas those on furosemide as an outpatient should receive at least as much as the intravenous equivalent of their prescribed oral dose. When higher doses of furosemide are being considered, particularly in elderly or fragile patients, it is important to consider the possibility of inducing severe drops in blood pressure, including stroke. One should consider discussing the use of high-dose furosemide with the ordering clinician.

Though infrequently used, 1 mg of intravenous bumetanide, another loop diuretic, is an acceptable alternative to DRS if furosemide is unavailable (14). Both furosemide and bumetanide contain a sulfonamide moiety similar to sulfur-containing antibiotics. Therefore, some practitioners prefer to avoid these drugs in patients with a known sulfa allergy and instead choose mannitol or ethacrynic acid (32,33). However, the concern for sulfur cross-reactivity has not been supported by research. A retrospective review of 88 patients who had a history of sulfa allergies and received intravenous furosemide demonstrated only 2 instances of potential allergic reactions. In both cases, minor rashes were treated effectively with a single dose of diphenhydramine (Benadryl; Johnson & Johnson) (34). Another study had similar reassuring results, showing no allergic reactions in 34 patients who had a reported history of sulfa allergies and were treated with sulfonamide-containing diuretics for intracranial hypertension (35). Hence, many experts now agree that these diuretics are safe for DRS in patients with a known sulfa allergy.

One of the most significant sources of debate in DRS concerns the timing of diuretic administration in relation to radiopharmaceutical administration. The parameter of the American College of Radiology and Society of Pediatric Radiology discusses 3 options, the F+20 (furosemide administered 20 min after the radiopharmaceutical), the F+0 (furosemide and radiopharmaceutical administered simultaneously), and the F−15 (furosemide administered 15 min before administration of the radiopharmaceutical).

The F+20 protocol is probably the most widely recognized approach, having been originally endorsed as the technique of choice by the SNMMI Pediatric Nuclear Medicine Council along with the Society of Fetal Urology (36). Unfortunately, up to 25% of examinations may result in equivocal results when a dilated renal pelvis empties very slowly after administration of the diuretic, preventing exclusion of a partial obstruction (37). This finding may occur when a large portion of the administered radiotracer is eliminated from the renal pelvis before the diuresis has a large enough impact on urine flow to demonstrate normal emptying (38).

In an attempt to reduce the number of equivocal results, the F−15 min approach was developed, taking advantage of the fact that maximal diuresis occurs 15–18 min after the intravenous administration of furosemide. Unfortunately, when this technique has been used, the examination has not been completed in up to 30% of patients because of the need to urinate before the study is over (10,39).

As a result, some experts have advocated for the F+0 protocol, a hybrid approach that shortens the procedure, reduces equivocal results, and improves patient comfort (40,41). However, the drawbacks to the early administration of diuretic (F−15 or furosemide and radiopharmaceutical administered simultaneously [F=0]) is that it precludes the observation of natural urine drainage kinetics, and in the setting of a poorly functioning kidney, these protocols may not allow enough time for filling of the CS and hence determination of outflow obstruction.

Thus, some experts still prefer to wait until 20 min (or later, such as F+30 or Fmax, a protocol in which the diuretic is not given until CS activity appears to have reached a maximum) after radiopharmaceutical administration to give the furosemide, whereas others have created additional protocol variants, such as F+2, F+5, and F+10, all of which likely provide diagnostic results in a large percentage of cases (10). Hence, it is still a matter of institutional and provider preference as to which approach is best for their patients. This preference is reflected in current practice patterns, with a total of 34 different approaches to the timing of diuretic administration in use among 107 sites undergoing genitourinary imaging accreditation with the IAC (24). That said, most of these sites (56%) use 1 of 5 approaches, F=0, F+10, F+15, F+20, or F+30, with the F+20 approach being most common (21% of sites).

One final note on the subject is that recently, there has been increasing interest in a variation termed F+10sp, which performs the examination with the patient in the seated position (sp) instead of supine as recommended in the guidelines. The seated position was used in the original 1978 F+20 studies introducing DRS but was changed to supine positioning as the test became widely adopted to reduce patient movement and avoid the risk of a fall secondary to potential diuresis-induced hypotension (42,43). The seated position takes into account the recognized importance of gravity assistance for the physiologic drainage of urine from a dilated CS.

ACQUISITION

For either ^{99m}Tc-MAG3 or ^{99m}Tc-DTPA, images from γ-cameras with a large field of view (400 mm) are ideally obtained with a low-energy all-purpose collimator or, as an acceptable alternative, a low-energy high-resolution collimator (20). A low-energy all-purpose collimator is preferred because, despite the slightly lower resolution, the higher counting rates result in reduced noise for quantitative measurements, particularly when using small cortical regions of interest (ROIs) (10).

Current guidelines and parameters recommend that the patient be positioned supine with the camera at the patient's back, to take advantage of the typically posterior position of native kidneys. However, for a transplanted pelvic kidney, the camera should instead be anterior (10,20). Given that drainage of a dilated CS may be delayed in this position,
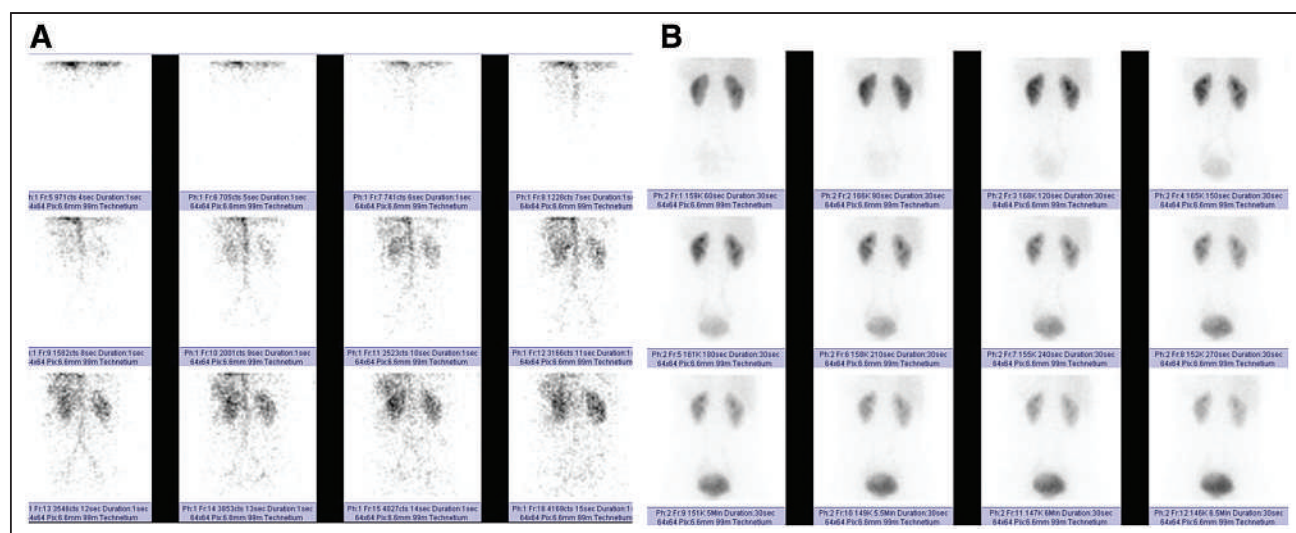
FIGURE 3. (A) First-minute blood flow phase with frames acquired every second (first 12 s displayed). (B) Dynamic phase with frames acquired every 30 s (minutes 2–7 displayed). Phase is helpful for assessing both parenchymal function and urine drainage.

even in the absence of obstruction, there is renewed interest in performing the examination with the patient seated to allow gravity to assist (44). Nevertheless, only 1 of the 107 sites undergoing nuclear medicine genitourinary accreditation at the end of 2018 used the seated position (4).

One topic of debate is how to address nephroptosis, a condition in which a native kidney drops into the pelvis when the patient is standing, potentially resulting in a transient obstruction. This finding has been observed in up to 22% of individuals referred for DRS and may negatively impact both the measured relative function and the CS drainage of the ptotic kidney, depending on the position used during imaging (45). Thus, 2 examinations of the patient—supine and seated—might be best in this scenario.

When DRS begins, the first minute of imaging is typically acquired using 1- to 3-s images to assess renal arterial flow (Fig. 3A). Starting with minute 2, all subsequent images are acquired for 15–60 s and are used to evaluate the parenchymal function and urine outflow from the CS (Fig. 3B). This technique can be performed as either a single or a 2-phase acquisition, depending on the timing of diuretic administration. Traditionally, if the diuretic is given before or simultaneously with the radiopharmaceutical, a single acquisition is used. If the diuretic is administered 20 min or later into the study, the acquisition is typically 2 separate phases based on the Santa Fe consensus (10). The first acquisition is performed for 20–30 min without diuretic augmentation; afterward, the patient stands or walks for a while and then voids. If the baseline study is suggestive of obstruction, the intravenous diuretic is given and an additional 20 min of imaging is performed (Fig. 4) (16).

Although imaging of renal perfusion using 1- to 3-s images of the initial radiopharmaceutical bolus as it transits the aorta and renal arteries is typical, it has not been demonstrated to provide useful information for interpretation of DRS. Therefore, experts agree that this traditional protocol component can be omitted, simplifying both interpretation and reporting while also lowering administered activity (28).

CS emptying can be delayed in the absence of obstruction when the patient is supine. A postvoid image is recommended by both the SNMMI–EANM guideline and the American College of Radiology–Society of Pediatric Radiology parameter to account for this delay. The image is obtained after the patient stands, ambulates for 5 min, and then voids before getting back into the supine position for this final image. The image should be acquired using the same interval (15–60 s) as the previous images to optimize comparison (10). Some experts consider measurement of the voided urine volume helpful. At least 200 mL of urine produced over a 20-min acquisition and 300 mL over a 30-min acquisition indicate adequate hydration and response to the diuretic (44). Despite the simple nature of
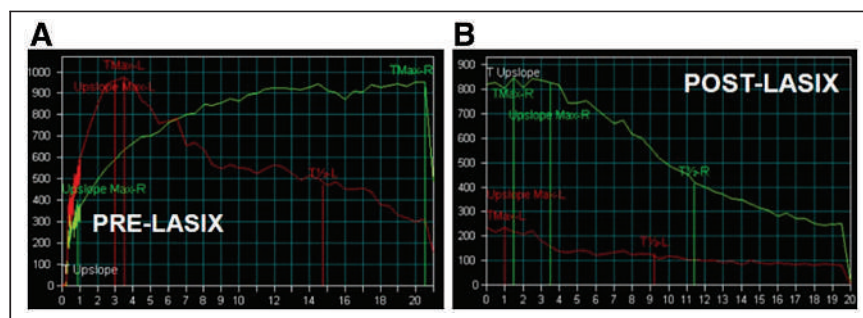
FIGURE 4. Dual-phase acquisition. (A) First 20 min of findings for right kidney are concerning for obstruction, necessitating diuretic administration. (B) Postdiuretic T-$\frac{1}{2}$ of slightly less than 10 min excludes obstruction. Green curve = right kidney; red curve = left kidney; Lasix (Aventis Pharma) = furosemide.

this potentially helpful adjunct, none of the facilities undergoing IAC accreditation during the cycle ending in 2018 included this step in their adult DRS protocol (*24*).

PROCESSING

Time–activity curves are generated by placing ROIs around all or portions of the kidneys. The whole-kidney (WK) ROI, which includes all of the renal parenchyma and pelvis, is necessary to assess relative function accurately. It may also be used to evaluate other parameters such as time-to-peak (Tpeak—the time from baseline to maximum activity in the WK ROI), T-$\frac{1}{2}$ emptying (the time for activity in the ROI to decrease by 50% from Tpeak), and 20-min/max (the percentage of activity remaining 20 min after Tpeak) (Fig. 5A). Because this curve is affected by activity in both the parenchyma and the pelvis, an abnormality in one can give the perception of an abnormality in another. As such, a diseased cortex as seen with chronic renal failure from disorders such as hypertension or glomerulonephritis can lead to a prolonged T-$\frac{1}{2}$ emptying in the absence of urine outflow obstruction, whereas stasis of activity in a dilated CS may result in a spuriously high 20-min/max and the appearance of cortical dysfunction.

To address problems from the WK ROI, additional ROIs may be created explicitly encompassing the renal cortex or the CS, and their subsequent time–activity curves can be used for analysis. The cortical ROI is created by delineating the cortex while excluding any activity in the pelvis and calyces, making it optimal for assessing parenchymal function parameters such as Tpeak and renal retention (Fig. 5B). In contrast, the CS ROI is limited to outlining the pelvis and calyces and has been shown to allow for more accurate measurement of T-$\frac{1}{2}$ emptying than the WK ROI (Fig. 5C) (*46*).

The relative function (also called the differential renal function or split function) is the percentage of renal function performed by each kidney in relation to the overall function. It is relative since it does not indicate the absolute function of each kidney (mL/min), just the percentage. Hence, a kidney with 50% renal function may be healthy but could also be poorly functioning in cases of bilateral medical renal disease, such as frequently seen with long-standing diabetes. Therefore, some facilities choose to combine the DRS examination with a plasma- or camera-based clearance measurement, such as the Christensen and Groth iterative method (single-sample plasma method) or the Gates method (camera-based method for ^{99m}Tc-DTPA) (*47,48*). The relative function is measured by 1 of 2 methods: either by placing a WK ROI over each kidney and measuring the integral of the counts between 1 and 2 min, 1 and 2.5 min, or 2 and 3 min after injection of the radiopharmaceutical (deconvolution method) or by using a technique called the Rutland method, which results in a Rutland–Patlak plot. Details and advantages of these techniques are provided in the consensus report by the Scientific Committee of Radionuclides in Nephrourology (*9*). In the integral method, if the diuretic is administered at the same time as the radiopharmaceutical, the 1- to 2-min or 1- to 2.5-min periods are preferred to minimize the possibility that activity will already have drained into the ureters and bladder and thus not be included in the WK ROI measurements, since asymmetric CS emptying would artifactually skew the results (*10*).

A background correction needs to be performed to correct for activity in the ROIs that is not actually in the kidney but in the blood, interstitial spaces, and tissues superficial and deep to the kidney. A separate background ROI is created beside each kidney ROI and is then normalized to account for the differences in size. The SNMMI–EANM guideline states that a perirenal background ROI, either C-shaped around most of the kidney or reniform-shaped and completely surrounding the WK ROI, 2 pixels in thickness, and 1 pixel away from the WK ROI to reduce scatter, is preferred over background rectangular or triangular shaped ROIs superior, medial, or inferior to the WK ROI (Fig. 5) (*49*). Fortunately, automated background assignments are an acceptable approach that reduces processing time and enhances reproducibility (*10*). When automated background assignments are used, it is important to review the location of the ROIs to ensure that an ROI is not drawn outside the body.

Before quantification, it is important to qualitatively evaluate the time–activity curve to assess for possible obstruction, nonobstruction, or other renal pathology. A standard, nonobstructed, time–activity curve demonstrates a rapid uptake phase based on the renal vascular supply and then a concentration and cortical transit phase, followed by an exponential excretion phase through the renal CS (left kidney in Fig. 4A). Obstruction can be suspected if a time–activity curve flattens after the peak, continues to rise throughout the time–activity curve (right kidney in Fig. 4B), or demonstrates an incomplete or delayed return to baseline. The qualitative analysis should always accompany the quantitative analysis to ensure fidelity.
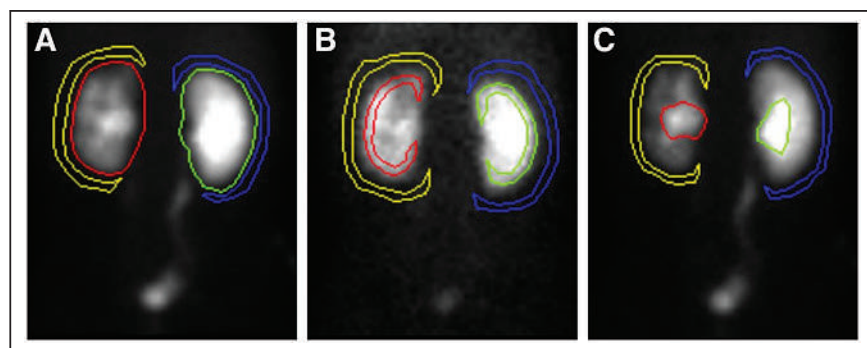
FIGURE 5. Kidney and background ROI techniques. (A) WK ROI with perirenal background. (B) Cortical ROI with perirenal background. (C) CS ROI with perirenal background. Yellow = left kidney background; red = left kidney; green = right kidney; blue = right kidney background.
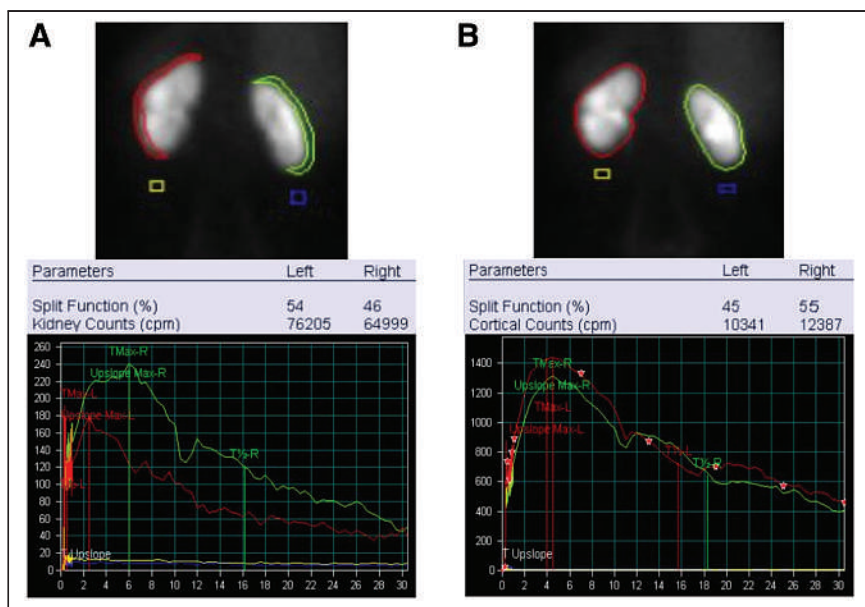
FIGURE 6. Cortical vs. WK for determination of relative function. (A) Cortical ROIs, calculated relative (split) function, and cortical time–activity curves. (B) WK ROIs, calculated relative (split) function, and WK time–activity curves. Cortical data incorrectly show right kidney to have decreased function compared with left, 46% vs. 54%. Correct data are shown by WK data, with right kidney having greater function than left, 55% vs. 45%, difference of 9%. Also note, a crescent shaped background region of interest is preferred over square background region (yellow and blue).

QUANTIFICATION

Although the shape of the time–activity curves created from the WK ROI, and cortical or CS ROIs, if used, are central to the accurate assessment of DRS, several quantitative values have been recognized as helpful in determining obstruction and risk of future renal function decline.

Relative function is a measure of what percentage of the total renal function is performed by each kidney. It is calculated by comparing the area under the left and right WK time–activity curves from anywhere between 1 and 3 min, with the 1- to 2-min and 30-s intervals preferred. If the measurement is made after a significant amount of activity has passed into the ureter or bladder, the relative uptake measurement may be skewed because the initial amount of urine drainage from each kidney may not be proportional (10). Normal values are between 45% and 55%, but many physicians allow for greater variability and consider 40%–60% the upper limit of normal for relative function. It is important to avoid the pitfall of using the cortical data for this measurement. Although cortical ROIs are optimal for other parenchymal assessments, they do not include the entire parenchyma and thus could artificially skew the results because of ROI asymmetry (Fig. 6).

Tpeak is a marker of parenchymal function. It should occur no later than 5 min after injection of the radiotracer for either ^{99m}Tc-MAG3 or ^{99m}Tc-DTPA, whether derived from the WK or the cortical ROI. One source of error is that this value is often derived automatically, with the software assigning it on the basis of the time of the highest point of the time–activity curve. However, there are often significant errors in the first minute of the time–activity curve during the flow-phase acquisition because of the very short acquisitions (1–3 s each), which are highly prone to motion artifacts. Hence, the time–activity curve and derived Tpeak should be reviewed and corrected appropriately (Fig. 7).

A second marker of parenchymal function is 20-min/max. No more than 35% of the activity should be remaining 20 min after Tpeak, as measured using the cortical ROI (50). A known pitfall is to calculate the value using the time point 20 min after the start of the examination instead of 20 min after Tpeak, leading to a spuriously high value.

T-$1/2$ emptying is an assessment of how quickly activity is leaving the CS. It is ideally obtained using the CS ROI but may also be accurately obtained from the WK ROI in the absence of significant parenchymal dysfunction. There is wide agreement that a value of no more than 10–15 min excludes obstruction (51). That said, a prolonged T-$1/2$ emptying is not diagnostic of obstruction given the other factors that may negatively impact this value (dehydration, poor renal function, severe hydronephrosis, and the presence of significant backpressure from a full or noncompliant bladder).

Additional Measures

In addition to the values discussed above, some supplementary values are recommended by the guidance documents of
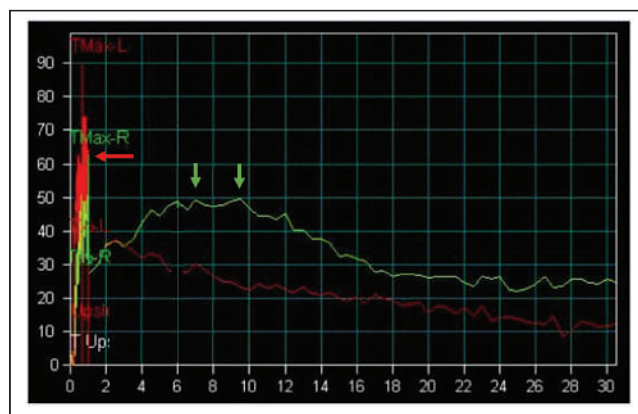
FIGURE 7. Extensive motion artifact involving first minute of time–activity curve representing flow phase acquired at 1 s per frame. This results in erroneous elevated value at 1 min due to ROIs overlapping vascular activity in liver and spleen (red arrow). Actual right kidney Tpeak is delayed (>5 min) in 7- to 9-min range (green arrows).

the SNMMI–EANM and International Scientific Committee of Radionuclides in Nephrourology for a more robust DRS interpretation (*10,44*). However, these values were assessed using specific protocols for the timing of the diuretic injection in relation to radiopharmaceutical administration. Thus, they cannot be universally applied to all approaches.

Postvoid kidney-to-maximum count is a simple ratio that incorporates gravity into the emptying assessment and provides valuable information. After the acquisition, the patient stands, walks, and then voids. Then, typically at 30 min after administration of the radiopharmaceutical, a supine 1-min postvoid image is acquired, and the postvoid counts in the WK or CS ROI of the kidney of concern are divided by the maximum counts normalized for time (*50*). In a study of 18 variables by Bao et al. at Emory, this value was most helpful for excluding obstruction (*46*).

Tissue transit time (also called parenchymal transit time) is based on the fact that urine outflow obstruction negatively affects the function of the nephrons (obstructive nephropathy). This impairment of nephron function results in slow transit of the radiotracer through the tissue. Although a prolonged tissue transit time is not specific for obstruction, it increases the likelihood that obstruction is present (*10*). The simplest method for determining tissue transit time is visual assessment based on the appearance of activity in the CS, which should occur within 5 min of the radiopharmaceutical injection. Appearance at 8 min or more is considered delayed (*52,53*).

Output Efficiency and Normalized Residual Activity

Even with these parameters, diseased kidneys with a suboptimal response to diuretics are still a diagnostic challenge, because the shape of the parenchymal phase influences the shape of the CS-emptying phase of the time–activity curve.

Output efficiency was developed as a metric to help overcome the negative effect that impaired renal function has on the perceived CS drainage. Output efficiency allows for an evaluation of the amount of activity remaining in the kidney as a percentage of what entered the kidney and is derived using the integral of the heart activity curve. A value of at least 82% has been shown as normal in a study of healthy individuals, though results are protocol-specific (*18,54*).

Given the relative complexity of determining the output efficiency and the need for specific processing software, a more simplified approach was developed with normalized residual activity. Normalized residual activity is simply a measurement of the renal activity at a given 1-min interval divided by the renal activity at 1–2 min after radiopharmaceutical injection (*55*). A value of less than 1.0 when comparing the 1- to 2-min interval with the 20- to 21-min interval or a value of less than 0.10 when using the 1-min interval acquired after voiding at 60 min from the examination start represents good renal drainage (*56*). Unfortunately, this technique lacks standardization and appears to be influenced more by renal function and background selection than by output efficiency. It also necessitates an accurate assessment of when the radiopharmaceutical reaches the kidneys (*57*).

Despite their diagnostic utility, output efficiency and normalized residual activity have not yet entered routine clinical practice. Neither variable appeared in the 174 adult DRS reports reviewed in a survey of IAC-accredited facilities (*24*).

CONCLUSION

DRS plays a critical diagnostic role by providing a physiologic means for differentiating between obstructive and nonobstructive hydronephrosis and by assessing the function of the affected kidney. The examination accuracy is highly dependent on and benefits from close attention to patient preparation, timing of diuretic, method of acquisition, processing, quantification, and interpretation criteria. Until standardized guidelines exist, it is critical for facilities to ensure application of a consistent high-quality approach that best meets the diagnostic needs of the referring providers and allows for accurate follow-up and comparison of results.

DISCLOSURE

Mary Beth Farrell is an employee of the IAC. No other potential conflict of interest relevant to this article was reported.

REFERENCES

1. Pouliot F, Lebel MH, Audet JF, Dujardin T. Comparative analysis of scintigraphic and clinical criteria to determine success after laparoscopic pyeloplasties. *J Urol.* 2008;179:284–285.
2. Itoh K. ⁹⁹ᵐTc-MAG3: review of pharmacokinetics, clinical application to renal diseases and quantification of renal function. *Ann Nucl Med.* 2001;15:179–190.
3. Jaffe RB, Middleton AW. Whitaker test: differentiation of obstructive from nonobstructive uropathy. *AJR.* 1980;134:9–15.
4. Whitaker RH. Diagnosis of obstruction in dilated ureters. *Ann R Coll Surg Engl.* 1973;53:153–166.
5. Koff SA, Thrall JH, Keyes JW Jr. Diuretic radionuclide urography: a noninvasive method for evaluating nephroureteral dilatation. *J Urol.* 1979;122:451–454.
6. O'Reilly PH, Lawson RS, Shields RA, Testa HJ. Idiopathic hydronephrosis: the diuresis renogram—a new noninvasive method of assessing equivocal pelvioureteral junction obstruction. *J Urol.* 1979;121:153–155.
7. Powers TA, Grove RB, Bauriedel JK, Orr SC, Melton RE, Bowen RD. Detection of obstructive uropathy using ⁹⁹ᵐtechnetium diethylenetriaminepentaacetic acid. *J Urol.* 1980;124:588–592.
8. Fritzberg AR, Kasina S, Eshima D, Johnson DL. Synthesis and biological evaluation of technetium-99m MAG3 as a Hippuran replacement. *J Nucl Med.* 1986;27:111–116.
9. Prigent A, Cosgriff P, Gates GF, et al. Consensus report on quality control of quantitative measurements of renal function obtained from the renogram: International Consensus Committee from the Scientific Committee of Radionuclides in Nephrourology. *Semin Nucl Med.* 1999;29:146–159.
10. Taylor AT, Brandon DC, De Palma D, et al. SNMMI procedure standard/EANM practice guideline for diuretic renal scintigraphy in adults with suspected upper urinary tract obstruction 1.0. *Semin Nucl Med.* 2018;48:377–390.
11. Furosemide (Lasix): drug monograph. Evidence-Based Medicine Consult website. https://www.ebmconsult.com/articles/drug-monograph-furosemide-lasix. accessed August 17, 2022.
12. Brater DC. Diuretic therapy. *N Engl J Med.* 1998;339:387–395.
13. Hunsche A, Press H, Taylor A. Increasing the dose of furosemide in patients with azotemia and suspected obstruction. *Clin Nucl Med.* 2004;29:149–153.
14. Voelker JR, Cartwright-Brown D, Anderson S, et al. Comparison of loop diuretics in patients with chronic renal insufficiency. *Kidney Int.* 1987;32:572–578.
15. Felker GM. Diuretic management in heart failure. *Congest Heart Fail.* 2010;16(suppl 1):S68–S72.
16. O'Reilly PH, Aurell M, Britton K, et al. Consensus on diuresis renography for investigating the dilated upper urinary tract. *J Nucl Med.* 1996;37:1872–1876.

17. Cosenza NN, Lau F, Lima MCL, et al. Influence of bladder fullness on the detection of urinary tract obstruction by dynamic renal scintigraphy. *Radiol Bras.* 2017; 50:237–243.

18. Eskild-Jensen A, Gordon I, Piepsz A, Frakiaer J. Interpretation of the renogram: problems and pitfalls in hydronephrosis in children. *BJU Int.* 2004;94:887–892.

19. Jones DA, Lupton EW, George NJ. Effect of bladder filling on upper tract urodynamics in man. *Br J Urol.* 1990;65:492–496.

20. Kim CK, Becker MD, Biyyam DR, et al. ACR-SPR practice parameter for the performance of renal scintigraphy. American College of Radiology website. https://www.acr.org/-/media/ACR/Files/Practice-Parameters/RenalScint.pdf. Published 1995. Revised 2017. Accessed August 17, 2022.

21. Taylor A Jr, Clark S, Ball T. Comparison of Tc-99m MAG3 and Tc-99m DTPA scintigraphy in neonates. *Clin Nucl Med.* 1994;19:575–580.

22. Eshima D, Taylor A Jr. Technetium-99m (^{99m}Tc) mercaptoacetyltriglycine: update on the new ^{99m}Tc renal tubular function agent. *Semin Nucl Med.* 1992;22:61–73.

23. Parikh KR, Davenport MS, Viglianti BL, Hubers D, Brown RK. Cost-savings analysis of renal scintigraphy, stratified by renal function thresholds: mercaptoacetyltriglycine versus diethylene triamine penta-acetic acid. *J Am Coll Radiol.* 2016;13: 801–811.

24. Banks KP, Farrell MB, Peacock JG, Costello M, Gordon LL. Diuretic renal scintigraphy: the state of practice and a potential opportunity for standardization. *J Am Coll Radiol.* 2021;18:1556–1563.

25. Gordon I, Piepsz A, Sixt R; Auspices of Paediatric Committee of European Association of Nuclear Medicine. Guidelines for standard and diuretic renogram in children. *Eur J Nucl Med Mol Imaging.* 2011;38:1175–1188.

26. Shulkin BL, Mandell GA, Cooper JA, et al. Procedure guideline for diuretic renography in children 3.0. *J Nucl Med Technol.* 2008;36:162–168.

27. el Maghraby TA, van Eck-Smit BL, de Fijter JW, et al. Quantitative scintigraphic parameters for the assessment of renal transplant patients. *Eur J Radiol.* 1998;28: 256–269.

28. Taylor AT, Folks RD, Rahman AKMF, et al. ^{99m}Tc-MAG3: image wisely. *Radiology.* 2017;284:200–209.

29. Banks KP, Farrell MB, Peacock JG, Costello M, Gordon LLUS. Diagnostic reference levels (DRLs) and achievable administered activities (AAAs) for adult renal scintigraphy: an analysis of the Intersocietal Accreditation Committee (IAC) nuclear laboratories. *J Nucl Med Technol.* 2021;49:246–249.

30. Ellison DH, Felker GM. Diuretic treatment in heart failure. *N Engl J Med.* 2017; 377:1964–1975.

31. Upsdell SM, Leeson SM, Brooman PJ, O'Reilly PH. Diuretic-induced urinary flow rates at varying clearances and their relevance to the performance and interpretation of diuresis renography. *Br J Urol.* 1988;61:14–18.

32. Zubeldia JM, Joo KG, Baeumler GR. Mannitol as an alternative to furosemide in Tc-99m MAG3 diuretic renography. *Clin Nucl Med.* 2000;25:554–556.

33. Nguyen BD, Roarke MC, Young JR, Yang M, Osborn HH. Diuretic renal scintigraphy in patients with sulfonamide allergies: possible alternative use of ethacrynic acid. *J Nucl Med Technol.* 2015;43:239–241.

34. Wang Y. Safety of administering furosemide during nuclear diuretic renography in patients with sulfonamide allergies. *AJR.* 2018;210:866–868.

35. Lee AG, Anderson R, Kardon RH, Wall M. Presumed "sulfa allergy" in patients with intracranial hypertension treated with acetazolamide or furosemide: cross-reactivity, myth or reality? *Am J Ophthalmol.* 2004;138:114–118.

36. Conway JJ, Maizels M. The "well tempered" diuretic renogram: a standard method to examine the asymptomatic neonate with hydronephrosis or hydroureteronephrosis—a report from combined meetings of the Society for Fetal Urology and members of the Pediatric Nuclear Medicine Council–the Society of Nuclear Medicine. *J Nucl Med.* 1992;33:2047–2051.

37. Taghavi R, Ariana K, Arab D. Diuresis renography for differentiation of upper urinary tract dilatation from obstruction: F+20 and F-15 methods. *Urol J.* 2007;4:36–40.

38. English PJ, Lawson RS, Carroll RNP, Edwards EC. Modified method of diuresis renography for the assessment of equivocal pelviureteric junction obstruction. *Br J Urol.* 1987;59:10–14.

39. Brown SCW, Upsdell SM, O'Reilly PH. The importance of renal function in the interpretation of diuresis renography. *Br J Urol.* 1992;69:121–125.

40. Türkölmez S, Atasever T, Turkolmez K, Gogus O. Comparison of three different diuretic renal scintigraphy protocols in patients with dilated upper urinary tracts. *Clin Nucl Med.* 2004;29:154–160.

41. Liu Y, Ghesani NV, Skurnick JH, Zuckier LS. The F + 0 protocol for diuretic renography results in fewer interrupted studies due to voiding than the F - 15 protocol. *J Nucl Med.* 2005;46:1317–1320.

42. O'Reilly PH, Testa HJ, Lawson RS, Farrar DJ, Edwards EC. Diuresis renography in equivocal urinary tract obstruction. *Br J Urol.* 1978;50:76–80.

43. Tartaglione G, Townsend DM, Bassi PF, Bolton RCD, Giammarile F, Rubello D. Diuresis renography in equivocal urinary tract obstruction: a historical perspective. *Biomed Pharmacother.* 2019;116: 108981.

44. Taylor AT. Radionuclides in nephrourology, part 2: pitfalls and diagnostic applications. *J Nucl Med.* 2014;55:786–798.

45. Tartaglione G, D'Addessi A, De Waure C, et al. ^{99m}Tc-MAG3 diuretic renography in diagnosis of obstructive nephropathy in adults: a comparison between F+10(sp) and a new procedure F+10(sp) in seated position. *Clin Nucl Med.* 2013;38:432–436.

46. Bao J, Manatunga A, Binongo JN, Taylor AT. Key variables for interpreting ^{99m}Tc-mercaptoacetyltriglycine diuretic scans: development and validation of a predictive model. *AJR.* 2011;197:325–333.

47. Blaufox MD, Aurell M, Bubeck B, et al. Report of the Radionuclides in Nephrourology Committee on renal clearance. *J Nucl Med.* 1996;37:1883–1890.

48. Bocher M, Shrem Y, Tappiser A, et al. Tc-99m mercaptoacetyltriglycine clearance: comparison of camera-assisted methods. *Clin Nucl Med.* 2001;26:745–750.

49. Taylor A, Thakore K, Folks R, Halkar R, Manatunga A. Background subtraction in technetium-99m-MAG3 renography. *J Nucl Med.* 1997;38:74–79.

50. Esteves FP, Taylor A, Manatunga A, Folks RD, Krishnan M, Garcia EV. ^{99m}Tc-MAG3 renography: normal values for MAG3 clearance and curve parameters, excretory parameters, and residual urine volume. *AJR.* 2006;187:W610–W617.

51. Mettler FA. *Essentials of Nuclear Medicine Imaging.* 6th ed. Saunders; 2012:315.

52. Durand E, Blaufox MD, Britton KE, et al. International Scientific Committee of Radionuclides in Nephrourology (ISCORN) consensus on renal transit time measurements. *Semin Nucl Med.* 2008;38:82–102.

53. Schlotmann A, Clorius JH, Clorius SN. Diuretic renography in hydronephrosis: renal tissue tracer transit predicts functional course and thereby need for surgery. *Eur J Nucl Med Mol Imaging.* 2009;36:1665–1673.

54. Chaiwatanarat T, Padhy AK, Bomanji JB, et al. Validation of renal output efficiency as an objective quantitative parameter in the evaluation of upper urinary tract obstruction. *J Nucl Med.* 1993;34:845–848.

55. Piepsz A, Tondeur M, Ham H. NORA: a simple and reliable parameter for estimating renal output with or without furosemide challenge. *Nucl Med Commun.* 2000; 21:317–323.

56. Piepsz A, Kuyvenhoven JD, Tondeur M, Ham H. Normalized residual activity: usual values and robustness of the method. *J Nucl Med.* 2002;43:33–38.

57. Piepsz A, Nogarède C, Tondeur M. Is normalized residual activity a good marker of renal output efficiency? *Nucl Med Commun.* 2011;32:824–828.

Diuretic Renal Scintigraphy

Mary Beth Farrell, Kevin P. Banks, and Justin G. Peacock

RATIONALE/INTRODUCTION

Hydronephrosis can be caused by obstruction or by nonobstructive disorders such as infection, vesicoureteral reflux, or congenital anomalies. Diuretic renal scintigraphy is critical in differentiating between obstructive and nonobstructive hydronephrosis. Under physiologic conditions, urine may pool in the renal pelvis during hydronephrosis because there is an anatomic obstruction or because of the reservoir effect, in which urine remains in the dilated renal pelvis until enough accumulates to spill over into the ureter. During diuretic administration, the resultant high flow condition can overcome the reservoir effect. The presence of obstruction can be assessed by evaluating the washout of radiopharmaceutical from the collecting system and assessing parenchymal function.

INDICATIONS

- Evaluation of obstructive renal nephropathy.
- Evaluation of hydronephrosis.
- Differentiation between obstructive hydronephrosis and nonobstructive collecting system dilation.

CONTRAINDICATIONS/TECHNICAL CONSTRAINTS

- Pregnancy/breastfeeding (pregnancy must be excluded in accordance with local institutional policy; if the patient is breastfeeding, appropriate radiation safety instructions should be provided).
- A recent nuclear medicine study (radiopharmaceutical-dependent).
- Furosemide (contraindicated in anuric or dehydrated patients).

PATIENT PREPARATION/EDUCATION

- The patient may eat and take medications as necessary before the study.
- The patient should be well hydrated and instructed to increase fluid intake the day before and morning of the study. Thirty minutes to 1 h before the study, the patient should drink an additional 500 mL (16 oz) of water. Children should receive intravenous hydration with a 10- to 15-mL/kg volume of normal saline over 30 min (5% dextrose for patients younger than 1 y).

- Diuretics should be discontinued 24 h before the study.
- A focused history containing the following elements should be obtained:
  - Past medical history, including diabetes, hypertension, kidney disease (urinary tract infections, calculi, renal surgery, stents), and autoimmune disease.
  - Signs and symptoms.
  - Current medications, especially the chronic use of diuretics.
  - The results of clinical laboratory tests, including serum creatinine or estimated glomerular filtration rate.
  - The results of other diagnostic tests, including ultrasonography, MRI, and CT (including contrast administration).
  - Fluid input and output.

RADIOPHARMACEUTICAL IDENTITY, DOSE, AND ROUTE OF ADMINISTRATION

Table 1 provides the radiopharmaceutical identity, dose, and route of administration.

ACQUISITION PARAMETERS: DYNAMIC/STATIC/PLANAR

Table 2 provides the dynamic, static, and planar acquisition parameters

ACQUISITION INSTRUCTIONS

- Instruct the patient to void immediately before the study to reduce the possibility of patient motion or of the need to terminate the study prematurely. Voiding also minimizes the backpressure effect of a distended bladder, which may slow draining of the upper urinary tracts.
- Position the patient supine on the imaging table with the camera in the posterior position, ensuring that the kidneys and bladder are in the field of view.
- Administer the radiopharmaceutical intravenously as a bolus, and begin imaging when the activity is about to enter the abdominal aorta.
- Acquire immediate blood flow images at 2–4 s/frame for 60–120 s to assess renal arterial flow.
- Acquire serial sequential images at 1–2 min/frame for 20–30 min to evaluate parenchymal function and urine outflow from the collecting system.
- On the basis of the Santa Fe consensus, have the patient stand and walk around for a few minutes,

TABLE 1
Radiopharmaceutical Identity, Dose, and Route of Administration

Identity	Dose	Route of administration
^{99m}Tc-MAG3 (recommended) or …	74 MBq (2 mCi); range: 37–185 MBq (1–5 mCi)	Intravenous
^{99m}Tc-diethylenetriamine pentaacetic acid	185 MBq (5 mCi); range: 185–370 MBq (5–10 mCi)	Intravenous
Pediatric dose: ^{99m}Tc-MAG3	Without flow study: 3.7 MBq/kg (0.10 mCi/kg); with flow study: 5.55 MBq/kg (0.15 mCi/kg); minimum administered activity: 37 MBq (1.0 mCi); maximum administered activity: 148 MBq (4 mCi)	Intravenous
Furosemide (based on creatinine level; mg/dL)		Intravenous
1.0	20 mg	
>1.5	40 mg	
2.0	60 mg	
3.0	80 mg	
Pediatric dose: furosemide	1 mg/kg to maximum of 40 mg	Intravenous

MAG3 = mercaptoacetyltriglycine.
^{99m}Tc-MAG3 is preferred tracer in patients with known impaired renal function.

followed by voiding of the bladder. The furosemide is then administered over 1–2 min by slow intravenous injection at the start of an additional 20-min acquisition at 1–2 min/frame.
- Obtain a prevoid and postvoid kidney and bladder 60-s image; an erect postvoid image is optional.

COMMON OPTIONS

If the patient is unable to void, bladder catheterization may be required. Increased bladder pressure may diminish the effect of the diuretic.

PROCESSING INSTRUCTIONS
- Draw regions of interest around the entire kidney and pelvis. Draw additional C-shaped perirenal

background regions 2 pixels thick and 1 pixel away from the whole kidney region (Fig. 1).
- Generate time–activity curves.
- Calculate the collection system clearance half-time or washout half-time (T$\frac{1}{2}$). T$\frac{1}{2}$ may be measured from the time the diuretic is given to the time it takes to reach half the original level. Computer quantitative software can more precisely calculate T$\frac{1}{2}$ by fitting a curve to the steepest portion of the washout time–activity curve. Normally, a T$\frac{1}{2}$ of less than 10 min indicates that no obstruction is present.
- Use the automatic software to calculate relative function (if available), which is the percentage of the total function of both kidneys. It is calculated by

TABLE 2
Acquisition Parameters: Dynamic/Static/Planar

Parameter	Characteristics	Standard/optional/preferred
Camera type	Large-field-of-view γ-camera	Standard
Energy peak	140 keV	Standard
Energy window	20%	Standard
Collimator	Low-energy, all-purpose, or low-energy, high resolution	Standard
Patient position	Supine	Standard
Camera position	Posterior	Standard
Injection-to-imaging time	Immediately on injection	Standard
Acquisition type	Dynamic	Standard
	Static	Standard
Views	Posterior	Standard
Additional views	Prevoid and postvoid supine kidneys and bladder	Standard
	Postvoid erect image	Optional
Matrix	128 × 128	Standard
Number of views	2–3	Standard
Time per view	Dynamic: 2–4 s/frame for 60–120 s and then 1–2 min/frame for 30 min	Standard
Additional view time per projection	Static: 500,000 to 1 million counts	Standard
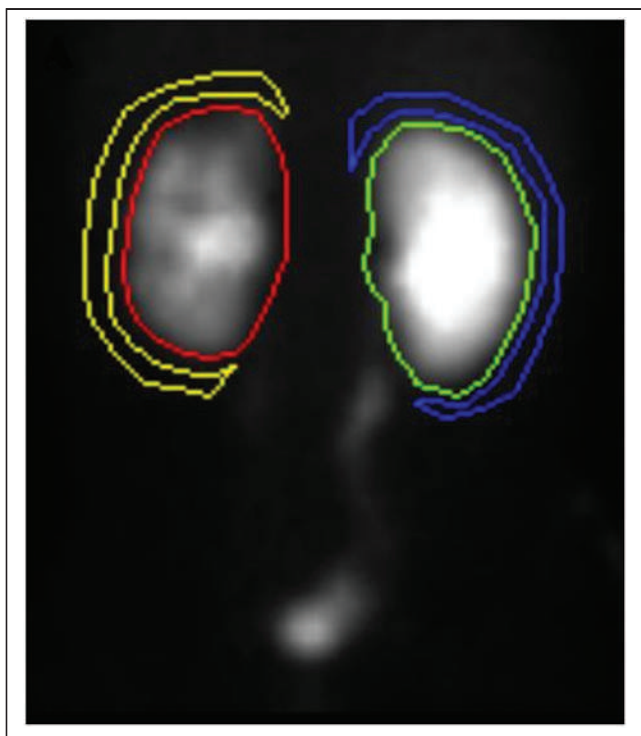
FIGURE 1. Whole kidney region of interest with perirenal background region. Yellow = left kidney background; red = left kidney; green = right kidney; blue = right kidney background.

comparing the area under the curve for both kidneys between the 1- and 3-min intervals. Normal values are between 45% and 55%.

- Sum the dynamic images, and display them for optimal visualization of the area of interest.
- Scale planar images to accurately visualize areas of normal anatomy and increased uptake.

PRECAUTIONS

Caution should be used when furosemide is given to patients who have just undergone urologic surgery, because of the increased urine flow rate.

SUGGESTED READING

1. Banks K, Farrell M, Peacock J. Diuretic renal scintigraphy protocol considerations. *J Nucl Med Technol.* May 24, 2022 [Epub ahead of print].
2. Mettler FA, Guiberteau MJ. *Essentials of Nuclear Medicine Imaging.* 5th ed. Saunders Elsevier; 2006:304–305, 539–540.
3. Shackett P. *Nuclear Medicine Technology and Techniques: Procedures and Techniques.* 2nd ed. Lippincott Williams & Wilkins; 2009:249–253.
4. Sharma A, Younglove SM. Genitourinary system. In: Waterstram-Rich KM, Gilmore D, eds. *Nuclear Medicine and PET/CT Technology and Techniques.* 8th ed. Mosby Elsevier; 2017:567–569.
5. Taylor A, Schuster DM, Alazraki N. *A Clinician's Guide to Nuclear Medicine.* 2nd ed. Society of Nuclear Medicine and Molecular Imaging; 2006:52–53.
6. Ziessman HA, O'Malley JP, Thrall JH, Fahey FH. *The Requisites: Nuclear Medicine.* 4th ed. Elsevier Saunders; 2014:168–203.
7. Taylor AT, Brandon DC, De Palma D, et al. SNMMI procedure standard/EANM practice guideline for diuretic renal scintigraphy in adults with suspected upper urinary tract obstruction 1.0. *Semin Nucl Med.* 2018;48:377–390.

Accuracy of ^{123}I-Sodium Thyroid Imaging in Calculating Thyroid Volume

Christopher Fecca[1], Jee Moon[2], David Posocco[1], Huaqing Zhao[1], and Simin Dadparvar[2]

[1]Lewis Katz School of Medicine, Philadelphia, Pennsylvania; and [2]Division of Nuclear Medicine and Molecular Imaging, Department of Radiology, Temple University Hospital, Philadelphia, Pennsylvania

Hyperthyroidism is often managed with radioactive iodine therapy. The dose of ^{131}I administered to the patient is based on the calculated size of the thyroid gland in grams and 24-h iodine uptake. Ultrasonography is a validated modality for determination of thyroid volume. Though necessary for assessing the degree of ^{123}I uptake, nuclear scintigraphy also allows for estimating thyroid volume. Here we compare volume measurements calculated on the basis of ultrasonography and nuclear scintigraphy in a cohort of hyperthyroid patients. **Methods:** This prospective study was designed to evaluate 110 consecutive hyperthyroidism patients who were undergoing thyroid ultrasonography and ^{123}I scintigraphy. Scintigraphy was performed after oral administration of approximately 11 MBq of ^{123}I-sodium, and uptake at 2 and 24 h was measured. At 24 h, thyroid scintigraphy was performed using a nuclear medicine camera with a low-energy high-resolution collimator next to the patient's chin. Thyroid measurements were calculated via the formula for determining a prolate ellipsoid. The formula was modified for radioactive iodine uptake because it is a planar image. Volumes calculated with these 2 modalities were subsequently analyzed and compared by linear regression. All patients had undergone ultrasonography at an average of 3 mo from nuclear scanning. All our patients' ^{131}I dosages were based on the thyroid measurements obtained by thyroid scintigraphy. **Results:** We included 110 patients (95 women, 15 men) with an age range of 20–95 y and an average age of 56 ± 17.4 y. Diagnoses included 66 cases of nodular goiter and 44 of Graves disease. There was a linear relationship between measurement of thyroid gland weight by the 2 modalities, which can be explained in the following formula: log US (g) = 0.84 + [0.65 × log NM (g)], where NM is thyroid scintigraphy and US is ultrasonography. **Conclusion:** We have validated that this method has helped obtain more accurate measurements of the thyroid gland by thyroid scintigraphy. Additionally, we have derived factors that convert the estimated thyroid volume calculated from thyroid scintigraphy to the expected ultrasonography value.

Key Words: Graves disease; toxic nodular goiter; antithyroid medication; thyroid scintigraphy; thyroid ultrasound; radioactive iodine therapy

Hyperthyroidism is one of the most common endocrine disorders in the United States, affecting more than 1 in 100 people (1). Thyrotoxicosis describes the syndrome that occurs secondary to systematically elevated thyroid hormone levels and is characterized by symptoms such as fatigue, heat intolerance, tremor, and weight loss, among others (2). The 2 major causes of hyperthyroidism are Graves disease and toxic nodular goiter (3,4), whereas Hashimoto thyroiditis accounts for most cases that occur as a result of passive release (5). These hyperthyroid conditions are diagnosed with the aid of thyroid scintigraphy, also known as thyroid scanning or radioactive iodine (RAI) uptake (6).

Per the American Thyroid Association, there are 3 clinical options for treating hyperthyroidism: antithyroid medication, surgical thyroidectomy, and RAI treatment (7). Importantly, treatment with RAI is feasible only in the context of thyroid hormone overproduction, such as Graves disease or toxic multinodular goiter.

Hyperthyroidism is generally treated in a stepwise fashion and begins by achieving a euthyroid state with antithyroid medication (8). Although antithyroid medication such as methimazole and propylthiouracil can be effective in achieving euthyroidism in hyperthyroid patients, this treatment is not a definitive approach to treating hyperthyroidism (9,10). The remission rate after a standard 12–18 mo of treatment is only 50%–55%, with some patients requiring antithyroid medication for up to 6 y if used as the sole method of treatment. Thus, in the event of recurrence after an antithyroid medication regimen, which has been shown to occur in over 52% of patients, either RAI or surgical thyroidectomy is recommended (11).

Surgical thyroidectomy is a highly effective treatment but is indicated in only certain circumstances. These indications include abnormal cytology on fine-needle aspiration, very large goiters, goiters that cause airway obstruction or dysphagia, and pregnancy (12). In the absence of these indications for surgical thyroidectomy, RAI treatment is the definitive treatment of choice if antithyroid medication proves ineffective. RAI is especially used in postmenopausal women and male patients, as there is no risk of fetal abnormalities as there is in fertile female patients who may unwittingly be pregnant at the time of treatment (13).

For the past 80 y, since Saul Hertz first applied ^{131}I as a treatment for hyperthyroidism in 1941 (14), RAI therapy
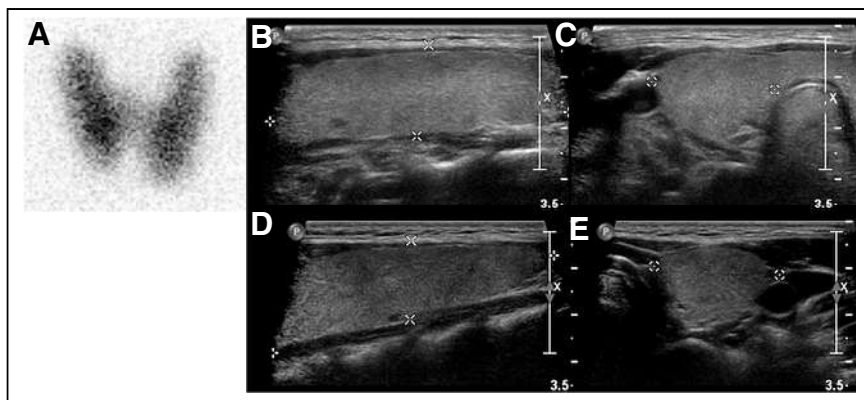
FIGURE 1. Planar ^{123}I scintigraphy imaging and ultrasonography of patient with Graves disease. (A) Thyroid scintigraphy (right lobe, 6.19 × 2.52 cm; left lobe, 6.48 × 25.4 cm). (B) Ultrasonography, left lobe (length × width, 6.4 × 1.7 cm). (C) Ultrasonography, left lobe (depth, 2.7 cm). (D) Ultrasonography, right lobe (length × width, 5.9 × 1.8 cm). (E) Ultrasonography, right lobe (depth, 2.4 cm).

has been the most commonly used definitive treatment for hyperthyroidism (*15,16*). The dose of ^{131}I administered to the patient is determined by 2 factors: the percentage of ^{123}I uptake in the thyroid at 24 h of an RAI uptake study and the calculated size of the thyroid gland in grams (*17*). For the calculation of the thyroid mass in grams, the density of the thyroid is generally assumed to be 1 g/cm^3 (*18*). More specifically, the equation for ^{131}I dose calculation (converted to MBq) in RAI is (*17*) …

$$\frac{2.8 - 7.4 \text{ MBq} \times \text{thyroid weight (g)}}{\% \text{ of } ^{123}\text{I uptake at 24 h}}.$$

As such, it is crucial to be able to determine the weight of the thyroid with great accuracy in order to establish a safe and effective dose for RAI.

Ultrasonography is a validated modality for determining thyroid volume (*19,20*). Though necessary for assessing the degree of ^{123}I uptake in RAI uptake studies, nuclear scintigraphy also allows for estimating thyroid volume. This study compared volume measurement calculations based on ultrasonography and nuclear scintigraphy in a cohort of patients with hyperthyroidism.

MATERIALS AND METHODS

From January 2018 to December 2019, this prospective study evaluated 110 consecutive hyperthyroid patients, all of whom had undergone thyroid ultrasonography and ^{123}I scintigraphy within 1 d to 6 mo of each other (91 d on average). Institutional review board approval for review of the patients' records was obtained. However, consent forms were not obtained from patients because thyroid ultrasonography is a routine

evaluation for all hyperthyroid patients to rule out thyroid malignancy before potential ^{131}I therapy. Patients with a clinical diagnosis of hyperthyroidism and elevated results on thyroid function tests were referred. Patients with a diagnosis of thyroid carcinoma were excluded. Thyroid imaging was performed at 24 h after administration of approximately 11.1 MBq of ^{123}I-sodium in anterior, left anterior oblique, and right anterior oblique views. Patients lay supine with the neck extended and were imaged at the level of the chin using a Millennium camera with low-energy high-resolution parallel-hole collimators (GE Healthcare) to best evaluate the thyroid gland dimensions. In patients with a normal or high count rate, the images were obtained for 35,000 counts. In patients with a low count rate, a 10-min image was obtained. Ultrasonography was conducted using dedicated IU 22 ultrasonography L12-5 linear transducers (Philips). Thyroid lobe volumes from ultrasonography were calculated by 0.5 × length × width × depth. This formula was derived from the geometric method for calculating the volume of a prolate ellipsoid (*21*). In a similar fashion, thyroid lobe volumes from ^{123}I scintigraphy were calculated by 0.5 × length × width × width. The volumes of both lobes and, if present, that of the isthmus were added together, resulting in the total thyroid volume. Representative images used for thyroid volume estimation for both Graves disease and multinodular goiter are shown in Figures 1 and 2, respectively. All thyroid scintigraphy and calculations were reviewed and analyzed by 3 experienced nuclear medicine physicians. All ultrasonography was performed and reviewed by the expert radiologists in the Radiology Department. Volumes calculated with these 2 modalities were subsequently analyzed.
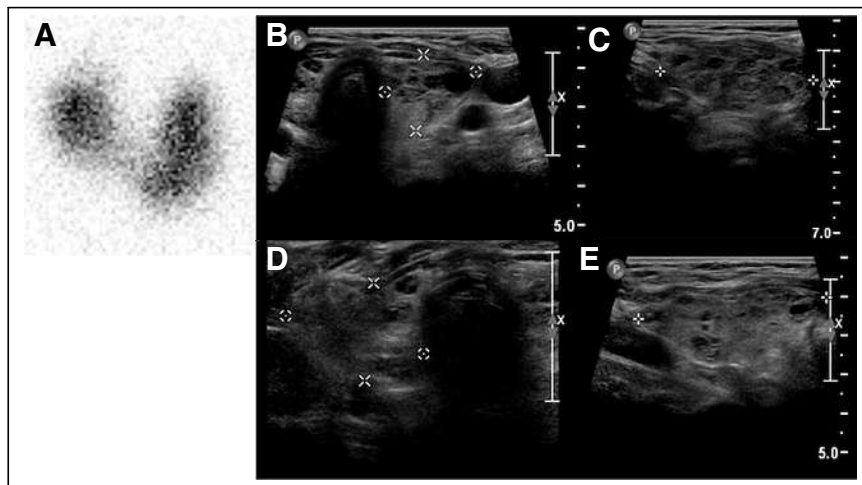
FIGURE 2. Planar ^{123}I thyroid scintigraphy and ultrasonography of patient with multinodular goiter. (A) Thyroid scintigraphy (right lobe, 5.4 × 2.9 cm; left lobe, 4.3 × 2.4 cm). (B) Ultrasonography, left lobe (length × width, 5.1 × 2.0 cm). (C) Ultrasonography, left lobe (depth, 2.4 cm). (D) Ultrasonography, right lobe (length × width, 5.2 × 1.7 cm). (E) Ultrasonography, right lobe (depth, 2.5 cm).
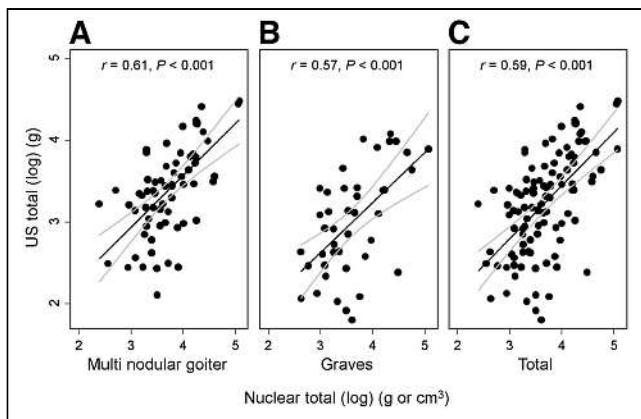
FIGURE 3. (A) Linear relationship between volume estimations from log US (g) and log NM (g) in patients with nodular goiter. (B) Linear relationship between volume estimations from log US (g) and log NM (g) in patients with Graves disease. (C) Linear relationship between volume estimations from log US (g) and log NM (g) from all patients included in study, regardless of diagnosis as nodular goiter or Graves disease.

Paired t testing was used to compare the thyroid gland weight between the ultrasonography and the thyroid scintigraphy. Pearson correlations were calculated between the thyroid gland weights measured by ultrasonography and thyroid scintigraphy. Linear regression models were used to explore the relation between measurement of thyroid gland weight by the thyroid scintigraphy and ultrasonography. To achieve normality, reduce variability, and fit the model better, logarithm transformations were used for measurements by the thyroid scintigraphy and ultrasonography in the linear regression model. All statistical analyses were done using Stata, version 17.0 (StataCorp LLC).

RESULTS

We included 110 patients (95 women, 15 men) with an age range of 20–95 y and an average age of 56 $\pm$ 17 y. Diagnoses included 66 cases of nodular goiter and 44 of Graves disease. The mean thyroid gland weights for patients with Graves disease were 33.1 $\pm$ 50.1 g via ultrasonography measurement and 50.0 $\pm$ 45.6 g via thyroid scintigraphy ($P = 0.001$).

For patients with a nodular goiter, however, the mean thyroid weight calculated by ultrasonography measurement was 34.1 $\pm$ 18.9 g whereas the thyroid scintigraphy method resulted in a mean of 47.8 $\pm$ 28.7 g ($P < 0.001$). In both Graves and nodular goiter patients, there was a good correlation between measurements by thyroid scintigraphy and by

ultrasonography ($r = 0.8327$ and $r = 0.7174$, respectively; $P < 0.001$). The overall correlation coefficient regardless of diagnosis was 0.7804 ($P < 0.001$). There was a linear relationship between measurement of thyroid gland weight by the 2 modalities (regardless of diagnosis), as can be explained in the following formula: US (g) = 0.84 + [0.65 $\times$ log NM (g)], where NM is thyroid scintigraphy and US is ultrasonography ($r = 0.59$, $P < 0.001$ for the slope; Fig. 3C). Moreover, there are separate linear relationships between measurement of thyroid weight between the 2 modalities with respect to the diagnosis of either Graves disease or nodular goiter.

For Graves patients, log US (g) = 0.77 + [0.62 $\times$ log NM (g)] ($r = 0.57$, $P < 0.001$; Fig. 3B), whereas for nodular goiter patients, log US (g) = 1.03 + [0.63 $\times$ log NM (g)] ($r = 0.61$, $P < 0.001$; Fig. 3A). Figure 3 shows that the relationship holds up better for thyroid glands of 20–55 g ($\exp^3$ to $\exp^4$), with a narrowed 95% CI. Linear regressions for log US (g) using log NM (g) as a predictor are shown in Table 1 by diagnosis and for all patients.

Figure 1 depicts both the ^{123}I thyroid scintigraphy and the thyroid ultrasonography for a 27-y-old woman with hyperthyroidism. The thyroid scintigraphy showed uniform uptake throughout the enlarged lobes of the thyroid gland, consistent with Graves disease. Thyroid uptake at 2 h was 26.5% (range, 5%–10%) at 2 h and 62.2% (range, 10%–35%) at 24 h. Ultrasonography showed bilaterally enlarged lobes with no nodules.

Figure 2 depicts both the ^{123}I thyroid scintigraphy and the thyroid ultrasonography for an 89-y-old woman with hyperthyroidism. The thyroid scintigraphy showed nonuniform uptake in the right lobe of the gland, consistent with multinodular goiter. Thyroid uptake was 4.2% (range, 5%–10%) at 2 h and 16.3% (range, 10%–35%) at 24 h, consistent with subclinical hyperthyroidism. Ultrasonography showed bilaterally enlarged glands with a nodule in the right upper pole.

DISCUSSION

Here, we have shown the ability to obtain accurate thyroid volume measurements through planar ^{123}I scintigraphy and imaging with a γ-camera using a high-resolution parallel-hole collimator. We used a modified ellipsoid formula based on dimensions obtained from a single anterior view, as well as a modified acquisition protocol characterized by placing a wide-view γ-camera at the patient's chin with the neck in hyperextension. We reasoned that these changes

TABLE 1
Linear Regression for Log US (g) Using Log NM (g) as Predictor by Diagnosis

Diagnosis	Intercept	SE	P	Slope	SE	P
Multinodular goiter	1.031	0.381	<0.001*	0.632	0.101	0.028*
Graves disease	0.775	0.512	0.14	0.613	0.140	<0.001*
Total	0.841	0.321	0.01*	0.649	0.086	<0.001*

*Statistically significant.

would aid in curtailing the volume overestimations that we had previously seen with scintigraphy at our institution. The ability to assess thyroid volume via scintigraphy has been well investigated and previously reported (22–24). However, the standard methodologies for estimation generally result in inaccuracies in measurement—either underestimating or overestimating the volume depending on the formula and the architecture of the gland (22). Ultrasonography has been shown to estimate volume more accurately and, for this reason, has generally been adopted as the gold standard imaging modality for volume estimation before RAI therapy (23,25,26).

To improve the accuracy of scintigraphy-based volume estimations, linear regression was used to compare scintigraphically obtained volumes with ultrasonographically obtained volumes. Regression analysis revealed a fairly strong linear relationship between the volumes derived from ultrasonography with those derived from scintigraphy (Fig. 3C). Importantly, this relationship allowed for derivation of a correction factor such that scintigraphically obtained volumes could be corrected to align more closely with volumes obtained ultrasonographically. This correction factor—which in our study predominantly corrected for the overestimation of scintigraphy relative to ultrasonography—allows for accurate volume estimation with scintigraphy alone (Figs. 3A–3C). Importantly, this estimation can be made more accurate by stratifying patients by Graves and nodular goiter, as the slopes of the regression lines obtained differ between these 2 patient cohorts (Figs. 3B and 3C). This, in turn, could streamline the preprocedural workup in patients awaiting radioiodine therapy, as scintigraphy could be used to determine radioiodine uptake and thyroid volume simultaneously. Although ultrasonography is generally considered accessible and cost-effective (24), scintigraphy is a requirement before RAI therapy. Extending its role to estimate volume in addition to radioiodine uptake would spare patients an additional test—a net gain to both patients and the health-care staff treating them.

Currently, there is debate on whether hyperthyroidism is better treated with standardized or calculated doses of [131]I. Treatment with standardized doses is based on general size (small, medium, or large) and applies a 185-, 370-, or 555-MBq dose of ^{131}I, respectively. Calculated doses use a formula that accounts for thyroid weight and RAI to determine the treatment dose. Peters et al. determined that outcomes are dependent on the radiation dose absorbed, which is inversely proportional to thyroid size (26). As such, patients with standardized doses had lower treatment success in larger thyroid goiters than patients who received calculated doses. Although an additional study found the 2 methods to be equally effective, this study did not take into account differences in thyroid volume (27). Furthermore, with the importance of personalizing treatments to the patient's own gland size, nodularity, treatment history, and longevity of illness, using a set dose for all patients may not adequately treat the patient or may expose patients with smaller thyroids to unnecessary levels of radiation. Therefore, taking into account each patient's thyroid volumes and diagnoses helps to individualize treatment.

Although our methodology improves volume estimation via scintigraphy, the methodology itself requires that a series of previous ultrasonography measurements be available on which regression analysis can be performed. For this reason, volume estimation using this correction factor suffers from the limitations inherent in ultrasonography: a tendency to underestimate volume and a lack of precision relative to slightly more robust modalities such as CT and MRI (25,28,29). Although CT and MRI have shown superior performance in volume estimation, both have shortcomings. MRI is expensive and time-consuming, whereas CT increases exposure to unnecessary radiation. The negative aspects of these 2 imaging modalities, relative to ultrasonography, make them less desirable in preprocedural thyroid volume estimations. It is generally uncommon for CT and MRI to be used as stand-alone modalities for estimation of thyroid volume. When these modalities are used for thyroid evaluation, it is usually in response to an incidental finding (30) such as was demonstrated in our study, in which only 3 of the 110 subjects had undergone CT specifically to evaluate the thyroid. Though reports from these 3 scans commented on the heterogeneity and overall appearance of the thyroid, only 1 of these scans reported a thyroid measurement for comparison with ultrasonography and scintigraphy. No patients underwent MRI specifically for evaluation of the thyroid—all thyroid evaluations stemmed from incidental findings on studies ordered for alternative indications. Thus, although some in the field have shown CT and MRI to be the most accurate modalities in thyroid volume determination, our institution did not have available the data needed to create a correction factor to convert volumes obtained via thyroid scintigraphy to more closely align with measurements obtained via CT and MRI (28). The task of creating such a correction factor should be further investigated at an institution in which thyroid volume estimations by CT and MRI are more commonplace.

CONCLUSION

The thyroid gland can be measured accurately using a γ-camera with a low-energy high-resolution parallel-hole collimator and by positioning patients accurately. Through this technique, we have validated thyroid scintigraphy as an accurate modality for determining thyroid weight before decision making in the treatment of hyperthyroidism. Additionally, we have derived conversion factors with which the estimated thyroid volume calculated from thyroid scintigraphy can be converted to the expected ultrasonography value. These conversion factors provide physicians with the potential to streamline the treatment pathway for patients with hyperthyroidism by obviating ultrasonography thyroid volume estimation before the RAI uptake study.

DISCLOSURE

No potential conflict of interest relevant to this article was reported.

KEY POINTS

QUESTION: Can ^{123}I thyroid scintigraphy be used to accurately assess thyroid volumes before treatment with ^{131}I-sodium?

PERTINENT FINDINGS: Thyroid volumes calculated with ultrasonography and thyroid scintigraphy showed a statistically significant linear relationship, creating a formula conversion factor that can accurately assess for thyroid weight using scintigraphy alone.

IMPLICATIONS FOR PATIENT CARE: Using an already-needed ^{123}I scan to evaluate both uptake values and thyroid volumes gives physicians the potential to remove the need for additional ultrasonography before treatment. This change would not only streamline the treatment process but also improve the cost effectiveness of hyperthyroidism management, as well as decreasing the financial and temporal burden on patients.

REFERENCES

1. Golden SH, Robinson KA, Saldanha I, Anton B, Ladenson PW. Clinical review: prevalence and incidence of endocrine and metabolic disorders in the United States: a comprehensive review. *J Clin Endocrinol Metab.* 2009;94:1853–1878.
2. Doubleday AR, Sippel RS. Hyperthyroidism. *Gland Surg.* 2020;9:124–135.
3. Davies TF, Andersen S, Latif R, et al. Graves' disease. *Nat Rev Dis Primers.* 2020; 6:52.
4. Can AS, Rehman A. Goiter. StatPearls website. https://www.statpearls.com/ ArticleLibrary/viewarticle/22351. Updated June 5, 2022. Accessed August 12, 2022.
5. Mincer DL, Jialal I. Hashimoto thyroiditis. StatPearls website. https://www. statpearls.com/ArticleLibrary/viewarticle/22579. Updated June 21, 2022. Accessed August 12, 2022.
6. Intenzo CM, dePapp AE, Jabbour S, Miller JL, Kim SM, Capuzzi DM. Scintigraphic manifestations of thyrotoxicosis. *Radiographics.* 2003;23:857–869.
7. Ross DS, Burch HB, Cooper DS, et al. 2016 American Thyroid Association guidelines for diagnosis and management of hyperthyroidism and other causes of thyrotoxicosis. *Thyroid.* 2016;26:1343–1421.
8. Brito JP, Schilz S, Singh Ospina N, et al. Antithyroid drugs: the most common treatment for Graves' disease in the United States: a nationwide population-based study. *Thyroid.* 2016;26:1144–1145.
9. Kahaly GJ, Bartalena L, Hegedus L, Leenhardt L, Poppe K, Pearce SH. 2018 European Thyroid Association guideline for the management of Graves' hyperthyroidism. *Eur Thyroid J.* 2018;7:167–186.
10. Abraham P, Avenell A, McGeoch SC, Clark LF, Bevan JS. Antithyroid drug regimen for treating Graves' hyperthyroidism. *Cochrane Database Syst Rev.* 2010; 2010:CD003420.
11. Sundaresh V, Brito JP, Wang Z, et al. Comparative effectiveness of therapies for Graves' hyperthyroidism: a systematic review and network meta-analysis. *J Clin Endocrinol Metab.* 2013;98:3671–3677.
12. Smithson M, Asban A, Miller J, Chen H. Considerations for thyroidectomy as treatment for Graves disease. *Clin Med Insights Endocrinol Diabetes.* 2019;12: 1179551419844523.
13. Tran P, Desimone S, Barrett M, Bachrach B. I-131 treatment of Graves' disease in an unsuspected first trimester pregnancy: the potential for adverse effects on the fetus and a review of the current guidelines for pregnancy screening. *Int J Pediatr Endocrinol.* 2010;2010:858359.
14. Hertz S, Roberts A. Radioactive iodine in the study of thyroid physiology; the use of radioactive iodine therapy in hyperthyroidism. *J Am Med Assoc.* 1946;131:81–86.
15. Lee SL. Radioactive iodine therapy. *Curr Opin Endocrinol Diabetes Obes.* 2012; 19:420–428.
16. Sundaresh V, Brito JP, Thapa P, Bahn RS, Stan MN. Comparative effectiveness of treatment choices for Graves' hyperthyroidism: a historical cohort study. *Thyroid.* 2017;27:497–505.
17. Kuanrakcharoen P. Radioiodine (1-131) dose for the treatment of hyperthyroidism in Rajavithi Hospital. *J Med Assoc Thai.* 2016;99(suppl 2):S123–S129.
18. Fujita N, Kato K, Abe S, Naganawa S. Variation in thyroid volumes due to differences in the measured length or area of the cross-sectional plane: a validation study of the ellipsoid approximation method using CT images. *J Appl Clin Med Phys.* 2021;22:15–25.
19. Shabana W, Peeters E, De Maeseneer M. Measuring thyroid gland volume: should we change the correction factor? *AJR.* 2006;186:234–236.
20. Blum M. Ultrasonography of the thyroid. Endotext website. https://www.endotext. org/chapter/ultrasonography-of-the-thyroid/. Updated April 11, 2020. Accessed August 12, 2022.
21. Nusynowitz ML. Geometric methods for determining left ventricular volume. *J Nucl Med.* 1991;32:552–555.
22. du Cret RP, Choi RE, Roe SJ, Boudreau RJ, Park HM, Loken MK. Improved prediction of thyroid lobar mass from parameters obtained by routine thyroid scintigraphy. *Clin Nucl Med.* 1987;12:436–439.
23. Wesche MF, Tiel-van Buul MM, Smits NJ, Wiersinga WM. Ultrasonographic versus scintigraphic measurement of thyroid volume in patients referred for ^{131}I therapy. *Nucl Med Commun.* 1998;19:341–346.
24. Himanka E, Larsson LG. Estimation of thyroid volume; an anatomic study of the correlation between the frontal silhouette and the volume of the gland. *Acta Radiol.* 1955;43:125–131.
25. van Isselt JW, de Klerk JM, van Rijk PP, et al. Comparison of methods for thyroid volume estimation in patients with Graves' disease. *Eur J Nucl Med Mol Imaging.* 2003;30:525–531.
26. Peters H, Fischer C, Bogner U, Reiners C, Schleusener H. Radioiodine therapy of Graves' hyperthyroidism: standard vs. calculated 131 iodine activity—results from a prospective, randomized, multicentre study. *Eur J Clin Invest.* 1995;25:186–193.
27. Jarløv AE, Hegedüs L, Kristensen LØ, Nygaard B, Hansen JM. Is calculation of the dose in radioiodine therapy of hyperthyroidism worth while? *Clin Endocrinol (Oxf).* 1995;43:325–329.
28. Bierig SMJA. Accuracy and cost comparison of ultrasound versus alternative imaging modalities, including CT, MR, PET, and angiography. *J Diagn Med Sonogr.* 2009;25:138–144.
29. Nygaard B, Nygaard T, Court-Payen M, et al. Thyroid volume measured by ultrasonography and CT. *Acta Radiol.* 2002;43:269–274.
30. Ní Mhuircheartaigh JM, Siewert B, Sun MR. Correlation between the size of incidental thyroid nodules detected on CT, MRI or PET-CT and subsequent ultrasound. *Clin Imaging.* 2016;40:1162–1166.

Blanching Defects at Pressure Points: Observations from Dynamic Total-Body PET/CT Studies

Yasser G. Abdelhafez[1,2], Kristin McBride[1], Edwin K. Leung[1,3,4], Heather Hunt[1], Benjamin A. Spencer[1], Javier E. Lopez[5,6], Kwame Atsina[5,6], Elizabeth J. Li[3], Guobao Wang[1], Simon R. Cherry[1,3], Ramsey D. Badawi[1,3], Fatma Sen[1], and Lorenzo Nardo[1]

[1]Department of Radiology, University of California, Davis, California; [2]Nuclear Medicine Unit, South Egypt Cancer Institute, Assiut University, Assiut, Egypt; [3]Biomedical Engineering, University of California, Davis, California; [4]UIH America, Inc., Houston, Texas; [5]Department of Internal Medicine, University of California, Davis, California; and [6]Cardiovascular Research Institute, University of California, Davis, California

Total-body PET/CT allows simultaneous acquisition of all body parts at a single bed position during the radiotracer uptake phase. Dynamic imaging protocols using total-body PET might demonstrate findings that may not have been previously visualized or described using conventional PET/CT scanners. We examined the characteristics of blanching defects—areas of markedly reduced (partial defect) or absent (complete defect) radiotracer uptake seen at the skin and subcutaneous tissues opposite the bony prominences at pressure points. **Methods:** In this observational study, 77 participants underwent dynamic total-body PET/CT imaging using ^{18}F-FDG (group 1, $n = 47$, 60-min dynamic, arms down, divided into 3 subgroups according to the injected dose) or ^{18}F-fluciclovine (group 2, $n = 30$, 25-min dynamic, arms up). Forty of the 47 participants in group 1 were reimaged at 90 min after being allowed off the scanning table. Blanching defects, partial or complete, were characterized opposite the bony prominences at 7 pressure points (the skull, scapula, and calcaneus bilaterally, as well as the sacrum). The association of the blanching defects with different clinical and technical characteristics was analyzed using uni- and multivariate analyses. **Results:** In total, 124 blanching defects were seen in 68 of the 77 (88%) participants at one or more pressure points. Blanching defects were higher, on average, in group 2 (3.5 ± 1.7) than in group 1 (2.1 ± 1.4; $P < 0.001$) but did not vary within group 1 for different ^{18}F-FDG dose subgroups. All defects resumed a normal pattern on delayed static (90-min) images, except for 14 partial defects. No complete blanching defects were seen on the 90-min images. By multivariate analysis, arm positioning above the head was associated with skull defects; scapular and sacral defects were significantly more common in men and in those with a lower body mass index, whereas calcaneal defects were not associated with any factor. **Conclusion:** Blanching defects opposite the bony pressure points are common on dynamic total-body PET/CT images using different radiopharmaceuticals and injection doses. Their appearance should not be immediately interpreted as an abnormality. The current findings warrant further exploration in a prospective setting and may be used to study various mechanopathologic conditions, such as pressure ulcers.

Key Words: total-body PET/CT; dynamic scans; pressure points; blanching defects; skin and subcutaneous tissue

Total-body PET/CT has recently been implemented in both research and clinical fields (*1,2*). The uEXPLORER total-body PET/CT scanner's long axial field of view of 194 cm not only allows for simultaneous acquisition of radiotracer kinetics across the entire body but also improves signal collection efficiency, which, coupled with high spatial resolution, results in high-resolution and high-quality images (*3*). For the first time, it is now possible to obtain high-quality total-body dynamic images that can be used in both research and the clinic (*4*). In the research field, total-body dynamic imaging has been described and is useful for such purposes as obtaining biomarkers characterizing the delivery and uptake of ^{18}F-FDG (e.g., K_1 and inhibition constant) via kinetic modeling (*5–9*). In the clinical field, dynamic imaging has been suggested by different groups for a variety of applications. For example, in the imaging of prostate cancer, dynamic imaging helps tumor detection and characterization, especially in the pelvis (*10–12*). Several guidelines have incorporated dynamic acquisitions as part of their recommended imaging protocols (*13–17*). However, the implementation of high-resolution and high-quality total-body acquisitions may enhance the prominence of additional findings that have not been previously described in the literature.

In this work, we characterized, for the first time to our knowledge, the presence of markedly reduced or absent radiotracer uptake at the skin and subcutaneous tissues opposite the bony prominences at pressure points, described hereafter as blanching defects, which were noted on dynamic total-body PET images performed with ^{18}F-FDG or ^{18}F-fluciclovine.

MATERIALS AND METHODS

Study Participants

This was a retrospective review of 4 institutional review board–approved studies prospectively acquired for other research purposes (approvals 1341792, 1374902, 1470016, and 1480948).

All participants provided written informed consent before being scanned. The participants were categorized into 2 groups according to the injected tracer: group 1 (^{18}F-FDG) included 47 participants under 3 subgroups according to the injected radiotracer dose (Table 1), and group 2 (^{18}F-fluciclovine) included 30 men with prostate cancer who were referred for a standard-of-care evaluation using ^{18}F-fluciclovine total-body PET/CT.

Total-Body PET/CT Scanning

All participants underwent list-mode dynamic PET/CT as part of their respective study protocol, on a total-body PET/CT scanner (uEXPLORER; United Imaging Healthcare) (3). The scanner has an axial field of view of 194 cm, a PET spatial resolution of no more than 3.0 mm in full width at half maximum near the center of the axial field of view, and an 80-detector-row CT component with a minimum slice thickness of 0.5 mm. Before acquisition of the dynamic PET data, a low-dose (tube current, ~50 mA) or ultralow-dose (tube current, ~5 mA) CT scan (both with a tube voltage of 140 kVp) was acquired for attenuation correction and anatomic localization. The tube current was automatically modulated by the scanner manufacturer's algorithm.

All PET data were acquired in list-mode format with the participants supine. Positioning aids were provided according to the participant's comfort level. For group 1, all participants were positioned with arms down and underwent dynamic, 60-min acquisitions, starting at the time of intravenous injection of an ^{18}F-FDG dose ranging from 17.2 to 393.8 MBq (dose groups are summarized in Table 1). The last 20 min of acquisition (40–60 min after injection) were reconstructed into a single frame for the purpose of reviewing. According to their respective protocols, 40 of the 47 participants in group 1 were reimaged for 20 min starting at 90 min after injection (i.e., ~30 min after the end of the dynamic acquisition). Participants were allowed to get off the scanner table between scans and empty their urinary bladder. The second scan was used to assess changes within the blanching defects noted on the first set of images (the dynamic acquisition). Seven participants in group 1, all with cancer, underwent a follow-up dynamic scan after a median of 16 d (range, 14–24 d) for other research purposes. These follow-up scans were used to monitor the stability of the distribution of blanching defects.

For group 2, arms were positioned above the head in 29 of the 30 subjects and to the sides in a single subject. PET images were acquired for a total of 25 min, starting immediately after injection of 314.6 ± 19.7 MBq (range, 287.2–389.6 MBq) of ^{18}F-fluciclovine. The PET data were reconstructed into two 10-min frames (4–14 min and 15–25 min) for the purpose of reviewing.

All images were reconstructed using the vendor's software, which uses a time-of-flight, ordered-subset expectation maximization algorithm, with 4 iterations and 20 subsets. Attenuation-corrected and non–attenuation-corrected images were generated for analysis. All PET corrections were applied to the attenuation-corrected images (scatter, randoms, dead time, and normalization). No point-spread function modeling or postreconstruction smoothing was applied. The reconstruction matrix size was 256×256, generating 2.344-mm isotropic voxels. The described reconstruction parameters are the same as used for the routine clinical readouts (1,2).

PET/CT Image Analysis

The reconstructed PET/CT images were transferred to an image viewing workstation running OsiriX MD, version 12.0 (Pixmeo), and reviewed independently by 2 nuclear medicine physicians (5 and 13 y of PET/CT experience after training). Agreement

between the 2 readers was considered the final reading. For discordant readings, a third nuclear medicine physician (20 y of experience) was consulted, masked to prior readings, and the final decision was based on the agreement of any 2 readers.

Both attenuation-corrected and non–attenuation-corrected images were reviewed side by side for any skin or subcutaneous areas of complete (grade 2) or partial (grade 1) absence of the expected normal radiotracer uptake (grade 0) compared with the surrounding tissues at different pressure points. Figure 1 illustrates examples of partial and complete defects. The pressure points were defined as the anatomic locations where a bony structure could restrict blood flow to the overlying tissues because of patient positioning or weight burden. For the current analysis, 4 locations, named after their bony prominences, were studied: skull, scapulae, sacrum, and calcaneus. Except for the sacrum, laterality was also noted as right, left, or bilateral. In the presence of bilateral defects with different defect grades, the higher grade was recorded for that pressure point.

For participants who underwent additional static scans at 90 min after injection, the images were read after recording the impression from the dynamic dataset.

PET/CT images were reviewed for any visual gross misregistration between PET and CT at the pressure points and for the presence of any anatomic abnormality in the studied pressure points (e.g., skin ulceration or masses). The CT window level was adjusted to identify and precisely locate the different positioning aids (e.g., back or knee cushions) on the CT images (Fig. 1).

Statistical Analysis

Differences in continuous data (e.g., age and body mass index [BMI]) were compared between the 2 primary groups (with and without blanching defects) using the independent-samples t test for normally distributed data and the Mann–Whitney U test for nonnormally distributed data. Differences in qualitative features were compared using the χ^2 test or the Fisher exact test, as appropriate. Both participant- and site-based analyses were performed. A participant with a blanching defect at one or more sites was considered positive for blanching defects. Individual factors that showed some association with the presence of blanching defects ($P < 0.05$) in univariate analysis were further analyzed using multivariate analysis with binary logistic regression. All models were adjusted for age, sex, injected dose, and BMI, in addition to the interactions between correlated variables (e.g., arm position and tracer group), as appropriate.

Agreement between the 2 primary readers on the total count of blanching defects per participant was compared using the intraclass correlation coefficient. Agreement on the qualitative evaluation (i.e., the presence or absence of blanching defects, laterality, and grade) was compared using Cohen κ-analysis.

RESULTS

Study Participants

The general characteristics of the study population are given in Table 1. Group 1 (^{18}F-FDG) included 18 women and 29 men with a mean age of 51.2 ± 13.2 y (range, 26.0–78.0 y). Compared with group 1, group 2 participants were all men ($P < 0.001$), older (71.0 ± 8.3 vs. 51.2 ± 13.3 y, $P < 0.001$), taller (178.1 ± 7.8 vs. 171.8 ± 9.8 cm, $P = 0.002$), and marginally heavier (91.0 ± 16.7 vs. 83.5 ± 16.9 kg, $P = 0.06$); however, their mean BMI was comparable to group 1. The groups had comparable setups regarding

TABLE 1
General Characteristics of Study Participants

Characteristic	^{18}F-FDG dose ($n = 47$)			Fluciclovine (standard dose)
	Low	Intermediate	Standard	
Age (y)	45 ± 11.1 (26–62)	51.7 ± 9.3 (39–66)	55.1 ± 15 (26–78)	71.0 ± 8.3 (54.1–89)
Weight (kg)	78.4 ± 16.1 (53.1–102.5)	95 ± 17.9 (77–131.7)	81.8 ± 15.1 (53–113)	91.0 ± 16.7 (68.4–148)
Height (cm)	173.6 ± 10.5 (157.5–195.6)	170.6 ± 12.4 (152.4–193)	171.1 ± 8.3 (157.5–185.4)	178.1 ± 7.8 (165.1–195.6)
BMI (kg/m^2)	25.8 ± 3.4 (20.4–32.2)	32.6 ± 4.5 (26.8–40.4)	28 ± 5.3 (19.4–37)	28.7 ± 5.4 (19.4–46.8)
Injected dose (MBq)	19.6 ± 1.7 (17.2–23.5)	188.4 ± 8.6 (175.7–196.7)	372.3 ± 17.0 (331.9–393.8)	314.6 ± 19.7 (287.2–389.6)
Fasting duration (h)	9.2 ± 3.0 (6–15)	11.4 ± 3.4 (6–18)	11 ± 2.9 (6–20)	6.9 ± 3.4 (4–16)
Blood glucose (mg/dL)	90.7 ± 19.2 (39–113)	94.3 ± 12.7 (76–113)	97.9 ± 21.8 (65–154)	Not applicable
Sex				
Female	7	2	9	0
Male	8	8	13	30
Disease				
Cancer	0	0	7	30
Cardiovascular	0	10	0	0
Healthy	15	0	15	0
Imaging time points				
Dynamic and delayed	15	10	15	0
Dynamic only	0	0	7	30
Arms position				
Above head	0	0	0	29
To sides	15	10	22	1
Attenuation-corrected CT dose				
Ultralow (5 mAs)	15	10	15	0
Low (50 mAs)	0	0	7	30
PET/CT misregistration				
No	10	8	17	25
Yes	5	2	5	5

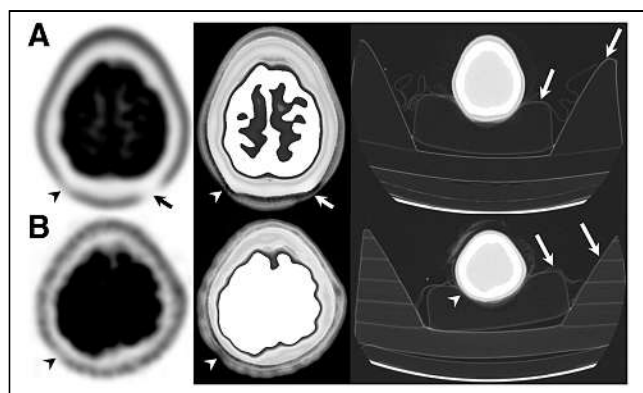Qualitative data are number; continuous data are mean and range.

FIGURE 1. Example of complete (A) and partial (B) blanching defects. (A) Images from 29-y-old healthy woman weighing 81 kg and 165 cm tall, injected with ^{18}F-FDG (369 MBq). PET image (left) demonstrates bilateral posterior parietooccipital scalp defects, complete on left side (arrow) and partial on right side (arrowhead). ^{18}F-FDG PET/CT image (middle) shows no CT abnormality. Lung window (right) outlines head support setup (arrows). (B) Images from 43-y-old healthy woman weighing 53 kg and 160 cm tall, injected with ^{18}F-FDG (18.5 MBq). PET image (left) demonstrates relative photopenia at right posterior parietal scalp region (arrowhead), representing partial blanching defect. Contralateral side (left side) shows no abnormality. ^{18}F-FDG PET/CT image (middle) shows no CT abnormality at site of partial defect. Lung window (right) outlines head position within support setup (arrows) and demonstrates minimal tilting of skull toward side of partial defect (arrowhead). Color version of this figure is available as supplemental file at http://tech.snmjournals.org.

the positioning aids (namely, the use of knee and back cushions). A head support was used for all participants.

Of the 77 participants, 37 had cancer (30 prostate and 7 with urothelial tumors) and 10 had cardiovascular disease (with a history of recent myocardial infarction), whereas the remaining 30 were healthy participants not known to have had a recent myocardial infarction or cancer.

Agreement Analysis

There was no significant difference in the number of reported blanching defects per participant between the 2 readers (2.5 ± 1.8 vs. 2.6 ± 1.6, $P = 0.5$), with an intraclass correlation coefficient of 0.90 (95% CI, 0.85–0.94). Also, there was moderate to substantial agreement (range, 0.66–0.88) on reporting of the blanching defect laterality and grade, both on a participant basis and on a site basis (Table 2).

Characteristics of Blanching Defects

All encountered blanching defects from both groups were seen in both attenuation-corrected and non–attenuation-corrected images. On the final reading, 124 blanching defects in total were seen in 68 of 77 (88%) participants at one or more pressure points.

The average number of defects was higher in group 2 (3.5 ± 1.7) than in group 1 (2.1 ± 1.4; $P < 0.001$) but did not vary within group 1 for different ^{18}F-FDG dose subgroups. On average, 2.2 ± 1.3, 2.0 ± 1.6, and 2.1 ± 1.5 defects were

TABLE 2
κ-Agreement on Defect Detection/Laterality and Grade between 2 Readers According to Scan Time Point and Evaluated Pressure Points

Scan timing and evaluated pressure points	Agreement	
	Detection*	Grade of defect
Dynamic only	0.81 (0.75–0.88)	0.81 (0.75–0.83)
90-min only	0.66 (0.44–0.88)	0.70 (0.49–0.91)
Skull	0.76 (0.62–0.89)	0.75 (0.60–0.89)
Scapulae	0.84 (0.74–0.95)	0.88 (0.80–0.95)
Sacrum	0.72 (0.55–0.89)	0.74 (0.60–0.89)
Calcaneus	0.78 (0.66–0.90)	0.82 (0.73–0.92)

*Agreement figures on detection also include agreement on laterality.
Data in parentheses are 95% CI.

observed per participant in the low-, intermediate-, and standard-dose groups, respectively ($P = 0.8$).

Blanching defects against the scapulae and calcaneus on dynamic imaging were the most frequent and tended to be bilateral and complete (Table 3). Only 14 partial defects from 9 participants were still seen on the delayed static images (90 min after injection) (Fig. 2). No complete blanching defects were seen on the 90-min images. The distribution of the blanching defects is summarized in Table 3. Among the 7 participants who had follow-up dynamic scanning, 6 defects were encountered at baseline compared with 8 in the follow-up scans. The distribution, laterality, and grade changed between the 2 scans within the same participant. For example, one participant who previously showed bilateral complete defects opposite the calcaneus demonstrated only a unilateral partial calcaneal defect on the repeated scan (Fig. 3).

Blanching defects beyond the above-described pressure points were not systematically evaluated; however, we noticed variable degrees of blanching defects at other sites where bony parts press against a tightened or hard structure: for example, prominent spinous processes at the cervicodorsal region at the site of transition between the head support and the scanner table; elbows against the scanning table or immobilization belts; distal parts of the legs against the end of knee cushions when the heels are not touching the scanning table; and the forefeet against the tightened immobilization aids (Fig. 4).

Factors Associated with Presence of Blanching Defects

On a participant basis, the presence or absence of blanching defects on dynamic scans did not vary according to age, sex, height, weight, BMI, injected dose, fasting hours, or blood glucose level. Also, the use of cushions (back or knee) and misregistration between the PET and CT were not associated with these defects. Twenty-nine of 30 participants in group 2 had their arms up and showed one or more defects, compared with 39 of 47 with arms to the side ($P = 0.01$).

TABLE 3
Distribution of Blanching Defects According to Anatomic Site, Laterality, and Grade on Dynamic and Delayed Imaging

Blanching defect	Dynamic (n = 77)				Delayed static (n = 40)*			
	Skull	Scapulae	Sacrum	Calcaneus	Skull	Scapulae	Sacrum	Calcaneus
Absent	53	43	58	9	37	37	38	32
Present	24	34	19	47	3	3	2	6
One or unilateral								
Partial	8	2	8	1	1	2	2	3
Complete	5	3	11	7	0	0	0	0
Two or bilateral								
Partial	3	8	NA	4	2	1	NA	3
Complete†	8	21	NA	35	0	0	NA	0
Outside field of view	0	0	0	21	0	0	0	2

*37 of original 77 participants did not undergo 90-min imaging.
†In presence of bilateral defects with different defect grades, higher grade was recorded for that pressure point.
NA = not applicable because sacrum was evaluated as single pressure point.

On a site basis (Supplemental Table 1; supplemental materials are available at http://jnmt.snmjournals.org), the clinical and scan features associated with the presence of blanching defects varied according to the anatomic site. On univariate analysis, both skull and scapular defects were seen more frequently in group 2 participants (older participants who were scanned with their arms up). Furthermore, scapular defects were encountered significantly more often in taller men. However, in multivariate analysis, only arm positioning above the head was associated with skull defects (odds ratio, 11.5; 95% CI: 3.7–35.7; $P < 0.001$) whereas scapular and sacral defects were associated with a lower BMI and the male sex. Defects around the calcaneus were not associated with any of the studied characteristics.

The use of back or knee cushions did not significantly affect the frequency or distribution of these defects. However, back pillows were used in only 4 participants. Knee cushions, on the other hand, were used for most participants; nevertheless, they were not associated with the presence of defects opposite the calcaneus.

FIGURE 2. Examples of partial and complete restoration of uptake within complete blanching defects seen at pressure points, from left to right, against skull and scapulae bilaterally, sacrum, and left calcaneus. (A–D) PET images from last 20 min of dynamic 60-min acquisition (A), their respective 20-min static acquisition at 90 min (C), and corresponding PET/CT images (B and D) in lung window, to demonstrate relationship with positioning setup and scanner table. Sites with complete defects on dynamic images are marked with arrowheads, and sites with partial restoration at 90-min time point are marked with arrows. Blanching defects against skull showed complete restoration on right side and partial restoration on left side, and those against scapulae and sacrum showed complete restoration, whereas defects opposite heel showed partial restoration on delayed 90-min image. Color version of this figure is available as supplemental file at http://tech.snmjournals.org.

DISCUSSION

In this study, we found that dynamic total-body PET/CT imaging frequently demonstrated multiple areas of absent or markedly diminished radiotracer uptake against pressure points. These areas included the sides of the scalp, being pressed against the parietal bones, and the skin and subcutaneous tissues opposite the bony prominences of the scapulae, sacrum, and calcaneus.

We hypothesize that these defects may be related to the absence of decreased perfusion induced by mechanical compression, or displacement of the
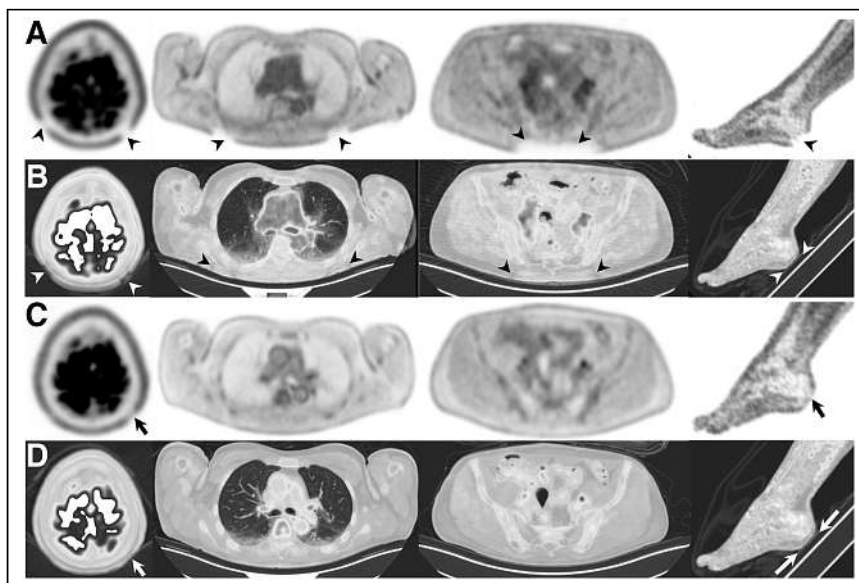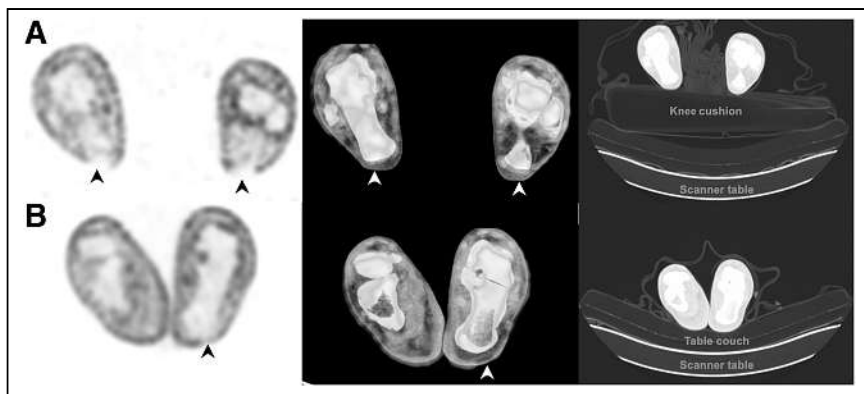
FIGURE 3. Changes in pattern of blanching defects against calcaneus in same subject across 2 dynamic scans, baseline (A) and follow-up (B), separated by 2 wk. Shown are representative images from 74-y-old man with genitourinary cancer weighing 74 kg and 170 cm tall. ^{18}F-FDG PET images demonstrate bilateral complete blanching defects opposite calcaneus (A, arrowheads), with no corresponding abnormality in PET/CT image (middle). Follow-up dynamic PET scan in same subject shows unilateral partial defect on left foot (B, arrowhead). CT images with lung window (right) outline positioning setup demonstrating relationship of heels with respect to knee cushion (top) and table couch (bottom) during respective scan time points. Color version of this figure is available as supplemental file at http://tech.snmjournals.org.

blood within the microcirculation at the pressure sites near the bony prominence, where the skin and subcutaneous tissue are known to be thinned and the pressure is high (*18*). This hypothesis is supported by several findings: that the defects followed a close anatomic distribution and photopenic patterns regardless of the uptake mechanism of the tracer, that the defects improved or resolved on delayed imaging when the participants were allowed to walk freely and return to the same scanning position, and that the defects lacked anatomic correlations at these sites on the CT images (e.g., skin discontinuity, ulceration, or necrotic masses). Though dynamic PET acquisitions have been well established, especially for brain imaging, the current observation has not previously been described, to our knowledge. One possible explanation, at least partially, is the outstanding gain in scanner sensitivity, which makes subtle observations far more obvious than with conventional scanners.

Although most PET/CT imaging centers use simplified static approaches in the clinical setting, dynamic acquisition protocols are increasingly included in guidelines (*13–17*). Therefore, identification and characterization of these blanching defects may have both clinical and research relevance, particularly for the interpretation of routine ^{18}F-fluciclovine scans. ^{18}F-fluciclovine PET/CT imaging guidelines (*16*) recommend early scanning around 3–5 min after injection (with the dynamic acquisition protocol being optional). Accordingly, most institutions inject the tracer while the patient is lying on the scanner table and then begin the PET data acquisition either immediately or around 4 min after injection, starting at the pelvis and moving cranially. This protocol is acquired primarily with the arms above the head. This position leads to scapular rotation upward and may also increase tension on the posterior paraspinal cervical muscles, thereby adding pressure on the skull. In our data, the scalp and scapular defects were encountered more frequently in group 2 participants.

In our work, 40 participants underwent delayed static imaging 30 min after the end of a 60-min dynamic PET acquisition. In 31 of them, the uptake was normalized at the pressure points. We assume that resumption of tracer delivery and uptake after prolonged cessation of circulation at these pressure points may be partially explained by a mechanism similar to the tourniquet effect (*19*), in which prolonged pressure may cause a temporary local decrease in perfusion and subsequent compensatory vasodilation after release of the pressure, redelivering part of the circulating tracer in the blood pool to the sites with defects. Only 9 participants continued to demonstrate partial defects at one or more pressure points (Table 3). We hypothesize that the magnitude of pressure (in terms of force and duration) may be related to the rate of resumption of the circulation at these points and may vary under different physiologic and pathologic conditions. This hypothesis may be clinically relevant for assessment of cutaneous microvascular circulation. Currently, the capillary refill-time test is commonly used as a simple means to assess macrovascular disease and cutaneous perfusion (*20*). In this test, the examiner applies firm external pressure by a finger to the distal phalanx of a finger or toe, and the time required to recover the normal skin color is recorded. The test, though simple and widely used, is not standardized regarding the magnitude or duration of the applied pressure, the cutoff for abnormality, or the interpretation criteria. Also, it lacks sensitivity and reliability, with wide inter- and intraobserver variability (*21*). Accordingly, many other methods for assessing peripheral perfusion have been introduced (*22*). The highly sensitive total-body PET scanners can capture and quantify radiotracer dynamic processes as they occur in real time, simultaneously with other organ and tissue kinetics (*7,8,23*), and may be used to study different mechanopathologic conditions such as pressure ulcers. These possibilities warrant further exploration in a prospective setting.

Finally, we note some limitations of the current study. Although the data were prospectively collected in the context of other projects, this study was based on retrospective serendipitous evaluation of these scans, and accordingly, potential clinical characteristics and additional tests that might relate to the current findings were not collected. For example, scapular and sacral defects were encountered
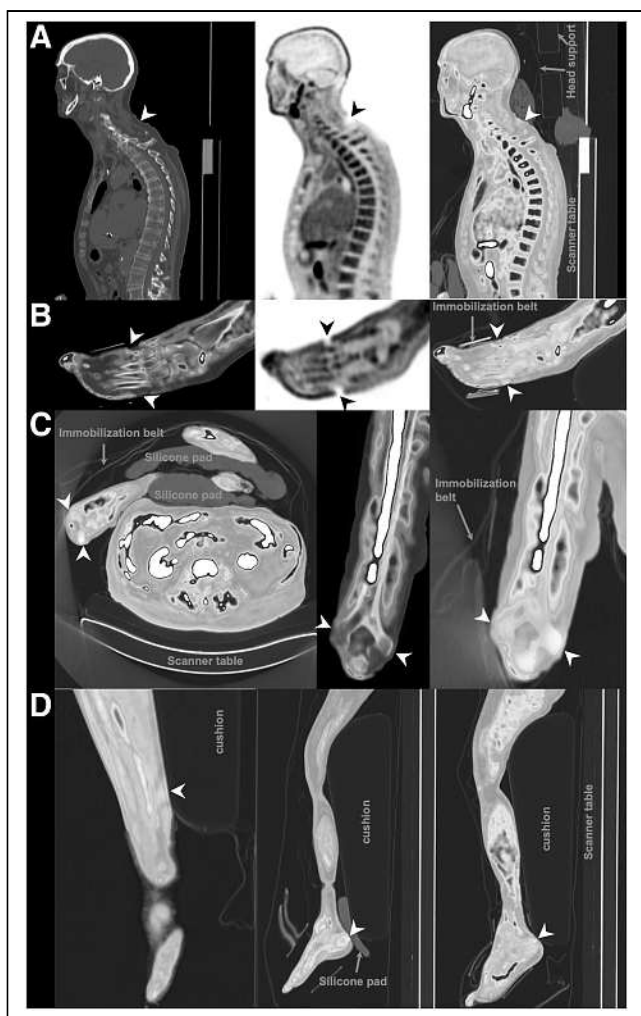
FIGURE 4. Examples of other nonsystematic blanching defects (arrowheads). (A) Absence of skin and subcutaneous ^{18}F-fluciclovine uptake opposite cervicodorsal vertebrae at site of transition between head support and scanner table, as might be caused by pressure against prominent spinous processes. (B) Absence of ^{18}F-FDG uptake at dorsum of foot at site of tightened immobilization belt. (C) Reduced-to-absent ^{18}F-fluciclovine uptake opposite medial and lateral epicondyles of right humerus at site of wrapped immobilization belt around elbows. (D) A few additional patterns of blanching defects in lower limb: at distal third of calf as it is pressing against end of knee cushion (left), opposite calcaneus although silicon pad was placed to minimize pressure (middle), and again opposite calcaneus at end of knee/leg cushion, where heels do not touch scanner table (right). Color version of this figure is available as supplemental file at http://tech.snmjournals.org.

more frequently in men with a lower BMI, potentially indicating that sex differences, hormonal status, and fat volume could contribute to the finding. Also, local skin conditions that could have been appreciated with direct inspection, the Raynaud phenomenon, or autoimmune diseases were not captured in this report. The microcirculation is tightly controlled under numerous external and internal

pathophysiologic mechanisms, and the current work cannot provide further direct clinical implications of the described findings. Also, because the study was retrospective, we could not demonstrate a clear association with the positioning setup of the participants—a setup that could be far more complex than mere descriptions of body build, cushion location, type, geometry, or any other characteristics of positioning aids. Additionally, we limited our results to 7 pressure points, whereas in realty a few other blanching defects could be encountered (Fig. 4). The sporadic nature of these defects prevents accurate systematic evaluation. Furthermore, the position of the arms was tightly linked to the tracer group. Although we compensated for the interaction term between these 2 variables, we believe that a homogenous distribution of arms up and arms down in each tracer group would be preferable. Another limitation was the relatively high frequency of misregistration between the PET and CT components of the images. In a total-body scanner, the whole body is covered within the field of view during the whole acquisition duration; accordingly, any motion in one region of the body could affect the attenuation correction and scatter correction in other regions (2). With the high sensitivity of total-body PET, data-driven motion compensation techniques could be explored as a potential solution (24).

CONCLUSION

Blanching defects opposite pressure points are common on dynamic total-body PET/CT imaging using the uEXPLORER scanner with different radiopharmaceuticals and injection doses. Their appearance should not be immediately interpreted as an abnormality. The changes in tracer distribution taking place at the pressure points across the body can be captured in real time on the high-sensitivity total-body PET/CT scanner and can be leveraged in a prospective setting to study various circulatory changes occurring in different mechanopathologic conditions such as pressure ulcers.

DISCLOSURE

ACKNOWLEDGMENTS

KEY POINTS

QUESTION: Are there any unusual findings opposite the pressure points on dynamic total-body PET imaging?

PERTINENT FINDINGS: Blanching defects, described as areas with markedly decreased or completely absent radiotracer uptake in the skin or subcutaneous tissue at the pressure points opposite the skull, scapulae, sacrum, and calcaneus, were seen in 39 of 47 (^{18}F-FDG) and 29 of 30 (^{18}F-fluciclovine) total-body dynamic scans.

IMPLICATIONS FOR PATIENT CARE: Blanching defects are commonly encountered on dynamic total-body PET imaging with both ^{18}F-FDG or ^{18}F-fluciclovine and should not be mistaken for any abnormality.

REFERENCES

1. Nardo L, Abdelhafez YG, Spencer BA, Badawi RD. Clinical implementation of total-body PET/CT at University of California, Davis. *PET Clin.* 2021;16:1–7.
2. Ng QK, Triumbari EKA, Omidvari N, Cherry SR, Badawi RD, Nardo L. Total-body PET/CT: first clinical experiences and future perspectives. *Semin Nucl Med.* 2022;52:330–339.
3. Spencer BA, Berg E, Schmall JP, et al. Performance evaluation of the uEXPLORER total-body PET/CT scanner based on NEMA NU 2-2018 with additional tests to characterize PET scanners with a long axial field of view. *J Nucl Med.* 2021;62:861–870.
4. Badawi RD, Shi H, Hu P, et al. First human imaging studies with the EXPLORER total-body PET scanner. *J Nucl Med.* 2019;60:299–303.
5. Wang G, Nardo L, Parikh M, et al. Total-body PET multiparametric imaging of cancer using a voxelwise strategy of compartmental modeling. *J Nucl Med.* 2022; 63:1274–1281.
6. Liu G, Hu P, Yu H, et al. Ultra-low-activity total-body dynamic PET imaging allows equal performance to full-activity PET imaging for investigating kinetic metrics of ^{18}F-FDG in healthy volunteers. *Eur J Nucl Med Mol Imaging.* 2021;48: 2373–2383.
7. Wu Y, Feng T, Zhao Y, et al. Whole-body parametric imaging of ^{18}F-FDG PET using uEXPLORER with reduced scanning time. *J Nucl Med.* 2022;63:622–628.
8. Feng T, Zhao Y, Shi H, et al. Total-body quantitative parametric imaging of early kinetics of ^{18}F-FDG. *J Nucl Med.* 2021;62:738–744.
9. Sarkar S, Matsukuma KE, Spencer B, et al. Dynamic positron emission tomography/computed tomography imaging correlate of nonalcoholic steatohepatitis. *Clin Gastroenterol Hepatol.* 2021;19:2441–2443.
10. Turkbey B, Mena E, Shih J, et al. Localized prostate cancer detection with ^{18}F FACBC PET/CT: comparison with MR imaging and histopathologic analysis. *Radiology.* 2014;270:849–856.
11. Tulipan AJ, Vlatkovic L, Malinen E, et al. Comparison of time curves from dynamic ^{18}F-fluciclovine positron emission tomography and dynamic contrast-enhanced magnetic resonance imaging for primary prostate carcinomas. *Phys Imaging Radiat Oncol.* 2018;7:51–57.
12. Uprimny C, Kroiss AS, Decristoforo C, et al. Early dynamic imaging in ^{68}Ga-PSMA-11 PET/CT allows discrimination of urinary bladder activity and prostate cancer lesions. *Eur J Nucl Med Mol Imaging.* 2017;44:765–775.
13. Morbelli S, Esposito G, Arbizu J, et al. EANM practice guideline/SNMMI procedure standard for dopaminergic imaging in Parkinsonian syndromes 1.0. *Eur J Nucl Med Mol Imaging.* 2020;47:1885–1912.
14. Law I, Albert NL, Arbizu J, et al. Joint EANM/EANO/RANO practice guidelines/SNMMI procedure standards for imaging of gliomas using PET with radiolabelled amino acids and [18F]FDG: version 1.0. *Eur J Nucl Med Mol Imaging.* 2019;46: 540–557.
15. Sciagrà R, Lubberink M, Hyafil F, et al. EANM procedural guidelines for PET/CT quantitative myocardial perfusion imaging. *Eur J Nucl Med Mol Imaging.* 2021;48: 1040–1069.
16. Nanni C, Zanoni L, Bach-Gansmo T, et al. [18F]fluciclovine PET/CT: joint EANM and SNMMI procedure guideline for prostate cancer imaging—version 1.0. *Eur J Nucl Med Mol Imaging.* 2020;47:579–591.
17. Varrone A, Asenbaum S, Vander Borght T, et al. EANM procedure guidelines for PET brain imaging using [18F]FDG, version 2. *Eur J Nucl Med Mol Imaging.* 2009;36:2103–2110.
18. Cichowitz A, Pan WR, Ashton M. The heel: anatomy, blood supply, and the pathophysiology of pressure ulcers. *Ann Plast Surg.* 2009;62:423–429.
19. Desaia A, Intenzo C. The "tourniquet effect." *J Nucl Med.* 1984;25:697–699.
20. Fleming S, Gill P, Jones C, et al. The diagnostic value of capillary refill time for detecting serious illness in children: a systematic review and meta-analysis. *PLoS One.* 2015;10:e0138155.
21. Pickard A, Karlen W, Ansermino JM. Capillary refill time: is it still a useful clinical sign? *Anesth Analg.* 2011;113:120–123.
22. Liu C, Correia R, Ballaji H, Korposh S, Hayes-Gill B, Morgan S. Optical fibre sensor for simultaneous measurement of capillary refill time and contact pressure. *Sensors (Basel).* 2020;20:1388.
23. Qi J, Matej S, Wang G, Zhang X. 3D/4D reconstruction and quantitative total body imaging. *PET Clin.* 2021;16:41–54.
24. Berg E, Revilla EM, Abdelhafez YG, et al. Framework design for comprehensive patient motion compensation in total-body PET. EventClass website. https://www.eventclass.org/contxt_ieee2020/online-program/session?s=M-10. Accessed August 11, 2022.

Continuous Bed Motion in a Silicon Photomultiplier–Based Scanner Provides Equivalent Spatial Resolution and Image Quality in Whole-Body PET Images at Similar Acquisition Times Using the Step-and-Shoot Method

Kodai Kumamoto[1], Hideaki Sato[1], Yuji Tsutsui[2], Shinichi Awamoto[3], Yasuo Yamashita[3], Shingo Baba[4], and Masayuki Sasaki[5]

[1]Department of Health Sciences, Graduate School of Medical Sciences, Kyushu University, Fukuoka, Japan; [2]Department of Radiological Science, Faculty of Health Science, Junshin Gakuen University, Fukuoka, Japan; [3]Division of Radiological Technology, Department of Medical Technology, Kyushu University Hospital, Fukuoka, Japan; [4]Department of Clinical Radiology, Graduate School of Medical Sciences, Kyushu University, Fukuoka, Japan; and [5]Department of Health Sciences, Faculty of Medical Sciences, Kyushu University, Fukuoka, Japan

This study investigated the spatial resolution and image quality of the continuous-bed-motion (CBM) method in a sensitive silicon photomultiplier–based PET/CT system compared with the traditional step-and-shoot (SS) method. **Methods:** A PET/CT scanner was used in this study. Data acquisition using the SS method was performed for 3 min per bed position. In the CBM method, the bed speed ranged from 0.5 to 3.3 mm/s. The acquisition time equivalent to the SS method was 1.1 mm/s for 2-bed-position ranges and 0.8 mm/s for 7-bed-position ranges. The spatial resolution was investigated using ^{18}F point sources and evaluated using the full width at half maximum. Image quality was investigated using a National Electrical Manufacturers Association International Electrotechnical Commission body phantom with 6 spheres 10, 13, 17, 22, 28, and 37 mm in inner diameter. The radioactivity concentration ratio of the ^{18}F solution in all spheres and the background was approximately 4:1. The detectability of each sphere was visually evaluated using a 5-step score. Image quality was physically evaluated using the noise-equivalent count rate, contrast percentage of the 10-mm hot sphere, background variability percentage, and contrast-to-noise ratio. **Results:** The spatial resolution was not affected by the difference in acquisition methods or bed speeds. The detectability of the 10-mm sphere with a bed speed of 2.2 mm/s or faster was significantly inferior to that of the SS 2-bed-position method. In evaluating image quality, we observed no significant difference in contrast percentage among the acquisition methods or speeds in the CBM method. However, the increasing bed speed in the CBM method increased the background variability percentage and decreased the noise-equivalent count rate. When comparing the SS 2-bed-position method with the CBM method at 0.8 mm/s, we observed no significant differences in any parameters. **Conclusion:** In whole-body PET images obtained with a silicon photomultiplier–based PET/CT scanner, the CBM method provides spatial resolution and image quality equivalent to the SS method, with the same acquisition time.

The step-and-shoot (SS) method has traditionally been used for PET data acquisition; however, the continuous bed motion (CBM) method was recently developed. In the SS method, multibed data are sequentially acquired only when the bed is stationary, not when the bed is moving (*1–10*). More than 1 min is wasted in a whole-body acquisition. Moreover, the axial acquisition range is determined by the number of bed positions, resulting in an unnecessary acquisition range and radiation exposure in a CT scan. In the CBM method, the bed continuously moves to acquire data (*2–10*), the axial acquisition range can be determined in a 0.1-mm unit, and the bed speed can be changed according to the body part (*2,3,6,8,9*). Moreover, generating a whole-body image by adding several fast whole-body scans should be useful if an examination is interrupted by patient motion or pain (*7,11*). It has been reported that patients preferred continuous bed movements over SS movements (*6*). Therefore, the CBM method may replace the SS method because of the flexibility of the PET examination for each patient. The usefulness of the CBM method in PET/CT using a photomultiplier tube system has been studied (*2–11*). Differences between the SS and CBM methods did not significantly affect SUV_{max} or SUV_{mean} in phantoms or tumors in clinical examinations (*3,4,6–9*). In contrast, the SS method has been reported to be superior to the CBM method in terms of variability in the background region (*4,9*).

Silicon photomultipliers (SiPMs), which are a type of semiconductor detector, were recently applied instead of the traditional photomultiplier tube in PET/CT scanners (*12–14*). Compared with conventional photomultiplier tube–based

PET scanners, SiPM-based PET scanners achieved a high gain and faster time response. This feature improves the sensitivity and time-of-flight timing resolution, thus resulting in good image quality, a short examination time, and a decrease in administered dose and radiation exposure (*15–17*). With these advantages, the CBM method using SiPM-based PET/CT scanners is expected to provide the same sufficient image quality with flexible examinations. However, the usefulness of the CBM method in SiPM-based PET/CT scanners has not been studied.

In this study, we investigated the image quality of the CBM method compared with the conventional SS method in SiPM-based PET/CT systems. Moreover, we evaluated the influence of varying bed speeds on image quality.

FIGURE 1. PET images of point source at coordinates (0,1) cm. Upper figure shows axial images, and lower one shows coronal images. No visual difference was observed among acquisition methods, whereas coronal images extended along with increase in slice thickness.

MATERIALS AND METHODS

PET/CT Scanner

PET data were acquired using a Biograph Vision PET/CT scanner (Siemens Healthineers). The PET system has 8 rings based on 38 detector blocks with lutetium oxyorthosilicate (Lu_2SiO_5:Ce) crystals ($3.2 \times 3.2 \times 20$ mm) and 6,400 crystals per ring. The transverse field of view was 700 mm, and the axial field of view was 263 mm. The spatial resolution at 1 cm was 3.7 mm in full width at half maximum (FWHM). The time-of-flight timing resolution was 214 ps, and the coincidence time window was 4.7 ns. These values were reported by the manufacturer. The CT system has 64 rows, and the rotation time was 0.33 s. CT images can be obtained using the following parameters: 70–120 kV, 20–666 mA, 0.5-s tube rotation, 0.8 pitch, and a 0.6-mm slice collimation. In this study, the voltage was 120 kVp and the tube current was set by CT automatic exposure control.

Point Source Phantom

The spatial resolution was investigated using ^{18}F point sources. One microliter of ^{18}F solution was put into glass capillaries with an inner diameter of 0.70 mm and an outer diameter of 0.97 mm. The radioactivity concentration was 30 MBq/mL. Point sources were placed at transaxial positions (1, 0), (10, 0), and (0, 10) cm on the same z-position.

Body Phantom

Image quality was investigated using a National Electrical Manufacturers Association (NEMA) International Electrotechnical Commission body phantom (Data Spectrum Corp.) with 6 spheres of 10-, 13-, 17-, 22-, 28-, and 37-mm inner diameter. The body phantom was an acrylic phantom that mimicked the torso of a human weighing 60 kg. The body phantom had a long diameter of 300 mm, a short diameter of 230 mm, a circumference of 840 mm, a height of 180 mm, and a volume of 9.7 L (Supplemental Fig. 1; supplemental materials are available at http://jnmt.snmjournals.org). The radioactivity concentration of ^{18}F solution in all spheres and the background was approximately 10.6 and 2.65 kBq/mL (ratio of 4:1), respectively. The radioactivity concentration was measured using an automatic well γ-counter (AccuFLEX γ7001; Hitachi Aloka Medical, Ltd.).
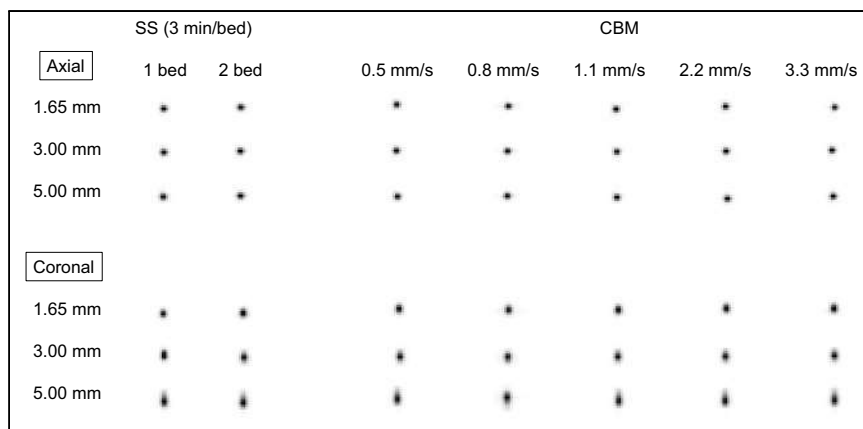
Data Acquisition and Image Reconstruction

In the SS method, data are acquired for 3 min/bed position × 1 bed position and 3 min/bed position × 2 bed positions in list mode according to the paper by Tsutsui et al. (*15*). The 1-bed-position acquisition was for the standard acquisition, whereas the 2-bed-position acquisition was for the overlapping acquisition. The overlap in multibed acquisitions was 49.8%, as determined by the manufacturer to improve the sensitivity distribution in the z-axis. In the CBM method, bed speeds of 0.5, 0.8, 1.1, 2.2, and 3.3 mm/s were investigated. Whole-body acquisition from the top of the head to the mid thigh usually require 7 or 8 bed positions in the standard SS method among Japanese institutions. The regional acquisition time of 0.8 mm/s in the CBM method was consistent with that of 8-bed acquisition at 3 min/bed position in the SS method. The 1.1 mm/s bed speed was consistent with a 2-bed-position acquisition at 3 min/bed position in the SS method.

In the spatial resolution investigation, PET images were reconstructed using filtered backprojection. The image matrix was 440 × 440 (1.65×1.65 mm), and the slice thicknesses were 1.65, 3.00, and 5.00 mm. Attenuation and scattering corrections were not used. In the image-quality investigation, PET images were reconstructed using ordered-subsets expectation maximization with point-spread-function correction and time-of-flight information. This study used 3 iterations and 5 subsets for the NEMA body phantom. Three iterations were done in accordance with our previous report (*15*). The Biograph Vision uses 5 subsets by default; this is fixed by the manufacturer and is unchangeable. CT attenuation correction was performed. Scatter correction was performed using single-scatter simulation. A gaussian filter was not used. The image matrix was 440 × 440, and the slice thickness was 1.65 mm.

Measurement of Spatial Resolution

The spatial resolution was evaluated using the FWHM. Profile curves of each point source in the x-, y-, and z-directions were created passing through the highest-count pixel on the highest-count slice using ImageJ (National Institutes of Health). In the profile curve, the maximum count was determined by a parabolic approximation using 1 point with the highest pixel count and 2 adjacent points. The FWHM of the 3 directions in each position was calculated by linearly interpolating between adjacent pixels at half the maximum value of the response function. FWHM $x_{(a,b)}$ is FWHM in the x-direction at
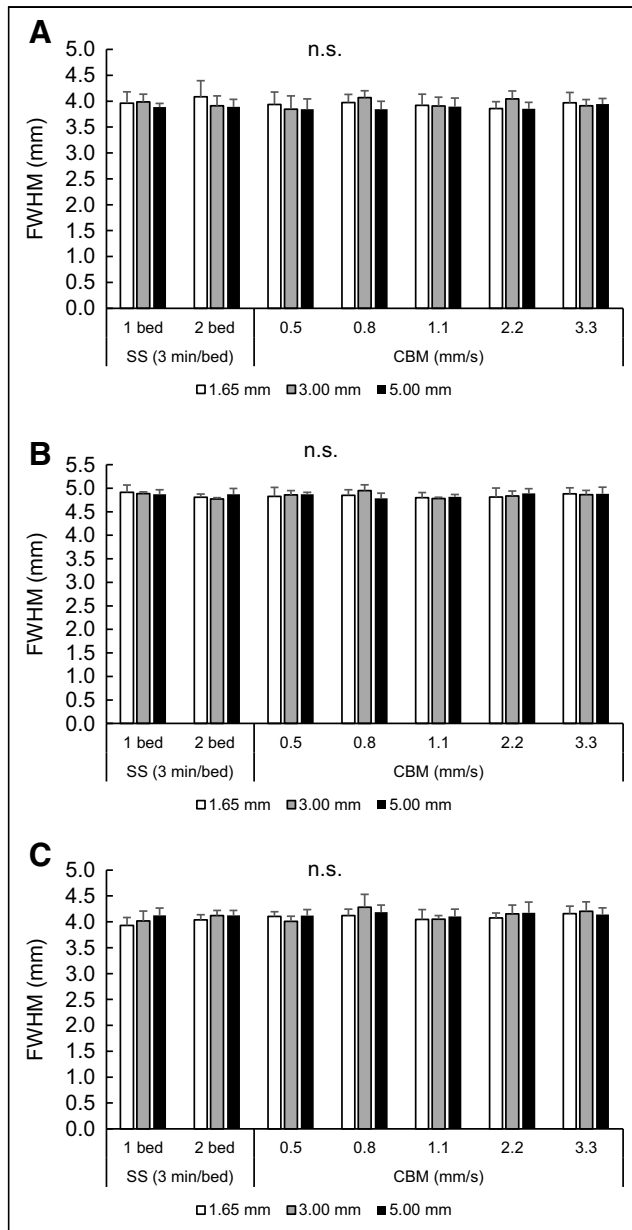
FIGURE 2. Comparison of FWHMs in axial plane of 1 cm radial (A), 10 cm radial (B), and 10 cm tangential (C). They did not significantly differ between SS and CBM methods or among different bed speeds in CBM method even when slice thickness was changed. n.s. = not statistically significant.

position (a,b). The spatial resolution was evaluated using a FWHM of 1 cm in the transverse direction, 10 cm in the transverse radial direction, and 10 cm in the transverse tangential and axial directions. These were calculated using the following equations:

- $\text{FWHM}_{1\,\text{cm}}$ $= \{\text{FWHM } x_{(0,1)} + \text{FWHM } y_{(0,1)}\}/2$
- $\text{FWHM}_{10\,\text{cm radial}}$ $= \{\text{FWHM } x_{(10,0)} + \text{FWHM } y_{(0,10)}\}/2$
- $\text{FWHM}_{10\,\text{cm tangential}}$ $= \{\text{FWHM } y_{(10,0)} + \text{FWHM } x_{(0,10)}\}/2$
- $\text{FWHM}_{\text{axial}}$ $= \{\text{FWHM } z_{(0,1)} + \text{FWHM } z_{(0,10)} + \text{FWHM } z_{(10,0)}\}/3.$

Assessment of Image Quality

The detectability of each sphere was visually evaluated using a 5-step score (1, not absolutely visualized; 2, may not be visualized;

3, uncertain; 4, may be visualized; and 5, absolutely visualized) by a board-certified nuclear medicine physician and 2 radiologic technologists. Scores were averaged for each sphere. Fukukita et al. reported that they decided to use the score of the 10-mm sphere as the reference value because image quality and spatial resolution are most affected by the ability to visualize the 10-mm sphere (18). Therefore, we evaluated the visual scores of mainly the 10-mm sphere. Interobserver agreement was evaluated using the κ-coefficient.

In the NEMA body phantom PET images, the slice in which the hot sphere was most clearly observed was designated as the center slice. A region of interest (ROI) on the 10-mm hot sphere was placed in the center slice with the same inner diameter. Twelve circular ROIs with diameters of 10 and 37 mm were placed in the background on the center slice at ±1 cm and ±2 cm from the center slice (60 ROIs in total). According to the phantom test procedure for whole-body PET imaging with ^{18}F-FDG (18), the noise-equivalent counts, contrast percentage of the 10-mm hot sphere, background variability percentage, and contrast-to-noise ratio were calculated using the following equations. True, scatter, and random coincidences were acquired from a sinogram header, and the scatter fraction and random scaling factor were acquired from a default value. These processes were performed using PMOD software (version 3.8; PMOD Technologies LLC).

$$\text{NEC}_{\text{phantom}} = (1-SF)^2 \frac{(T+S)^2}{(T+S)+(1+k)fR} \text{ (Mcounts)}$$

$$f = \frac{S_a}{\pi r^2},$$

where $\text{NEC}_{\text{phantom}}$ is the noise-equivalent counts and *T, S,* and *R* correspond to true, scatter, and random coincidences acquired within the scanning period, respectively. Moreover, *SF* and *k* are the scatter fraction and random scaling factor, respectively. The scatter fraction of Biograph Vision scanners is fixed at 0.39 by the manufacturer. The *k* is set to 0 because we used variance reduction techniques for estimating a smooth random distribution (18). The *f* is the ratio of object size to field of view. S_a is the cross-sectional area of the phantom. Finally, *r* is the radius of the detector ring diameter.

$$Q_{H,\,10\,\text{mm}} = \frac{C_{H,\,10\,\text{mm}}/C_{B,\,10\,\text{mm}} - 1}{a_H/a_B - 1} \times 100 \ (\%),$$

where $C_{H,\,10\,\text{mm}}$ is the average count in the ROI for a 10-mm sphere, $C_{B,\,10\,\text{mm}}$ is the average count of the 60 background ROIs of 10-mm diameter, and a_H and a_B are the radioactivity concentrations in the hot sphere and background, respectively.

$$N_{10\,\text{mm}} = \frac{SD_{10\,\text{mm}}}{C_{B,\,10\,\text{mm}}} \times 100 \ (\%)$$

$$SD_{10\,\text{mm}} = \sqrt{\sum_{k=1}^{K}(C_{B,\,10\,\text{mm},\,k} - C_{B,\,10\,\text{mm}})^2/(K-1)}, K = 60,$$

where $SD_{10\,\text{mm}}$ is the SD of the background ROIs of 10-mm diameter and $N_{10\,\text{mm}}$ is the background variability percentage (contrast-to-noise ratio):

$$Q_{10\,\text{mm}}/N_{10\,\text{mm}}.$$

Statistical Analysis

JMP Pro, version 15 (SAS Institute Inc.), was used for statistical analysis. The Tukey test was used to analyze the significance of the differences between the SS 2-bed-position method and the
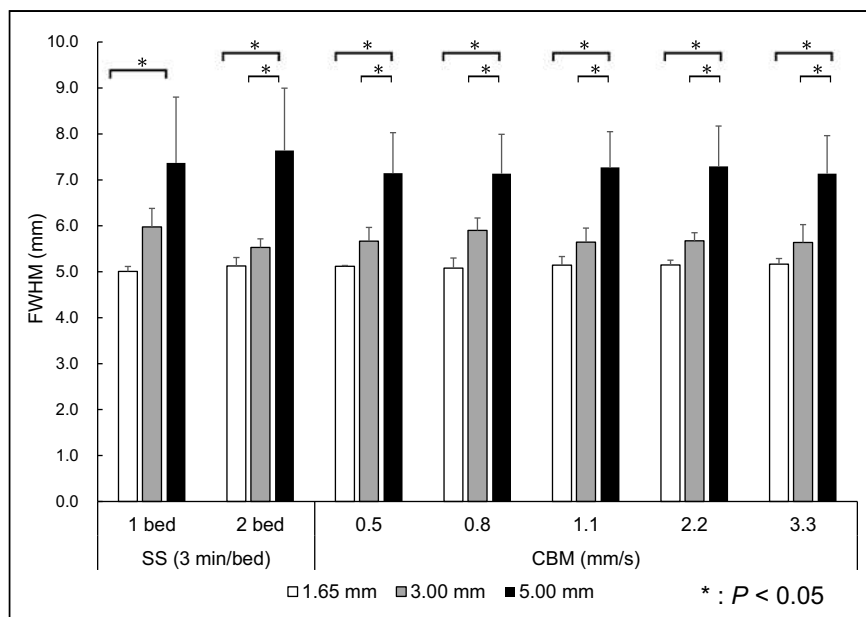
FIGURE 3. Comparison of FWHMs of body axial direction. They did not significantly differ among different acquisition methods and bed speeds, whereas FWHM significantly increased in thicker slices.

CBM method at each bed speed. P values of less than 0.05 were used to denote statistical significance.

RESULTS

Comparison of the Spatial Resolution

Figure 1 shows the PET images of point sources at position (0,1) cm. In the axial images, the shape and size did not differ among acquisition methods or bed speeds. In the coronal images, the image extended in the body axis direction in association with an increase in slice thickness. However, no differences in shape or size were seen among the different bed speeds.

Figure 2 shows the FWHM of the x- and y-directions. No significant differences in the 1-cm FWHM, 10-cm radial FWHM, or 10-cm tangential FWHM were observed between the SS and CBM methods. Moreover, the difference in the FWHM results when varying the slice thickness was insignificant. Figure 3 shows the axial

FIGURE 4. PET images of body phantom using SS method (top) and CBM method (bottom). In CBM method, images with faster bed speeds show high background variability.

FWHM. As the slice thickness increased, the axial FWHM significantly increased. However, no significant difference in the axial FWHM was observed between the SS and CBM methods or among the various bed speeds in the CBM method.

Assessment of Image Quality

Figure 4 shows the PET images of the NEMA body phantom in the SS and CBM methods. In the SS method, the clarity of the hot spheres and background variability were not visually different between 1-bed-position and 2-bed-position acquisitions. In the CBM method, the background variability increased as the bed speed increased. Figure 5 shows the results of the visual evaluation. The detectability of the 10-mm sphere with bed speeds faster than 2.2 mm/s was significantly inferior to that with the SS 2-bed-position method ($P < 0.05$). In the SS method, the score of the 10-mm sphere was above 4. In the CBM method, the bed speed should be 1.1 mm/s or slower to exceed the 10-mm sphere score of 3. Interobserver agreement was moderate ($\kappa = 0.55$).

Figure 6 compares the noise-equivalent counts. In the CBM method, the noise-equivalent counts decreased as the bed speed increased. The noise-equivalent counts in the CBM method with a bed speed of 1.1 mm/s or faster were significantly inferior to those in the SS 2-bed-position method ($P < 0.05$). Figure 7 shows the results of the physical assessment of image quality. No significant difference in contrast percentage of the 10-mm hot sphere was observed between the SS and CBM methods or among the various bed speeds in the CBM method (Fig. 7A). Figure 7B compares the background variability percentage. In the SS method, no difference in background variability percentage was observed between 1-bed-position and 2-bed-position acquisitions. In the CBM method, background variability percentage increased as bed speed increased. The background variability percentage in the CBM method with bed speeds of 1.1 mm/s or faster was significantly inferior to that in the SS 2-bed-position method ($P < 0.05$). Figure 7C compares the contrast-to-noise ratio. The contrast-to-noise ratio did not differ within the SS method, whereas in the CBM method, it decreased as the bed speed increased. The contrast-to-noise ratio in the CBM method with bed speeds of 2.2 mm/s or faster was significantly lower than that in the SS 2-bed-position method ($P < 0.05$).
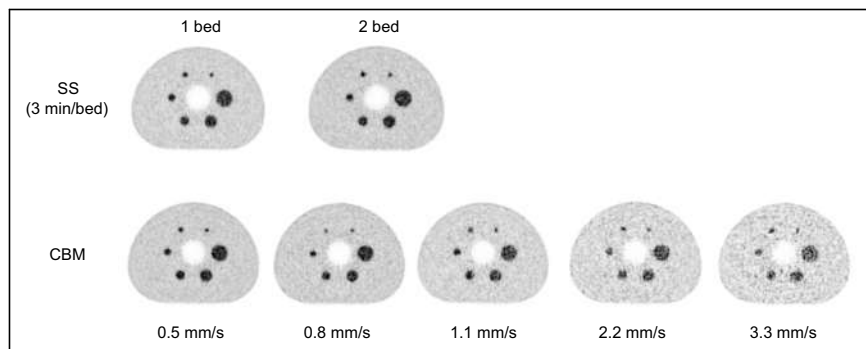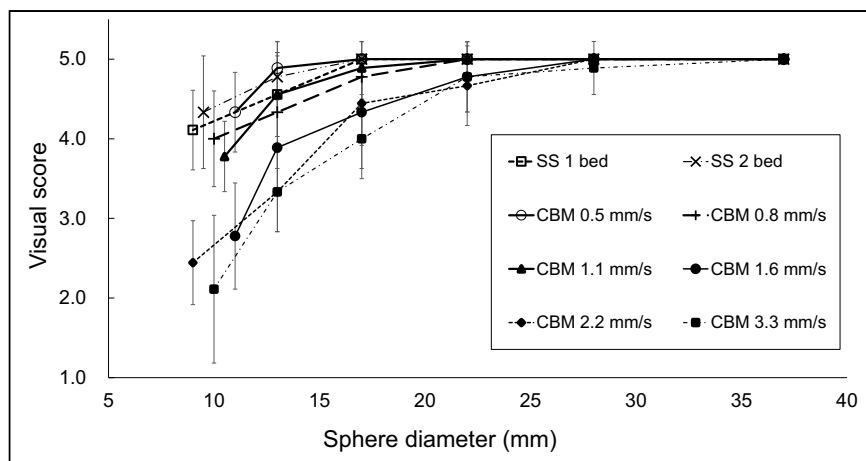
FIGURE 5. Visibility of hot spheres. Visual score of 10-mm sphere does not differ between SS 2-bed-position acquisition and 0.8 mm/s of CBM method. In CBM method, visual score decreased as bed speed increased.

DISCUSSION

Using the SiPM-based PET/CT scanner, the spatial resolution did not significantly differ between the SS and CBM methods or among the different bed speeds in the CBM method even when the slice thickness was changed. The noise-equivalent counts decreased as the bed speed increased in the CBM method. In assessing image quality, we found that the background variability significantly increased as the bed speed increased. However, the contrast of the hot sphere did not differ among acquisition methods or bed speeds.

The spatial resolution did not significantly differ between the SS and CBM methods or among the bed speeds in the CBM method. In the coronal planes, the FWHM increased

FIGURE 6. Noise-equivalent counts of SS and CBM methods. In CBM method, noise-equivalent counts significantly decreased as bed speed increased. Bed speeds of 1.1 mm/s or faster showed significantly inferior noise-equivalent count to that in SS 2-bed-position method. NEC$_{phantom}$ = noise-equivalent counts.

as the slice thickness increased, but no significant difference was observed between the acquisition methods or among the different bed speeds. Because the PET data were acquired during continuous movement in the CBM method, image blurring was considered to increase the body axial FWHM. Furthermore, the increase in bed speed was also considered to exacerbate the spatial resolution. In the CBM method, when the bed position was shifted by a distance equal to the separation between sinogram planes, the events from the same detector were assigned to the next image plane. In the scanner used in this study, the CBM method data were separated and organized by the same axial sampling of 1.65 mm as in the SS method (5). Objects smaller than the pixel size were distributed uniformly over the entire pixel rather than at the center of the pixel. Thus, no significant difference was observed when the bed speed was changed by this function. In the transverse slice, the FWHM did not change when the slice thickness was increased because the pixel sizes were all the same.

The noise-equivalent counts using the NEMA body phantom showed no significant difference between the SS 2-bed-position acquisition and 0.8 mm/s using the CBM method. The noise-equivalent counts decreased as the bed speed increased. Because the acquisition time decreased as the bed speed increased, the noise-equivalent counts decreased because of reduced coincidence counts. This result is consistent with that reported previously (7,15). The background variability also increased as the bed speed increased. The increase in variability with decreasing counts is consistent with that reported previously (15,19). Regarding background variability, the SS method on the photomultiplier tube–based scanner was significantly superior to the CBM method using the same acquisition time (4,9). In contrast, that of the SS method was comparable to that of the CBM method on the SiPM-based scanner in this study. The improvement of the scanner's sensitivity and extension of the axial field of view in the SiPM system in this study is considered to improve the image quality of the CBM method. The visibility of the 10-mm hot sphere did not differ between the SS 2-bed-position acquisition and 0.8 mm/s using the CBM method, and the visual score decreased as the
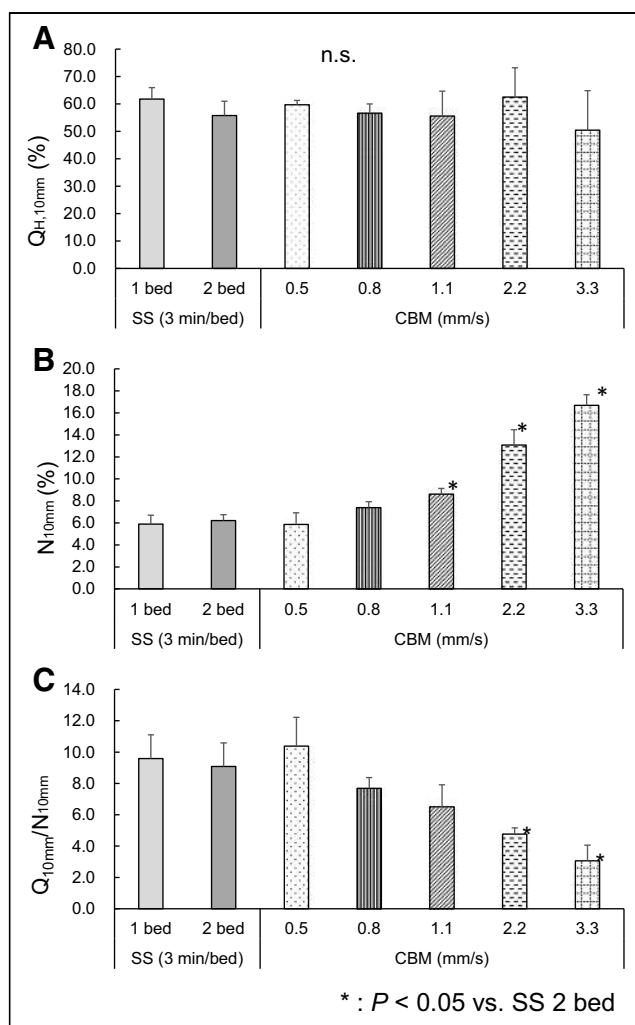
FIGURE 7. Physical assessment of PET image quality of SS and CBM methods. (A) Contrast percentage of 10-mm hot sphere did not significantly differ between SS and CBM methods or among different bed speeds in CBM method. (B) Bed speeds of 1.1 mm/s or faster showed background variability percentage significantly inferior to that in SS method. (C) Contrast–noise ratio in CBM method with bed speeds of 2.2 mm/s or faster was significantly lower than that in SS 2-bed-position method. N_{10mm} = background variability percentage; $Q_{H,10mm}$ = contrast percentage of 10-mm hot sphere; $Q_{H,10mm}/N_{10mm}$ = contrast-to-noise ratio.

bed speed increased. This is probably due to the increase in noise caused by the decrease in coincidence counts (*20*). The contrast values remained the same at all bed speeds. This tendency was also shown in a past study (*9,15*).

This study had some limitations. First, the number of bed speeds examined was limited. An examination with further varieties in bed speeds might reveal the appropriate bed speed equivalent to the SS method. Second, the CBM method was performed in only a single way. The image quality of the summed to-and-fro pass images should be examined. Third, the axial sampling size was fixed at 1.65 mm. A smaller axial sampling size may improve axial spatial resolution. Lastly,

further clinical examinations should be conducted to compare the SS and CBM methods.

CONCLUSION

For SiPM-based PET/CT systems, image quality metric results were comparable between the SS method for 3 min/bed position and the CBM method for speeds of 0.8 mm/s at almost the same acquisition time in whole-body acquisitions. It is expected that the CBM method will be chosen in some cases depending on the combination of bed speeds.

DISCLOSURE

No potential conflict of interest relevant to this article was reported.

KEY POINTS

QUESTION: Can the CBM method preserve the spatial resolution and image quality of the traditional SS method in an SiPM PET/CT scanner?

PERTINENT FINDINGS: No difference in spatial resolution or image quality was observed between the SS method and the CBM 0.8 mm/s method at similar acquisition times in whole-body acquisitions.

IMPLICATIONS FOR PATIENT CARE: Since the CBM method preserves the same image quality as the SS method and provides a more flexible examination, it is expected to be widely used in future when whole-body acquisitions are performed with semiconductor PET/CT systems.

REFERENCES

1. Dahlbom M, Hoffman EJ, Hoh CK, et al. Whole-body positron emission tomography: part I. Methods and performance characteristics. *J Nucl Med.* 1992;33: 1191–1199.
2. Acuff SN, Osborne D. Clinical workflow considerations for implementation of continuous-bed-motion PET/CT. *J Nucl Med Technol.* 2016;44:55–58.
3. Osborne DR, Acuff S, Cruise S, et al. Quantitative and qualitative comparison of continuous bed motion and traditional step and shoot PET/CT. *Am J Nucl Med Mol Imaging.* 2014;5:56–64.
4. Rausch I, Cal-González J, Dapra D, et al. Performance evaluation of the Biograph mCT Flow PET/CT system according to the NEMA NU2-2012 standard. *EJNMMI Phys.* 2015;2:26.
5. Panin VY, Smith AM, Hu J, Kehren F, Casey ME. Continuous bed motion on clinical scanner: design, data correction, and reconstruction. *Phys Med Biol.* 2014;59: 6153–6174.
6. Schatka I, Weiberg D, Reichelt S, et al. A randomized, double-blind, crossover comparison of novel continuous bed motion versus traditional bed position whole-body PET/CT imaging. *Eur J Nucl Med Mol Imaging.* 2016;43:711–717.

7. Yamamoto H, Takemoto S, Maebatake A, et al. Verification of image quality and quantification in whole-body positron emission tomography with continuous bed motion. *Ann Nucl Med.* 2019;33:288–294.

8. Meier JG, Erasmus JJ, Gladish GW, et al. Characterization of continuous bed motion effects on patient breathing and respiratory motion correction in PET/CT imaging. *J Appl Clin Med Phys.* 2020;21:158–165.

9. Yamashita S, Yamamoto H, Nakaichi T, Yoneyama T, Yokoyama K. Comparison of image quality between step-and-shoot and continuous bed motion techniques in whole-body ^{18}F-fluorodeoxyglucose positron emission tomography with the same acquisition duration. *Ann Nucl Med.* 2017;31:686–695.

10. Siman W, Kappadath SC. Comparison of step-and-shoot and continuous-bed-motion PET modes of acquisition for limited-view organ scans. *J Nucl Med Technol.* 2017;45:290–296.

11. Osborne DR, Acuff S. Whole-body dynamic imaging with continuous bed motion PET/CT. *Nucl Med Commun.* 2016;37:428–431.

12. Rausch I, Ruiz A, Valverde-Pascual I, Cal-González J, Beyer T, Carrio I. Performance evaluation of the Vereos PET/CT system according to the NEMA NU2-2012 standard. *J Nucl Med.* 2019;60:561–567.

13. Hsu DFC, Ilan E, Peterson WT, Uribe J, Lubberink M, Levin CS. Studies of a next-generation silicon-photomultiplier-based time-of-flight PET/CT system. *J Nucl Med.* 2017;58:1511–1518.

14. van Sluis J, de Jong J, Schaar J, et al. Performance characteristics of the digital Biograph Vision PET/CT system. *J Nucl Med.* 2019;60:1031–1036.

15. Tsutsui Y, Awamoto S, Himuro K, Kato T, Baba S, Sasaki M. Evaluating and comparing the image quality and quantification accuracy of SiPM-PET/CT and PMT-PET/CT. *Ann Nucl Med.* 2020;34:725–735.

16. Wagatsuma K, Miwa K, Sakata M, et al. Comparison between new-generation SiPM-based and conventional PMT-based TOF-PET/CT. *Phys Med.* 2017;42:203–210.

17. Surti S, Viswanath V, Daube-Witherspoon ME, Conti M, Casey ME, Karp JS. Benefit of improved performance with state-of-the art digital PET/CT for lesion detection in oncology. *J Nucl Med.* 2020;61:1684–1690.

18. Fukukita H, Suzuki K, Matsumoto K, et al. Japanese guideline for the oncology FDG-PET/CT data acquisition protocol: synopsis of version 2.0. *Ann Nucl Med.* 2014;28:693–705.

19. Hashimoto N, Morita K, Tsutsui Y, Himuro K, Baba S, Sasaki M. Time-of-flight information improved the detectability of subcentimeter spheres using a clinical PET/CT scanner. *J Nucl Med Technol.* 2018;46:268–273.

20. Akamatsu G, Ikari Y, Nishida H, et al. Influence of statistical fluctuation on reproducibility and accuracy of SUVmax and SUVpeak: a phantom study. *J Nucl Med Technol.* 2015;43:222–226.

Influence of Minimum Count in Brain Perfusion SPECT: Phantom and Clinical Studies

Akie Sugiura[1,2], Masahisa Onoguchi[2], Takayuki Shibutani[2], and Yasuhisa Kouno[1]

[1]Department of Radiological Technology, Kariya Toyota General Hospital, Kariya, Japan; and [2]Department of Quantum Medical Technology, Graduate School of Medical Sciences, Kanazawa University, Kanazawa, Japan

The count per pixel in brain perfusion SPECT images depends on the administered dose, acquisition time, and patient condition and sometimes become low in daily clinical studies. The aim of this study was to evaluate the effect of different acquisition counts on qualitative images and statistical imaging analysis and to determine the minimum count necessary for accurate examinations. **Methods:** We performed a brain phantom experiment simulating normal accumulation of ^{99m}Tc-ethyl cysteinate dimer as a brain uptake of 5.5%. The SPECT data were acquired in a continuous repetitive rotation. Ten types of SPECT images with different acquisition counts were created by varying the number of rotations added. We used normalized mean squared error and visual analysis. For the clinical study, we used images of 25 patients. The images were acquired in a continuous repetitive rotation, and we created 6 brain images with different acquisition counts by varying the number of rotations added from 1 to 6. The contrast-to-noise ratio was calculated from the mean counts within regions of interest in gray and white matter. In addition, the severity, extent, and ratio of disease-specific regions were evaluated as indices of statistical imaging analysis. **Results:** For the phantom study, the curve of normalized mean squared error tended to converge from approximately 23.6 counts per pixel. Furthermore, the visual score showed that images with 23.6 counts per pixel or less were barely diagnosable. For the clinical study, the contrast-to-noise ratio was significantly decreased at 11.5 counts per pixel or less. Severity and extent tended to increase with decreasing acquisition counts, and a significant increase was shown at 5.9 counts per pixel. On the other hand, there was no significant difference in ratios among different acquisition counts. **Conclusion:** On the basis of a comprehensive assessment of phantom and clinical studies, we suggest that 23.6 counts per pixel or more are necessary to maintain the quality of qualitative images and to accurately calculate indices of statistical imaging analysis.

Key Words: brain perfusion imaging; statistical imaging analysis; artifact; acquisition counts; SPECT

Brain perfusion SPECT has an important role in diagnosing the severity of cerebral vascular disorders, determining their prognosis, and identifying dementia, which contribute to clinical management of patients (*1*). SPECT has a lower spatial resolution than morphologic neuroimaging techniques such as CT and MRI but allows for visualization and quantification of brain function and metabolism, which are difficult to evaluate by other modalities.

In addition to visual interpretation, SPECT images can be interpreted using statistical image analysis such as 3-dimensional stereotactic surface projections (*2*) and statistical parametric mapping (*3*). In these widely applied methods, the individual brain image is transformed into a template and the relative regional uptake is compared voxel by voxel with the reference database to generate the *z* score of hypoperfusion (*4*). The results are projected onto the brain surface to create a surface representation of the *z* score (*5*), which facilitates diagnosis in areas that are difficult to assess visually (*6*).

However, counts per pixel in brain perfusion SPECT images depend on the administered dose, acquisition time, and patient condition and sometimes become low in daily clinical studies. It is well known that statistical noise has a significant impact on image quality. The relationship between statistical noise (*N*) and counts per pixel (*n*) is expressed as $N = \sqrt{n}/n \times 100$ (*7*), where the signal-to-noise ratio of the SPECT image is proportional to the square root of all counts. As the number of acquisition counts decreases, statistical noise increases and image quality deteriorates.

The purpose of this study was to evaluate the effect of different acquisition counts on qualitative images and statistical imaging analysis and to determine the minimum acquisition count necessary for accurate examinations. When clinical limitations result in low acquisition counts, we can attend to interpretation of the qualitative images and the indices. Although published studies are available on the influence of acquisition and reconstruction methods (*8–10*), this is the first time—to our best knowledge—that minimum acquisition count has been addressed.

MATERIALS AND METHODS

Phantom Design

A Hoffman 3-dimensional brain (Kyoto Kagaku Co., Ltd.) that simulates gray-matter and white-matter structures with a 4:1 activity concentration was used as the phantom (*11*). This phantom was filled with a 37 kBq/mL solution of ^{99m}Tc. The total activity in the phantom was 44.4 MBq at the acquisition start. There is assumed to be a normal accumulation of ^{99m}Tc-ethyl cysteinate dimer with

a dose of 822 MBq as a brain uptake of 5.5% (12). The dose was determined with reference to the subjects used in the clinical studies.

Patients

Images of 25 patients (16 men and 9 women; mean age, 75 ± 11.3 y) who underwent resting-state brain perfusion ^{99m}Tc-ethyl cysteinate dimer SPECT from March 2016 to March 2019 were retrospectively used. These patients had degenerative nerve diseases ($n = 22$) or cerebrovascular diseases ($n = 3$). The imaging diagnosis indicated decreased cerebral blood flow in all cases. Permission for this study was obtained from the hospital ethics committee.

Image Acquisition

In both phantom and clinical studies, the SPECT acquisition was performed with a dual-head γ-camera (Discovery NM/CT 670 Q.Suite Pro; GE Healthcare Japan) equipped with a low-energy high-resolution collimator. The main energy window was 140.5 keV ± 10% width. The subwindows were set at 159.5 keV ± 3% and 121.5 keV ± 4% for scatter correction. The matrix size was 128 × 128, and the pixel size was 2.94 mm (×1.5 zoom). The data were acquired in continuous mode in a 360° circular orbit (radius of rotation, 150 mm) and 90 projections of a 4° step angle.

For the phantom study, the SPECT acquisition time was set as 3.5 min with 6 rotations and, subsequently, as 7.5 min with 16 rotations (Fig. 1A). For the clinical study, ^{99m}Tc-ethyl cysteinate dimer (Fujifilm Toyama Chemical Co., Ltd.) of 805 ± 40.1 MBq was injected intravenously; 15 min later, images were acquired for 6 rotations at 3.5 min per projection (Fig. 1B).

Image Reconstruction

The SPECT images were reconstructed using filtered backprojection with a Ramachandran filter in the phantom and clinical studies. A Butterworth filter (order, 16; cutoff frequency, 0.55 cycles/cm) was used for the prefilter for smoothing. The cutoff frequency of 0.55 cycles/cm was optimized in advance by calculating the normalized mean squared error (NMSE) from high-quality images with a long acquisition time. Attenuation correction with the Chang method was performed assuming a uniform attenuation coefficient of 0.13 cm^{-1} and a 10% attenuation threshold. The triple-energy-window method (13) was used for scatter correction. All images were reconstructed on a workstation using Xeleris, version 3.1 (GE Healthcare Japan).

Image Evaluation

To measure the mean acquisition counts (counts per pixel), we drew a region of interest (ROI) surrounding whole brain on the anterior planar image of the projection data for the phantom (Fig. 2A) (14). Brain images were created with 10 different acquisition counts (123.6, 92.3, 61.0, 30.8, 23.6, 19.9, 16.0, 12.0, 7.9, and 4.0 counts per pixel). The NMSE and visual analysis were used to assess each phantom image.

NMSE. The NMSE is given using the following equation:

$$\text{NMSE} = \frac{\sum_{x=0}^{x=n-1}\sum_{y=0}^{y=m-1}(f(x,y)-g(x,y))^2}{\sum_{x=0}^{x=n-1}\sum_{y=0}^{y=m-1}f(x,y)^2},$$

where $f(x,y)$ is equal to the ideal image, $g(x,y)$ is equal to each phantom image, m means matrix size for y, and n means matrix size for x. In this study, the ideal image was created by projections with high acquisition counts (123.6 counts per pixel) to reduce the statistical noise. To precisely assess the convergence of the NMSE in relation to acquisition counts, we evaluated the derivative value of NMSE.

Visual Analysis. Using visual analysis, we scored 10 types of brain images on the basis of how high the counts were. Five observers with expertise in nuclear medicine interpreted the transverse images (Fig. 3) To reduce variability in visual analysis, pretraining was performed using sample images. At that time, we told the observers to assume clinical use, not scientific use, and to observe the cortical accumulation. In a masked manner, they assessed all series and scored them using a scale of 0–4 (4, very good; 3, sufficient for diagnosis; 2, barely diagnosable; 1, cannot be diagnosed responsibly; 0, cannot be diagnosed). The average score for all observers was calculated. The color lookup table was set to inverted grayscale, and the upper and lower limits of the window level were set to 0% and 100%, respectively. Furthermore, enlargement and reduction of the images, observation distance, and observation time were arbitrary. We obtained written consent for all observers to participate in this study.

By varying the number of added rotations on a workstation, we created 6 patient brain images comprising different acquisition counts. The mean acquisition counts were measured by setting an ROI on the normal or mild side on the anterior planar image of the projection data (Fig. 2B) (14). Patient images with a minimum of 30 counts per pixel were used. From the results of NMSE and
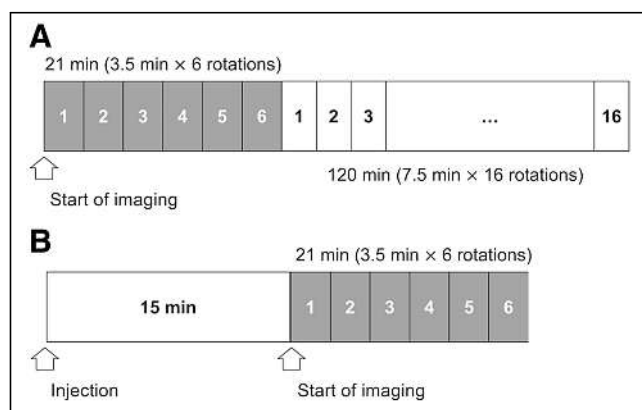
FIGURE 1. SPECT acquisition protocols in this study. (A) Phantom study. Images are acquired for 3.5 min with 6 rotations and subsequently 7.5 min with 16 rotations. (B) Brain perfusion SPECT protocol using ^{99m}Tc-ethyl cysteinate dimer in clinical study. Images are acquired for 21 min [(3.5 min/rotation) × 6 rotations], beginning 15 min after injection.
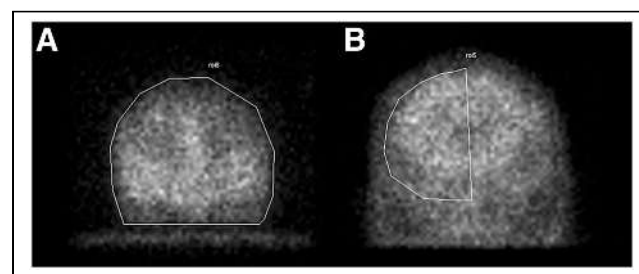
FIGURE 2. (A) ROI for phantom study set to surround whole brain on anterior planar image of projection data. (B) ROI for clinical study set to surround normal or mild side on anterior planar image of projection data.
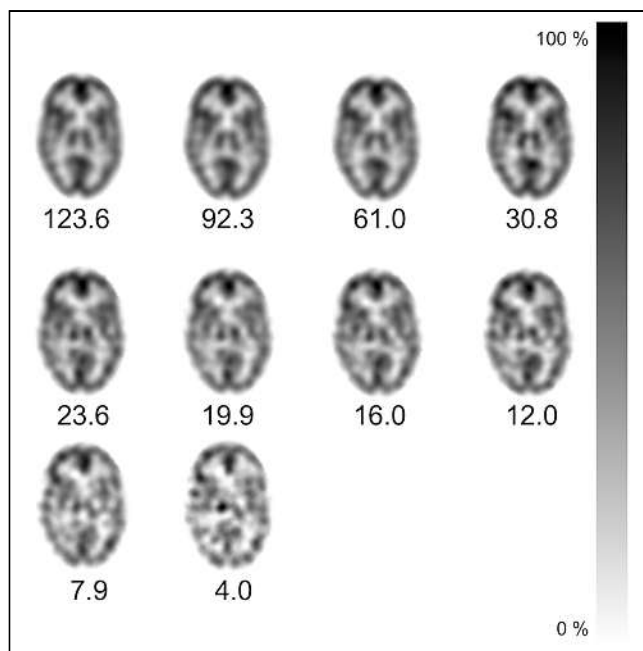
FIGURE 3. Representative slices of images for visual analysis. Images were created from 10 types of projection data with different acquisition counts (123.6, 92.3, 61.0, 30.8, 23.6, 19.9, 16.0, 12.0, 7.9, and 4.0 counts per pixel).

FIGURE 4. NMSE as function of counts per pixel in brain phantom.

visual analysis, we determined the image with 30 counts per pixel or more to be sufficient for diagnosis.

We used the contrast-to-noise ratio (CNR) and the indices from the easy z score imaging system (eZIS) (4) to assess the influence of low acquisition counts on qualitative images and statistical imaging analysis.

CNR. ROIs were automatically drawn on transverse images using the 3-dimensional stereotactic ROI template software, and average reconstructed image counts were calculated by dividing the brain into 12 segments (15). The CNR is given using the following equation:

$$CNR = (decreases\ in\ rCBF\ signal - background)/$$
$$standard\ division\ (background),$$

where decreases in regional cerebral blood flow (rCBF) signal are the average reconstructed-image counts in an ROI surrounding the areas diagnosed as decreases in rCBF on brain perfusion SPECT, background is the average reconstructed image counts of cerebellum ROIs, and standard division (background) is the standard division of cerebellum ROIs (16). Therefore, patients with decreases in rCBF in the cerebellum were excluded from the study. The CNR was obtained from the 6 brain images and normalized by the value of the 6-rotation image.

eZIS Analysis. eZIS analysis discriminates early Alzheimer disease from other types of dementia using computer-assisted statistical analysis. The indices of eZIS that characterize decreases in rCBF in patients with very early Alzheimer disease—namely severity, extent, and ratio—were calculated, automatically analyzing the specific volume of interest (VOI) in the posterior cingulate gyrus, precuneus, and parietal cortices. The severity and extent show the degree and percentage of rCBF decrease in the VOI. The ratio shows the percentage of rCBF decrease in the VOI to a whole brain. The severity, extent, and ratio were obtained from
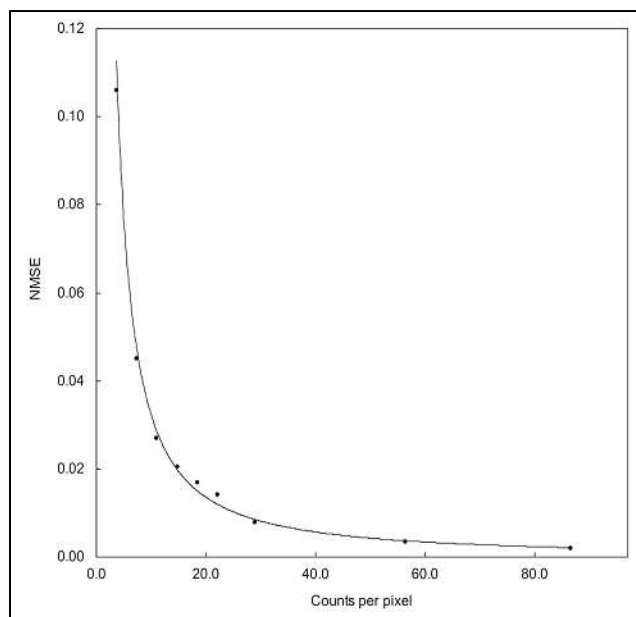
6 brain images of different acquisition counts for each patient and were normalized by the values of the 6-rotation image. Patients with degenerative nerve diseases ($n = 22$) were analyzed because eZIS was used in the differential diagnosis of dementia. We performed the eZIS analysis using a Daemon research image processor, version 1.1.0.0 (DRIP; Fujifilm Toyama Chemical Co., Ltd.)

Statistical Analysis

All statistical analyses were performed using the statistical package EZR (version 1.38) (17). Visual scores were compared for differences using the Kruskal–Wallis/Steel test. Wilcoxon signed-rank testing with the Bonferroni adjustment was used to analyze CNR, severity, extent, and ratio among all image sets. A P value of less than 0.01 was considered statistically significant.

RESULTS

Phantom Study

In the curve of NMSE in relation to acquisition counts, a tendency toward convergence was observed with increasing acquisition counts (Fig. 4). The curve of the derivative value of NMSE rapidly increased at low acquisition counts, followed by saturation as close to zero as possible above 23.6 counts per pixel (Fig. 5).

The visual score increased with increasing acquisition counts and showed a score higher enough than "2, barely diagnosable" at 23.6 counts per pixel or more and a score higher enough than "3, sufficient for diagnosis" at 30 counts per pixel or more (Fig. 6).

Clinical Study

The CNR was significantly decreased at 11.5 counts per pixel or less ($P < 0.01$, Table 1).

Severity and extent tended to increase with decreasing acquisition counts, and a significant increase was shown at
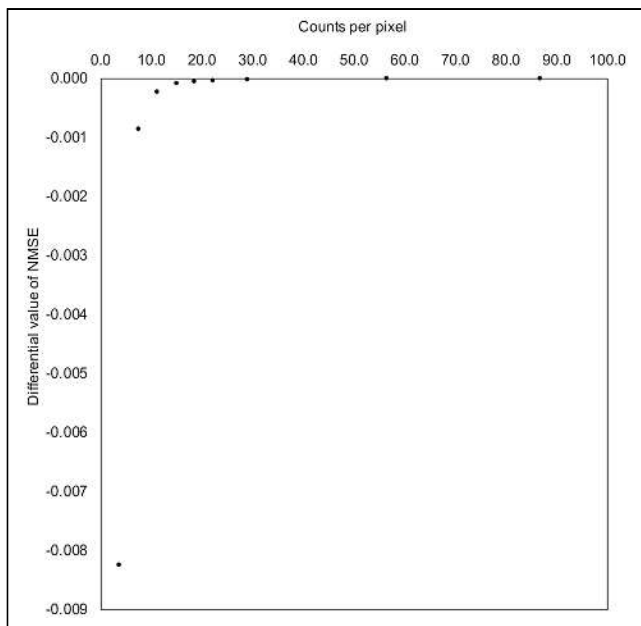
FIGURE 5. Differential value of NMSE as function of counts per pixel.

5.9 counts per pixel ($P < 0.01$). On the other hand, ratio was independent of acquisition counts, and there was no significant difference in ratios among acquisition counts (Table 2). Differences in the average counts per pixel between Tables 1 and 2 were caused by differences in the numbers of patients analyzed in CNR and eZIS analysis. Figure 7 compares the 6-rotation image (32.9 counts per pixel) with the image
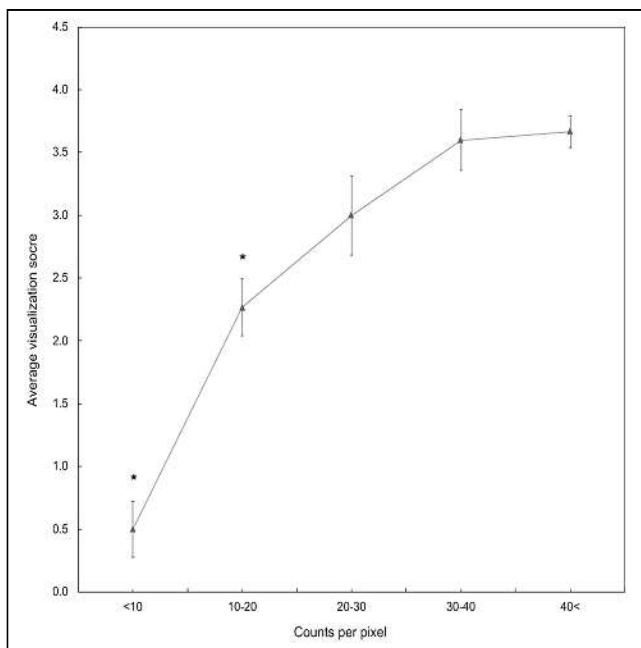
FIGURE 6. Relationship between average visualization score and each range of counts per pixel. *Versus 40 counts per pixel or more, $P < 0.01$.

obtained at a low acquisition count (6.2 counts per pixel) using statistical imaging analysis.

DISCUSSION

Recent dementia practice guidelines recommend use of morphologic imaging (MRI or CT) to exclude neurosurgical dementia and then use of functional imaging (brain perfusion SPECT or dopamine transporter scintigraphy) to make a differential diagnosis (18). Brain perfusion SPECT is commonly used in differential diagnosis of dementia to assess the pattern of hypoperfusion for each type of dementia and is also expected to be used for early diagnosis of Alzheimer disease in patients with mild cognitive impairment (19). On the other hand, in daily practice for patients with dementia, the characteristic symptoms may force interruption or shortening of the scan. A consequence is that they sometimes lead to low acquisition counts. Therefore, it is important to study the effects of different acquisition counts and to determine the minimum count necessary for accurate examinations. We believe that our study will prove useful in daily clinical practice.

Much previous research has dealt with improving image quality in brain perfusion SPECT by reducing image noise. As a result, it is now possible to obtain images with less statistical noise by optimizing the low-pass filter or using multipinhole collimators (8,9). Furthermore, it has been reported that iterative reconstruction technology with resolution recovery algorithms can improve spatial resolution while suppressing statistical noise (10). However, studies on decreases in acquisition counts are insufficient, although such decreases may occur in daily clinical practice.

As a result of the phantom study, we considered 23.6 counts per pixel or more necessary to maintain image quality, because the NMSE showed a convergence at 23.6 counts per pixel or more and the score with visual analysis was higher enough than "2, barely diagnosable" at 23.6 counts per pixel or more. NMSE is commonly used to optimize the low-pass filter or the iteration number and well reflects the influence of statistical noise on SPECT images (8,10). Furthermore, it was assumed that statistical noise did not affect the ideal image of the NMSE because we reconstructed the ideal image from projection data with statistical noise lower than 10%, applying an optimized Butterworth filter. In addition, visual assessment by scoring is also widely used in nuclear medicine imaging (20). Therefore, the obtained results are reliable.

In the clinical study, the value of CNR showed a significant decrease at 11.5 counts per pixel, and we decided that 17.2 counts per pixel or more did not affect the detection of decreases in rCBF. The severity and extent tended to increase with decreasing acquisition counts, and a significant increase was shown at 5.9 counts per pixel ($P < 0.01$). It was assumed that statistical noise was determined as a hypoperfusion area in the specific VOI during eZIS analysis (21), and we need to note false-positives in differential diagnosis of dementia using eZIS analysis. We decided that

TABLE 1
Average and SD of CNR at Different Counts per Pixel in patients with degenerative nerve diseases ($n = 22$) and cerebrovascular diseases ($n = 3$)

Parameter	6 rotations	5 rotations	4 rotations	3 rotations	2 rotations	1 rotation
Counts per pixel	33.6 ($\pm$4.25)	28.3 ($\pm$3.55)	22.7 ($\pm$2.86)	17.2 ($\pm$2.17)	11.5 ($\pm$1.45)	5.9 ($\pm$0.73)
Normalized CNR	1.00 ($\pm$0.0)	0.99 ($\pm$0.08)	0.96 ($\pm$0.10)	0.92 ($\pm$0.16)	0.84 ($\pm$0.17)*	0.56 ($\pm$0.25)*

*Versus 33.6 counts per pixel, $P < 0.01$.

TABLE 2
Average and SD of Indices (Severity, Extent, and Ratio) at Different Counts per Pixel in Patients with Degenerative Nerve Diseases ($n = 22$)

Parameter	6 rotations	5 rotations	4 rotations	3 rotations	2 rotations	1 rotation
Counts per pixel	33.9 ($\pm$4.45)	28.5 ($\pm$3.72)	22.9 ($\pm$2.99)	17.3 ($\pm$2.28)	11.6 ($\pm$1.52)	5.9 ($\pm$0.77)
Normalized severity	1.00 ($\pm$0.0)	1.01 ($\pm$0.05)	1.05 ($\pm$0.06)	1.05 ($\pm$0.08)	1.07 ($\pm$0.15)	1.50 ($\pm$0.47)*
Normalized extent	1.00 ($\pm$0.0)	1.00 ($\pm$0.12)	1.11 ($\pm$0.15)	1.18 ($\pm$0.55)	1.11 ($\pm$0.41)	2.34 ($\pm$2.12)*
Normalized ratio	1.00 ($\pm$0.0)	0.97 ($\pm$0.11)	1.02 ($\pm$0.14)	1.01 ($\pm$0.51)	0.84 ($\pm$0.28)	1.33 ($\pm$1.17)

*Versus 33.9 counts per pixel, $P < 0.01$.

11.6 counts per pixel or more did not affect the severity and extent. The minimum acquisition count for severity and extent is lower than that for CNR because of the smoothing process included in the eZIS analysis process (22). On the other hand, the ratio was independent of the acquisition counts, suggesting that the statistical noise influenced not only the specific VOI but also the whole brain. The phantom study simulated normal human brain, whereas the clinical study addressed detection of cerebral hypoperfusion.

FIGURE 7. Typical brain perfusion images using statistical image analysis obtained at different counts in patient: reference images obtained at 32.9 counts per pixel (A) and images obtained at 6.2 counts per pixel (B). False-positives were observed in specific VOI (red border).

Therefore, we considered that differences occurred between visual analysis in the phantom study and the results of the clinical investigation.

On the basis of comprehensive assessment of phantom and clinical studies, we determined that 23.6 counts per pixel were the minimum to maintain the quality of qualitative images and to accurately calculate indices of statistical imaging analysis. Generally, more than 100 counts per pixel were needed to suppress statistical noise (7). Stelter et al. (23) also suggested 50 counts per pixel or more for sufficient image quality. We considered that our result differed from previous studies because this research dealt with the minimum acquisition count, not with sufficient image quality. The presence of cerebral ventricles in the ROI that we set may also affect the acquisition counts. For routine brain perfusion SPECT examinations, we recommend using the proposed minimum acquisition count either as the criterion for reexamination or as a warning to the physician.

There were some limitations to this study. First, we categorized 10 types of brain images to 5 scales of image quality by visual analysis, but having 5 scales of image quality is actually vague and may include various aspects of image quality such as observer preference. Therefore, when setting the cutoff for the counts, we selected 30.0 counts per pixel or 23.6 counts per pixel, at which the score was higher enough than 3 or 2 to have margins. Further study should be conducted to clarify the differences in the 5 scales and to reveal the relationship between less-than-ideal image quality and diagnostic accuracy. A second limitation was the difference between the devices. Differences in reconstruction methods, low-pass filters, or various correction methods are surmised to affect the minimum acquisition count.
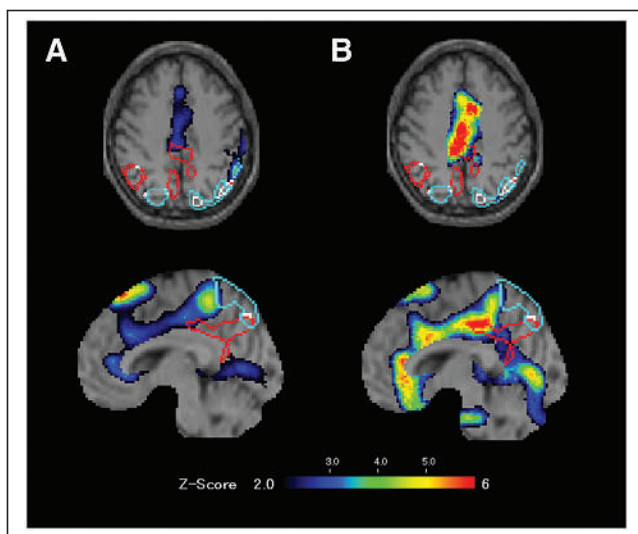
But we considered the results of statistical imaging analysis to be widely applicable to other devices because the analysis reduces differences between devices by anatomic standardization and smoothing. The minimum acquisition count can lead to precise diagnosis and shorter scan times. Furthermore, in young patients, use of a minimum count is expected to reduce radiation exposure by optimizing the radiopharmaceutical dose. Therefore, in the future, it is desirable to determine the minimum acquisition count, considering differences between devices.

CONCLUSION

On the basis of this comprehensive assessment of phantom and clinical studies, we suggest that 23.6 counts per pixel or more are necessary to maintain the quality of qualitative images and to accurately calculate indices of statistical imaging analysis. The proposed minimum acquisition count will help raise the reliability of brain perfusion SPECT, such as by serving as the criterion for reexamination or as a warning to the physician.

DISCLOSURE

ACKNOWLEDGMENT

KEY POINTS

QUESTION: What is the minimum acquisition count for brain perfusion SPECT?

PERTINENT FINDINGS: In this phantom and clinical study, the minimum acquisition count was 23.6 per pixel.

IMPLICATIONS FOR PATIENT CARE: The proposed minimum acquisition count will help raise the reliability of brain perfusion SPECT.

REFERENCES

1. Camargo EE. Brain SPECT in neurology and psychiatry. *J Nucl Med.* 2001;42: 611–623.
2. Minoshima S, Frey KA, Koeppe RA, Foster NL, Kuhl DE. A diagnostic approach in Alzheimer's disease using three-dimensional stereotactic surface projections of fluorine-18-FDG PET. *J Nucl Med.* 1995;36:1238–1248.
3. Friston KJ, Frith CD, Fletcher P, Liddle PF, Frackowiak RS. Functional topography: multidimensional scaling and functional connectivity in the brain. *Cereb Cortex.* 1996;6:156–164.
4. Kanetaka H, Matsuda H, Asada T, et al. Effects of partial volume correction on discrimination between very early Alzheimer's dementia and controls using brain perfusion SPECT. *Eur J Nucl Med Mol Imaging.* 2004;31:975–980.
5. Matsuda H, Mizumura S, Nagao T, et al. Automated discrimination between very early Alzheimer disease and controls using an easy Z score imaging system for multicenter brain perfusion single-photon emission tomography. *AJNR.* 2007;28: 731–736.
6. Imabayashi E, Matsuda H, Asada T, et al. Superiority of 3-dimensional stereotactic surface projection analysis over visual inspection in discrimination of patients with very early Alzheimer's disease from controls using brain perfusion SPECT. *J Nucl Med.* 2004;45:1450–1457.
7. Todd-Pokropek AE, Jarritt PH. The noise characteristics of SPECT systems. In: Ell PJ, Holman BL, eds. *Computed Emission Tomography.* Oxford University Press; 1983:361–389.
8. Minoshima S, Maruno H, Yui N, et al. Optimization of Butterworth filter for brain SPECT imaging. *Ann Nucl Med.* 1993;7:71–77.
9. Chen L, Tsui BM, Mok GS. Design and evaluation of two multi-pinhole collimators for brain SPECT. *Ann Nucl Med.* 2017;31:636–648.
10. Yokoi T, Shinohara H, Onishi H. Performance evaluation of OSEM reconstruction algorithm incorporating three-dimensional distance-dependent resolution compensation for brain SPECT: a simulation study. *Ann Nucl Med.* 2002;16:11–18.
11. Hoffman EJ, Cutler PD, Diby WM, Mazziotta JC. Three dimensional phantom to simulate cerebral blood flow and metabolic images for PET. *IEEE Trans Nucl Sci.* 1990;37:616–620.
12. Kubo A, Nakamura K, Tsukatani Y, et al. Phase I clinical study of ^{99m}Tc-ECD. *Kaku Igaku.* 1992;29:1019–1027.
13. Ogawa K, Harata Y, Ichihara T, Kubo A, Hashimoto S. A practical method for position-dependent Compton-scattered correction in single photon emission CT. *IEEE Trans Med Imaging.* 1991;10:408–412.
14. Yamanaga T, Hasegawa S, Imoto A, et al. Guidelines for standardization of brain perfusion SPECT imaging 1.0. *Kakuigaku Gijutsu.* 2017;37:505–516.
15. Takeuchi R, Yonekura Y, Matsuda H, Konshi J. Usefulness of a three-dimensional stereotaxic ROI template on anatomically standardised ^{99m}Tc-ECD SPET. *Eur J Nucl Med Mol Imaging.* 2002;29:331–341.
16. Matsuda H, Mizumura S, Nagao T, et al. An easy Z-score imaging system for discrimination between very early Alzheimer's disease and controls using brain perfusion SPECT in a multicentre study. *Nucl Med Commun.* 2007;28:199–205.
17. Kanda Y. Investigation of the freely available easy-to-use software 'EZR' for medical statistics. *Bone Marrow Transplant.* 2013;48:452–458.
18. Ngo J, Holroyd-Leduc JM. Systematic review of recent dementia practice guidelines. *Age Ageing.* 2015;44:25–33.
19. Ito K, Mori E, Fukuyama H, et al. Prediction of outcomes in MCI with ^{123}I-IMP-CBF SPECT: a multicenter prospective cohort study. *Ann Nucl Med.* 2013; 27:898–906.
20. Fukukita H, Suzuki K, Matsumoto K, et al. Japanese guideline for the oncology FDG-PET/CT data acquisition protocol: synopsis of version 2.0. *Ann Nucl Med.* 2014;28:693–705.
21. Yanamoto T, Onishi H, Murakami T, Takahashi M, Odajima S, Uchida K. Research report: accuracy and evaluation of the stereotactic statistical imaging analysis of the brain. *Nippon Hoshasen Gijutsu Gakkai Zasshi.* 2008;64:752–765.
22. Yamamoto Y, Onoguchi M. Statistical image analysis method to use for cerebral blood flow SPECT examination: difference and matters that require attention of processing of eZIS and iSSP. *Nippon Hoshasen Gijutsu Gakkai Zasshi.* 2011;67: 718–727.
23. Stelter P, Junik R, Krzyminiewski R, Gembicki M, Sowin'ski J. Semiquantitative analysis of SPECT images using $^{99}Tc^m$-HMPAO in the treatment of brain perfusion after the attenuation correction by the Chang method and the application of the Butterworth filter. *Nucl Med Commun.* 2001;22:857–865.

The Complementary Role of ^{68}Ga-DOTATATE PET/CT in Diagnosis of Recurrent Meningioma

Min J. Kong[1], Aaron F. Yang[1], Sujay A. Vora[2], Jeffrey S. Ross[1], and Ming Yang[1]

[1]Department of Radiology, Mayo Clinic, Scottsdale, Arizona; and [2]Department of Radiation Oncology, Mayo Clinic, Scottsdale, Arizona

Contrast-enhanced brain MRI is the imaging modality of choice in diagnosis and posttreatment evaluation, but its role is limited in distinguishing recurrent lesions from postoperative changes. ^{68}Ga-DOTATATE is a somatostatin analog PET tracer that has high affinity to meningioma expressing somatostatin receptor. **Methods:** In this case series review, we describe 8 patients with brain MRI showing suspected recurrent meningioma who underwent focused ^{68}Ga-DOTATATE PET/CT for radiation treatment planning. **Results:** The combined brain MRI and PET/CT improved the conspicuity of the lesions and aided radiation treatment planning. The time from the initial surgery to PET/CT varied widely, ranging from 1 to 12 y. Three patients underwent PET/CT shortly after the initial surgery (1–3 y) and underwent targeted radiation therapy. Subsequent imaging showed no evidence of recurrence. Four patients had a prolonged time between the PET/CT and the initial surgery (7–12 y), which showed an extensive tumor burden. All 4 patients died shortly after the last PET/CT scan. **Conclusion:** ^{68}Ga-DOTATATE PET shows a promising complementary role in detection and treatment planning of recurrent meningioma.

Key Words: meningioma; somatostatin receptor; DOTATATE; octreotide

Meningioma is the most common primary tumor of the central nervous system, accounting for approximately 27% of all intracranial tumors (*1–3*). On the basis of histologic features and its local aggressiveness, meningiomas are grouped into 3 grades (I–III) on the World Health Organization (WHO) scale. Although most meningiomas are grade I, factors such as mitoses and aggressive histology can predict a higher rate of recurrence (*4*). The most common locations of meningioma are the sites of dural reflection, including falx cerebri, tentorium cerebelli, and venous sinuses (*5*). Certain locations are associated with increased morbidity and mortality and pose challenges in treatment, regardless of grade.

The standard treatment for symptomatic meningioma is surgical resection, with complete removal of the tumor being the main determinant of its prognosis. Meningioma recurrence requiring a second operation is a poor prognostic factor, along with malignant degeneration of the recurrent tumors (*6,7*). Radiation therapy is another treatment option for malignant and recurrent meningioma, although its role in benign meningioma remains controversial (*7*). Despite these therapeutic options, the overall 10-y survival of benign meningioma is 87%, and the 10-y survival for malignant meningioma remains approximately 60% (*8*).

Contrast-enhanced (CE) MRI is the imaging modality of choice in diagnosis, treatment planning, and postoperative evaluation of meningioma. However, CE MRI has a limited role in distinguishing recurrent tumor from postoperative changes. (*9*) Meningiomas exhibit strong somatostatin receptor expression, especially type 2, which can be detected by octreotide-based scintigraphy (^{111}In-octreotide SPECT [OctreoScan; Mallinckrodt Pharmaceuticals]) (*10,11*). In the last decade, ^{68}Ga-labeled somatostatin analog PET tracers have been used in the diagnosis and staging of gastroenteropancreatic neuroendocrine tumor. Among them, ^{68}Ga-DOTATATE has gained growing popularity in imaging of meningioma given its high specificity and nearly 10-fold increased affinity to somatostatin receptor 2 (SSTR-2) compared with ^{111}In-octreotide SPECT. ^{68}Ga-DOTATATE PET/CT plays a complementary role in imaging meningioma, including recurrent and residual lesions (*10,12–15*).

In this article, we report our initial experience in using combined brain CE MRI and ^{68}Ga-DOTATATE PET/CT to identify recurrent meningioma and aid radiation therapy. We also discuss the potential theragnostic application of ^{68}Ga-DOTATATE in management of recurrent or nonresectable meningioma.

MATERIALS AND METHODS

This study was conducted under the approval of the institutional review board. Patients who were diagnosed with recurrent meningioma or were suspected of having recurrent meningioma in 2017–2021 were retrospectively identified.

Surveillance CE MRI with ^{68}GaDOTATATE PET/CT was performed on all patients. Brain MRI was performed on 1.5-T or 3-T scanners under a routine MRI brain tumor protocol with multiple sequences consisting of 3-dimensional T1-weighted, T2-weighted, fluid-attenuated inversion recovery, diffusion-weighted, gadolinium CE 3-dimensional T1-weighted, and T1-weighted spoiled gradient echo. Dedicated brain MR images were interpreted by fellowship-trained neuroradiologists. To further define the tumor burden and

TABLE 1
Demography of Meningioma Patients

Patient no.	Sex	WHO grade	Age (y)	Initial location	Onset	Treatment history	PET/CT time (y)	PET/CT findings	Follow-up therapy	Outcome
1	F	1	69	Right frontal	2005	Craniotomy × 3, CyberKnife embolization	12	Positive	Bevacizumab, octreotide	Died
2	F	2	82	Right sphenoid	2016	Craniotomy × 2	1	Positive × 2	Proton beam therapy	Survived
3	M	2	72	Bifrontal	2009	Craniotomy × 3, radiation therapy	8	Positive	Octreotide	Died
4	M	2	59	Left skull base	2008	γ-knife	10	Positive	Octreotide	Died
5	M	2	77	Bifrontal	2012	Radiosurgery, craniotomy × 2	7	Positive	Octreotide, bevacizumab	Died
6	M	2	72	Left frontoparietal	2015	Craniotomy × 1, radiation therapy	3	Positive	Proton beam therapy	Survived
7	F	3	47	Right frontal	2008	Craniotomy × 1	12	Negative × 2	Surveillance	Survived
8	F	1	68	Right skull base	2021	Partial resection	1	Positive	Radiation therapy	Survived

guide the subsequent treatment strategy, patients with suggestive focal enhancement on post-CE MR images underwent ^{68}Ga-DOTATATE PET/CT.

^{68}Ga-DOTATATE PET/CT of the head was performed 40 min after intravenous injection of 185 ($\pm$10%) MBq of ^{68}Ga-DOTA-TATE, with additional bone algorithm reconstruction CT images. Head PET/CT images were sent to an independent workstation (MIM Software, Inc.) for interpretation by nuclear radiologists who were dually board-certified (American Board of Radiology and American Board of Nuclear Medicine).

The ultimate diagnosis of meningioma recurrence was based on imaging: on CE MRI, a dura-based enhancing focus at the surgical bed or a new enhancing meningeal focus at other meningeal regions, and on ^{68}Ga-DOTATATE PET/CT, focal meningeal radiotracer uptake with a corresponding dura-based mass on unenhanced CT.

The head PET/CT data were subsequently coregistered with high-resolution 3-dimensional spoiled gradient echo brain MRI sequences for further localization.

RESULTS

Eight patients with a histopathologically proven meningioma after surgical resection were identified (Table 1). Each underwent CE MRI and ^{68}GaDOTATATE PET/CT as a part of the postsurgical surveillance.

One patient showed no evidence of disease recurrence on 2 consecutive PET/CT scans after surgical resection (patient 7) and remained well as of his last clinic visit, without evidence of recurrence. The remaining 7 patients had PET-positive recurrent lesions corresponding to the findings visualized on CE MRI.

The time from the initial surgery to obtaining the PET/CT scans varied widely, ranging from 1 to 12 y (mean, 6.75 y). Three patients (patients 2, 6, and 8) underwent the PET/CT in a relatively short period from the initial surgery (1, 3, and 1 y, respectively), and both PET and MRI showed recurrence. Plans for proton beam therapy and stereotactic radiation therapy were adjusted on the basis of the PET/CT findings. The adjustments included changes in the radiation beam entry point and the trajectory of the radiation. The patients showed improvement in tumor burden on subsequent follow-up CE MRI and were doing well as of the last clinical follow-up visit, without evidence of recurrence.

Four patients (patients 1, 3, 4, and 5) underwent PET/CT after a longer time from the initial surgery (12, 8, 10, and 7 y, respectively). Although octreotide
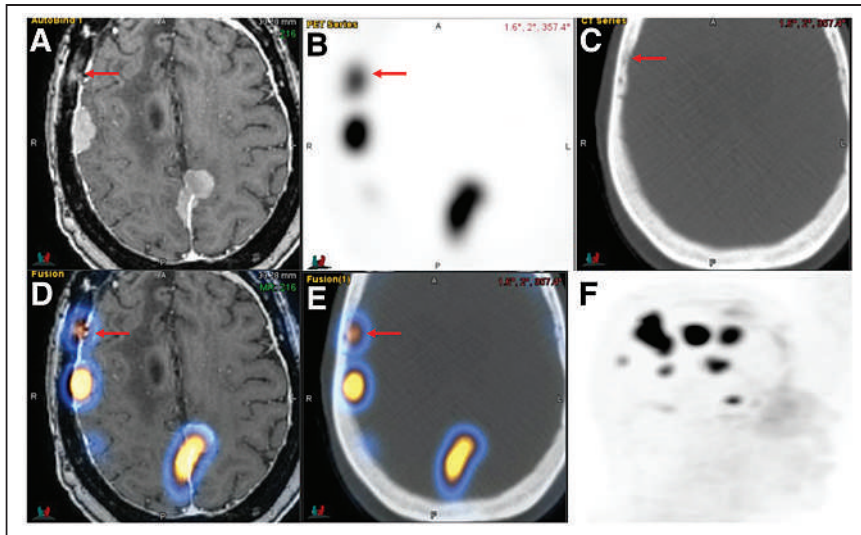
FIGURE 1. Multiple variable-sized, dura-based enhancing lesions exhibit somatostatin receptor positivity on ^{68}Ga-DOTATATE PET/CT. One tracer-avid bone marrow focus on right frontal bone is concerning for meningioma transosseous infiltration (arrows). Maximum-intensity projection exhibits extensive tumor burden of recurrent meningioma. Shown are CE MR image (A), ^{68}Ga-DOTATATE PET image (B), low-dose CT image (C), PET/MR image (D), PET/CT image (E), and PET maximum-intensity projection (F).

therapy was initiated on the basis of the PET/CT findings, all 4 patients showed an extensive tumor burden on the initial PET/CT images and died shortly afterward.

Patient 1

A 69-y-old woman had a clinical history of recurrent WHO grade 1 meningiomatosis and had undergone 3 craniotomies and 1 course of CyberKnife (Accuray) therapy. CE MRI revealed multiple recurrent meningiomas. To accurately evaluate the recurrent tumoral burden, ^{68}Ga-DOTATATE PET/CT was performed. The combined brain MR and PET images depicted multiple variably sized CE, somatostatin receptor–positive meningiomas. The patient received embolization therapy followed by bevacizumab and octreotide and died from disease progression 1 y after the PET/CT scan (Fig. 1).

Patient 2

An 82-y-old woman had a history of WHO grade 2 atypical meningioma with invasion of the right temporalis muscle, calvarium, and dura and had undergone subtotal resection. A large, enhancing mass was confirmed on CE MRI. After surgical resection of the tumor, ^{68}Ga-DOTATATE PET/CT was performed and showed recurrent disease at the surgical bed. This recurrence was not identified on CE MRI because of surrounding postsurgical changes. The ^{68}Ga-DOTATATE PET/CT findings led to repeat craniotomy and definitive proton beam therapy and were used to assist planning of the proton beam therapy. The patient remained free of residual tumor after the radiotherapy (Fig. 2).

Patient 6

A 72-y-old man had a history of left frontal–parietal atypical meningioma (WHO grade 2) and had undergone total tumor resection. The ^{68}Ga-DOTATATE PET images showed 2 recurrent foci at the vertex, which were not seen well on CE MRI given their locations. Radiation therapy planning was adjusted on the basis of the PET/CT findings, including changes in the radiation beam trajectory. The patient received 6,000 cGy of external beam therapy and has been symptom free since then (Fig. 3).

DISCUSSION

CE MRI is the imaging method of choice in the diagnosis of recurrent and residual meningioma. However, its role is limited as it cannot accurately distinguish viable tumors from posttreatment changes. Somatostatin receptor is a G-protein–coupled cell membrane receptor and can be activated by somatostatin or its synthetic analogs. In the brain, expression of SSTR-2 has been observed in meningioma (11,16). Although ^{111}In-octreotide SPECT is a traditionally complementary imaging modality in surveillance of meningioma in posttreatment patient populations, ^{68}Ga-DOTATATE PET/CT is shown to be more effective in imaging meningioma given its high specificity and robust affinity to SSTR-2, with a 10-fold increase compared with ^{111}In-octreotide SPECT (10,17,18). Accumulating literature has shown that PET/CT ligated to ^{68}Ga-DOTA analogs, including DOTATOC,
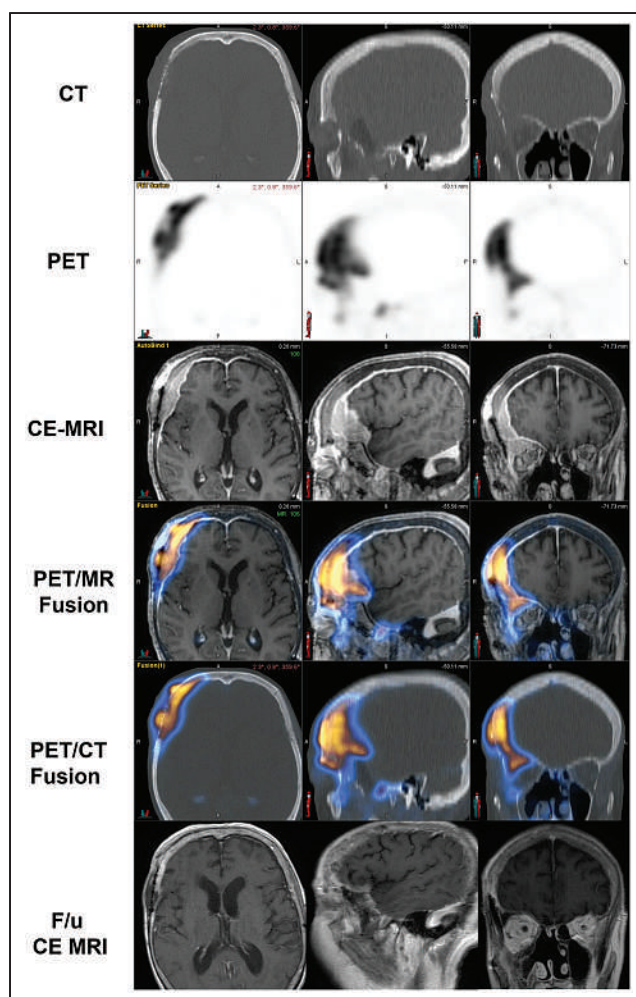
FIGURE 2. ^{68}Ga-DOTATATE PET/CT/MRI series, adapted for radiation therapy planning for proton bean therapy, showed enhancing lesions centered at right temporal craniectomy site, indicating residual tumor after subtotal resection. Three-year follow-up CE MRI showed deceased size of tumor, indicating favorable response to radiation therapy. F/u = follow-up.

DOTANOC, and DOTATATE, has a promising role in identifying and localizing meningioma and may play a complementary role in guiding therapy and predicting survival in select patients (12–15,19–23).

^{68}Ga-DOTATATE uptake can be seen in other primary and secondary brain tumors besides meningioma, including hemangiopericytoma and intracranial metastatic neuroendocrine tumor. The pituitary gland also demonstrates physiologic SSTR-2 expression, which could limit evaluation of an adjacent meningioma in the skull base (24–26). Combined molecular imaging with CE MRI is extremely helpful in this setting, as it may help define the tumor margin and avoid unnecessary exposure of the patient to radiation. We implemented a bone reconstruction algorithm in our PET/CT protocol to aid visualization of osseous tumoral infiltration, given its superiority in detecting subtle transosseous involvement (27).

FIGURE 3. In ^{68}Ga-DOTATATE PET/CT/MRI series, CE MRI demonstrated enhancing focus at parietal vertex, which exhibited PET avidity (red arrows). PET/CT was able to identify another PET-avid focus at parasagittal left frontal region, indicative of recurrence (green arrows).

octreotide and a peptide receptor radionuclide. Clinical trials have shown the role of long-acting somatostatin analogs in inhibiting proliferation of meningiomas. Schulz et al. used 30 mg of octreotide to treat 8 patients with a progressive residual skull base meningioma after surgery. The investigators found that octreotide stabilized the progression of a recurrent skull base meningioma despite no convincible imaging evidence of tumor regression (28). In our small cohort, 4 patients received octreotide therapy, with ^{68}Ga-DOTATATE PET/CT being used to identify potential candidates for this pharmacologic therapy. Unfortunately, all 4 patients died shortly after initiation of the therapy, probably because of a limited octreotide therapy response due to the already extensive tumor burden at the time of diagnosis. Perhaps the treatment approach with the greatest potential for recurrent meningioma is somatostatin receptor–targeted peptide receptor radionuclide therapy, which is a novel theragnostic approach using either β-emission ^{90}Y or ^{177}Lu agents. Clinical trials for nonresectable and recurrent meningiomas have confirmed that peptide receptor radionuclide therapy has a promising role in the treatment of unresectable meningioma, with improved progression-free status, and may be an alternative approach for patients with an unfavorable response to traditional therapy (29–33).

Our small retrospective case series had several limitations. Histopathologic correlation of the ^{68}Ga-DOTATATE PET/CT findings was not available for any of our patients, and the diagnosis was based solely on visual inspection of brain CE MRI and ^{68}Ga-DOTATATE PET/CT images. We did not apply SUVs to aid the diagnosis, since no standard imaging protocol for meningioma has been established among the different institutions. Use of an SUV_{max} cutoff of 2.3, as applied by Rachinger et al., to differentiate tumor from tumor-free tissue is one example of what can be tried in future studies (15). Another limitation is lack of a direct comparison of the diagnostic performance of brain MRI and ^{68}Ga-DOTATATE PET/CT in lesion detection, given the lack of histopathologic evidence as a gold standard and the nature of the study. Future large-scale, prospective investigations of ^{68}Ga-DOTATATE PET/CT in diagnosis of recurrent meningioma need to overcome the shortcomings of this study.

Our single-center experience with fusion of ^{68}Ga-DOTATATE PET/CT and CE MRI in a small cohort concurred with prior work that demonstrated the vital role of a complementary ^{68}Ga-DOTATATE PET/CT scan in identifying recurrent meningioma. For example, in patient 2—the patient who had a WHO II meningioma that recurred after initial craniotomy—follow-up ^{68}Ga-DOTATATE PET/CT demonstrated focal uptake suggestive of recurrence despite no evidence of recurrence on CE MRI. This finding prompted repeat craniotomy and targeted proton beam therapy. The patient was clinically well as of the last visit, without evidence of recurrence on follow-up CE MRI.

^{68}Ga-DOTATATE PET may also provide therapeutic potential in patients for whom surgery has a limited role. The somatostatin receptor–targeted treatments consist of

CONCLUSION

^{68}Ga-DOTATATE PET/CT is a promising complementary molecular imaging tool in the detection of recurrent meningioma. It may improve diagnostic accuracy and confidence in guiding clinical management, particularly in surgically challenging patients. ^{68}Ga-DOTATATE PET/CT also serves a vital role in radiation therapy planning. With somatostatin receptor–targeted therapy on the horizon, ^{68}Ga-DOTATATE PET/CT may aid in selection of appropriate patients for peptide receptor radionuclide therapy, an emerging theragnostic approach in the management of meningioma.

DISCLOSURE

ACKNOWLEDGMENT

KEY POINTS

QUESTION: What is the role of ^{68}Ga-DOTATATE PET/CT in imaging meningioma?

PERTINENT FINDINGS: For recurrent meningioma, combined use of ^{68}Ga-DOTATATE PET/CT may enhance diagnostic accuracy and further guide clinical management. It has great potential to improve treatment outcomes and life expectancy.

IMPLICATIONS FOR PATIENT CARE: ^{68}Ga-DOTATATE PET and brain MRI play a complementary role in imaging of complicated recurrent meningioma.

REFERENCES

1. Baldi I, Engelhardt J, Bonnet C, et al. Epidemiology of meningiomas. *Neurochirurgie*. 2018;64:5–14.
2. Davis FG, Kupelian V, Freels S, McCarthy B, Surawicz T. Prevalence estimates for primary brain tumors in the United States by behavior and major histology groups. *Neuro Oncol*. 2001;3:152–158.
3. Wrensch M, Minn Y, Chew T, Bondy M, Berger MS. Epidemiology of primary brain tumors: current concepts and review of the literature. *Neuro Oncol*. 2002;4:278–299.
4. Louis DN, Perry A, Reifenberger G, et al. The 2016 World Health Organization classification of tumors of the central nervous system: a summary. *Acta Neuropathol (Berl)*. 2016;131:803–820.
5. Whittle IR, Smith C, Navoo P, Collie D. Meningiomas. *Lancet*. 2004;363:1535–1543.
6. Condra KS, Buatti JM, Mendenhall WM, Friedman WA, Marcus RB Jr, Rhoton AL. Benign meningiomas: primary treatment selection affects survival. *Int J Radiat Oncol Biol Phys*. 1997;39:427–436.
7. Marosi C, Hassler M, Roessler K, et al. Meningioma. *Crit Rev Oncol Hematol*. 2008;67:153–171.
8. Ostrom QT, Patil N, Cioffi G, Waite K, Kruchko C, Barnholtz-Sloan JS. CBTRUS statistical report: primary brain and other central nervous system tumors diagnosed in the United States in 2013–2017. *Neuro Oncol*. 2020;22:iv1–iv96.
9. Nowosielski M, Galldiks N, Iglseder S, et al. Diagnostic challenges in meningioma. *Neuro Oncol*. 2017;19:1588–1598.
10. Dromain C, Deandreis D, Scoazec JY, et al. Imaging of neuroendocrine tumors of the pancreas. *Diagn Interv Imaging*. 2016;97:1241–1257.
11. Schulz S, Pauli SU, Schulz S, et al. Immunohistochemical determination of five somatostatin receptors in meningioma reveals frequent overexpression of somatostatin receptor subtype sst2A. *Clin Cancer Res*. 2000;6:1865–1874.
12. Bashir A, Larsen VA, Ziebell M, Fugleholm K, Law I. Improved detection of postoperative residual meningioma with [^{68}Ga]Ga-DOTA-TOC PET imaging using a high-resolution research tomograph PET scanner. *Clin Cancer Res*. 2021; 27:2216–2225.
13. Galldiks N, Albert NL, Sommerauer M, et al. PET imaging in patients with meningioma-report of the RANO/PET Group. *Neuro Oncol*. 2017;19:1576–1587.
14. Ivanidze J, Roytman M, Lin E, et al. Gallium-68 DOTATATE PET in the evaluation of intracranial meningiomas. *J Neuroimaging*. 2019;29:650–656.
15. Rachinger W, Stoecklein VM, Terpolilli NA, et al. Increased ^{68}Ga-DOTATATE uptake in PET imaging discriminates meningioma and tumor-free tissue. *J Nucl Med*. 2015;56:347–353.
16. Dutour A, Kumar U, Panetta R, et al. Expression of somatostatin receptor subtypes in human brain tumors. *Int J Cancer*. 1998;76:620–627.
17. Klutmann S, Bohuslavizki KH, Brenner W, et al. Somatostatin receptor scintigraphy in postsurgical follow-up examinations of meningioma. *J Nucl Med*. 1998;39: 1913–1917.
18. Nathoo N, Ugokwe K, Chang AS, et al. The role of ^{111}indium-octreotide brain scintigraphy in the diagnosis of cranial, dural-based meningiomas. *J Neurooncol*. 2007;81:167–174.
19. Afshar-Oromieh A, Giesel FL, Linhart HG, et al. Detection of cranial meningiomas: comparison of ^{68}Ga-DOTATOC PET/CT and contrast-enhanced MRI. *Eur J Nucl Med Mol Imaging*. 2012;39:1409–1415.
20. Afshar-Oromieh A, Wolf MB, Kratochwil C, et al. Comparison of ^{68}Ga-DOTA-TOC-PET/CT and PET/MRI hybrid systems in patients with cranial meningioma: initial results. *Neuro Oncol*. 2015;17:312–319.
21. Collamati F, Pepe A, Bellini F, et al. Toward radioguided surgery with β^{-} decays: uptake of a somatostatin analogue, DOTATOC, in meningioma and high-grade glioma. *J Nucl Med*. 2015;56:3–8.
22. Henze M, Dimitrakopoulou-Strauss A, Milker-Zabel S, et al. Characterization of ^{68}Ga-DOTA-D-Phe^1-Tyr^3-octreotide kinetics in patients with meningiomas. *J Nucl Med*. 2005;46:763–769.
23. Nyuyki F, Plotkin M, Graf R, et al. Potential impact of ^{68}Ga-DOTATOC PET/CT on stereotactic radiotherapy planning of meningiomas. *Eur J Nucl Med Mol Imaging*. 2010;37:310–318.
24. Hoberück S, Michler E, Zophel K, Platzek I, Kotzerke J, Brogsitter C. Brain metastases of a neuroendocrine tumor visualized by ^{68}Ga-DOTATATE PET/CT. *Clin Nucl Med*. 2019;44:50–52.
25. Kota G, Gupta P, Lesser GJ, Wilson JA, Mintz A. Somatostatin receptor molecular imaging for metastatic intracranial hemangiopericytoma. *Clin Nucl Med*. 2013;38: 984–987.
26. Moradi F, Jamali M, Barkhodari A, et al. Spectrum of ^{68}Ga-DOTA TATE uptake in patients with neuroendocrine tumors. *Clin Nucl Med*. 2016;41: e281–e287.
27. Kunz WG, Jungblut LM, Kazmierczak PM, et al. Improved detection of transosseous meningiomas using ^{68}Ga-DOTATATE PET/CT compared with contrast-enhanced MRI. *J Nucl Med*. 2017;58:1580–1587.
28. Schulz C, Mathieu R, Kunz U, Mauer UM. Treatment of unresectable skull base meningiomas with somatostatin analogs. *Neurosurg Focus*. 2011;30:E11.
29. Bartolomei M, Bodei L, De Cicco C, et al. Peptide receptor radionuclide therapy with ^{90}Y-DOTATOC in recurrent meningioma. *Eur J Nucl Med Mol Imaging*. 2009;36:1407–1416.
30. Gerster-Gilliéron K, Forrer F, Maecke H, Mueller-Brand J, Merlo A, Cordier D. ^{90}Y-DOTATOC as a therapeutic option for complex recurrent or progressive meningiomas. *J Nucl Med*. 2015;56:1748–1751.
31. Kreissl MC, Hanscheid H, Lohr M, et al. Combination of peptide receptor radionuclide therapy with fractionated external beam radiotherapy for treatment of advanced symptomatic meningioma. *Radiat Oncol*. 2012;7:99.
32. Seystahl K, Stoecklein V, Schuller U, et al. Somatostatin receptor-targeted radionuclide therapy for progressive meningioma: benefit linked to ^{68}Ga-DOTATATE/-TOC uptake. *Neuro Oncol*. 2016;18:1538–1547.
33. Goldbrunner R, Minniti G, Preusser M, et al. EANO guidelines for the diagnosis and treatment of meningiomas. *Lancet Oncol*. 2016;17:e383–e391.

Making the Case for Brain ^{18}F-FDG PET Subtraction in Medically Refractory Epilepsy: A Novel, Useful Tool—Practical Points?

Mehdi Djekidel

QMC, Farmington, Michigan

^{18}F-FDG PET plays a major role in the presurgical evaluation of medically refractory epilepsy patients. The current standard of care is performing interictal evaluations of glucose metabolism. Use of this method is related mostly to the tracer kinetics of ^{18}F-FDG because of a long uptake phase that would translate into ictal injections that have low sensitivity and low specificity and demonstrate not only ictal but postictal changes. This limitation can be overcome in some status epilepticus scenarios in which prolonged seizures can then correlate better with ^{18}F-FDG uptake kinetics. In these cases, focal visual qualitative hot spots are suggestive of the seizure-onset zone. However, by using advanced subtraction techniques, the prolonged ^{18}F-FDG uptake phase can be overcome in a variety of other cases as well, opening the door to a slightly larger set of patients who may benefit from this higher-resolution PET method. This article presents 4 cases in which a novel subtraction ^{18}F-FDG PET technique was used and elucidates its impact in these specific cases.

Key Words: brain PET; FDG; epilepsy; subtraction PET

Ⅰn about one third of epilepsy patients, the disease is resistant or not well controlled on multiple medications (*1–5*). This subset of medically refractory patients may have improved outcomes with surgery (*1,4–6*). Surgical success requires accurate delineation of the seizure-onset zone (SOZ). Imaging plays a major role, with MRI, SPECT, and PET being essential elements of the work-up (*1,7*). The current nuclear medicine standard of care for PET (*1,2,5–8*) is to image patients interictally since the long uptake phase of ^{18}F-FDG in contrast to the short duration of seizures limits evaluation of the ictal phase (*8–11*). On the other hand, ictal PET has been reported in status epilepticus scenarios, in which prolonged seizures can correlate better with slow ^{18}F-FDG uptake kinetics (*12*). In these cases, focal visual qualitative hot spots are suggestive of the SOZ (*12*). Additionally, subtraction ictal–interictal ^{99m}Tc-hexamethylpropyleneamine oxime or ^{99m}Tc-ethyl

cysteinate dimer SPECT, not PET, is used successfully in select cases because of the very short uptake phase—a few seconds—of the cerebral blood flow SPECT radiopharmaceuticals (*9–11,13*). This article outlines the benefit of using advanced imaging subtraction techniques with ^{18}F-FDG PET. Subtraction is defined as the difference between 2 time points or 2 different conditions/states, and these can be represented by the ictal–interictal time points or 2 different ictal or interictal phases along the continuum of the patient's disease, including during the pre- and postoperative periods as well as during and after a brain insult such as encephalitis. Advanced semiquantitative or processing techniques are essential tools in the nuclear medicine epilepsy practice.

Use of advanced techniques allows one not only to understand the SOZ but also to uncover propagation pathways and the severity of the seizures (*1,14–16*). Subtraction ^{18}F-FDG PET is novel and can localize the SOZ for intracranial recording or for surgical resection in lesional and nonlesional epilepsy. It may also directly guide management or lesionectomy if multiple lesions are present.

Subtraction ictal–interictal ^{18}F-FDG PET was performed in the current study. ^{18}F-FDG PET scans were obtained in the ictal and interictal phases after injection of radiopharmaceutical activities according to the guidelines of the Society of Nuclear Medicine and Molecular Imaging and the European Association of Nuclear Medicine. Subtraction was performed using MIMneuro software (MIM Software Inc.). Both PET volumes and the patient's most recent MRI were coregistered. Subtraction of both PET scans was followed by a cluster statistical analysis to define the area of highest significance. The results were coregistered and displayed on the patient's MRI scan. The patient's clinical and imaging results were further evaluated at a multidisciplinary epilepsy team meeting. MR images and ^{18}F-FDG PET ictal and interictal scans were reviewed qualitatively. ^{18}F-FDG PET scans were also reviewed semiquantitatively using a reference database control, with z score results displayed on stereotactic surface projections (SSPs) of the patient's MR images. Subtraction ^{18}F-FDG PET/MRI results were also discussed.

CASE PRESENTATION 1

A 6-y-old right-handed boy had intractable seizures, which began at the age of 4 y. The seizure semiology was
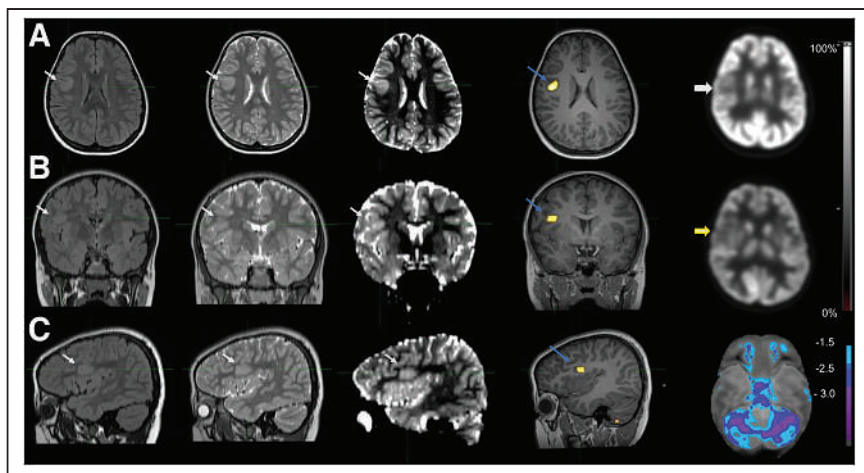
FIGURE 1. Axial (A), coronal (B), and sagittal (C) views of, from left to right, fluid-attenuated inversion recovery MRI, T2-weighted MRI, diffusion-weighted MRI, subtraction ^{18}F-FDG PET fused with T1-weighted MRI, and interictal ^{18}F-FDG PET (in A); ictal ^{18}F-FDG PET (in B); or z score SSP of ^{18}F-FDG PET hypometabolism (in C). Thin white arrows show lesion missed on initial MRI. Thick white arrow shows mild hypometabolism. Yellow arrow shows improved metabolism ictally. Blue arrows show cluster of significance in right Rolandic operculum, corresponding to SOZ.

CASE PRESENTATION 2

The second case was a 13-y-old boy with intractable seizures. The onset of seizures was at 1 y old in the form of a febrile seizure. The first unprovoked seizure was at 2 y old. The seizure semiology was in the form of loss of consciousness and loss of muscle tone for about 10 s and occurring about 20–25 times a day. Historically, the patient had a trial of 4 different antiepileptic drugs, and he was receiving 2 antiepileptic drugs during the current work-up. His autoimmune and inflammatory workup findings were negative. Interictal electroencephalography showed left frontal slow disturbance and abundant epileptic discharges arising from the left anterior frontal region. Ictal electroencephalography showed multiple seizures, which began in the left frontal region and spread to the right frontal region. No generalized seizures were noted. The patient was injected with ^{18}F-FDG in the nuclear medicine department approximately 1 min after having a seizure. Then, 2 min after the injection, he had another seizure, and he had an additional 3 seizures during the remainder of the uptake phase before his scan. MRI showed subtle loss of differentiation between the gray matter and white matter in the entire left frontal lobe;

represented by tonic seizures of the upper limbs lasting 25–30 s and occurring about 30–40 times a day. Generalized seizures also occurred twice a week. Historically, he had a trial of 9 different antiepileptic drugs, and he was currently receiving triple-antiepileptic-drug treatment. His stay in the epilepsy monitoring unit revealed evidence of focal epileptic seizures arising from the right frontal region.

Subtraction ^{18}F-FDG PET was of value in uncovering the SOZ in the right Rolandic operculum (Fig. 1). A small lesion was initially missed on the MRI because of poor technique and the subtle nature of the lesion and was reported only on follow-up MRI (Fig. 1) and only after the subtraction PET revealed the lesion and SOZ. The interictal ^{18}F-FDG PET scan (Fig. 1A) showed a somewhat large area of mild hypometabolism in the right frontal lobe (Fig. 1A). This area had slightly improved metabolism ictally (pseudonormalization of glucose metabolism) (Fig. 1B). Because there were no areas of increased glucose metabolism on the ictal PET, there was no obvious ictal focus to report. However, the subtraction ictal–interictal technique revealed the cluster of significance to be in the right Rolandic operculum, corresponding to the SOZ (Fig. 1). The subtraction technique accurately detected the SOZ and showed its extent, which was much larger on the raw PET data.

FIGURE 2. (A) From left to right: 2 basal and left lateral z score SSP views for each of, respectively, preoperative cerebral blood flow ^{99m}Tc-hexamethylpropyleneamine oxime SPECT image, postoperative cerebral blood flow ^{99m}Tc-hexamethylpropyleneamine oxime SPECT image, and postoperative ^{18}F-FDG PET image. Arrows show ^{18}F-FDG PET hypometabolism, which improved postoperatively. (B) Subtraction preoperative and postoperative ^{18}F-FDG PET/MR images displayed in coronal, sagittal, and 3 axial slices. (C) Subtraction ^{18}F-FDG PET/MR images in all 3 planes showing 2 sites of clusters of significance in left frontal and left parietooccipital lobes. Arrows show 2 potential areas for SOZ. On color scale, yellow-red indicates hypermetabolism and blue-purple indicates hypometabolism.
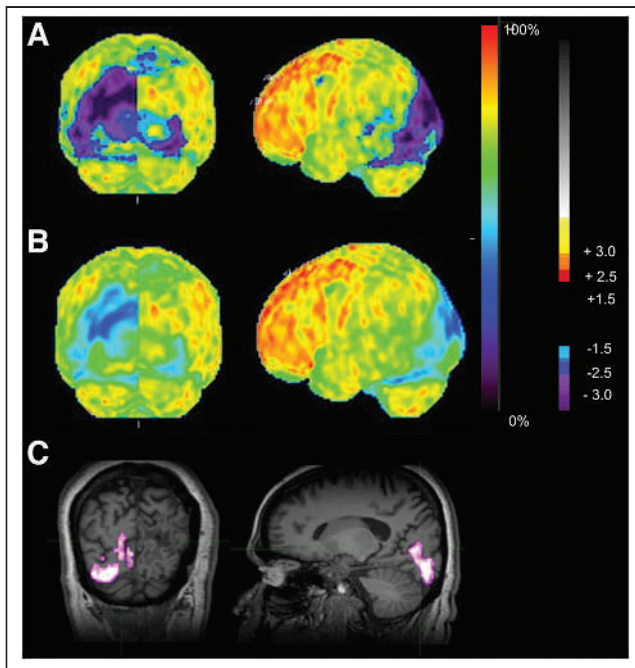
FIGURE 3. (A) Three-dimensional SSPs showing significant areas of hypometabolism in left occipital lobe interictally. (B) Three-dimensional SSPs showing no areas of hypermetabolism in left occipital lobe ictally or elsewhere; however, severity of hypometabolism in left occipital region has diminished (pseudo-normalization of glucose metabolism). (C) Subtraction ictal–interictal ^{18}F-FDG PET/MR image showing cluster of significance in left occipital lobe (SOZ).

this finding was most apparent after review of the ^{18}F-FDG PET scan, but the scan findings were initially reported as unremarkable. However, no anatomic or morphologic changes were discernable in the left parietal or parietooccipital regions. Additionally, no obvious ictal region with increased glucose metabolism was noted.

In this case, the raw interictal and ictal ^{18}F-FDG PET data showed a much higher sensitivity at detecting left-hemisphere abnormalities, which were very subtle on the MRI. Additionally, SSPs showed changes in metabolism across the entire brain and how they changed during the ictal phase. The subtraction technique allowed identification of 2 potential areas for the SOZ in the left frontal and left parietooccipital lobes (Fig. 2). This identification guided patient management significantly by defining the SOZ better than was possible on the MRI and raising the possibility of multifocal seizures, as well as allowing for improved selection of the proper

surgical approach (lesionectomy, disconnection, or other), including contemplation of intracranial mapping that would cover both seizure clusters.

CASE PRESENTATION 3

The third case was a 40-y-old man with medically refractory epilepsy due to prior encephalitis. The seizure semiology consisted of simple partial visual seizures, which started when the patient was in his 30s. There were no generalized seizures. ^{18}F-FDG PET scans were performed ictally and interictally. Ictal ^{18}F-FDG PET (Fig. 3B) did not show any areas suggestive of increased glucose metabolism when reviewed as a single study or even when compared with a reference database. Persistent hypometabolism was seen, but when compared with the interictal exam (Fig. 3A), hypometabolism showed improvement in the left occipital region ictally. Therefore, there was a so-called relative increased glucose metabolism ictally that was uncovered only when compared with the interictal study. The subtraction technique clearly uncovered and defined a cluster of significance in the left occipital lobe (Fig. 3C), as looking at the ictal ^{18}F-FDG PET alone showed changes in the SOZ and along the propagation pathway (network effect). Pseudonormalization can also occur in other areas of the brain, hence the value of the subtraction technique. In essence, the ictal ^{18}F-FDG PET scan as an independent examination is limited. However, this limitation can be overcome through comparison to the interictal scan and especially with advanced techniques such as statistical mapping and subtraction using healthy controls as demonstrated here (Fig. 3).
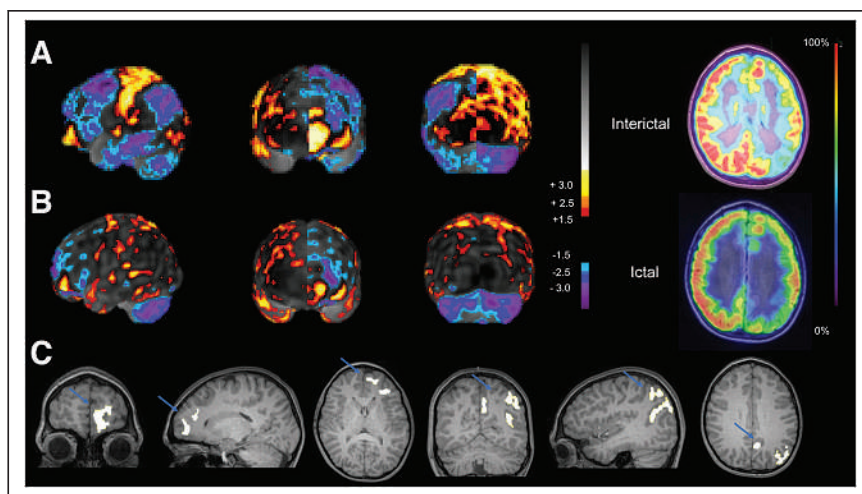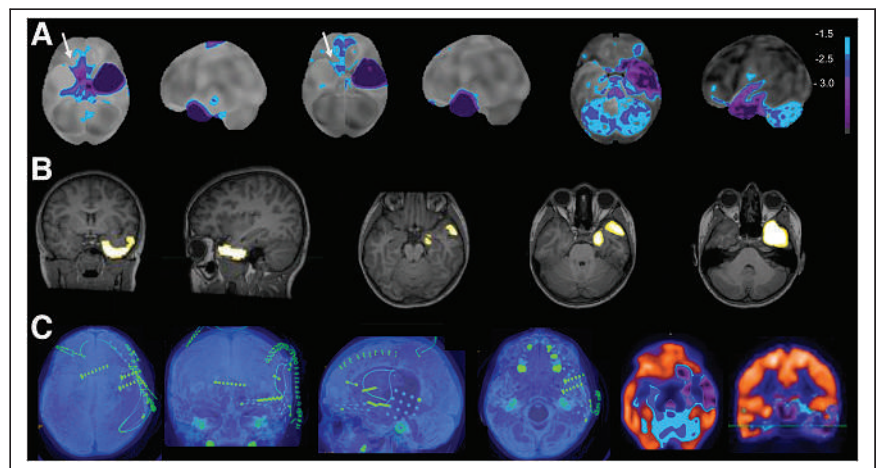

FIGURE 4. (A) From left to right: 2 basal and left lateral z score SSP views for each of, respectively, preoperative cerebral blood flow ^{99m}Tc-hexamethylpropyleneamine oxime SPECT image, postoperative cerebral blood flow ^{99m}Tc-hexamethylpropyleneamine oxime SPECT image, and postoperative ^{18}F-FDG PET image. Arrows show ^{18}F-FDG PET hypometabolism, which improved postoperatively. (B) Subtraction preoperative and postoperative ^{18}F-FDG PET/MR images displayed in coronal, sagittal, and 3 axial slices. (C) Left: intracranial mapping with grid, strip, and depth electrodes; right: z score hypometabolism on preoperative ^{18}F-FDG PET images.

CASE PRESENTATION 4

The fourth case was a 10-y-old right-handed girl with intractable epilepsy of the left temporal lobe after removal of that lobe and left medial amygdalohippocampectomy. Her seizures started at the age of 5 y. She continued to have seizures after the surgery, with a similar semiology to the preoperative seizures. Scalp electroencephalography recordings after surgery showed a mild, focal, intermittent slow disturbance of cerebral activity in the right frontotemporal region, as well as a multifocal epileptic abnormality seen independently in the left and right anterior head regions. During her stay in the epilepsy monitoring unit, 6 stereotyped seizures were noted, with no definite localizing or lateralizing features. Some seizures were associated with subtle δ-slowing in the bifrontal region, at times with left frontopolar predominance, whereas others were associated with a clear right frontotemporal postictal slowing. These consensus findings from the multidisciplinary epilepsy team suggested a deep left hemispheric epileptogenic focus (orbitofrontal vs. insular), although an independent right-sided focus could not be excluded, considering the electroencephalogram findings. A further evaluation with invasive recordings was performed to further localize the SOZ. Before intracranial mapping, interictal postoperative ^{18}F-FDG PET was performed (Supplemental Fig. 1; supplemental materials are available at http://jnmt.snmjournals.org). Subtraction images of pre- and postoperative interictal ^{18}F-FDG PET scans (Fig. 4B) excluded any focus in the contralateral right hemisphere, allowing intracranial grids, strips, and depth electrodes to be placed in the left hemisphere only (orbitofrontal, left insular, left cingulate and left posterior temporal regions) (Fig. 4C). Subtraction also suggested that the SOZ extended posteriorly in the left temporal lobe (Fig. 4B). Contralateral right-sided medial temporal lobe hypometabolism seen on the preoperative ^{18}F-FDG PET scan improved postoperatively (Fig. 4A arrows). This change was reported to be associated with better Engel outcomes.

CONCLUSION

^{18}F-FDG PET subtraction techniques offer a significant advantage over traditional interictal ^{18}F-FDG PET evaluations and can be used successfully to delineate the SOZ and guide the management of medically refractory epilepsy patients. It is hoped that the results of the current study will encourage wider use and larger datasets for proper comparison and further expansion of the pool of patients who may benefit.

DISCLOSURE

No potential conflict of interest relevant to this article was reported.

KEY POINTS

QUESTION: Can advanced novel PET imaging techniques impact clinical management in medically refractory epilepsy patients?

PERTINENT FINDINGS: Advanced ^{18}F-FDG PET subtraction techniques allow better delineation of the SOZ in medically refractory epilepsy patients.

IMPLICATIONS FOR PATIENT CARE: Advanced ^{18}F-FDG PET subtraction techniques enhance clinical management in medically refractory epilepsy patients.

REFERENCES

1. Goffin K, Dedeurwaerdere S, Van Laere K, Van Paesschen W. Neuronuclear assessment of patients with epilepsy. *Semin Nucl Med.* 2008;38:227–239.
2. Siegel AM. Presurgical evaluation and surgical treatment of medically refractory epilepsy. *Neurosurg Rev.* 2004;27:1–18.
3. Guerrini R, Scerrati M, Rubboli G, et al.; Commission for Epilepsy Surgery of the Italian League Against Epilepsy. Overview of presurgical assessment and surgical treatment of epilepsy from the Italian League Against Epilepsy. *Epilepsia.* 2013;54(suppl 7):35–48.
4. Consales A, Casciato S, Asioli S, et al. The surgical treatment of epilepsy. *Neurol Sci.* 2021;42:2249–2260.
5. Marathe K, Alim-Marvasti A, Dahele K, et al. Resective, ablative and radiosurgical interventions for drug resistant mesial temporal lobe epilepsy: a systematic review and meta-analysis of outcomes. *Front Neurol.* 2021;12:777845.
6. Vakharia VN, Duncan JS, Witt JA, Elger CE, Staba R, Engel J Jr. Getting the best outcomes from epilepsy surgery. *Ann Neurol.* 2018;83:676–690.
7. Steinbrenner M, Duncan JS, Dickson J, et al. Utility of ^{18}F-fluorodeoxyglucose positron emission tomography in presurgical evaluation of patients with epilepsy: a multicenter study. *Epilepsia.* 2022;63:1238–1252.
8. Kaewchur T, Chamroonrat W, Thientunyakit T, et al. Thai national guideline for nuclear medicine investigations in epilepsy. *Asia Ocean J Nucl Med Biol.* 2021;9:188–206.
9. Suárez-Piñera M, Mestre-Fusco A, Ley M, et al. Perfusion SPECT, SISCOM and PET ^{18}F-FDG in the assessment of drug-refractory epilepsy patients candidates for epilepsy surgery. *Rev Esp Med Nucl Imagen Mol.* 2015;34:350–357.
10. Elkins KC, Moncayo VM, Kim H, Olson LD. Utility of gray-matter segmentation of ictal-interictal perfusion SPECT and interictal ^{18}F-FDG-PET in medically refractory epilepsy. *Epilepsy Res.* 2017;130:93–100.
11. Desai A, Bekelis K, Thadani VM, et al. Interictal PET and ictal subtraction SPECT: sensitivity in the detection of seizure foci in patients with medically intractable epilepsy. *Epilepsia.* 2013;54:341–350.
12. Gugger JJ, Husari K, Probasco JC, Cervenka MC. New-onset refractory status epilepticus: a retrospective cohort study. *Seizure.* 2020;74:41–48.
13. Perissinotti A, Setoain X, Aparicio J, et al. Clinical role of subtraction ictal SPECT coregistered to MR imaging and ^{18}F-FDG PET in pediatric epilepsy. *J Nucl Med.* 2014;55:1099–1105.
14. Mayoral M, Marti-Fuster B, Carreño M, et al. Seizure-onset zone localization by statistical parametric mapping in visually normal ^{18}F-FDG PET studies. *Epilepsia.* 2016;57:1236–1244.
15. Haemels M, Van Weehaeghe D, Cleeren E, et al. Predictive value of metabolic and perfusion changes outside the seizure onset zone for postoperative outcome in patients with refractory focal epilepsy. *Acta Neurol Belg.* 2022;122:325–335.
16. Radhakrishnan A, James JS, Kesavadas C, et al. Utility of diffusion tensor imaging tractography in decision making for extratemporal resective epilepsy surgery. *Epilepsy Res.* 2011;97:52–63.

Emotional Intelligence and Productive Relationships with Patients and Colleagues

Josie Currie[1] and Geoffrey M. Currie[2]

[1]*Riverina Anglican College, Wagga Wagga, Australia; and* [2]*Charles Sturt University, Wagga Wagga, Australia*

A higher degree of emotional intelligence among health professionals has been shown to result in better patient care and improved well-being of the health professional. For nuclear medicine, the emotional competence of staff and emotional proficiency of institutions are important expectations. Nonetheless, there is a paucity of material outlining purposeful honing of emotional intelligence, or the tools for such development, across the literature. Although the hidden curriculum provides powerful and authentic educational opportunities, incidental or accidental (organic) capability development does not benefit overall professionalism. Deliberate curricula can be achieved through a scaffold of emotional training and immersion programs that allow the nuclear medicine student or practitioner to recognize and foster emotionally safe environments. This requires careful planning to drive the emotional intelligence pipeline. Central to this is an understanding of learning taxonomies. There remain substantial gaps between the most and least emotionally insightful that could be addressed by rich immersive activities targeting emotional proficiency among students and the graduate workforce.

Key Words: emotional intelligence; personality; conflict resolution; interprofessional relationships

When the interaction between health professionals and patients is positive, there is an improvement in compliance, satisfaction, and outcomes for the patient, and clinical decisions and leadership are enhanced for the health professional (*1–3*). Importantly, a higher degree of emotional intelligence among health professionals has been shown to result in better patient care and improved well-being for the health professional (*4*). Interestingly, one study used an emotional intelligence inventory to report that, among nearly 2,000 diagnostic radiography workers, the highest emotional intelligence was among mammographers and the lowest was among nuclear medicine technologists (*5*).

Emotional intelligence is the acuity of one's own and of others' emotions and the use of this acuity to shape actions, guide attention, and focus motivations with a view toward gaining more productive interactions (*6*). There are 4 general

aspects of emotional intelligence (*6*): the emotions need to be expressed, contextualized, understood, and controlled (*6*). Generally, scores for emotional intelligence will be expressed from a global context (overall emotional intelligence) and then from subcategories that include emotionality, sociability, self-control, and well-being. In the often-stressful health-care setting, emotional intelligence among health professions affords situational awareness and the ability to modify interactions to produce more emotionally safe environments for colleagues, self, and patients. In turn, this ability creates more productive, effective, and satisfying interactions. Central to developing emotional intelligence is a rich understanding of and interplay between personality traits: one's own and those of others. It is also important to recognize that emotional intelligence can be associated with intuitive or organic aptitude but can be learned, honed, and engineered for a purpose.

There is a comprehensive inventory of tools and battery of techniques to hone one's emotional intelligence. These range from mindfulness or meditation exercises through purpose-built training programs. In this article, enriching the understanding of individual personality traits and the dynamic between interacting individuals will be explored as one such tool and technique aimed at providing higher-order emotional taxonomies. Central to capability building in emotional intelligence and unpacking personality traits is the capability of health professions to be critically and deeply reflective. Despite the value and importance, there is a paucity of literature providing insights into educational initiatives to develop foundations of emotional intelligence among health professionals, including undergraduate nuclear medicine students.

STREAMLINED PERSONALITY INVENTORY

Generally, personality refers to the characteristics or traits that an individual exhibits when interacting with others (*7*). Health professionals such as those in nuclear medicine interact with patients and colleagues on the basis of spontaneous and unconscious impressions of personality. Clearly, these impressions rely on intuition, lack context, and may lack insight, especially when made under stress (observer or the observed). Indeed, bias and prejudice are likely to confound these interpretations and interactions. For some, informal or formal learning associated with psychology might afford improved accuracy and outcomes. Nonetheless, there remains a paucity of formal training and structured experience in

understanding personality and applying such insights with emotional intelligence to produce positive relationships and effective conflict resolution. Confounding attempts to develop emotional intelligence is a wide variety of models for classifying personality, varying degrees of complexity of the same, and contradiction among the models. Furthermore, interactions with patients and colleagues might be fleeting, affording little chance for rigorous baseline and trait evaluation. The application of the science associated with personality psychology does not fit the fluid environment in which potential benefits could be produced.

There is a requirement, therefore, to develop an intuitive model that requires a foundation of theoretic insight applied in the dynamic environment. Personality traits and subtraits are complex, and a usable model requires simplification without losing accuracy. There needs to be recognition that any individual may have a mix of personality traits that may change weighting in different situations. The value of honing both the science and the art of emotional intelligence is that emotional competence improves interactions with patients and colleagues, which is vitally important in a patient-facing, personalized medicine environment. Although these insights do not allow changing of the personalities of others, emotional intelligence allows health professionals to adjust patient care or communication to better fit the individual patient: personalized care. In a study of women with breast cancer, investigators showed that understanding patient personality traits allowed more appropriate patient care and interventions (8). Emotional intelligence might be thought of as the capability of using casual impressions to objectively predict traits to inform adjustments to communication in real time while being conscious of the nuances associated with personality, the lack of detailed evaluation inventory (e.g., validated question bank), and the potential for a wide variety of biases.

Application of emotional intelligence training and providing students or practitioners with a framework for real-time personality trait assessment needs context. Importantly, these simplified tools vary substantially with intuition and experience and assume the absence of personality disorders. Furthermore, manifestation of personality traits and behaviors will vary with increasing levels of stress for both patients and colleagues (e.g., patient is confronting serious illness). Finally, the health professional observing, or the patient or colleague being observed, can be functioning in varying levels of emotional intensity (magnitude with which emotions are experienced or felt), emotional flux (frequency with which different emotions are experienced or felt), and emotional density (concentration of different emotional stimuli in the environment) or could be confronting emotional exhaustion (burnout), all of which influence the emotional acuity.

There are several well-recognized compact inventories for personality evaluation. At a very rudimentary level, a 2-trait approach might classify individuals as introverts or extroverts. The big 5 using the OCEAN acronym is also common and classifies individuals using the traits openness, conscientiousness, extraversion, agreeableness, and neurosis (9). A variation on this model adds honesty as a sixth trait and modifies neurosis to emotionality (HEXACO: honesty–humility, emotionality, extraversion, agreeableness, conscientiousness, openness to experience). A useful 4-trait model using the acronym DISC classifies individuals as a mix of the traits dominance, influence, steadiness, and compliance. The DISC model will be discussed in more detail below.

EMOTIONAL INTELLIGENCE PIPELINE

There are similarities between the emotional intelligence pipeline and the cultural proficiency pipeline previously reported (10). At the foundation of patient care and interprofessional relationships is emotional safety. Patients and staff value emotionally safe places characterized by respect. To provide an emotionally safe environment requires more than emotional knowledge and awareness, it demands emotional intelligence through engagement with values and attitudes (Fig. 1). Part of emotional safety in nuclear medicine is related to education of the health professional. The unequal power relationships between health practitioners and patients, and among colleagues, contributes to communication asymmetry.

Broadly, emotional competence is the capacity to respond to variations in emotional needs, values, styles, and circumstances. This includes understanding and respecting variations in individual beliefs, values, preferences, behaviors, thresholds of tolerance and resilience, expectations, compliance, and attitudes. Emotional competence is an important strategy for addressing communication asymmetry and potential conflict for patients and colleagues but requires more than emotional awareness. Emotional competence is the attitudes and behaviors, reinforced through policy and practice, that enable effective productive relationships and effective communication among individuals.

Success in building an emotionally competent health workforce is constrained by a lack of consistent definition and language around emotional competence and lack of evidence of training impact or appropriate performance indicators. Emotional competence requires mastery of the capacity for self-assessment, critical reflection, management of emotional dynamics, emotional knowledge, adaptation of actions, recognition of emotional differences, and understanding the impact difference makes. Recognizing emotional difference and understanding the value that those differences bring to interactions is an important part of emotional competence (Fig. 1). This quality allows easy demarcation from lower levels of emotional development, where differences might be seen as opportunity for exploitation (e.g., bullying) or be inappropriately responded to. Emotional proficiency demands the same capabilities at individual and institutional levels but also requires capacity for emotional humility. Beyond the capabilities of emotional competence, emotional proficiency recognizes differences and is equipped to respond effectively and affirmingly both individually and institutionally (Fig. 1).
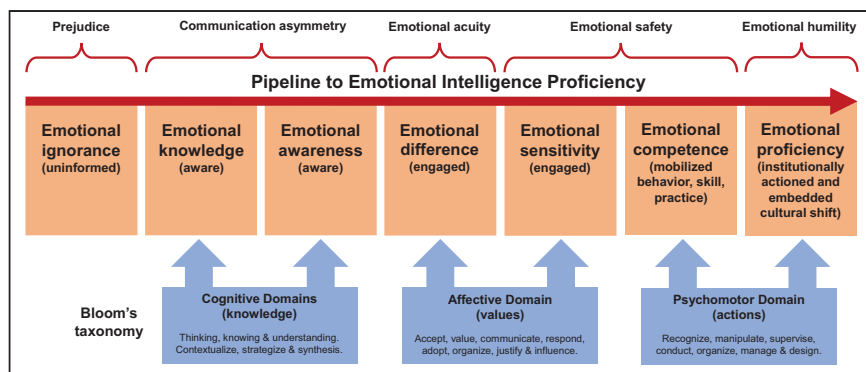
FIGURE 1. Bloom's taxonomy mapped against emotional intelligence proficiency pipeline.

EMOTIONAL INTELLIGENCE TRAINING

Using stand-alone emotional intelligence workshops for health-care workers and students, there have been initiatives that may be seen to satisfy human resource–driven performance metrics to build emotional awareness. More effective programs might develop stronger insights through rich and deep understanding. The journey through emotional awareness to emotional competence or proficiency requires more structured and deliberate learning. Relying on organic development of emotional intelligence among students as they progress through their studies and training has been shown to fail in radiography students, with no difference in emotional intelligence metrics among students followed across 3 y of study at multiple institutions (11). At Charles Sturt University, undergraduate nuclear medicine students are provided a preliminary workshop creating awareness and understanding associated with emotional competence. The knowledge is enriched with immersive exercises that are linked to reflective tasks to connect the learning with experience. Students are then released into the clinical environment, where further application and reflection are used to hone emotional intelligence.

The journey for students and health professionals to cultural competence is richer through a cultural immersion style of learning but also relies on appropriate learning taxonomies. Both undergraduate and continuing education training programs across a wide array of topics adopt a cognitive focus. Bloom's cognitive taxonomies are effective to scaffold the learning at lower-order capabilities such as knowing and understanding. Progression to emotional acuity and emotional safety requires attention on Bloom's affective domain, where feelings, attitudes, and values are scaffolded. The step to emotional competence and proficiency requires command of the capabilities of Bloom's taxonomies in the psychomotor domain. Here, the emphasis is on behaviors, skills, and actions (Fig. 1).

THE CHARLES STURT UNIVERSITY EXPERIENCE

At Charles Sturt University, nuclear medicine students participate in workshops that build emotional intelligence and capabilities using the DISC 4-trait model (12). DISC is an acronym for dominance, influence, steadiness and compliance although the S has also been defined as social or submission. Classification relies on behavior around risk, pace, focus, self, and response among others. Although useful as a real-time tool, experience suggests that the language introduces bias. Dominance is often viewed as a negative trait, and there is frequently, among students, an inclination to deny having a high degree of dominance as a trait. Indeed, dominance can be associated with bullying and rudeness but it can also produce leadership and decision making beyond the other 3 traits. Conversely, influence is often seen positively as having an impact on others, and students are eager to associate themselves with this trait without considering the deeper meaning. Often, students take offense at being classified as steady or compliant, seemingly implying a boring personality. It is only with deeper immersion in the Charles Sturt University workshop that students appreciate the strengths and weaknesses of each trait and the complex interplay and balance of traits each individual exhibits.

The foundation of the emotional intelligence program at Charles Sturt University is knowledge development, with students learning the theory associated with both emotional intelligence and personality trait assessment. This knowledge is delivered at Charles Sturt University via a tutorial and actually represents the cognitive portion of the taxonomies. Scaffolded to the knowledge is the development of values and acuity in 2 phases, the first being through a workshop and the second via authentic clinical experience with reflection. Ongoing application of the knowledge and skills in the clinical environment, especially during final-year clinical placement and the early years as a qualified practitioner, lead to (for some graduates) emotional competence. Emotional proficiency is modeled in the hidden curriculum throughout the course at Charles Sturt University and reflects institutional emotional proficiency.

The DISC program delivered at Charles Sturt University is not a detailed personality tool but rather provides insight into individual styles to allow prediction of behaviors and an individual's (including self) general approach using an accessible and easily interpreted model. Nonetheless, DISC does not reflect knowledge, skills, or intelligence. There is a diverse array of applications of the skills and capabilities developed in this program. From a student context, including shortly after graduation, it can be used to improve interactions with colleagues and patients to produce more productive outcomes and, in doing so, becomes a powerful career development tool. Charles Sturt University students also use the DISC program to enrich self-awareness and to manage conflict or difficult personalities. This is especially powerful for students or junior staff navigating stressful or hostile clinical environments where they may feel disempowered at the lower end of the hierarchy. In recent research among student diagnostic

radiographers, 21% indicated that the clinical environment negatively impacted their well-being associated with emotionally challenging situations (*13*). Within the clinical dynamic, these tools can be used for conflict resolution, avoiding conflict, producing productive teams, and driving staff morale. Leadership and management can adopt these same tools to recruit the right staff members who will assimilate best into the established workforce and environment, to drive cultural integration, to inform performance management, and to redeploy staff when necessary.

Students are challenged to see the advantage in modifying one's own behaviors to optimize interactions with others. Nonetheless, it is not immediately apparent that a given individual has the range of behaviors to cope with the complexity and variability of patient and colleague interactions. Before breaking down the characteristics of each of the 4 DISC traits, recognition should be made that no trait is better or worse than others, that we all have a mix of all 4 traits, that most of us have 1–2 traits that predominate, that the trait predominance can change with environments, and that there is a large range of subtraits to consider. For example, in the absence of a dominant "I" in a working environment, a typical "S" may morph into an "I" in that environment. Similarly, a "C" may manifest an inner "D" in the absence of a "D" in the working environment.

Dominance is associated with assertiveness, control, and power. The typical "D" wants to be in charge and have the authority to make decisions. A "D" is task-focused and results-focused. Decision making is quick and decisive. A "D" enjoys change and challenges but can lack emotion and can be overbearing, too ambitious and competitive, skeptical, suspicious, and aggressive, particularly when targeting a goal. Harnessed appropriately, a "D" can be a good leader and decision maker who thrives in challenging environments but without considering consequences (including human) before actions. The typical "D" is expressive and extraverted, which can produce communication challenges. Communication lacks detail, is instructive, and can be uncontrolled. When interacting with "D" patients or colleagues, one should focus on results and outcomes, avoid detailed explanations, be prepared by understanding all available information, be assertive and strong so as to not compromise that which is important, be flexible and accommodating and not take anything personally, and give them ownership of an idea to generate vigorous support. Under stress, a "D" can be abrupt, blunt, aggressive, loud, irrational, and rude and can revert to bullying.

Influence is associated with communication style and social interactions. An "I" likes to be the center of attention; is enthusiastic and often talkative, animated, persuasive, and optimistic; interacts positively in most situations; is interested in the emotions and feelings of others; is a confident and good communicator; and adapts to new environments fairly well. Being motivated by relationships and the need to feel accepted, an "I" does not cope well with rejection or exclusion. Although warm and relaxed, "I" individuals do not fit structured environments and follows their own path without considering consequences. When interacting with "I" patients or colleagues, one should be assertive to get them focused, provide praise and approval, utilize their enthusiasm and energy, and be personal and friendly. Under stress, an "I" becomes more talkative, gets flustered, loses focus, imparts blame, sulks, and can become dramatic.

Steadiness is associated with patience, persistence, and thoughtfulness. An "S" is relationship-focused and enjoys teamwork but thrives in relaxed, calm, and supportive environments; does not like change or confrontation; and prefers to have time to plan and execute tasks. An "S" is gentle, open, warm, sympathetic, supportive, and introverted; generally has a small circle of trusted friends; and looks to more socially assertive people to initiate relationships. An "S" has the highest organic level of emotional intelligence; is a good listener, dependable, and loyal; and is good at laborious tasks but needs a support network. Although "S" individuals toil away at tasks, they do not like interruption, tend not to like multitasking, adapt slowly to change or new environments, and can be slow at completing tasks. When interacting with an "S," one should provide reassurance and support, be patient and calm, not introduce surprises, provide detailed information, be organized, and make eye contact during communication. Under stress, an "S" becomes emotional, socially withdrawn, and indecisive and will lose confidence.

Compliance is associated with structure and organization. A "C" sets high standards, likes having time to achieve excellence, is persistent, is eager to improve, and focuses on the detail. "C" individuals can appear emotionally disconnected, impassive, and cold, but this appearance relates to control and reluctance to unnecessarily reveal themselves or information. They are ambitious but use structured rules rather than assertiveness to progress. They are organized and quick-thinking but structured and logical, which means they need certainty before proceeding (risk-averse). A "C" is passive socially, naturally suspicious of others, and develops relationships associated with mutual interests. "C" individuals appreciate (demand) detail, value accuracy and precision (will correct errors others think are inconsequential), are cooperative, and prefer compromise over confrontation. Interactions with "C" individuals require accuracy, patience, consistency, confidence, and a clinical approach (unemotional) but can be enhanced by setting time limits on tasks, praising their expertise, and helping them see the broader context. Under stress, a "C" will become critical, shut down, and stop communicating.

Armed with these insights, students undertake several reflective exercises that require identification of traits among classmates, authentic clinical experiences in which patients or colleagues exhibited specific traits, and identification of one's own balance of traits. When patients are an "I," for example, they may be ignorant of the test and purpose, will answer questions in a convoluted fashion that may be a complete tangent, and are likely to forget information told to them. Communication needs closed questions or

limited-choice questions, staff need to be assertive without being impatient, explaining the process in stages and having the patient repeat instructions back, and instructions might need to be written down. A "D" might be aggressive, try to take charge, and give the impression that staff are an inconvenience. Assertiveness is required without being unprofessional, and one should stay focused, provide a concise explanation, and not take it personally. An anxious patient exhibiting traits of a "C" or "S" could appear distracted and noncommunicative. Here, open questions might be used to draw the patient out. Eye contact, a friendly disposition, and reassurance is needed to gain confidence and trust. A summary of DISC traits and actions is outlined in Table 1 and Figure 2.

Students are challenged to consider interactions between dominant traits and compatibilities. This reflection should go beyond the clinical environment to include relationships associated with sport, family, and friends. For example, a classic "D" or "C" is effective in individual sports and in working alone whereas "S" and "I" personalities are more receptive to a team environment. Although a "D" and an "S" are opposites, they can also be complementary, remembering that an "S" will look to a "D" or "I" to initiate a relationship. Nonetheless, students generally identify situations in which an "S" is directly or incidentally bullied by the actions of a "D." Although a "D" and a "C" are task-focused, they can clash over structure, pace, process, and detail. A "D" can assume the credit for a group task, whereas a "C" in the group will covertly manipulate the environment to not only reveal the error but also expose the actions of the "D." Group work is a key capability in any undergraduate course, and students quickly adapt their understanding of DISC to reflect on group dynamics: the "D" who takes over the project, the "I" who wants to be center stage without contributing, the "S" who brings snacks to make everyone feel better, and the "C" who tries to redo the work of others to a higher standard. The complexity of this simple 4-trait model and the richness of its use are exhibited in the following reflection (from a student assessment):

> I identify all 4 traits as dominant in different scenarios. The nature of my work in radiation really draws out the "C" in me, and it has allowed me to excel in my career. Realizing I have been overlooked for leadership positions, I have been consciously tapping into my inner "S" and "D" at various times. This is fairly natural because I lean on my "D" characteristics when I play sport, including as team captain, and I fill the otherwise vacant "S" role among my family that has been referred to as the glue keeping everything together. But I have a narrow circle of trusted friends among whom I feel safe enough to lower barriers, and that is when my inner "I" is revealed. Otherwise, I am socially withdrawn in the absence of alcohol. Sometimes I felt like multiple people, and certainly people in different aspects of my life see me very differently, but it was not until I understood DISC that I could provide this insight; until now, these different trait manipulations were accidental. I also see now that my strongest relationships are built with those that are predominantly "S," I clash strongly when a "D" is

aggressive or rude to others, and without clashing, I tend to be irritated by those that are predominantly "I." When challenged, stressed, or confronted, my default position is the safety of my inner "C."

A key part of patient care, good teamwork, and emotional intelligence is the ability to listen and observe. An "S" and a "C" tend to be good listeners, observant, and appreciative of detail. Conversely, a "D" and an "I" are poor listeners and pay little attention to detail. Nevertheless, an "I" and a "C" together are best equipped to convert this knowledge (cognitive domain) to actual emotional intelligence (psychomotor domain). To be better health professionals and colleagues, there is a need to balance the 4 traits to ensure that, regardless of predominance, there is enough balance in other traits to ensure emotional intelligence.

One of the intriguing aspects of DISC for students studying science-based courses is the conversion of the DISC model from psychology to biology. Although DISC was developed in 1923, 2005 saw the development of the Fisher temperament inventory (14), which classifies personality traits on the basis of biochemical predominance. Fisher identifies 4 key traits (Fig. 3): directing, exploring, negotiating, and building. Directors are testosterone-dominant, with a tendency to be logical, decisive, and skeptical and to have a direct communication style that is very much like the "D" trait in DISC. Explorers are dopamine-dominant, with a tendency to be risk takers, creative, spontaneous, energetic, optimistic, and impulsive, as aligns closely with the "I" trait of DISC. Negotiators are estrogen-dominant and rely on social skills, empathy, and relationship building, as matches the "S" in DISC. Builders are serotonin-dominant and like structure, routine, and conformation to rules, as is similar to the "C" in DISC. Fisher uses these traits to describe compatibility among romantic partners, for whom opposites attract and like attracts like. That is, other than attraction between people with the same trait, builders and explorers attract and directors and negotiators attract. This recognizes the same opposition in DISC, with "D" and "S" being opposites but often forming productive teams or relationships whereas the "C" and "I" of DISC mirror the builders and explorers of the Fisher temperament inventory. Whether biochemical or psychosocial, a degree of care needs to be exercised when managing conflict or teamwork between DISC-based "C" and "D" traits (builders and directors in the Fisher temperament inventory) and between "S" and "I" traits (negotiators and explorers in the Fisher temperament inventory).

CONFLICT RESOLUTION

Communication is the key to emotional intelligence and conflict resolution. Although there are several approaches to conflict resolution, emotionally intelligent people will focus on the issue, not the person, and will be honest, assertive but controlled, and agreeable and understanding. They will listen and acknowledge all perspectives, avoid being drawn

TABLE 1
Variables Associated with DISC Traits

| Variable	D	I	S	C
Motivation	Power, authority, outcome, success	Attention, friendship, fun	Relationship building, people helping, appreciation	Consistency, value, excellence
Key value	Power	Recognition	Approval	Respect
High priorities	Action, results, achievement	Enthusiasm, collaboration, action	Support, stability, collaboration	Attention to detail, use of expertise, knowledge growth
Low priorities	Relationships	Routine	Change	Relationships
Task focus	Get immediate and fast results	Do not rush but make it fun	Form team and take time to complete	Do it yourself and do it properly
Comfort needs	Dominance and challenge	Recognition and interaction	Appreciation and service	Quality and accuracy
Response style	Reactive	Reactive	Reflective	Reflective
Risk approach	Does not consider consequences	Does not consider consequences	Is risk-averse	Is risk-averse; assesses risk
Dynamic style	Nature	Nurture	Nurture	Nature
Fears	Losing control, being vulnerable, appearing weak	Being rejected, ignored, or disapproved of	Experiencing change, disharmony, conflict	Being criticized, making errors, showing excess emotion
Actions	Confident, direct, insensitive, impatient	Charismatic, optimistic, impulsive, disorganized	Patient, teamwork, indecisive, accommodating	Skeptical, precise, analytic, critical, isolated
Strong skills	Decisive	Persuasive	Diplomatic	Problem solver
Weak skills	Listening	Checking	Initiating	Deciding
Conflict default	Demands own way	Makes personal attack	Complies	Avoids confrontation
Stress default	Takes charge	Is argumentative	Is withdrawn	Seeks more data
For productive interactions	Lets them take charge	Gets them excited	Provides support	Provides information
Avoiding conflict	Not being competitive	Letting them get ahead	Relaxing and not pressuring them	Letting them set pace
Conflict follow up	Results	Attention	Support	Service
Effort areas for interactions	Concise and efficient	Interesting and interested	Cooperative and supportive	Accurate and idea generator
Supporting them	Empower	Encourage	Care	Provide structure
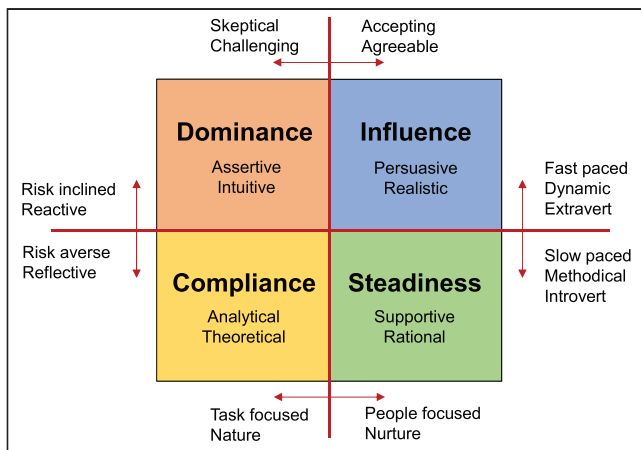
FIGURE 2. Characteristics of DISC traits.

into an argument, offer blameless but sincere apology, and provide action. As an exercise, students at Charles Sturt University are asked to role-play a variety of scenarios of conflict with patients or colleagues. They are encouraged to consider the context and draw on authentic experiences to explain exactly how they feel, describe the specific action that made them feel that way, and describe the impact this or repeated incidents will have. This method creates accountability without the need for assertiveness. For example, an event that is not so uncommon is a student being openly criticized or rebuked in front of staff or patients. Disempowered students lack the inventory to express their concerns or to challenge the behavior, with a possible result being that they learn and repeat these behaviors when they are supervising students in the future. An understanding of DISC allows an emotionally intelligent student to identify specific traits and likely drivers and to privately express something to the effect of "I appreciate your feedback and interest in helping me develop my clinical skills, but when you openly criticize me in front of patients I feel humiliated and unprofessional, which undermines my confidence and the respect patients and other staff have for me."
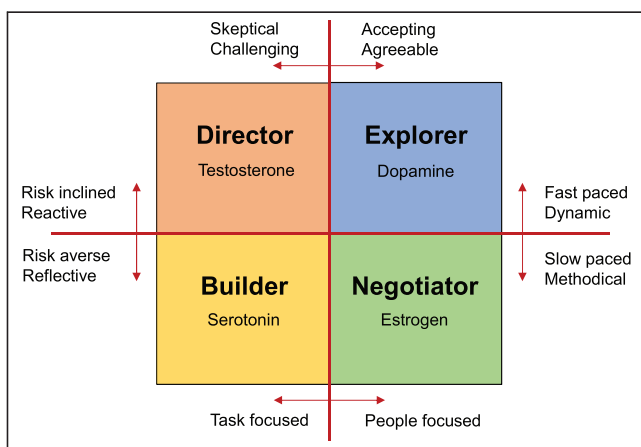
Unsurprisingly, conflict resolution can adopt several strategies that align with the characteristics of the various DISC traits (Fig. 4). Emotional intelligence allows improved conflict resolution by finding a balance or middle ground. The compromise accommodates the DISC traits of all parties involved in the conflict and provides a model for proactive prevention of conflict. Emotional intelligence at the initiation of group work, for example, allows preemption of issues and mitigation of initiated actions.

Students at Charles Sturt University are challenged to understand their own personality traits and communication style more deeply. Although real-time analysis is useful in honing interpersonal skills as described above, a strong foundation underpinned by deeper insight into self ensures that interactions and conflict resolution are initiated from a sound platform. Table 2 provides a series of descriptors for DISC traits. With omission of row 1 in the table, so that students would not know which descriptors apply to which traits, the students would be asked to check off those that apply to themselves. A simple summation of the number of ticks in each column represents the weighting of the DISC trait. Once students have determined and debated their balance of traits, they should be challenged to consider how they might best modify their own behaviors in order to get the most out of interactions with others, including those with the same trait dominance (Table 3). These then become the foundation for authentic capability development in the clinical environment, and students are encouraged to reflect on their learning, their interactions, and how emotional intelligence helped or could have improved the scenario. This represents honing of the psychomotor skills required for emotional competence.

Students need to consider their own dominant traits and learn to modify their behavior to accommodate the needs of patients and staff. For example, students with predominantly "D" traits are likely to clash with most patients and staff through ego, impatience, or communication differences.
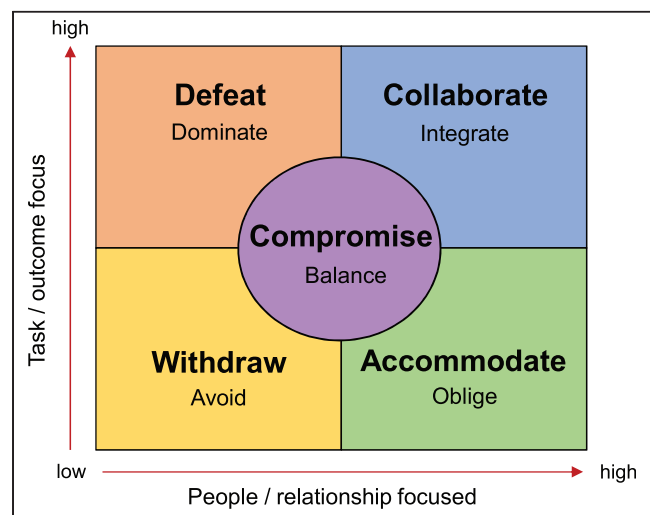

FIGURE 3. Characteristics of Fisher temperament inventory traits match closely those of DISC.

FIGURE 4. Task- vs. people-focused conflict resolution strategies match closely those of DISC.

TABLE 2
Inventory for Self-Determining DISC Trait Balance (Adapted from (15))

D	I	S	C
Action-orientated	Ambitious	Adaptable	Accurate and precise
Adventurous	Creative	Calm and relaxed	Cautious
Competitive	Energetic	Team-oriented	Conscientious
Controlling	Enjoys change	Supportive	Consistent
Decisive	Enthusiastic	Enjoys popularity	Detailed
Firm or forceful	Friendly and fun	Enjoys routine	Enjoys instruction
Results-oriented	Impulsive	Good listener	Factual
Independent	Group-oriented	Loyal	Impersonal
Assertive	Initiator	Not demanding	Inquisitive
Quick to judge	Inspirational	Nurturing	Logical
Persistent and determined	Confident	Patient	Orderly and systematic
Productive	Emotional	Trusting	Organized and controlled
Purposeful	Mixes easily	Organized	Perfectionistic
Seeks power	Motivator	Respectful	Persistent
Self-reliant	Optimistic	Sensitive	Analytic
Direct	Animated	Sympathetic	Problem solver
Strong-willed	Spontaneous	Thoughtful	Scheduled and organized
Takes control	Takes risks	Tolerant	Sensitive

When dealing with staff or patients who are any of the 4 DISC traits, the students would be wise to channel their "S." Conversely, if students are predominantly an "S" and working in an environment dominated by a "D," "I," or "C," the capacity to draw on their own "D," "I," or "C" could bring balance that allows productive interactions. A working example might be a student trying to get a supervisor to sign off that the student has met a capability or standard. A "D" supervisor might appreciate the comment, "You asked me to spend time with person X performing bone scans so you can sign my paperwork. Is that OK to do now?" An "I" might appreciate the comment, "I have really enjoyed shadowing you while you do bone scans and picked up some amazing techniques that have enhanced the way I do things." For an "S," a small gesture could be provided such as a card or a note of thanks expressing, "I could not have learned so much without your amazing support. I wish all supervisors were like you." Finally, the "C" will be the most difficult. Students should be prepared to answer questions and provide firm details on how many procedures have been completed, such as "I have read the standards and have performed X bone scans that meet category A and Y bone scans that meet category B, with all paperwork and reflections completed and submitted, but would appreciate your scrutiny to determine whether I am ready for sign-off." Similar application of DISC and emotional intelligence can help improve patient compliance and satisfaction as evidenced in the following reflection (from a student assessment):

> A patient arrived 15 minutes late. I observed that the patient was agitated and aggressive, and I wondered what the root

TABLE 3
Interactions Associated with DISC Traits

Individual communicating	Individual being communicated with			
	D	I	S	C
D	Avoid ego collision and be flexible enough to compromise	Invest time in socializing and be open and friendly	Slow pace, soften tone, and provide support and assurance	Provide facts but be patient, firm, and decisive
I	Be concise, respect personal space, and do not take it personally	Do not compete for recognition or attention; focus on issue	Earn trust without being overly social; provide support and assurance	Provide facts, do not bluff, and respect personal space
S	Be confident, do not take it personally, but do not be intimidated	Accept their enthusiasm and friendliness but do not waste time	Be assuring, confident, and assertive to expedite time lines	Be confident, provide facts, and do not be discouraged by skepticism
C	Avoid too much detail and focus on key points and results	Be friendly and enthusiastic, avoid detail, and focus on person	Allow time for information to be digested; be friendly and assuring	Stay in control, consider all perspectives, and do not let discussion drag on

cause was. Were they exhibiting "D" traits, or were they an "I" under stress? As a student predominantly an "S," I did not have the confidence to ask, as I felt intimidated by the situation. I should have taken the initiative and tried to determine if the patient was OK and thus should have recognized the need to have professional confidence to better help patients and staff. I think better interpersonal skills, communication, and emotional intelligence could have helped improve outcomes. The overall mood for the day changed, as did the team work. I felt upset that I had failed the patient in some way. I could imagine the patient was stressed and anxious about the seriousness of the health situation and that a wider emotional intelligence inventory would have been well received. The scenario helped me understand that my "S" predominance helps me empathise with the patient and potentially provide quality care. Realising this for the first time allowed me to proactively push myself to find the inner "D," "I," or "C" when appropriate. Several patients over the subsequent week were also difficult for their own reasons, and I actively channeled my "D" instead of being passive, which gave me the confidence to be active and with that deliver the "S"-based care. The patient experiences were improved by my understanding and application of DISC, and my confidence and capability were enhanced.

Armed with these basic skills and insights, there is an opportunity to participate in a workshop before students encounter an authentic clinical environment. Classes are generally divided into large groups of 6–8 students to ensure there is a reasonable blend of DISC traits. A simple task of classification or ranking can then be used for individuals to score and then, by negotiation, for the group to settle on a score that represents group consensus. The grounded-truth rank can be used to sum the differences from that grounded truth for both the individual and the group. The comparison of difference scores between the individual and the group may reflect their ability to influence the other members of the group. Nonetheless, the most important learning from the task is the student reflections on group dynamics and how emotional intelligence was used within the task. One such activity is the "lost at sea" ranking exercise (https://insight.typepad.co.uk/lost_at_sea.pdf).

CONCLUSION

Emotional intelligence is a powerful tool in enhancing interactions with patients and colleagues. Although some have organic capabilities in emotional intelligence, there is a need to deliberately integrate skills and capabilities in curricula of nuclear medicine programs and, more broadly, across the health sector. Formal curricula in emotional intelligence promote patient advocacy, improve outcomes, and are consistent with the philosophy of personalized medicine. Rich immersive professional development activities targeting emotional proficiency using cognitive, affective, and psychomotor taxonomies could readily be woven into didactic and authentic learning environments in undergraduate programs and in continuing education activities for those already in the workforce.

DISCLOSURE

No potential conflict of interest relevant to this article was reported.

REFERENCES

1. Hojat M, Spandorfer J, Louis DZ, Gonnella JS. Empathic and sympathetic orientations toward patient care: conceptualization, measurement, and psychometrics. *Acad Med.* 2011;86:989–995.
2. Kim SS, Kaplowitz S, Johnston MV. The effects of physician empathy on patient satisfaction and compliance. *Eval Health Prof.* 2004;27:237–251.
3. Skinner C, Spurgeon P. Valuing empathy and emotional intelligence in health leadership: a study of empathy, leadership behavior and outcome effectiveness. *Health Serv Manage Res.* 2005;18:1–12.
4. Karimi L, Leggat SG, Bartram T, Afshari L, Sarkeshik S, Verulava T. Emotional intelligence: predictor of employees' wellbeing, quality of patient care, and psychological empowerment. *BMC Psychol.* 2021;9:93.
5. Mackay SJ, Hogg P, Cooke G, Baker RD, Dawkes T. A UK-wide analysis of trait emotional intelligence within the radiography profession. *Radiography.* 2012;18:166–171.
6. Jiménez-Picón N, Romero-Martín M, Ponce-Blandón JA, Ramirez-Baena L, Palomo-Lara JC, Gómez-Salgado J. The relationship between mindfulness and emotional intelligence as a protective factor for healthcare professionals: systematic review. *Int J Environ Res Public Health.* 2021;18:5491.
7. Redelmeier DA, Najeeb U, Etchells EE. Understanding patient personality in medical care: five-factor model. *J Gen Intern Med.* 2021;36:2111–2114.
8. Cerezo MV, Blanca MJ, Ferragut M. Personality profiles and psychological adjustment in breast cancer patients. *Int J Environ Res Public Health.* 2020;17:9452.
9. Atkinson RL, Atkinson RC, Smith EE, Bem DJ. *Introduction to Psychology.* 11th ed. Harcourt Brace College Publishers; 1992:524–573.
10. Currie G. *Yindyamarra winhanganha*: a conduit to indigenous cultural proficiency. *J Nucl Med Technol.* 2022;50:66–72.
11. de Galvão E Brito Medeiros A, Lewis S, McNulty J, White P, Lane S, Mackay S. Emotional intelligence development in radiography curricula: results of an international longitudinal study. *J Med Imaging Radiat Sci.* 2017;48:282–287.
12. Marston WM. *Emotions of Normal People.* K. Paul, Trench, Trubner & Co. Ltd.; 1928:1–405.
13. Girn R, Punch A, Jimenez YA. Diagnostic radiography students' perceptions of working in the clinical environment: a focus on emotional challenges. *Radiography (Lond).* 2022;28:492–498.
14. Fisher HE, Island HD, Rich J, Marchalik D, Brown LL. Four broad temperament dimensions: description, convergent validation correlations, and comparison with the Big Five. *Front Psychol.* 2015;6:1098.
15. Merrill DW, Reid RH. *Personal Styles and Effective Performance: Make Your Style Work for You.* Chilton Books; 1999.

Building Program Efficiencies Using JRCNMT Compliance Forms

George Patchoros and Grace Wenzler

Department of Engineering, Physics and Technology, Bronx Community College, Bronx, New York, New York

In the past, program assessment was considered a supplemental activity designed to analyze program performance once instruction had concluded. This process was often a summative activity that ignored the possibility of being able to change instruction throughout the implementation of the curriculum. However, the assessment process has evolved in such a way that assessment can now be considered an integral part of curriculum development. Forms J and L of the Joint Review Committee on Educational Programs in Nuclear Medicine Technology (JRCNMT) requirements for the annual report have recently been updated to support Nuclear Medicine Technology (NMT) programs in JRCNMT's effort to meet and exceed industry standards. At Bronx Community College, the NMT program has taken advantage of these newly developed forms to streamline program assessment. These modifications have changed not only how assessment is implemented at the end of the program but also how students are evaluated throughout their coursework.

Key Words: assessment; student learning outcomes; compliance; forms J and L; program outcomes

The reason for instituting an assessment plan into a program or curriculum is based on the need for overall improvement. Considering this goal, an assessment plan must be designed to address a particular set of learning outcomes. As described by the University of Central Florida, "behavioral and cognitive learning outcomes are given to highlight how Bloom's taxonomy can be incorporated into the larger-scale educational goals or guidelines" (*1*). At Bronx Community College (BCC), the hierarchical structure of Bloom's taxonomy is used as a guiding principle in the creation of appropriate and meaningful learning outcomes. The Nuclear Medicine Technology (NMT) program at BCC executes various levels of assessment, with the intention of creating a continually evolving program based on its assessment findings.

Program assessment happens at 2 levels. The first (and most frequent) level is to ensure the program is able to satisfy student-level outcomes (SLOs) set forth by the college and approved by the Joint Review Committee on Educational Programs in Nuclear Medicine Technology (JRCNMT). The director of the NMT program and the college administration collaborate to determine which goals the program should target for assessment purposes. These outcomes are then clearly defined in the college's course catalog as well as in the individual course syllabi. The idea is to ensure that the students are aware of what is required of them and how they will be evaluated throughout the course as a formative assessment and ultimately, at the end of the course, as a summative measure. Generally speaking, and as a practice at BCC, these outcomes are accompanied by a rubric that acts not only as a metric for formative assessment for the instructor but also as a guide for student expectations.

The second level of assessment is a directive from the JRCNMT. In recent years, the JRCNMT has begun to foster a strong emphasis on assessment (at both the student and the program level). As part of this emphasis, the JRCNMT has established assessment standards that are reflected on several forms that are the basis of the assessment portion of both the required annual report and the larger self-study report.

ASSESSMENT RESOURCES

It stands to reason that NMT programs across the country will likely have similar resources when it comes to assessment. At BCC, the NMT program benefits from the guidance of the college's Assessment Council, wherein each department has its own representation. This council was created to help design assessment strategies that address the stated outcomes for each program as listed in the course catalog.

In past years, the NMT program at BCC had to rely on this council to determine how to properly use the gathered data to formulate a strategy for overall improvement. This strategy was designed on the basis of the program-level outcomes and SLOs that were ultimately decided on by the college administration, NMT advisory board, and JRCNMT. Recently, the JRCNMT has increased its involvement in assessment by devoting more resources to and creating new streamlined metrics for its assessment requirements (i.e., Form J, Assessment of Program Student Learning Outcomes; Form L, Program Effectiveness Data).

SLOs

According to Cornell University, SLOs can be defined as "measurable statements that articulate at the beginning what

students should know, be able to do, or value as a result of taking a course or completing a program" (*2*).

Each institution is required to create its own SLOs based on JRCNMT guidelines and requirements for the accredited program. Recent communications from the JRCNMT have offered guidance focusing on the development and implementation of SLOs. Through a collaborative effort between the NMT program director, department assessment coordinator, and college administration, BCC has embraced these suggestions and consequently updated the college's current SLO statements.

SLO DEVELOPMENT

Developing learning outcomes for the program is a multifaceted process. These outcomes must serve several purposes. First, the list of SLOs should be designed in such a way that, in theory, when all are met, the student possesses the skills and knowledge required for graduation. This list should address the most important skills, knowledge, and aptitude that students should acquire across the entire program. To be effective, this list is published in the course catalog, making it available for incoming (or current) students to use as a rubric for self-assessment. Through data analysis of final grades, class participation efforts, and direct observation reports from both instructors and clinical supervisors as part of the formal assessment procedures for the college, it has been determined that students who remain cognizant of these outcomes tend to perform at higher levels because of increased understanding of course and program requirements. To supplement the effectiveness of "publicly" posting these SLOs, BCC requires inclusion of the list of SLOs on each course's syllabus, which is distributed to the students at the beginning of each semester.

Previously, the number of SLOs for the NMT program at BCC was 10; these were created based on the requirements of each course. However, through feedback provided by the assessment coordinator and the JRCNMT, we found this list of outcomes to be too cumbersome for assessment to be properly performed. The original intent was to try and link individual SLOs to individual courses. However, program-level outcomes are not designed to address specific course outcomes; instead, they provide an overall evaluation of the skills and knowledge a student acquires over the entire program. After evaluating the number of SLOs (not necessarily the SLOs themselves), it was determined there was a redundancy between these outcomes that resulted in inaccurate assessment due to aligning program outcomes to individual courses thus diluting the differentiation between the two.

To rectify this redundancy, we elected to reduce the number of SLOs to 5. However, to accomplish this reduction and still have the list represent all the skills and knowledge the students are required to obtain, the SLOs had to be rewritten. The new list of SLOs is general enough to encompass all that is required but still retain an alignment to specific assessment tools for proper evaluation.

The next issue that had to be addressed was to determine the assessment vehicle that was to perform the assessment on each of these SLOs. At this point, a collaborative effort materialized between the teaching faculty and the assessment and program coordinators. The goal was to look at the syllabus of each course in the NMT program and determine which courses offered the content or activities that addressed the specific SLOs. We would then look toward the formative or summative evaluations of those activities (e.g., tests, presentations) and use that data for the assessment vehicle for a particular SLO.

As a welcomed, yet unintended, consequence, we encountered another set of redundancies, which involved multiple assessment vehicles for each of the SLOs. This time, however, these redundancies would benefit the assessment process. Having multiple assessment vehicles for the same SLO allows the SLOs to be assessed uninterrupted, through each assessment cycle. For example, because of the current coronavirus disease 2019 pandemic, some of the assessment methods in each course had to be modified to satisfy the change in teaching modality. Because there are multiple ways of assessing each SLO, we are less likely to be in a situation that does not allow the assessment of any particular outcome due to a change or omission of the curriculum. Ultimately, being able to use multiple assessment vehicles across various courses for the same SLO assured the college that each SLO was able to be implemented and assessed.

PROGRAM EFFECTIVENESS DATA & BENCHMARKING

Once a proper method of evaluating SLOs has been constructed, and assessment vehicles chosen to address specific SLOs, the data collected must be analyzed for the ultimate purpose of improving the learning experience for students. Again, this is a multifaceted process.

The method chosen to evaluate a program's effectiveness is useful only when compared with a standard. This standard is known as a benchmark. According to the Center for Community College Student Engagement (CCCSE), "Benchmarking is the systematic process of comparing an organizations performance on key measures to the performance of others" (*3*).

At BCC, the Nuclear Medicine Technology Program has established benchmarks that can be found on the recently updated Forms J and L of the JRCNMT compliance report.

The benchmarks found on Form J reflect the level of competence required of each student as stated in the published SLOs. These benchmarks were chosen on the basis of several factors. First, historical assessment data of the program were analyzed to determine an appropriate and reasonable goal (as described by the SLOs) for the students to achieve. Historical assessment data were used to minimize the "shot-in-the-dark" attempts at establishing reasonable student goals. These goals are ultimately assessed through both formative and summative means in various courses and throughout various stages of a student's progress through the program.

Another consideration in the formulation of a benchmark is how it compares with outside requirements. Benchmarks that reflect individual student performance are created at the "local" level and tend to address the requirements of the college. Although these benchmarks are designed with academic performance in mind, they must also align with industry performance as well.

Form L of the JRCNMT compliance report establishes the benchmarks at the industry level. Largely influenced by accrediting standards, these benchmarks are designed as an assessment tool for the program. These benchmarks are influenced by assessment data gathered on an occupational level and reflect a common standard throughout the profession.

Regardless of either a program or student level, a benchmark that will yield accurate assessment data is overwhelmingly assessing a quantitative activity. Because of the objective nature of quantitative analysis, program data can be gathered and assessed across the curriculum, regardless of who is performing the evaluation. This is an extremely crucial aspect of assessment when dealing with program-level effectiveness. To yield accurate assessment results, limiting the amount of subjective variance is critical.

Effective assessment needs to happen at multiple levels at varying times to yield meaningful results. To compile the most accurate data possible, it is up to the instructor to maintain a focus on addressing the student and program outcomes. At the program level, although data are collected on a continual basis, outcomes are generally assessed every 2 y (which represents a full program cycle). These outcomes should differ from those that are course-level outcomes or SLOs.

Over the past few years, our program at BCC has implemented several tools to streamline the process of completing Forms J and L while ensuring that the SLOs are met. The feedback from the JRCNMT has helped to restructure our program by targeting more efficient ways to retain records, organize data, and implement teaching tools. Below is a summary of some elements that we have already restructured to improve the assessment process of our program while also focusing on plans to enhance the monitoring of our SLOs.

WEB-BASED COURSE MANAGEMENT SYSTEMS

Web-based course management systems (such as Blackboard) have served as an integral tool for program assessment, allowing for thorough record keeping that helps track individual grades on assignments and exams. Writing assignments can now be kept in a digital format rather than in paper form, which often required not only numerous paper files for each student but also storage for the files. In addition, the use of discussion boards has allowed students to interact with their classmates, resulting in an environment that promotes immediate and meaningful feedback, as compared to a more traditional strategy of assignment submission that does not allow such interaction. Another major benefit of these course management systems is the ability to run reports and statistics on assignments or exams. If all students in the course have their assignment recorded in the grade center of Blackboard, for example, the instructor can simply select the Column Details option from the drop-down menu. This will determine the average, median, SD, and range of grades, and

COLUMN DETAILS

Column
Sp 21 Mock (Test)

Points Possible
100

Description

STATISTICS		STATUS DISTRIBUTION		GRADE DISTRIBUTION	
Count	12	Null	0	Greater than 100	0
Minimum Value	75.50	In Progress	0	90 - 100	7
Maximum Value	98.50	Needs Grading	0	80 - 89	4
Range	23.00	Exempt	0	70 - 79	1
Average	91.45833			60 - 69	0
Median	NaN			50 - 59	0
Standard Deviation	8.03756			40 - 49	0
Variance	64.60243			30 - 39	0
				20 - 29	0
				10 - 19	0
				0 - 9	0
				Less than 0	0

FIGURE 1. Example of one of the reports that can be run in BlackBoard. It allows for quantitative analysis of selected parameters.

more (Fig. 1). Using a course management system improves teaching methods as well as calculates benchmark results on Form J. Administering exams on Blackboard (especially if done in-person in a monitored computer lab) can also be beneficial. By limiting (and in some cases eliminating) the need for traditional test evaluation methods, such as "by-hand" markup, the instructor can provide immediate feedback with the added benefit of reducing student testing anxiety. In addition, taking an online exam while being monitored in the classroom sets up an environment similar to that for board exams. We found that administering a "mock board exam," with the same amount of time and number of questions set by the American Registry of Radiologic Technologists, has better prepared students for their licensure exams. Finally, the way the course material is presented to the student through Blackboard has improved overall student organization. Web-based course management allows the student to access materials all in 1 location. The course syllabus, lectures, homework assignments, learning outcomes, handbooks, and more can be placed in 1 location for the student. This has been an incredible asset in improving student performance and retention within our courses.

ONLINE SURVEYS

Transitioning from a paper-based collection method to an online format has had some challenges; however, it is proving to be a more efficient method of record keeping. In the past, all of our surveys were administered on paper and retained for the appropriate amount of time. This not only took up a lot of space but also made data analysis a daunting task. In recent years, we have begun the transition to online surveys, which has immensely improved our organization and collection. Surveys administered to students for individual course instruction, clinical site evaluation, and overall program effectiveness are now administered online. Administering the surveys in this format has allowed us to quickly run reports based on student feedback, aiding in assessment and program improvement. Addressing JRCNMT standard D3.1 g (Evaluating graduate assessment of program effectiveness) has been particularly helpful with conducting online surveys. In this online format, the program can put together several questions that pertain to program effectiveness, sending them to the students to easily complete. These results serve as an integral component in completing assessment questions on Form L (Fig. 2). Currently, the surveys that we give the clinical instructors for evaluating student performance are still on paper. This has created some recent issues, because analyzing the data on specific questions that relate to individual SLOs can be time consuming. In addition, if a clinical instructor is busy with other tasks, they sometimes fill out the form incorrectly and will eventually have to redo it, creating inefficiencies for both the clinical coordinators and the affiliate education supervisors. Moving forward, we will begin to implement these surveys online as well. We feel that this will streamline the process of student evaluations, allowing us to easily interpret trends and areas we need to address with the entire class and improving student performance and assessment strategies.

EPORTFOLIOS

Electronic portfolios are valuable tools that improve student learning while also aiding in assessment strategies. These portfolios allow students to create individual work that they can store electronically and on which they can continue to reflect at their leisure, thus enhancing their learning. In addition, electronic portfolios allow students to access information not only while they're enrolled in the program but also even after graduation. Our
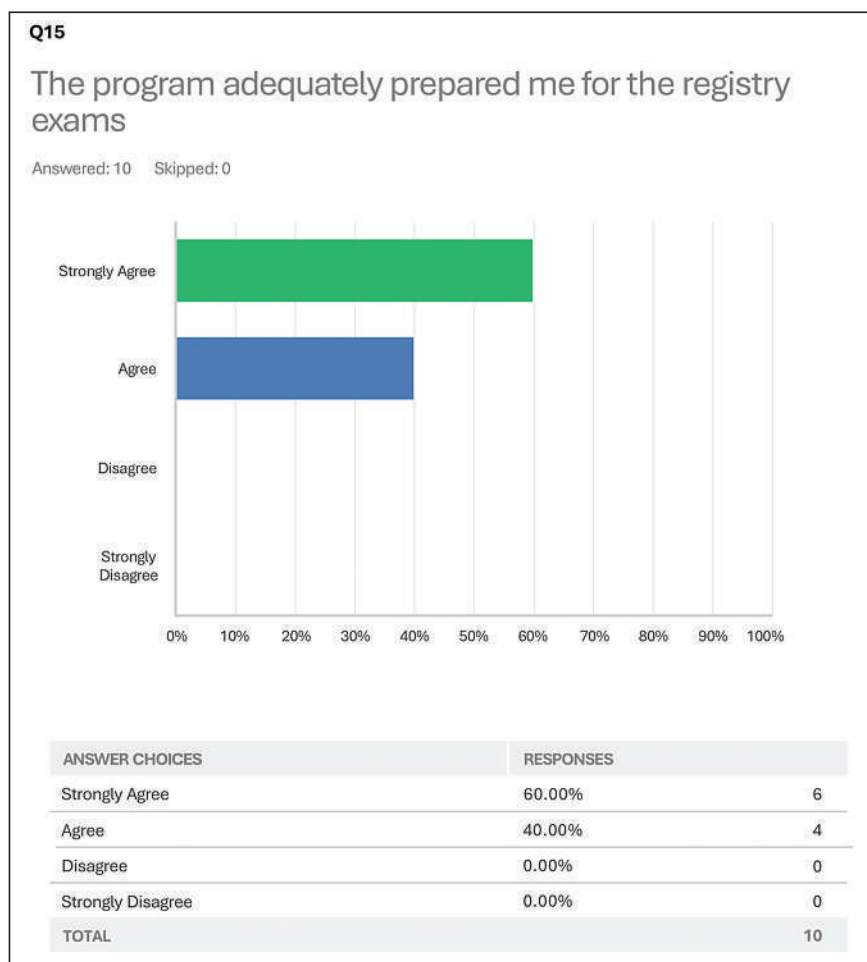

FIGURE 2. Example of an online survey that can be created via Survey Monkey. This method was particularly useful in conducting our graduate surveys.

program has created an NMT EPortfolio for students enrolled in the program. Currently, it is being used for resources to be stored in 1 easy location. In our current EPortfolio, our handbooks, blank evaluations/rubrics, student learning outcomes, and competency forms can all be accessed from the same site. Moving forward, we plan to add a collaborative area for job postings, allowing both recent graduates and instructors to post information about current job openings. We plan to use this to improve the job placement assessment portion of Form L. The main benefit of this database in comparison to the Blackboard learning management system is that students can still access it after graduation. Helpful resources such as job postings, CT competency forms, board exam information, and the like can all be accessed in this 1 location.

VIDEO CONFERENCING

The pandemic has brought unforeseen challenges, which required instructors to quickly adapt to new teaching methods and technology. Although the incorporation of video conferencing software, such as Zoom, was a definite transition, it has proved very useful with both teaching and assessment.

Our program has primarily been using Zoom for a combination of online instruction, meetings, and advisement since the pandemic began in March 2020. This online conferencing platform has allowed us to improve some of our teaching methods as well as assessment. Using this technology has allowed us to hold online information sessions for incoming and prospective students, largely improving the participation at these events while still allowing us to share our screen to show PowerPoints, course expectations, prerequisites, and more. In addition, it still allows students to ask any questions they may have about the nuclear medicine field or program expectations. We feel strongly that the increased participation at the information sessions will improve student retention in the program.

Many of our students are considered "nontraditional" (i.e., not fresh out of high school but rather older than 25 y). According to an article published in *Contemporary Issues in Education Research,* "a vast majority of fresh-out-of-high-school 'traditional' aged (18–24) enrollees have shifted toward a wave of 'nontraditional' aged (25+) students, featuring displaced workers, first-generation college attendees, returning students, and those who desire a change in career (either due to financial hardship or preference), administrators have no choice but to alter collegiate curriculums, services, and overall philosophies. An overwhelming majority of institutions affected by this trend are community colleges" (*4*). Many of our nontraditional students often deal with the challenges associated with balancing work, family, and school. With these students, in particular, we feel it is important to hold detailed information sessions specifying program requirements and expectations. During the clinical internship portion of the program, we feel that this transparency is imperative to improve student retention and graduation rates.

Form L in the compliance report asks for an assessment of the graduation rate, which the colleges' learning management system (LMS) should help to improve.

Aside from an increase in information session participation, we also have noticed an increase in participation at the advisory board meetings since these began to be held online. Although the pandemic forced a transition to online, because of the noticeable increase in attendance we plan to retain this format. In addition, many of the clinical instructors find it challenging to commute to our campus after they finish work for the day. Traffic, weather, and our proximity to Yankee stadium can cause immense delays in travel time to our campus during rush hours. Fortunately, Zoom use for our advisory board meetings has allowed board members to call in from anywhere, largely increasing our advisory board attendance and improving assessment strategies on Form L.

Last, using this technology has helped us to communicate with students in a private setting. We can now easily hold individual Zoom sessions for radiation badge review, midrotation clinical evaluations, and advisement. Zoom sessions can easily be worked around students' clinical internship schedules while accommodating the instructors. As we transition out of the pandemic, our plan is to continue these meetings online.

STUDENT RESOURCES

The annual compliance report has helped our program to recognize areas in need of improvement, especially due to additional challenges associated with the pandemic. More than ever, students are dealing with additional pressures, whether they be financial, psychologic, or physical. Over the last few years, we have worked to compile resources offered to our students, easing the burden of some of the financial constraints associated with attending college while also working to improve their job outlook on graduation.

In the last few years, we have been fortunate enough to have applied for and received grant funding for the program. We have used this funding to jumpstart tutoring, CT instruction, review classes, allocations for conferences, and textbooks. Students in the program now have an option for free tutoring, where select second-year students tutor the first-year students. The second-year students receive an hourly wage (helping them make some money during clinical internship) while the first-year students can review core nuclear medicine topics. Similarly, we have recently begun review sessions for the board exams with past lecturers or outside speakers. Both tutoring and these review sessions are free for the students and helped to improve both program retention and board exam pass rates.

In addition, with the growing need for PET/CT technologists, we felt it was imperative to incorporate CT instruction

into the program. This grant funding has allowed us to hold an elective CT course for students, again at no additional charge. Also secured within this grant funding are allocations for conference attendance. We have been able to recently secure funding for hotel and travel expenses to the annual Greater New York Chapter of Society of Nuclear Medicine (GNYCSNM) conference. This conference allows students to present abstracts while increasing their opportunity to network within the industry. These resources have largely helped to improve job placement rates on graduation, again allowing us to more easily meet our benchmarks on Form L.

As with any program, there is a direct correlation between the support that it receives and how well it meets its intended goals. When using the feedback from the JRCNMT compliance report, specifically Forms J and L, the NMT program at BCC has been able to restructure the tools used for assessment. This restructuring allowed us to not only to improve areas of instruction and assessment that focus on student success but also to streamline data collection for future analyzation. We plan to continue using the resources provided by the JRCNMT to track trends within assessment data while focusing on overall student performance.

DISCLOSURE

No potential conflict of interest relevant to this article was reported.

REFERENCES

1. Blooms taxonomy. University of Central Florida website. https://fctl.ucf.edu/teaching-resources/course-design/blooms-taxonomy/. Accessed August 26, 2022.
2. Center for Teaching Innovation, Cornell University. Setting learning outcomes. Cornell University website. https://teaching.cornell.edu/teaching-resources/designing-your-course/setting-learning-outcomes. Accessed August 26, 2022.
3. Center for Community College Student Engagement. *Benchmarking & Benchmark: Effective Practice with Entering Students.* University of Texas at Austin, Community College Leadership Program, 2009.
4. Jesnek L. Empowering the non-traditional college student and bridging the "digital divide." *Contemp Issues in Edu Res (CIER)*. 2012;5:1–8.

Differential Tumor Biology Between Locoregional and Distant Metastasis in a TENIS Patient with Tyrosine Kinase Inhibitor–Resistant Recurrent Disease: Comparative Evaluation with ^{18}F-FDG, ^{68}Ga-DOTATATE, and ^{68}Ga-PSMA-11 PET/CT

Sunita Nitin Sonavane and Sandip Basu

Radiation Medicine Centre, Bhabha Atomic Research Centre, Tata Memorial Hospital Annexe, Parel, India, and Homi Bhabha National Institute, Mumbai, India

We present the molecular PET/CT imaging profile of an interesting case of differentiated thyroid carcinoma that later transformed into TENIS (thyroglobulin elevation and negative iodine scintigraphy) with tyrosine kinase inhibitor–resistant recurrent, aggressive disease. The patient was evaluated to assess somatostatin receptor 2 or PSMA expression to explore whether there might be any effective targeted nuclear therapy. ^{18}F-FDG, ^{68}Ga-DOTATATE, and ^{68}Ga-PSMA-11 PET/CT scans were obtained, all of which revealed tracer avidity in extensive locoregional disease. A large, ill-defined retropharyngeal and retrotracheal soft-tissue mass was seen to be eroding the cricoid cartilage and extending into the tracheal lumen and the left-sided strap muscles. In contrast, there was no definite uptake in the multiple lung nodules that were present bilaterally. The scan findings indicated a differential tumor biology between locoregional and distant metastasis.

Key Words: thyroid carcinoma; TENIS; ^{18}F-FDG; ^{68}Ga-DOTATATE; ^{68}Ga-PSMA-11; PET/CT

TENIS (thyroglobulin elevation and negative iodine scintigraphy) is the major cause of mortality and morbidity in patients with differentiated thyroid carcinoma, as no definitive or effective targeted nuclear therapy is available. In approximately 20%–30% of patients with metastatic or recurrent differentiated thyroid carcinoma, there is evidence of lack of sodium iodide symporter expression, with the disease producing negative findings on radioiodine scintigraphy and, thus, being refractory to radioiodine treatment. Preliminary reports show that such tumors may express somatostatin receptor (SSTR) 2 on their cell surfaces, or there can be prostate-specific membrane antigen (PSMA)

overexpression secondary to formation of the tumor neovasculature; PSMA is expressed by the vascular endothelium in a variety of cancers (*1*). Use of PSMA expression in TENIS to determine potential treatment options was confirmed by recent studies on differentiated thyroid cancer (*2–4*). Thus, noninvasive imaging for SSTR-2 or PSMA expression in TENIS is being explored in the search for potential definitive or effective treatment options.

CASE REPORT

An 85-y-old man who had papillary thyroid cancer with no extrathyroidal or nodal involvement underwent total thyroidectomy followed, 2 y later, by surgery for locoregional recurrence. After another 3 y, the patient experienced a relapse comprising locoregional inoperable disease, for which he was treated with multiple sessions of oral radioiodine therapy (cumulative dose, 22.94 GBq [620 mCi]). On subsequent follow-up, his ^{131}I whole-body scan was negative, but he had persistent locoregional disease and an elevated thyroglobulin level and, thus, underwent external radiotherapy. Despite thyroxin suppression, his thyroglobulin level persisted in rising, and ^{18}F-FDG PET/CT showed an ill-defined hypermetabolic mass in the tracheoesophageal groove, abutting the trachea anteriorly and the esophagus posteriorly and reaching the paravertebral region at D1/D2. Multiple tiny ametabolic lung nodules (largest, 1.3 cm) were observed bilaterally. The patient was prescribed a tyrosine kinase inhibitor (sorafenib and, later, lenvatinib) and was monitored by ^{18}F-FDG PET/CT. While taking the tyrosine kinase inhibitor, the patient began to have difficulty swallowing and his serum thyroglobulin levels rose to 351.27 ng/mL, despite his having adequate suppression of thyroid-stimulating hormone and being negative for antithyroglobulin antibodies.

The patient lacked sodium iodide symporter expression. After approval by the institutional ethics committee, he was evaluated by whole-body ^{18}F-FDG, ^{68}Ga-DOTATATE (assessing primarily *SSTR2* expression in tumor cells), and ^{68}Ga-PSMA-11 (assessing PSMA expression in neovascular
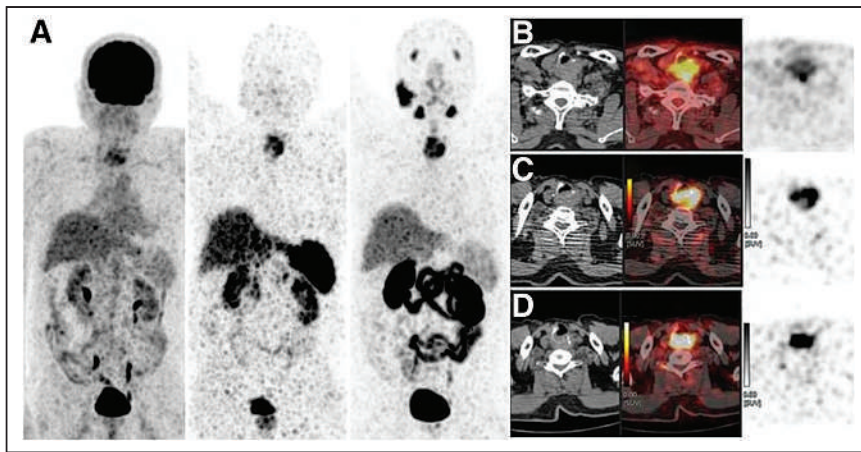
FIGURE 1. Images showing soft tissue in retropharyngeal space with tracheal invasion and posteriorly abutting prevertebral fascia. (A) Maximum-intensity-projection anterior PET images: ^{18}F-FDG, ^{68}Ga-DOTATATE, and ^{68}Ga-PSMA-11 (from left to right). (B–D) Axial CT, PET/CT, and PET images (from left to right) obtained with ^{18}F-FDG (B), ^{68}Ga-DOTATATE (C), and ^{68}Ga-PSMA (D).

endothelium) PET/CT to determine whether there might be any effective targeted nuclear therapy (Figs. 1 and 2). The 3 scans were compared. There was a locoregional, ill-defined retropharyngeal and retrotracheal soft-tissue mass measuring $5.0 \times 3.7 \times 3.5$ cm eroding the cricoid cartilage, extending anteriorly into the tracheal lumen, abutting the prevertebral fascia posteriorly, involving the strap muscles on the left side, and abutting the common carotid artery. Quantitation of each tracer revealed an ^{18}F-FDG SUV$_{max}$ of 5.8, an ^{68}Ga-DOTATATE SUV$_{max}$ of 18.3 and Krenning score of 3 (liver, 14.4; spleen, 36.6), and an ^{68}Ga-PSMA-11 SUV$_{max}$

of 19.5 and molecular imaging PSMA score of 3 (parotid, 18.3). There were multiple distant lung nodules bilaterally, with the largest measuring 1.3×1.1 cm in the right middle lobe; none showed definite uptake on any of the 3 studies (Figs. 1 and 2). Palliative ^{177}Lu-PSMA-617 therapy began. A posttherapy scan showed adequate uptake in the upper mediastinal soft tissue and was to be followed up by another scan after 2 mo. Relief of locoregional pain and greater ease in swallowing indirectly improved the quality of life within 1 mo after therapy. This case demonstrated—in the same individual—differential tumor biology between tracer-positive extensive locoregional disease (^{18}F-FDG, ^{68}Ga-PSMA-11, and ^{68}Ga-DOTATATE with a high molecular imaging PSMA score and a high Krenning score) and tracer-negative distant lung metastases.

DISCUSSION

Silberstein stated that physicians caring for patients with TENIS syndrome are urged to enter them into clinical therapeutic studies whenever possible (5). TENIS tumors show variable expression of SSTR-2 on their cell surfaces (6–8) or PSMA in the neovasculature of the apical surface of endothelial cells (9). ^{68}Ga-DOTATOC or ^{68}Ga-DOTATATE PET/CT can be used for visualization of SSTR-2–expressing lesions. However, not all patients with TENIS lesions express SSTR-2 (6–8). Use of PSMA expression in TENIS as a way to determine potential treatment options was confirmed by studies on differentiated thyroid cancer (1,10,11). PSMA, representing a marker of neovasculature formation expressed by differentiated thyroid carcinoma, has been proposed to contribute to the prediction of tumor aggressiveness and patient outcome (4). One reason for lack of uptake by any of the 3 tracers in the lung metastases could also be the limited PET spatial resolution and the partial-volume effect, particularly considering how small most lesions were. In TENIS, visual evaluation using the Krenning score (^{68}Ga-DOTATATE) and the molecular imaging PSMA (^{68}Ga-PSMA-11) score is a promising approach in exploring tumor biology in metastatic disease and can create the possibility of targeted therapy with^{177}Lu-DOTATATE
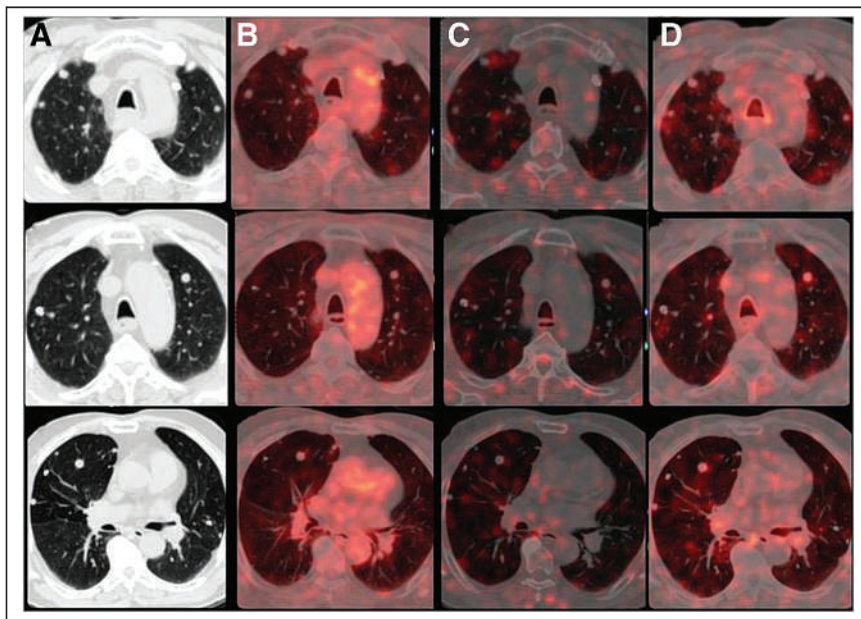

FIGURE 2. Axial lung-window images at 3 different levels showing non–tracer-avid multiple bilateral lung nodules: CT (A), ^{18}F-FDG PET/CT (B), ^{68}Ga-DOTATATE PET/CT (C), and ^{68}Ga-PSMA PET/CT (D).

and ^{177}Lu-PSMA, depending on tracer avidity on ^{68}Ga-DOTA-TATE and ^{68}Ga-PSMA-11 PET/CT (*12*). A high uptake (such as in this case, with a molecular imaging PSMA score of 3 and a Krenning score of 3 for uptake in aggressive locoregional disease) potentially qualifies the patient for targeted SSTR- or PSMA-based therapies as promising options in the absence of other treatments.

CONCLUSION

The present case highlights the differential tumor biology between positive extensive locoregional disease and negative distant lung metastasis, explored by molecular imaging with PET/CT.

DISCLOSURE

No potential conflict of interest relevant to this article was reported.

REFERENCES

1. Chang SS, Reuter VE, Heston WD, et al. Five different anti-prostate specific membrane antigen (PSMA) antibodies confirm PSMA expression in tumor-associated neovasculature. *Cancer Res.* 1999;59:3192–3198.
2. Lütje S, Gomez B, Cohnen J, et al. Imaging of prostate-specific membrane antigen expression in metastatic differentiated thyroid cancer using ^{68}Ga-HBED-CC-PSMA PET/CT. *Clin Nucl Med.* 2017;42:20–25.
3. Sun X, Li Y, Liu T, Li Z, Zhang X, Chen X. Peptide-based imaging agents for cancer detection. *Adv Drug Deliv Rev.* 2017;110–111:38–51.
4. Sollini M, di Tommaso L, Kirienko M, et al. PSMA expression level predicts differentiated thyroid cancer aggressiveness and patient outcome. *EJNMMI Res.* 2019;9:93.
5. Silberstein EB. The problem of the patient with thyroglobulin elevation but negative iodine scintigraphy: the TENIS syndrome. *Semin Nucl Med.* 2011;41:113–120.
6. Versari A, Sollini M, Frasoldati A, et al. Differentiated thyroid cancer: a new perspective with radiolabeled somatostatin analogues for imaging and treatment of patients. *Thyroid.* 2014;24:715–726.
7. Görges R, Kahaly G, Müller-Brand J, et al. Radionuclide-labeled somatostatin analogues for diagnostic and therapeutic purposes in nonmedullary thyroid cancer. *Thyroid.* 2001;11:647–659.
8. Mourato FA, de Almeida MA, Brito AET, Leal ALG. FDG PET/CT versus somatostatin receptor PET/CT in TENIS syndrome: a systematic review and meta-analysis. *Clin Transl Imaging.* 2020;8:365–375.
9. Bravaccini S, Puccetti M, Bocchini M, et al. PSMA expression: a potential ally for the pathologist in prostate cancer diagnosis. *Sci Rep.* 2018;8:4254.
10. Lawhn-Heath C, Yom SS, Liu C, et al. Gallium-68 prostate-specific membrane antigen ([^{68}Ga]Ga-PSMA-11) PET for imaging of thyroid cancer: a feasibility study. *EJNMMI Res.* 2020;10:128.
11. Bychkov A, Vutrapongwatana U, Tepmongkol S, et al. PSMA expression by microvasculature of thyroid tumors: potential implications for PSMA theranostics. *Sci Rep.* 2017;7:5202.
12. Jois B, Asopa R, Basu S. Somatostatin receptor imaging in non-^{131}I-avid metastatic differentiated thyroid carcinoma for determining the feasibility of peptide receptor radionuclide therapy with ^{177}Lu-DOTATATE: low fraction of patients suitable for peptide receptor radionuclide therapy and evidence of chromogranin A level-positive neuroendocrine differentiation. *Clin Nucl Med.* 2014;39:505–510.

Thyroid Scintigraphy and SPECT/CT in a Rare Case of Dual Ectopic Thyroid

Sanchay Jain[1], Suruchi Jain[2], and Deepa Singh[3]

[1]Department of Nuclear Medicine, All India Institute of Medical Sciences, Bhopal, India; [2]Department of Nuclear Medicine, All India Institute of Medical Sciences, Bhopal, India; and [3]Department of Nuclear Medicine, All India Institute of Medical Sciences, Bhopal, India

A dual ectopic thyroid, a rare disorder occurring as a result of aberrant embryonic development, is characterized by the simultaneous presence of thyroid tissue at 2 ectopic sites. ^{99m}Tc-pertechnetate thyroid scintigraphy remains the gold standard in confirming ectopic thyroid tissue. This case highlights the importance of thyroid scintigraphy and SPECT/CT in the evaluation of ectopic thyroid tissue and a dual ectopic thyroid that manifested during the patient's pregnancy.

Key Words: thyroid scintigraphy; SPECT/CT; dual ectopic thyroid

Ectopic thyroid tissue (ETT) is a rare disorder of embryonic development of the thyroid gland (1). In particular, the simultaneous presence of 2 ETTs—dual ectopic thyroid (DET)—is even rarer, with only a few reported cases. ^{99m}Tc-pertechnetate thyroid scintigraphy is the gold standard in evaluating ETT (2). We present an interesting case of DET that first manifested during pregnancy and that reinforced the importance of thyroid scintigraphy and SPECT/CT in its evaluation vis-à-vis conventional methods such as clinical examination and ultrasound.

CASE REPORT

A 24-y-old woman presented with painless midline tongue swelling that she first noticed during her pregnancy, which resulted in the birth of a healthy child about 1 y previously. This swelling was not accompanied by obstruction or any other symptoms. On clinical examination, midline swelling was visible at the base of the tongue. She was initially evaluated with neck ultrasonography, which showed a vascular hypoechoic solid, cystic soft-tissue mass in the lingual region at the midline, measuring about 1.9 × 1.5 cm. The thyroid gland was not visualized in the neck on ultrasonography. Her serum thyroid-stimulating hormone concentration was raised (20 μIU/mL), but serum total triiodothyronine and total thyroxine concentrations were within the reference range. The patient was then referred for thyroid scintigraphy to confirm the clinical suspicion of a lingual thyroid gland. After intravenous injection of 185 MBq (5 mCi) of ^{99m}Tc-pertechnetate, perfusion and static images of the head, neck, and mediastinal regions were acquired, followed by a SPECT/CT acquisition. Anterior perfusion images revealed a focus of mildly increased
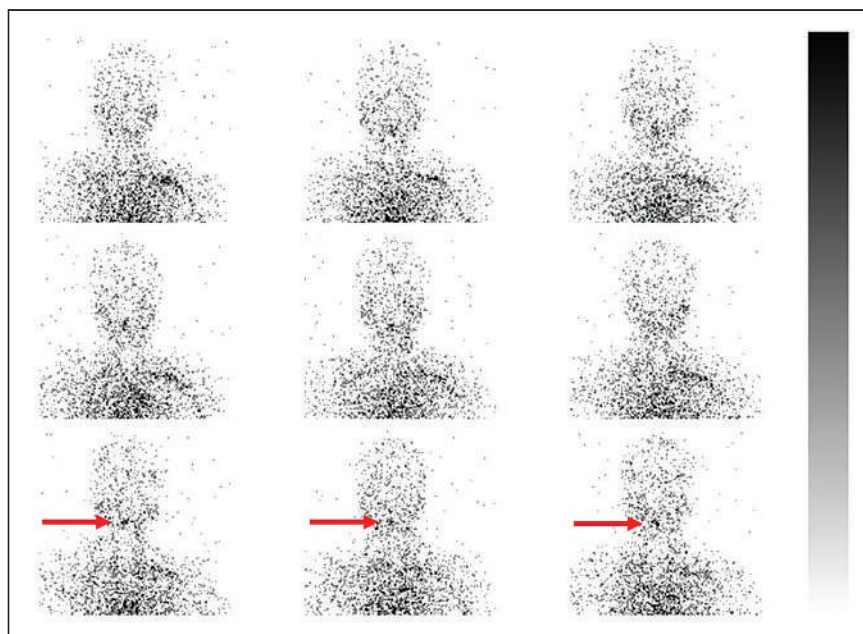

FIGURE 1. Anterior perfusion images of head, neck, and mediastinum show focus of mildly increased tracer flow in region of oral cavity (arrows).

tracer flow in the region of the mouth (Fig. 1). Subsequent planar images showed uptake in the midline of the oral cavity and submental region (Fig. 2), which, on SPECT/CT images, localized to 2 distinct foci of uptake in the midline at the base of
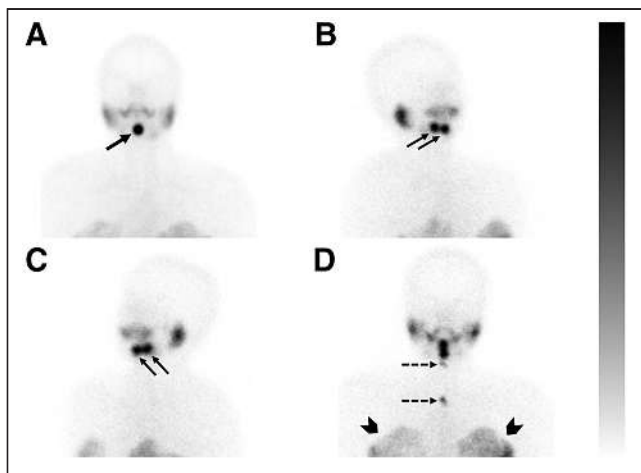
FIGURE 2. Planar images acquired 20 min after tracer injection show 2 distinct foci of uptake in oral cavity and submental region (arrows in oblique views, B and C). These foci were superimposed on anterior image (arrow in A). Anterior view acquired with further neck extension (D) shows 2 distinct foci of uptake (upper and lower dashed arrows represent markers placed at chin and suprasternal notch, respectively). Thyroid is not visualized at its normal location in neck. Tracer distribution in thoracic region is suggestive of uptake in both breasts (arrowheads in D).
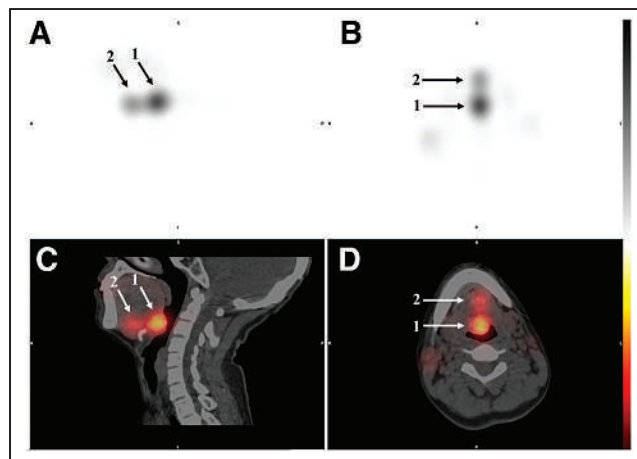

FIGURE 3. Sagittal and transaxial SPECT (A and B, respectively) and SPECT/CT (C and D, respectively) images. Increased uptake is seen in soft-tissue density at base of tongue at midline (arrow 1), and smaller ill-defined focus of increased uptake is seen in floor of mouth in suprahyoid–submental region (arrow 2).

tongue and in the floor of mouth (submental–suprahyoid region) (Fig. 3). No focal uptake was noted in the neck or mediastinum. The patient reported that her infant has been healthy and achieving age-appropriate milestones. She was advised about appropriate radiation safety precautions, especially with regard to breastfeeding. The patient was then started on thyroxine replacement.

DISCUSSION

The estimated prevalence of ETT is about 1 per 100,000–300,000 people and 1 per 4,000–8,000 patients with thyroid disorders. DET is even rarer, with fewer than 100 cases reported in the English-language literature. About half of the patients with DET are euthyroid, whereas the remaining are hypothyroid (*3*). As seen in this patient, the ETT may become apparent and detected during times of increased physiologic demand for thyroid hormones, such as pregnancy, puberty, and adolescence (*1*). The sensitivity of scintigraphy to detect ETT is higher than that of ultrasonography alone, as is also evident in this case, in which ultrasonography could characterize only the clinically evident lingual swelling but not ETT in the floor of the mouth (*4*). The fact that thyroid scintigraphy and SPECT/CT can also help to distinguish ETT from other midline cervical masses (e.g., thyroglossal duct cysts) may help prevent unnecessary surgery (*3*). In addition to its rarity,

this case highlights the importance of thyroid scintigraphy and SPECT/CT in identifying and localizing ETT in a clinically diagnosed case of ectopic lingual thyroid that, in turn, was a case of DET.

CONCLUSION

DET is a very rare entity. ^{99m}Tc-pertechnetate thyroid scintigraphy and SPECT/CT are valuable in evaluation of ETT and DET because of high sensitivity and specificity for detecting thyroid tissue. The addition of SPECT/CT to planar imaging further enhances its value by helping in precise anatomic localization and detection of a small ETT that may otherwise be missed on clinical examination or morphologic imaging modalities such as ultrasonography alone.

DISCLOSURE

No potential conflict of interest relevant to this article was reported.

REFERENCES

1. Guerra G, Cinelli M, Mesolella M, et al. Morphological, diagnostic and surgical features of ectopic thyroid gland: a review of literature. *Int J Surg.* 2014;12(suppl 1): S3–S11.
2. Matta-Coelho C, Donato S, Carvalho M, Vilar H. Dual ectopic thyroid gland. *BMJ Case Rep.* 2018;2018:bcr2018225506.
3. Noussios G, Anagnostis P, Goulis DG, Lappas D, Natsis K. Ectopic thyroid tissue: anatomical, clinical, and surgical implications of a rare entity. *Eur J Endocrinol.* 2011;165:375–382.
4. Karakoc-Aydiner E, Turan S, Akpinar I, et al. Pitfalls in the diagnosis of thyroid dysgenesis by thyroid ultrasonography and scintigraphy. *Eur J Endocrinol.* 2012; 166:43–48.

Evaluation of Hepatopulmonary Syndrome with ^{99m}Tc-Macroaggregated Albumin Scintigraphy

Fathima Fijula Palot Manzil, Iqbal Haq, and Xiaofei Wang

Department of Radiology, University of Arkansas for Medical Sciences, Little Rock, Arkansas

Hepatopulmonary syndrome is characterized by intrapulmonary vascular dilatation causing hypoxemia in patients with liver disease. ^{99m}Tc-macroaggregated albumin (^{99m}Tc-MAA) scintigraphy has diagnostic value in suspected hepatopulmonary syndrome by detecting a clinically significant right-to-left shunt. In the presence of cirrhosis, ^{99m}Tc-MAA scanning with extrapulmonary organ visualization is specific for intrapulmonary shunting. ^{99m}Tc-MAA scintigraphy also provides the added value of quantification of the shunt.

Key Words: hepatopulmonary syndrome; ^{99m}Tc-MAA scintigraphy; intrapulmonary shunt

We report a case of hepatopulmonary syndrome (HPS) confirmed by ^{99m}Tc-macroaggregated albumin (^{99m}Tc-MAA) scintigraphy. HPS is an uncommon condition in which there is hypoxemia due to intrapulmonary vascular dilatation in the context of liver disease.

CASE REPORT

A 38-y-old man presented with dyspnea on exertion and thrombocytopenia. The patient was extensively evaluated, including MRI and liver biopsy, which demonstrated cirrhosis. The patient had a consistently low partial pressure of oxygen ($\approx$55 mm Hg). The alveolar arterial oxygen gradient was 25 mm Hg. A transthoracic echocardiogram with saline showed microbubbles in the left heart chambers 4 cardiac cycles after contrast appearance in the right heart, suggestive of an extracardiac shunt—likely pulmonary arteriovenous malformation. ^{99m}Tc-MAA lung scintigraphy after injection of 144.3 MBq (3.9 mCi) of radiotracer showed increased tracer uptake in the brain, kidneys, spleen, and subcutaneous tissues, indicating a right-to-left shunt—likely an intrapulmonary shunt in the setting of cirrhosis (Fig. 1). On quantification, the brain shunt fraction was 20.3% (Fig. 2). An elevated alveolar–arterial gradient with a partial pressure of oxygen of less

than 60, echocardiographic and scintigraphic evidence of intrapulmonary shunting, and no known chronic lung disease in the setting of cirrhosis were consistent with HPS in
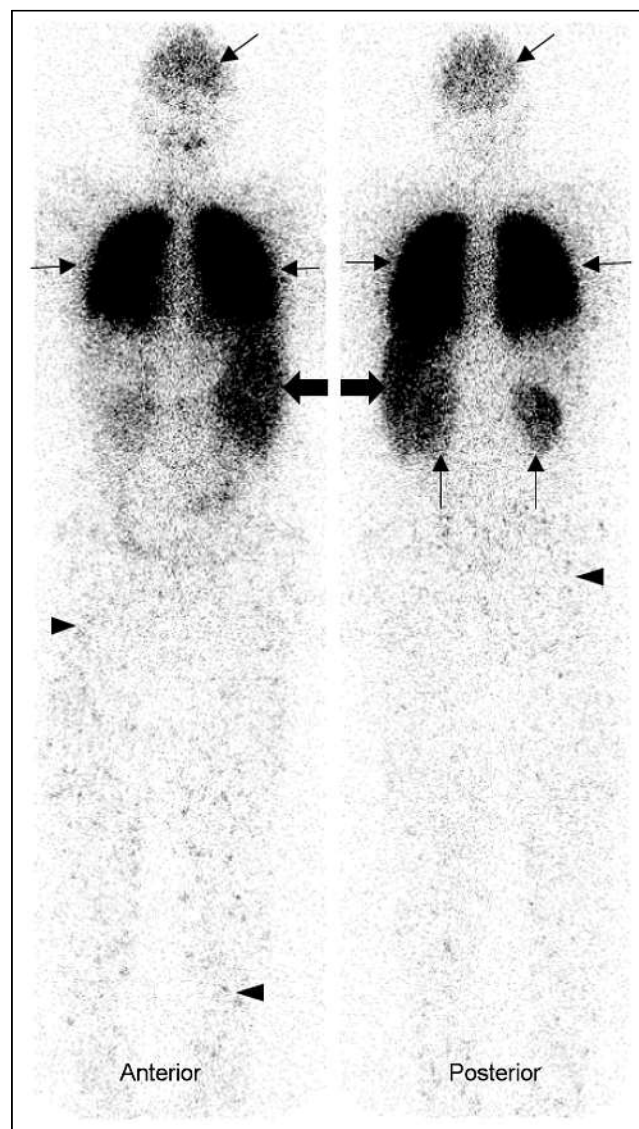

FIGURE 1. ^{99m}Tc-MAA planar whole-body image in anterior and posterior projections show intense radiotracer uptake in lungs (thin transverse arrows) and shunted activity in brain (oblique arrows), spleen (thick transverse arrows), kidneys (vertical arrows), and subcutaneous tissues (arrowheads).

Right lateral brain   Left lateral brain

Anterior lungs   Posterior lungs

Pulmonary brain shunt = $\frac{\text{Geometric mean (GM) brain}}{\text{GM brain + GM lung}} \times 100 = 20.3\%$ (Normal: <6%)
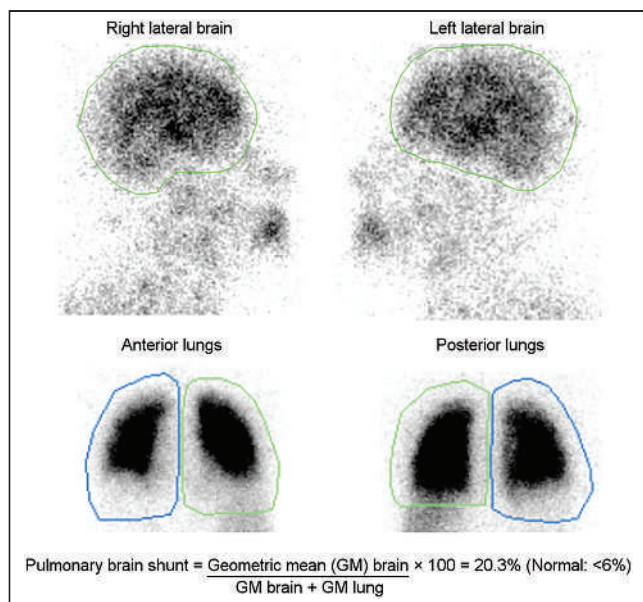
FIGURE 2. Planar images of brain in right and left lateral projections and of lungs in anterior and posterior projections show areas of interest drawn to calculate lung–brain shunt.

our patient. The patient is currently undergoing evaluation for a liver transplant.

DISCUSSION

The pathognomonic intrapulmonary vascular dilatations in HPS cause impaired oxygen transfer from alveoli to red blood cells, inducing an intrapulmonary right-to-left shunt. In HPS, hypoxemia and dyspnea may increase in the upright position because of preferential perfusion of dilated vessels in the lung bases (1). The severity of HPS based on the degree of hypoxemia is described as mild, moderate, severe, and very severe if PaO_2 is 80 or more, 60–79, 50–59, and less than 50 mm Hg, respectively. HPS is frequently underdiagnosed (2). Currently, the only effective treatment for HPS is liver transplantation. It is important to diagnose HPS as early as possible to expedite treatment for a better outcome. Hypoxemia can be distinguished from HPS and other etiologies through bubble echocardiography, with arrival of bubbles in the left heart at least 3 cardiac cycles after contrast appearance in the right heart, or through ^{99m}Tc-MAA scintigraphy showing uptake in the brain (3). ^{99m}Tc-MAA scintigraphy is more specific than echocardiography and also can quantify and measure the degree of the shunt.

Under good quality control measures and absence of a shunt, no extrapulmonary organs should be visualized, as the injected ^{99m}Tc-MAA particles are trapped in the pulmonary microvasculature. However, when there is an intrapulmonary shunt, a fraction of the particles enters the systemic circulation, leading to visualization of other organs and systems. The standard technique of calculating the percentage of lung–brain shunting is done by drawing regions of interest around the brain and lungs and determining the geometric mean of the brain and lung counts (4,5). HPS is suggested if the alveolar arterial oxygen gradient is at least 15 mm Hg or at least 20 mm Hg for patients more than 64 y old and the pulmonary brain shunt quantitative index for ^{99m}Tc-MAA is at least 6%. A whole-body ^{99m}Tc-MAA uptake calculation is another method for detecting intrapulmonary vascular dilatation (6).

CONCLUSION

Patients with a history of chronic liver disease along with dyspnea should be further evaluated for possible HPS. In patients with an elevated alveolar arterial gradient, bubble echocardiography or ^{99m}Tc scintigraphy aids in diagnosis of an intrapulmonary shunt. Though echocardiography is sensitive, it lacks specificity by providing false-positive results in patients with concomitant lung diseases. A positive ^{99m}Tc-MAA scan with tracer uptake in extrapulmonary organs in a cirrhotic patient is specific for HPS. ^{99m}Tc-MAA scintigraphy also quantifies the extent of a shunt.

DISCLOSURE

No potential conflict of interest relevant to this article was reported.

REFERENCES

1. Koch DG, Fallon MB. Hepatopulmonary syndrome. *Clin Liver Dis.* 2014;18:407–420.
2. Hoeper MM, Krowka MJ, Strassburg CP. Portopulmonary hypertension and hepatopulmonary syndrome. *Lancet.* 2004;363:1461–1468.
3. Rodríguez-Roisin R, Krowka MJ. Hepatopulmonary syndrome: a liver-induced lung vascular disorder. *N Engl J Med.* 2008;358:2378–2387.
4. Abrams GA, Nanda NC, Dubovsky EV, et al. Use of macroaggregated albumin lung perfusion scan to diagnose hepatopulmonary syndrome: a new approach. *Gastroenterology.* 1998;114:305–310.
5. Surasi DS, Manapragada P, Bhambhvani P. Lung perfusion imaging in hepatopulmonary syndrome using ^{99m}Tc macroaggregated albumin. *J Nucl Cardiol.* 2015;22:586–588.
6. Zhao H, Tsauo J, Zhang XW, et al. Technetium-99m-labeled macroaggregated albumin lung perfusion scan for diagnosis of hepatopulmonary syndrome: a prospective study comparing brain uptake and whole-body uptake. *World J Gastroenterol.* 2020;26:1088–1097.

Bilateral Pelvic Kidney Masquerading as Horseshoe Kidney in Fanconi Anemia

Tanigassalam Sindhu[1], Venkata Subramanian Krishnaraju[1], Ashwani Sood[1], Piyush Aggarwal[1], Anish Bhattacharya[1], Deepak Bansal[2], and Pritam Singha Roy[2]

[1]Department of Nuclear Medicine, Post Graduate Institute of Medical Education and Research, Chandigarh, India; and [2]Department of Paediatrics, Post Graduate Institute of Medical Education and Research, Chandigarh, India

Fanconi anemia (FA) is a genetic disease associated with a risk of congenital malformations, bone marrow failure, and a predisposition to cancer. Congenital abnormalities of the kidney and urinary tract are not infrequent in FA, with renal ectopia being among them. The incidence of bilateral pelvic kidney is restricted to only a few reported cases; however, its association with FA has never, to our knowledge, been reported in the literature. We present a case of FA in a girl whose ^{99m}Tc-dimercaptosuccinic acid planar scan showed apparently fused kidneys, which were confirmed to be bilateral pelvic kidney on hybrid cross-sectional imaging.

Key Words: Fanconi anemia; bilateral pelvic kidney; DMSA; fused kidney; SPECT/CT

Fanconi anemia (FA) is an inherited disease associated with various congenital and developmental abnormalities. The incidence of congenital abnormalities of the kidneys and urinary tract is reported to be around 30% (*1*). It is important to include anatomic and functional imaging studies in the diagnostic workup of FA. Furthermore, knowledge of renal disease is important in the management of FA at diagnosis and when planning during the clinical course (*2*). To the best of our knowledge, the incidence of bilateral pelvic kidney associated with FA has never been reported in the literature. We present an interesting case of FA with bilateral pelvic kidney masquerading as fused kidneys on a ^{99m}Tc-dimercaptosuccinic acid (^{99m}Tc-DMSA) planar scan; the fused kidneys were confirmed to be bilateral pelvic kidney on SPECT/CT imaging.

CASE HISTORY

An 11-y-old girl presented to the pediatric emergency ward with complaints of easy fatiguability and decreased oral intake for the last 10 d. Her blood investigations revealed pancytopenia. She received 2 transfusions of packed red blood cells and

underwent bone marrow aspiration to evaluate the cause of the pancytopenia. She had experienced similar complaints in the past, for which she was given blood transfusions at other hospitals. Clinical manifestations and detailed laboratory tests revealed that the patient had FA. An abdominal radiograph followed by abdominal ultrasound raised the possibility of bilateral fused, low-lying kidneys. She was referred to our department for functional imaging in the form of a ^{99m}Tc-DMSA scan to diagnose the fused kidneys and to evaluate their individual functioning. A planar scan of the abdomen was obtained 3 h after intravenous injection of 92.5 MBq (2.5 mCi) of ^{99m}Tc-DMSA. The images, which were acquired in anterior, posterior, right lateral, and left lateral views (Figs. 1A, 1B, 1E, and 1F), revealed bilateral low-lying kidneys in a paramedian location, with the kidneys appearing to be fused at the midline. The differential function for the left and right kidneys was 43% and 57%, respectively. However, SPECT/CT acquired for confirmation showed the kidneys to be separate from each other on transaxial and coronal images from the low-dose CT portion of the study (Figs. 1C and 1G) and on the corresponding fused SPECT/CT images (Figs. 1D and 1H).

DISCUSSION

FA is an inherited disease resulting from defects in the FA/BRCA pathway for DNA interstrand crosslink repair. Around a third to a half of these patients may have associated congenital abnormalities of the kidneys and urinary tract pointing to a deranged normal ascent of the embryonic kidneys and resulting in iliac or pelvic renal ectopia (*2,3*). The incidence of pelvic kidney is around 1 in 2,200–3,000 people; however, bilateral pelvic kidney is a very rare developmental renal anomaly and is diagnosed mostly when patients develop symptoms due to obstruction, infection, and renal calculi (*4*). Anatomic and functional evaluation of renal malformations in patients with FA is important for the diagnostic work-up and for long-term management to improve the outcome by appropriate treatment. Every patient with renal abnormalities should be evaluated first with ultrasound and then by other imaging modalities. ^{99m}Tc-DMSA SPECT/CT has the advantage of providing both an anatomic and a functional evaluation for ectopic renal tissue anywhere from the thorax to the pelvis with a high degree of sensitivity in a single session (*5*).
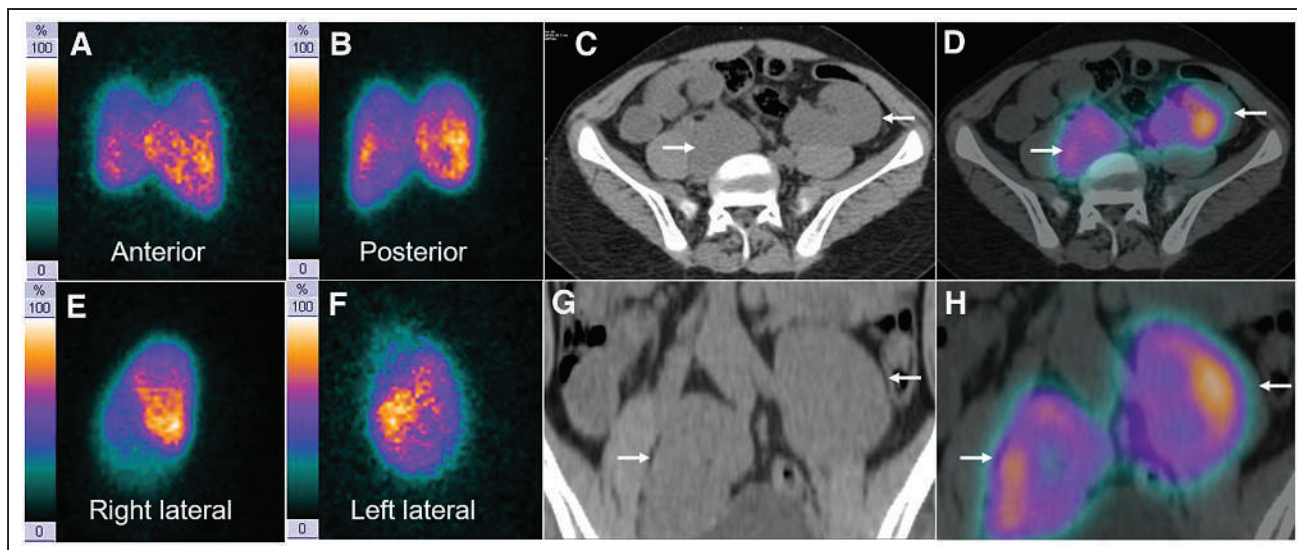
FIGURE 1. ^{99m}Tc-DMSA planar scan in anterior, posterior, right, and left lateral views (A, B, E, and F) revealed low-lying kidneys bilaterally in paramedian location, with the 2 kidneys apparently fused at midline. On transaxial and coronal SPECT/CT, kidneys were clearly separate from each other both on low-dose CT component (C and G, arrows) and on fused images (D and H, arrows).

CONCLUSION

Our case highlights the role of SPECT/CT to detect morphologic anomalies and cortical defects and to avoid misinterpretation of findings on planar scintigraphy.

DISCLOSURE

No potential conflict of interest relevant to this article was reported.

REFERENCES

1. Glanz A, Fraser FC. Spectrum of anomalies in Fanconi anaemia. *J Med Genet.* 1982;19:412–416.
2. Sathyanarayana V, Lee B, Wright NB, et al. Patterns and frequency of renal abnormalities in Fanconi anaemia: implications for long-term management. *Pediatr Nephrol.* 2018;33:1547–1551.
3. Kottemann MC, Smogorzewska A. Fanconi anaemia and the repair of Watson and Crick DNA crosslinks. *Nature.* 2013;493:356–363.
4. Knipe HC. A case of bilateral pelvic kidneys. *J Med Imaging Radiat Oncol.* 2019; 63:639–640.
5. Sözübir S, Demir H, Ekingen G, Güvenç BH. Ectopic thoracic kidney in a child with congenital diaphragmatic hernia. *Eur J Pediatr Surg.* 2005;15:206–209.

An Unusual Cause of γ-Camera Contamination

David L. Francia[1], Kathy P. Willowson[1,2], and Dale L. Bailey[1,3]

[1]Department of Nuclear Medicine, Royal North Shore Hospital, Sydney, New South Wales, Australia; [2]Institute of Medical Physics, University of Sydney, Sydney, New South Wales, Australia; and [3]Faculty of Medicine and Health, University of Sydney, Sydney, New South Wales, Australia

This report is of an unusual case of radioactive contamination of a γ-camera after scanning 2 individuals who had been treated 3 d beforehand with ablative doses of ^{131}I for thyroid cancer. A combination of observed half-life and pulse-height spectroscopy was used to identify the contaminant. The source of the contamination was eventually found to be a single human hair, presumably contaminated when the individual was sucking her hair while waiting for the scan to start. This case demonstrates that hair can be contaminated by saliva and potentially other bodily fluids in the postablation setting and that using physical measurements, in this case the observed half-life and pulse-height spectroscopy, can be useful in identifying the radioactive contaminant.

Key Words: instrumentation; quality assurance; radiation physics; contamination; gamma camera; radioiodine

The nuclear medicine department in our institution has 3 dual-detector γ-cameras and 1 PET/CT camera. Two of the γ-cameras are SPECT/CT devices. Of these, one has a thicker (16 mm) detector crystal than is standard (Symbia Intevo 6; Siemens Healthineers) and so is preferentially used when imaging higher-energy γ-photons from radionuclides such as ^{131}I (364 keV), ^{177}Lu (208 keV), ^{67}Ga (93, 185, and 300 keV), ^{67}Cu (93 and 185 keV), and ^{111}In (171 and 245 keV). During a routine acquisition of a low-dose ^{131}I scan on this γ-camera on a Monday (the first day of our working week), a low level of contamination was noticed on one of the detectors (Fig. 1). An intrinsic uniformity image acquired using ^{99m}Tc as part of routine quality control earlier that day did not show any evidence of contamination. Up to the time that the contamination was noticed, only patients who had been administered ^{67}Ga and ^{131}I had been scanned.

QUALITY ANALYSIS

The system was inspected, and possible sources of the contamination were checked. The contamination remained fixed in location with respect to the detector when the detector heads were rotated to different angular positions, suggesting that the contamination was on the collimator or detector rather than on the scanning bed, the floor, or other nondetector location. The external face of the collimator was thoroughly cleaned with a decontamination solution, but the contamination persisted. The collimators were removed and inspected, but no obvious source of the contamination was identified. The Symbia Intevo 6 SPECT/CT system has a combination of automated collimator exchanger for low- and medium-energy collimators plus an additional manual cart exchanger for high-energy collimators. Because of the persisting contamination, the system was taken out of service for the rest of the day.

The following day, the contamination was still present, suggesting that it was not from a short-lived radionuclide such as ^{99m}Tc. Images using ^{67}Ga energy window settings were acquired on both detectors, and the contamination was clearly seen (Fig. 2, top row). Count rates from the previous day's images were determined and compared with the current ones in an attempt to assess the rate of decay of the contamination. A pulse-height energy spectrum was also acquired with the medium-energy collimators fitted.

A region of interest drawn over the area of contamination was corrected for background from an identical region of interest on the same detector in a mirrored location on the images acquired on the successive days. The decline in the count rate suggested a half-life of around 7–8 d. Using the system's pulse-height analyzer, we found that the energy spectrum demonstrated a slight peak above background at around 360 keV. This finding suggested that the contamination was from ^{131}I. Further images were acquired using an ^{131}I window (Fig. 2, bottom row), which showed the contamination with better definition and a higher count rate.

On the day the contamination was first noticed, the subjects had been scanned after treatment with ablative oral doses of ^{131}I (by capsule) for primary thyroid cancer or had been scanned using ^{67}Ga-citrate because of suspected infection. It is our institution's practice to hospitalize all subjects treated with at least 1 GBq of ^{131}I. Those subjects who are treated with the largest doses that we deliver (6 GBq) are preferentially admitted to the hospital, treated Friday, and then scanned before discharge Monday morning (∼64 h later). This practice allows for extended decay and elimination of the ^{131}I from the body, compared with our normal
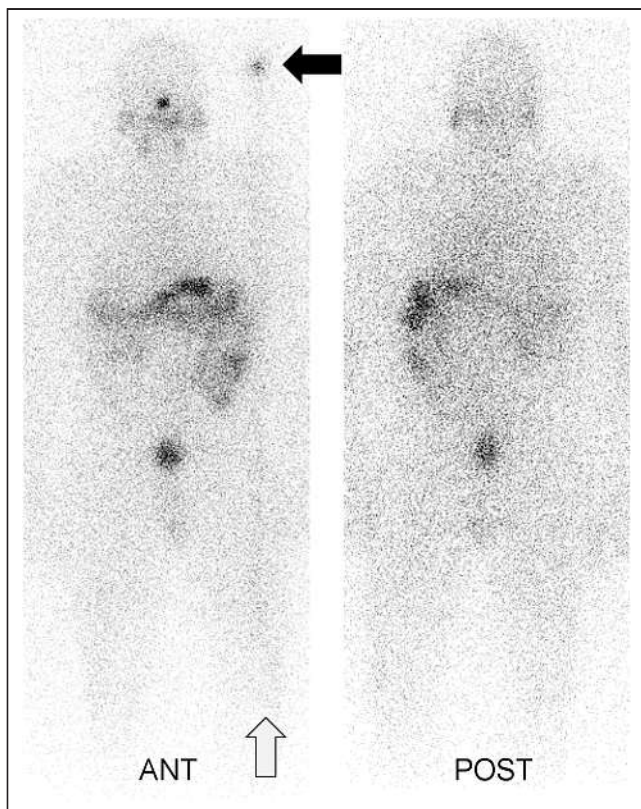
FIGURE 1. Whole-body planar post–recombinant thyroid-stimulating hormone ^{131}I (80 MBq) scan demonstrating contamination (solid arrow) on anterior projection (detector 1). Effect of fixed site of contamination in whole-body scan where body moves continuously under detector's z-direction is to introduce streak down image in line with site of contamination (open arrow).
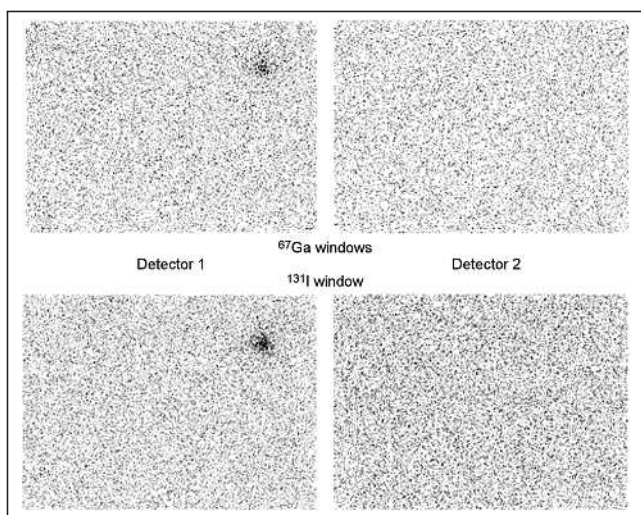

FIGURE 2. Images on both detectors without any source of radioactivity present and collimators in place, demonstrating contamination on detector 1. Images are shown in both summed triple-window pulse-height analyzer settings for ^{67}Ga (top row) and single window for ^{131}I (bottom row).

practice, which is to scan and discharge the subjects treated with 1–4 GBq of ^{131}I approximately 40 h after their treatment (admitted Monday afternoon for treatment and discharged Wednesday morning, or admitted Wednesday afternoon and discharged Friday morning). On the day in question, postablation ^{131}I scans had been acquired on 2 female subjects, each treated with 6 GBq of ^{131}I on the previous Friday afternoon. No contamination was visible in either of these subjects' scans, however, presumably because the amount of ^{131}I contained within the body in these individuals remained much higher than in the diagnostic scan, which demonstrated the artifact. However, although the radionuclide had been identified, the source of the contamination was still not identified.

The collimators were removed to allow further inspection. On closer inspection of the detector surface, a single dark human hair was found on the detector (Fig. 3). The hair was removed and placed on the bench, and a handheld radiation survey meter was used to test whether the hair was contaminated. This, in fact, turned out to be the case, as it registered an increase in event rate on the meter and contamination was no longer evident on the γ-camera detector. The contamination therefore had to be from 1 of the 2 ^{131}I ablation subjects who had been treated and hospitalized over the weekend. In retrospect, it was noted that the younger of the 2 subjects who had been treated had long, dark hair and was particularly anxious. One of our staff members recalled that while waiting for her scan, she had been sucking the ends of her hair. We therefore presume that the contamination came from saliva from her mouth.

This unusual source of contamination illustrates that saliva on a single human hair was able to contaminate the scanner. It is not clear how the hair came to be lodged between the underside of the collimator and the detector crystal surface.

CORRECTIVE ACTION

There were 3 observations that led to identification of this contamination. First, the fixed relationship between the contamination and the location on the detector—independent of the orientation of the γ-camera detectors—indicated that
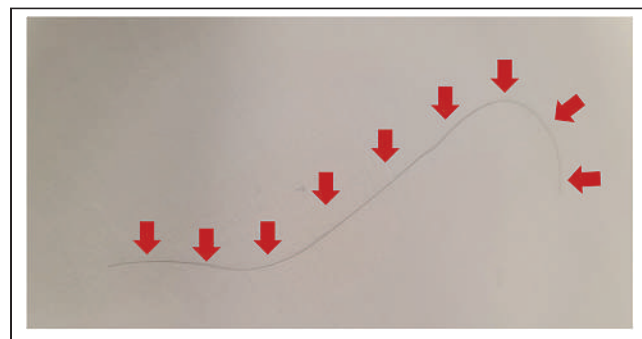

FIGURE 3. Hair that was found to be source of contamination.

the contamination was intrinsic to the detector and not from an external source such as the scanning bed or the floor. Second, the observed count rate over the first 2 d (in a ^{67}Ga pulse-height analyzer window) appeared to decrease, with a half-life of around 7 d, which excluded some short-lived tracers such as [99m]Tc. This count rate also suggested that the contaminant was not [67]Ga (half-time, 78 h) and was more likely to be [131]I (half time, 8 d). Finally, pulse-height spectroscopy using the NaI(Tl) detector and pulse-height analyzer of the γ-camera showed a faint peak at around 360 keV, again supporting the case for the contaminant to be [131]I. Once the identified hair was found and removed, the γ-camera did not display any further contamination.

VERIFICATION OF EFFECTIVENESS

The routine practice in our institution is to instruct all subjects treated with ^{131}I for thyroid cancer to take a shower and wash their hair thoroughly on the morning of the day that they are due to be discharged from the hospital and before they have their postablation ^{131}I scan, as it is known that human hair can become contaminated with [131]I (*1,2*). Our staff considers a possible site of contamination to be a subject's hair, as well as any site that a subject's saliva, sebum, or other bodily fluids (e.g., nasal secretions, mucus, and gastric reflux) might be able to contaminate. Using the physical characteristics (half-life, positional orientation, pulse-height analyzer of energy of emissions) of the contamination is also more relied upon now to quickly identify contamination and location. The ability for a contamination source to be located between the collimator and the detector surface is also considered.

The possibility of contamination persistence increases when large amounts of long-lived radiation are used for therapy (*3*), compared with most diagnostic procedures, which use lower amounts of radionuclides with typically shorter half-lives. This possibility is likely to become more of an issue as the number of radionuclide therapies administered in nuclear medicine departments increases.

CONCLUSION

Contamination of the γ-camera can arise from several causes both external to the scanning system and in the system itself. Early assessment using translation and rotation of the detectors should determine whether the contamination has a fixed geometry relative to the system or is external. Using physical characteristics such as the photon energy of the contamination and the half-life can help to identify the radionuclide and, therefore, the potential cause of the contamination. In this case, a single human hair that had become contaminated with ^{131}I, presumably due to saliva, was able to become lodged between the underside of the collimator and the detector surface.
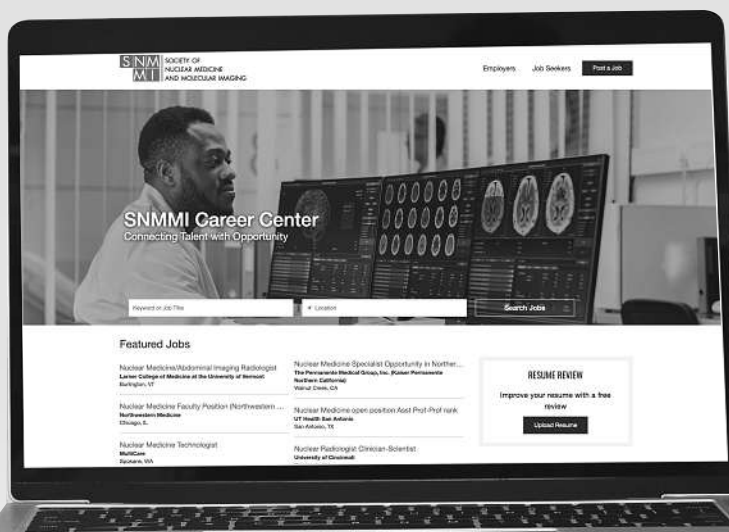
DISCLOSURE

No potential conflict of interest relevant to this article was reported.

REFERENCES

1. Zakavi SR, Kakhki VD. Exercise-induced radio-iodine accumulation in scalp and hair during admission of ^{131}I therapy for thyroid cancer. *Thyroid.* 2006;16: 1185–1186.
2. Yan D, Doss M, Mehra R, Parsons RB, Milestone BN, Yu JQ. False-positive scalp activity in ^{131}I imaging associated with hair coloring. *J Nucl Med Technol.* 2013;41: 43–45.
3. Dhingra J, Santana C, Harvey J, et al. Root cause analysis of Na[131]I contamination. *J Nucl Med Technol.* 2021;49:350–353.

UNITED STATES POSTAL SERVICE ®

Statement of Ownership, Management, and Circulation
(All Periodicals Publications Except Requester Publications)

1. Publication Title	2. Publication Number	3. Filing Date
JOURNAL OF NUCLEAR MEDICINE TECHNOLOGY	966 – 500	10/1/2022

4. Issue Frequency	5. Number of Issues Published Annually	6. Annual Subscription Price
QUARTERLY	4	$249 US/Can; $265 Intl

7. Complete Mailing Address of Known Office of Publication *(Not printer) (Street, city, county, state, and ZIP+4®)*

1850 Samuel Morse Dr., Reston, VA 20190

Contact Person: Rebecca Maxey
Telephone *(Include area code)*: 703-652-6772

8. Complete Mailing Address of Headquarters or General Business Office of Publisher *(Not printer)*

1850 Samuel Morse Dr., Reston, VA 20190

9. Full Names and Complete Mailing Addresses of Publisher, Editor, and Managing Editor *(Do not leave blank)*

Publisher *(Name and complete mailing address)*

Society of Nuclear Medicine and Molecular Imaging, 1850 Samuel Morse Dr., Reston, VA 20190

Editor *(Name and complete mailing address)*

Kathy S. Thomas, 1850 Samuel Morse Dr., Reston, VA 20190

Managing Editor *(Name and complete mailing address)*

Rebecca Maxey, 1850 Samuel Morse Dr., Reston, VA 20190

10. Owner *(Do not leave blank. If the publication is owned by a corporation, give the name and address of the corporation immediately followed by the names and addresses of all stockholders owning or holding 1 percent or more of the total amount of stock. If not owned by a corporation, give the names and addresses of the individual owners. If owned by a partnership or other unincorporated firm, give its name and address as well as those of each individual owner. If the publication is published by a nonprofit organization, give its name and address.)*

Full Name	Complete Mailing Address
Society of Nuclear Medicine and Molecular Imaging	1850 Samuel Morse Dr., Reston, VA 20190

11. Known Bondholders, Mortgagees, and Other Security Holders Owning or Holding 1 Percent or More of Total Amount of Bonds, Mortgages, or Other Securities. If none, check box → ☒ None

Full Name	Complete Mailing Address

12. Tax Status *(For completion by nonprofit organizations authorized to mail at nonprofit rates) (Check one)*
The purpose, function, and nonprofit status of this organization and the exempt status for federal income tax purposes:
☒ Has Not Changed During Preceding 12 Months
☐ Has Changed During Preceding 12 Months *(Publisher must submit explanation of change with this statement)*

PS Form **3526**, July 2014 *[Page 1 of 4 (see instructions page 4)]* PSN: 7530-01-000-9931   **PRIVACY NOTICE:** See our privacy policy on *www.usps.com.*

---

13. Publication Title	14. Issue Date for Circulation Data Below
JOURNAL OF NUCLEAR MEDICINE TECHNOLOGY	SEPTEMBER 2022

15. Extent and Nature of Circulation			Average No. Copies Each Issue During Preceding 12 Months	No. Copies of Single Issue Published Nearest to Filing Date
a. Total Number of Copies *(Net press run)*			2303	2588
b. Paid Circulation *(By Mail and Outside the Mail)*	(1)	Mailed Outside-County Paid Subscriptions Stated on PS Form 3541 (Include paid distribution above nominal rate, advertiser's proof copies, and exchange copies)	2011	2176
	(2)	Mailed In-County Paid Subscriptions Stated on PS Form 3541 (Include paid distribution above nominal rate, advertiser's proof copies, and exchange copies)	0	0
	(3)	Paid Distribution Outside the Mails Including Sales Through Dealers and Carriers, Street Vendors, Counter Sales, and Other Paid Distribution Outside USPS®	127	229
	(4)	Paid Distribution by Other Classes of Mail Through the USPS (e.g., First-Class Mail®)	0	0
c. Total Paid Distribution *(Sum of 15b (1), (2), (3), and (4))*		▶	2139	2405
d. Free or Nominal Rate Distribution *(By Mail and Outside the Mail)*	(1)	Free or Nominal Rate Outside-County Copies included on PS Form 3541	0	0
	(2)	Free or Nominal Rate In-County Copies Included on PS Form 3541	0	0
	(3)	Free or Nominal Rate Copies Mailed at Other Classes Through the USPS (e.g., First-Class Mail)	0	0
	(4)	Free or Nominal Rate Distribution Outside the Mail *(Carriers or other means)*	26	26
e. Total Free or Nominal Rate Distribution *(Sum of 15d (1), (2), (3) and (4))*			26	26
f. Total Distribution *(Sum of 15c and 15e)*		▶	2165	2431
g. Copies not Distributed *(See Instructions to Publishers #4 (page #3))*		▶	138	157
h. Total *(Sum of 15f and g)*			2303	2588
i. Percent Paid *(15c divided by 15f times 100)*		▶	98.80%	98.93%

* If you are claiming electronic copies, go to line 16 on page 3. If you are not claiming electronic copies, skip to line 17 on page 3.

16. Electronic Copy Circulation		Average No. Copies Each Issue During Preceding 12 Months	No. Copies of Single Issue Published Nearest to Filing Date
a. Paid Electronic Copies	▶		
b. Total Paid Print Copies (Line 15c) + Paid Electronic Copies (Line 16a)	▶		
c. Total Print Distribution (Line 15f) + Paid Electronic Copies (Line 16a)	▶		
d. Percent Paid (Both Print & Electronic Copies) (16b divided by 16c × 100)	▶		

☒ I certify that 50% of all my distributed copies (electronic and print) are paid above a nominal price.

17. Publication of Statement of Ownership

☒ If the publication is a general publication, publication of this statement is required. Will be printed   ☐ Publication not required.

in the ___December 2022___ issue of this publication.

18. Signature and Title of Editor, Publisher, Business Manager, or Owner	Date
Rebecca Maxey	10/1/2022

We Are Here for Him
So He Is There for Her

Patient Convenience. Targeted Detection

At **Jubilant Radiopharma**, our pharmacies are ready to dispense **PSMA-11 (gallium Ga68 gozetotide)** to your PET imaging center. If your department needs flexibility, reliability and confidence contact your local nuclear sales manager for more information by scanning the **QR code** or visiting **www.jubilantradiopharma.com**

Proudly Offering Both

Illuccix®
(kit for the preparation of gallium Ga68 gozetotide injection)

LOCAMETZ®
(kit for the preparation of gallium Ga68 gozetotide injection)

Proud Leadership Circle Members of the SNMMI Value Initiative

JUBILANT RADIOPHARMA

Streamlined. Simple. Accurate.

CRC® Dose Calibrator Family

Combine the speed and accuracy you need to measure and prepare doses with the performance and reliability that you've come to expect in one of the industry's finest packages.

CRC® - PC Smart Chamber
Network Ready with Remote Connectivity
The Most Advanced in Dose Calibration.

CRC®-55tPET Dose Calibrator (Touch Screen)
Speed and accuracy to measure
and prepare doses.

Driving Innovation… Together

Two leading brands of nuclear medicine products and technology, the
Capintec™ and **Biodex™** teams have joined forces under Mirion Medical.

CAPINTEC
A MIRION MEDICAL COMPANY

Visit capintec.com to learn
how we can support your
unique requirements.